Stony Brook University

Bose Gases in Tailored Optical and Atomic Lattices

A Dissertation Presented

by

Bryce Russell Gadway

to

The Graduate School

in Partial Fulfillment of the Requirements

for the Degree of

Doctor of Philosophy

in

Physics

Stony Brook University

August 2012

Stony Brook University

The Graduate School

Bryce Russell Gadway

We, the dissertation committee for the above candidate for the Doctor of Philosophy degree, hereby recommend acceptance of this dissertation.

Dominik A. Schneble – Dissertation Advisor
Associate Professor, Department of Physics and Astronomy

Harold J. Metcalf – Chairperson of Defense
Distinguished Teaching Professor, Department of Physics and Astronomy

Tzu-Chieh Wei
Assistant Professor, C. N. Yang Institute for Theoretical Physics,
Department of Physics and Astronomy

Robert Konik
Associate Physicist
Brookhaven National Laboratory

This dissertation is accepted by the Graduate School.

Charles Taber
Interim Dean of the Graduate
School

Abstract of the Dissertation

Bose Gases in Tailored Optical and Atomic Lattices

by

Bryce Russell Gadway

Doctor of Philosophy

in

Physics

Stony Brook University

2012

Quantum degenerate atomic gases offer a unique platform for the exploration of a wide variety of interacting many-body systems in a pristine environment, based on a set of powerful tools for the coherent control of the atoms' internal and external degrees of freedom. Here, we present experimental studies of strongly interacting bosonic mixtures in one-dimensional (1D) systems, in which the mobilities of the two species are independently controlled with a state-selective optical lattice. In a first experiment, we freeze out the tunneling of one species from a binary mixture, and study the formation of "quantum emulsion" states, where immobile atoms serve as a static, random disorder for a more mobile species. We investigate the 1D superfluid-to-insulator transition in the presence of this disorder, and make comparisons to the effects of quasi-disorder from an incommensurate optical lattice. We observe enhanced localization in the more random potential, highlighting the important role of correlations in disordered systems. Through a combined measurement of transport, localization, and excitation

spectra, we are able to obtain strong evidence for observation of a disordered, insulating quantum phase, the 1D Bose glass.

In a second experiment, we introduce a new experimental technique for the characterization of ultracold gases held in optical lattices. In analogy to neutron diffraction from solids, we use atomic de Broglie waves to non-destructively probe the spatial structure of 1D Mott insulators through elastic Bragg diffraction, and to probe inelastic band-structure excitations of more weakly interacting 1D Bose gases. Furthermore, we use the diffraction of matter waves to detect the formation of forced-antiferromagnetic ordering in a crystalline atomic spin mixture.

Lastly, we study the dynamical response of matter waves to a periodically pulsed, incommensurate optical lattice, a situation that realizes a system of two coupled kicked quantum rotors. We observe that the coupling induces a suppression of energy growth at quantum resonances, and a localization-to-delocalization transition in momentum space for off-resonant driving. Our observations confirm a long-standing theoretical prediction for the two-rotor system, and illustrate how classical behavior can emerge from the evolution of a simple quantum system.

Contents

List of Figures

Acknowledgements

First and foremost, I want to thank my advisor Dominik Schneble. Dominik has been a great teacher and a terrific advisor, and I've learned most of what I know about experimental physics from doing research in his group. He's always been around - typically in the lab - to offer advice and motivation, as well as coffee, Haribo gummy bears, and other fuels for research. It's been a really great opportunity to work in his group, and I'll always be thankful for my years spent here at Stony Brook.

Secondly, I want to thank my former labmate Daniel Pertot. Working alongside Daniel my first few years was a real godsend, as I was able to learn quite a lot about ultracold atoms and about experimental research in general from Daniel. He is an extremely smart and uniquely talented physicist, and also just a really nice guy and good friend. Also, I was very fortunate to have joined a fully functional BEC lab, forged through the hard work of Daniel and a number of other students over the years. In particular, I'd like to thank the students with whom I had some overlap, including Rebekah Schiller, Daniel Greif, René Reimann, and Matthias Vogt, as well as a number of undergraduate researchers, namely Bartosz Bogucki, Gaku Nagashima, Justin Tian and David Meltzer.

I'd also like to thank the current members of the BEC lab, Jeremy Reeves and Ludwig Krinner. It's been a pleasure to work alongside Jeremy for the past few years, as he's a really talented and dedicated physicist, and more recently with Ludwig, who has proven to be an invaluable addition to the BEC team. I'm looking forward to hearing about all the interesting physics they will be pursuing in the years to come.

Marty Cohen, a visiting scholar, has been a great help to the lab and to me, and I thank him for all of his advice and feedback over the years. I also would like to thank Tom Bergeman, who has been a theory collaborator with the group for several years, and who has helped provide insight on a number of topics. I'd like to thank Petr Anisimov for some really helpful conversations about quantum optics and quantum atom optics.

For first pointing me in the direction of Stony Brook many years ago, I

thank my undergraduate advisor, Kiko Galvez. Since arriving at Stony Brook, no one has helped me to maneuver through life within the department more than Hal Metcalf. Hal has also been a great teacher over the years, and I'd like to thank him for all his help. I would also like to thank Tom Weinacht, who has always been there to lend equipment, and to provide insightful questions and comments at the AMO seminars. I'd also like to thank John Noe of the Laser Teaching Center (LTC), as he and Marty helped to guide me through the physics of laser beams carrying orbital angular momentum.

I owe a lot of thanks to my thesis committee: Hal for serving as the chair, as well as the internal and external committee members Tzu-Chieh Wei and Robert Konik. For their help in guiding me towards the end of the graduate school tunnel, I am indebted to Department Chairs past and present, Peter Koch and Laszlo Mihaly, as well as to our Graduate Program Director Jac Verbaarschot. Moreover, I need to thank a number of others for their help in this regard, including Linda Dixon, Sara Lutterbie, Pat Peiliker, Socoro Delquaglio, Maria Hofer, Diane Diaferia, Maryann Lodato, and Nathan Leoce-Schappin. Thanks also to everybody in the machine shop, including Mark, Paul and Jeff, and to Rich and Bob for keeping the building running, and especially to Frank Chin, who was nice enough to give my car a jump one Winter day.

It has been a real pleasure to attend grad school with some really nice folks, and knowing them has made it a highly enjoyable experience. For lending me their optics, the occasional beer, and many delightful conversations, I'd like to thank fellow basement dwellers Chris, John, Dan, the original J. Reeves, Xiaoxu, Claire, Brian, Dominik, Marija, Peter, CoCo, Steve, Oumarou, Hyunoo, and Zhedong.

I also need to thank my friends from outside of physics for providing on many a night's a diversion from research – thanks Jeremy, Andy and all my other friends from Colgate, as well as Lance, Ryan, Merchant, Garret and other friends from home. More locally, I'd like to thank my good friends and housemates Peter and Kyle. I am indebted to them for many fond memories, and to their girlfriends Heather and Devon for many leftover meals.

I owe a great deal of thanks to my family, as over the years my brothers and sister, and all of their spouses and kids, have provided lots of encouragement. I am especially thankful for the support of my parents Russ and Pam, who throughout my life have been never-ending sources of love and encouragement.

Thanks to Andrea for being, in so many ways, the wind beneath my wings. The joys of doing physics research often pale in comparison to the joys of being with her, and her patience and support these past few years have made it possible for me to finish my Ph. D.

We thank the Optical Society of America and the American Physical Society for the right to reproduce, in part, several works that are discussed in this thesis.

We are also thankful for the generous support of the Research Foundation of the State of New York, the Department of Education, the Office of Naval Research, and the National Science Foundation.

Chapter 1

Introduction

Since the first observations of Bose–Einstein condensation [1–3] in dilute atomic gases in 1995 [4–7], atomic systems have served as an ideal testing ground for a myriad of many-body quantum phenomena. The subsequent achievements of quantum degeneracy in atomic Fermi gases [8, 9] and in ultracold molecular gases [10–12] (and near-degeneracy in gases of polar molecules [13, 14]) have made ultracold atomic physics an even more expansive and diverse arena of study. Ultracold quantum gases allow for the investigation of hydrodynamics, superfluidity, vortices and gases under rotation [15], collective enhancement and suppression [16, 17], transport in optical lattices [18], ultracold collisions, Feshbach resonances [19], few-body physics [20], and the BEC-BCS crossover [21–24], just to name a few. Atomic physics thus has made connections to a variety of other fields, including but not limited to condensed matter physics, nuclear physics, mathematical physics, and quantum information science.

Studies of strongly correlated many-body physics [25, 26] in atomic systems were opened up a decade ago with the experimental realization [27] of a quantum phase transition between superfluid and Mott insulator [28, 29], based on the controlled competition between tunneling and repulsive on-site interaction energies of bosons confined to an optical lattice. More recently, explorations of phase transitions to new quantum states have been undertaken in a number of strongly-interacting [30–32] and weakly-interacting [33–35] systems. Many of these have been aimed at studying systems of increased complexity in the form of, for example, long-range interactions (such as with dipolar gases [36]), disordered potentials [37], synthetic gauge potentials [38], and magnetic interactions [39]. Due to their versatility and dynamical tunability, experiments with ultracold quantum gases promise to be of continued importance for the study of strongly correlated physics [25, 26], including non-equilibrium dynamics [40] and quantum critical phenomena [41–43], as well as many other areas

of study.

In this thesis, I shall discuss several experiments with systems of both weakly- and strongly-interacting Bose gases, aimed at studying novel quantum phases of matter. In particular, we have studied several effects that can occur in strongly-interacting mixtures of bosonic gases in optical lattices, in which the mobility of each species can be independently controlled [44, 45]. The focus of these studies has been to look at effects going beyond those found in the single-species Bose–Hubbard model. In the case that the second species is a superfluid supporting phonon modes, it can mediate effective long-range (off-site) interactions between atoms of the first species. In contrast, if the second species consists of randomly positioned atoms pinned in place, it can act as a static disordered potential. Using such atomic impurities, we have studied spectral and transport properties of disordered one-dimensional Bose gases, and observed a disorder-induced shift of the superfluid-to-insulator transition [46]. The resulting state is insulating and has a flat excitation spectrum, consistent with the formation of a quantum emulsion state [47], whose properties are similar to those of an equilibrium Bose glass [28, 48]. Furthermore, the study of bosonic mixtures in state-dependent optical lattices has allowed us to develop a new experimental technique, based on the scattering of atomic matter-waves [49], which may possibly aid in future endeavors to characterize novel quantum states. Lastly, we have explored a localization-to-delocalization transition occurring in a system of weakly-interacting matter waves that are periodically "kicked" by two incommensurate optical lattices [50], realizing a system of coupled kicked quantum rotors.

Atomic mixtures in state-dependent lattices [44]

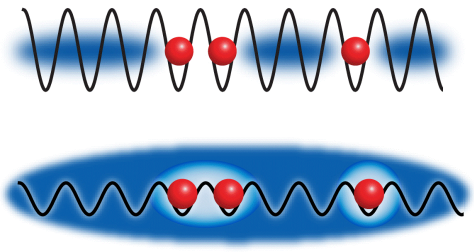

While the single-species Bose gas in an optical lattice still presents a very active area of study, new classes of physical effects can be found in systems of increased complexity. In this vein, Hubbard models involving more than one species have been studied both for Bose–Bose [51–53] and Bose–Fermi [54–57] mixtures (not to mention Fermi–Fermi mixtures or studies of SU(N) physics with multi-species alkaline-earth mixtures [58]). Aside from studies of quantum magnetism [59–62] that one may hope to explore at very low temperatures, novel interactions leading to physics beyond the single-species Hubbard model, with relevance to condensed matter systems, are expected to appear in two-species mixtures.

In studies with atoms of different masses (or effective masses in a lattice), lighter atoms can be used to mediate effective long-range interactions between the heavier particles [63, 64]. This can be thought of as the heavier particles coupling to phonons, or density excitations, in the lighter species. Phonon-coupling is important to many phenomena in real materials (while it is absent in optical lattices per se). In atomic systems, phonon-mediated coupling in multi-component mixtures may, for example, lead to the emergence of supersolidity [65]. In a study of the response of one species of atoms in a lattice to a second superfluid species ("bath"), we observed a reduction of the apparent superfluid coherence of the atoms near the superfluid-to-Mott transition. These observations are consistent with the formation of lattice polarons [63], composed of an atom on a given site and an induced density dip of the superfluid bath, resulting from repulsive interspecies interactions. In addition to a reduction of mobility as compared to bare atoms, such a polaronic dressing of atoms is predicted to lead to the formation of clusters due to induced off-site attraction [63, 64].

A second effect that can be studied with atomic mixtures is the influence of disorder. It has been proposed [66, 67] that localized atoms of one state, randomly placed at sites of an optical lattice, can serve as a nearly ideal form of random disorder. One advantage as compared to optical methods (such as two-color incommensurate lattices [68] or speckle potentials [69]) is that the correlations of such an atomic disordered potential decay on a very short length-scale, making the disorder essentially uncorrelated from site-to-site. For this situation, a metastable out-of-equilibrium state known as a quantum emulsion has been predicted [47], with properties very similar to those of a Bose glass [47, 70, 71]. In the experiment, we studied such a scenario in the limit where an added second species is much less mobile than the first, and observed a sharp decrease of the superfluid coherence due to interactions with the localized species, consistent with the formation of such a quantum emulsion.

Glassy behavior in a binary atomic mixture [46]

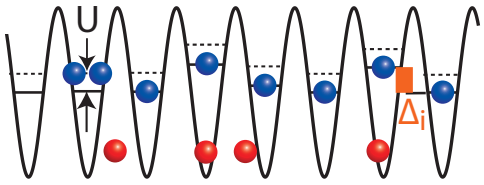

For non- and weakly-interacting particles placed into a random potential landscape at low energies [33, 34, 72, 73], Anderson localization can occur due to destructive interference between different quantum trajectories. It has been shown that weak repulsive interactions between particles can screen the disordered potential and can destroy such localization [74], leading to a

transition to a superfluid phase. On the other hand, the interplay between disorder and interactions is less clear-cut in systems of strongly-interacting particles, where the presence of interaction gaps (Mott-gaps) can result in insulating behavior even in the absence of disorder [28, 48]. When disorder is added, the presence of several mechanisms that each promote insulating behavior leads to the emergence of a new quantum phase known as the Bose glass, which is a gapless and compressible insulator, making it distinct from both the Mott insulator and the Anderson glass. Despite some preliminary experiments aimed at studying this Bose glass phase [68, 69, 75], no clear observations have been made to date.

In this experiment, we have studied one-dimensional (1D) lattice-trapped gases of bosons subject to disorder, formed by either localized atomic impurities or by an incommensurate optical lattice. In the first case, one species of a two-species mixture is pinned in place to a state-selective lattice, thereafter serving as a static disorder potential for the more mobile species. As mentioned earlier, it is predicted that the resultant disordered quantum emulsion should behave much like an equilibrium Bose glass state. One motivation for using the fine-grained impurity disorder [66], as opposed to standard optical disorders (pseudorandom incommensurate lattices [33, 68] and speckle patterns [69, 75]), is to explore the role of spatial correlation properties. For both types of disorder, we study the excitation and transport properties of the one-dimensional Bose gases, and for deep lattice confinement observe behavior consistent with the formation of a Bose glass, i.e. insulating behavior with a flat, gapless excitation profile. However, we find that near to the expected superfluid-to-insulator transition in 1D, the uncorrelated atomic disorder (representing "white noise") much more strongly drives the system towards an insulating, localized state. These observations reinforce the notion that the details of a disorder potential, such as its correlation properties, play an integral role in defining the ground state and excited state properties of a system, and that there is no universal phase diagram of the disordered Bose–Hubbard model defined solely by the amplitude of disorder.

Probing an ultracold-atom crystal with matter waves [49]

In recent years, several approaches have been taken for the characterization of strongly-interacting atomic gases in optical lattices. High-resolution *in-situ* imaging methods based on absorption [76] and fluorescence [77, 78] imaging of 2D planar systems have been utilized, as well as ones based on electron microscopy [79]. The observation of new quantum phases of matter, such as magnetically-ordered spin states and systems with non-trivial topological properties, will likely be enabled by advanced detection techniques.

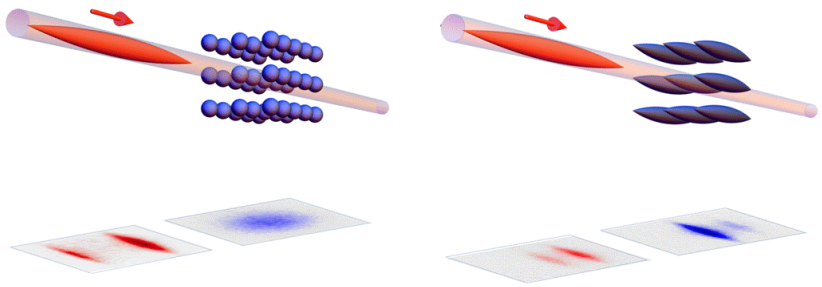

Here, motivated by the usefulness of matter-wave scattering techniques in various scientific disciplines, we explore the scattering of atomic matter waves from samples of strongly correlated gases confined in optical lattices [80], providing information on spatial ordering and excitations in these systems. Our method is analogous to the diffraction of electron and neutron de Broglie waves from crystalline materials, but at energies that are a billion times lower. We "shine" one-dimensional Bose gases (probe) onto a Mott insulator (target), and observe Bragg diffraction peaks that reveal the spatial ordering and localization of atoms on individual lattice sites. For weak lattice confinement, we study excitations and inelastic scattering processes in the target, connecting to 1D collisions between distinguishable bosons in the free-atom limit. The elastic scattering of matter waves provides a non-destructive *in-situ* interrogation technique, with a large tunability over the de Broglie wavelength, allowing for the probing of structure and ordering across a wide range of length scales. We demonstrated the versatility of our technique, as well as its suitability for characterizing spin-ordered phases, by using atomic de Broglie waves to detect forced-antiferromagnetic ordering in a crystalline atomic spin mixture.

Quantum dynamics of matter waves in a pulsed incommensurate lattice [50]

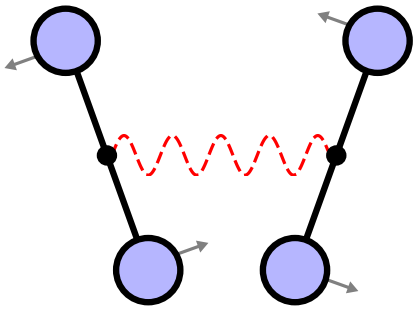

According to the correspondence principle [81] the predictions of quantum mechanics should, in the classical limit, be in agreement with those of classical mechanics. However, the conditions that specify "the classical limit" are not uniquely defined. For non-interacting particles, the classical limit can relate to the thermal occupation of a large number of quantized energy levels, where effects of quantization become less important to the description of the system. It may also be reached in

systems of a macroscopic number of interacting particles, which are faithfully described by the predictions of classical statistical mechanics. A fundamental, outstanding problem is how exactly classical behavior emerges in closed quantum systems, i.e. without invoking a coupling to some environment that is divorced from the system.

Here, we study the dynamics of a system that is based on the so-called δ-kicked rotor, in which a particle is subject to a time-periodic series of "kicks". In the classical case, the rotor dynamics are chaotic, giving rise to a diffusive increase of the action variable. However, in the quantum case, interferences lead to a suppression of growth by an effect known as *dynamical localization* [82], which is analogous to Anderson localization in one dimension [83]. The system that we specifically consider consists of *two* coupled kicked rotors. Here, the coupling has been predicted to induce diffusive, classical-like transport behavior [84]. We realized this system, for the first time, by periodically pulsing two incommensurate optical lattices onto an atomic Bose–Einstein condensate. For off-resonant kicking, we observed a breakdown of the dynamical localization that is found in the single-rotor case, relating to a transition from quantum to classical dynamics. Additionally, we observed a suppression of ballistic momentum-space transport in the case of resonant kicking of one of the rotors. Our findings shed new light on the correspondence between quantum and classical dynamics in multi-dimensional systems, and provide a route towards further experimental studies of higher-dimensional nonlinear, chaotic systems.

Outline of the thesis

In Chapter 2, I describe some basic theoretical concepts for weakly-interacting Bose–Einstein condensates in optical lattices. Chapter 3 provides a brief overview of the experimental methods used for producing and for probing our Bose–Einstein condensates. In Chapter 4, I discuss in more detail a general method for lattice depth determination based on Kapitza–Dirac diffraction in the long-pulse regime. Chapter 5 presents our experiments on a system of coupled kicked quantum rotors. Chapters 6 and 7 introduce some important theoretical and experimental methods used to describe and characterize systems of strongly-interacting bosons. In Chapter 8, I discuss our methods for creating atomic mixtures, and for creating lattices that address the atoms in a spin-dependent manner. I discuss in brief our study of strongly-interacting mixtures in such state-dependent lattices. Chapter 9 presents our study of quantum emulsion states in a one-dimensional bosonic mixture, where one species ("impurities") acts as an effectively random disorder potential for the second species. In Chapter 10, I describe our experiments aimed at determin-

ing the structural properties and excitations of strongly-interacting lattice gas "targets" via the scattering of weakly-interacting 1D matter-wave "probes", as well as detecting the introduction of forced-antiferromagnetic spin-ordering in a crystalline target. Lastly, Chapter 11 provides a conclusion and an outlook for future endeavors.

Publications of this PhD work (described either in part or in full):

- Chapter 3
  Versatile transporter apparatus for experiments with optically trapped Bose–Einstein condensates
  D. Pertot, D. Greif, S. Albert, B. Gadway, and D. Schneble
  J. Phys. B: At. Mol. Opt. Phys. **42**, 215305 (2009)

- Chapter 4
  Analysis of Kapitza–Dirac diffraction patterns beyond the Raman–Nath regime
  B. Gadway, D. Pertot, R. Reimann, M. G. Cohen, and D. Schneble
  Opt. Express **17**, 19173 (2009)

- Chapter 5
  Quantum dynamics of matter waves in a pulsed incommensurate lattice
  B. Gadway, J. Reeves, L. Krinner, and D. Schneble
  arXiv:1203.3177v1 (2012)

- Chapter 8
  Collinear Four-Wave Mixing of Two-Component Matter Waves,
  D. Pertot, B. Gadway, and D. Schneble
  Phys. Rev. Lett. **104**, 200402 (2010)

  Superfluidity of Interacting Bosonic Mixtures in Optical Lattices,
  B. Gadway, D. Pertot, R. Reimann, and D. Schneble
  Phys. Rev. Lett. **105**, 045303 (2010)

- Chapter 9
  Glassy Behavior in a Binary Atomic Mixture
  B. Gadway, D. Pertot, J. Reeves, M. Vogt, and D. Schneble
  Phys. Rev. Lett. **107**, 145306 (2011)

- Chapter 10
  Probing an Ultracold-Atom Crystal with Matter Waves
  B. Gadway, D. Pertot, J. Reeves, and D. Schneble
  Nature Phys. **8**, 544-549 (2012)

Chapter 2

Weakly interacting Bose gases I: theoretical concepts

In this chapter, we discuss some theoretical concepts that are fundamental to the study of degenerate Bose gases in optical lattices.

2.1 Bose–Einstein condensates

Bose–Einstein condensation was predicted by Einstein in 1924 [1] to occur for an ideal gas of massive particles obeying Bose statistics, as developed by Bose for photons [2]. A Bose–Einstein condensate is characterized by the "condensation" of a macroscopic fraction of particles into the single-particle ground state. In 1938, not long after its prediction in noninteracting gases, London proposed [85] that the λ-phenomenon (discontinuity in heat capacity) in liquid ^{4}He associated with the transition to a superfluid state was related to Bose–Einstein condensation. However, strong interactions between helium atoms greatly reduce the condensate fraction in this system, and make for a complicated and somewhat convoluted theoretical description.

In contrast, a nearly ideal system for the study of Bose–Einstein condensation can be found in dilute, ultracold atomic vapors, where typically the spacing between particles greatly exceeds the characteristic length scale of interactions. Following advances in the laser-cooling and trapping of neutral atoms [86] (leading to the 1997 Nobel prize in physics [87–89]), and also of stable confinement [90] and evaporative cooling in magnetic traps [90–92], first observations of Bose–Einstein condensation in dilute atomic vapors were made in gases of rubidium at Boulder [4] and sodium at MIT [5] in 1995 (and also

reported evidence [6] for BEC in lithium-7 at Rice that same year, confirmed in 1997 [7]). The realization of BEC in dilute atomic gases (for which the 2001 Nobel prize in physics [93, 94] was awarded) has since led to great advances in the understanding and application of this novel state of matter (for some reviews, see for example [3, 95, 96]).

2.1.1 Non-interacting gases

The phenomenon of Bose–Einstein condensation, characterized by the emergence of a macroscopic population in the ground state, can be motivated by examining the Bose distribution function at finite temperature. Here, we consider a gas in the grand canonical ensemble, with temperature T and particle number N determined by coupling to a thermal and particle reservoir having temperature T and chemical potential μ. The populations N_i in levels of energy ϵ_i are given as

$$N_i = \frac{1}{e^{(\epsilon_i - \mu)/k_B T} - 1} \ . \tag{2.1}$$

where μ is kept less than the ground state energy ϵ_0 to avoid negative populations. If the chemical potential is made to approach ϵ_0, N_0 will diverge, and for fixed particle number $N = \sum_i N_i$, the population will condense into the ground state.

We can also consider a more physical picture for the temperature-driven transition from a normal (thermal) state to a Bose–Einstein condensate, occurring in a gas of bosonic particles (atoms) at fixed density n. Furthermore, a simple estimate of the transition temperature may be obtained in this manner, where we relate the atoms' thermal kinetic energy $k_B T/2 \sim p^2/2m$ (momentum p) to the thermal de Broglie wavelength (coherence length) $\lambda_{dB} \sim h/p$ of the atomic wavefunctions,

$$\lambda_{dB} = \hbar\sqrt{2\pi/m k_B T} \ . \tag{2.2}$$

For decreasing temperature, the spatial extent of the wavefunctions will increase and at some point they will begin to overlap, such that distinguishability of the atoms by spatial coordinate is lost. This defines quantum degeneracy in the gas, occurring when the de Broglie wavelength exceeds the mean interparticle spacing, i.e. when

$$\lambda_{dB} \gtrsim n^{-1/3} \ , \tag{2.3}$$

or more accurately in free 3D space when $n\lambda_{dB}^3 > 2.612...$ ($\zeta(3/2)$, where ζ is the Riemann zeta function) [97]. For dilute gases of alkali atoms with typical densities of $10^{13} - 10^{14}$ cm^{-3}, this corresponds to temperatures in the 100 nK

range.

In the experiments that will be described in this thesis, the starting condensate temperatures are on the order of several nK, orders of magnitude below T_c, such that thermal depletion of the condensate is negligible. In the limit of zero temperature, atoms of a non-interacting Bose gas are all condensed into the single-particle ground state $\psi(\mathbf{x})$ of the system. For an N-particle system, the many-particle wavefunction is just given as a product state of N such identical wavefunctions,

$$\Psi_N(\mathbf{x}_1, \mathbf{x}_2, \ldots \mathbf{x}_\mathrm{N}) = \prod_{i=1}^{N} \psi(\mathbf{x}_\mathrm{i}) \ . \tag{2.4}$$

In the limit of large N, we can describe the condensate by one macroscopic wave function, or complex order parameter,

$$\phi(\mathbf{x}) = \sqrt{N}\langle\hat{\psi}(\mathbf{x})\rangle \ . \tag{2.5}$$

Here, we have replaced the bosonic field operator $\hat{\psi}$ by a classical field with uniform global phase (relating to a spontaneously broken symmetry at the BEC phase transition). The condensate wave function has a normalization $\int d\mathbf{x}|\phi(\mathbf{x})|^2 = N$, such that the particle density is given as $n(\mathbf{x}) = |\phi(\mathbf{x})|^2$.

2.1.2 Interacting gases

In reality, interactions between atoms often play an important role, and are necessary for describing the equilibrium and dynamical properties of a condensate (and they are a necessary ingredient for reaching degeneracy in thermal equilibrium through evaporative cooling). The Hamiltonian of a gas of interacting particles in second-quantization of the field can be written as

$$\hat{H} = \int d\mathbf{x}\hat{\psi}^\dagger(\mathbf{x})\Big[-\frac{\hbar^2\nabla^2}{2m} + V_{pot}(\mathbf{x})\Big]\hat{\psi}(\mathbf{x}) + \frac{1}{2}\int\int d\mathbf{x}d\mathbf{x}'\hat{\psi}^\dagger(\mathbf{x})\hat{\psi}^\dagger(\mathbf{x}')V_{at}(\mathbf{x}-\mathbf{x}')\hat{\psi}(\mathbf{x})\hat{\psi}(\mathbf{x}') \ , \tag{2.6}$$

where $\hat{\psi}^\dagger(\mathbf{x})$ and $\hat{\psi}(\mathbf{x})$ are the field creation and annihilation operators obeying bosonic commutation relations. Here, we have included the influence of some external potential $V_{pot}(\mathbf{x})$, typically used to confine the atoms in space, as well as nonlinear atom-atom interactions characterized by the two-particle interaction potential $V_{at}(\mathbf{x}-\mathbf{x}')$. At ultralow temperatures, only the lowest s-wave term of a partial wave expansion will contribute to the scattering amplitude

between two atoms. With an s-wave scattering length a_s typically less than the interparticle spacing in dilute gases ($na_s^3 \ll 1$, weakly interacting limit), we can then effectively describe these interactions by a δ-function pseudopotential of the form

$$V_{at}(\mathbf{x}-\mathbf{x}') \approx g \cdot \delta(\mathbf{x}-\mathbf{x}') \ , \tag{2.7}$$

where $g = 4\pi\hbar^2 a_s/m$ is the coupling constant characterizing atom-atom interactions.

By transforming to the Heisenberg picture, we can write down equations of motion describing the time evolution of the field operators as

$$i\hbar\partial_t\hat{\psi}^\dagger(\mathbf{x},t) = \left[-\frac{\hbar^2\nabla^2}{2m}+V_{pot}(\mathbf{x})+g\int d\mathbf{x}'\hat{\psi}^\dagger(\mathbf{x}',t)\delta(\mathbf{x}-\mathbf{x}')\hat{\psi}(\mathbf{x}',t)\right]\hat{\psi}^\dagger(\mathbf{x},t) \ . \tag{2.8}$$

If we again (as in Eq. 2.5) assume a macroscopic wave function of the field given by the expectation value of the creation (annihilation) operator, a nonlinear Schrödinger equation (known in this context as the Gross–Pitaevskii [98, 99] equation) for the matter-wave field can be written as

$$i\hbar\partial_t\phi(\mathbf{x},t) = \left[-\frac{\hbar^2\nabla^2}{2m} + V_{pot}(\mathbf{x}) + g|\phi(\mathbf{x},t)|^2\right]\phi(\mathbf{x},t) \ . \tag{2.9}$$

Here, $g|\phi(\mathbf{x},t)|^2$ represents the time-dependent mean-field potential of the condensate, where $n(\mathbf{x},t) = |\phi(\mathbf{x},t)|^2$ is the condensate density. For attractive interactions $g < 0$, this can lead to unstable condensate dynamics [100]. For positive scattering lengths, as are typically used in experiment, the repulsive mean-field potential simply acts to modify the ground-state wave functions. The atomic interactions lead to an effective Hartree–Fock-type potential, which counteracts the (typically harmonic) trapping potential $V_{pot}(\mathbf{x})$, resulting in a larger extent of the wave function.

By assuming a time-independent form of the Hamiltonian, and taking $\phi(\mathbf{x},t) = \varphi(\mathbf{x})e^{-i\mu t/\hbar}$ where μ is the condensate's chemical potential, we can write

$$\left(-\frac{\hbar^2\nabla^2}{2m} + V_{pot}(\mathbf{x}) + g|\varphi(\mathbf{x})|^2\right)\varphi(\mathbf{x}) = \mu\varphi(\mathbf{x}) \ . \tag{2.10}$$

For a sufficiently large numbers of atoms, an approximate form of the ground state wave function can be found by neglecting the kinetic contribution to the energy (sufficiently far away from the edges of the cloud, see below), where the chemical potential can then be related to the density of the central or peak condensate density as $\mu/g = n_c$. This so-called Thomas–Fermi approximation

leads to a density profile of the form

$$n(\mathbf{x}) = \frac{\mu - V_{pot}(\mathbf{x})}{g} \tag{2.11}$$

for regions of $\mathbf{x}$ fulfilling $\mu > V_{pot}(\mathbf{x})$, and vanishing density outside these regions. We now consider a weakly interacting BEC confined to a 3D harmonic trapping potential

$$V_{pot}(\mathbf{x}) = \frac{m}{2}\left(\omega_x^2 x^2 + \omega_y^2 y^2 + \omega_z^2 z^2\right) \tag{2.12}$$

with trapping frequencies $\omega_{x,y,z}$, and with mean harmonic trapping frequency $\omega_{\rm HO} = (\omega_x\omega_y\omega_z)^{1/3}$ and mean harmonic oscillator length $a_{\rm HO} = \sqrt{\hbar/m\omega_{\rm HO}}$. The Thomas–Fermi profile of a condensate in such a potential is then given by

$$n(\mathbf{x}) = \frac{\mu}{g}\prod_{\alpha\in\{x,y,z\}}\left(1 - \frac{x_\alpha^2}{R_\alpha^2}\right)\Theta\left[1 - \frac{x_\alpha^2}{R_\alpha^2}\right] , \tag{2.13}$$

with Θ the Heaviside step function. Here, the chemical potential is related to the total atom number by

$$\mu = \frac{\hbar\omega_{\rm HO}}{2}\left(\frac{15Na_s}{a_{\rm HO}}\right)^{2/5} , \tag{2.14}$$

the Thomas–Fermi radii of the condensate along the directions x_α are determined by setting

$$\mu = m\omega_\alpha^2 R_\alpha^2/2 . \tag{2.15}$$

In Fig. 2.1, we compare the condensate density profiles of harmonically-trapped atoms for the cases of clouds with no interactions, with interactions, and for an interacting condensate in the Thomas–Fermi approximation. We see that compared to the non-interacting case, the profile is broader for a repulsively interacting condensate. Also, at the edge of the distribution, the Thomas–Fermi approximation leads to discrepancies on the order of the healing length $\xi = (8\pi n a_s)^{-1/2}$. For simplicity and clarity, and in anticipation of the discussion in Chapter 6 on one-dimensional (1D) systems, we have plotted the condensate density profiles for a 1D scenario, assuming particles of mass m set to that of ^{87}Rb and assuming a trapping frequency $\omega/2\pi = 100$ Hz along the one direction. To account for interactions, we incorporate an effective 1D coupling constant $g_{\rm 1D}/\hbar = 2\times10^5$ m/s, and assume a fixed total particle number $N = \int n_{\rm 1D}(z)\mathrm{d}z = 150$, where $n_{\rm 1D}(z)$ is the 1D density profile. We

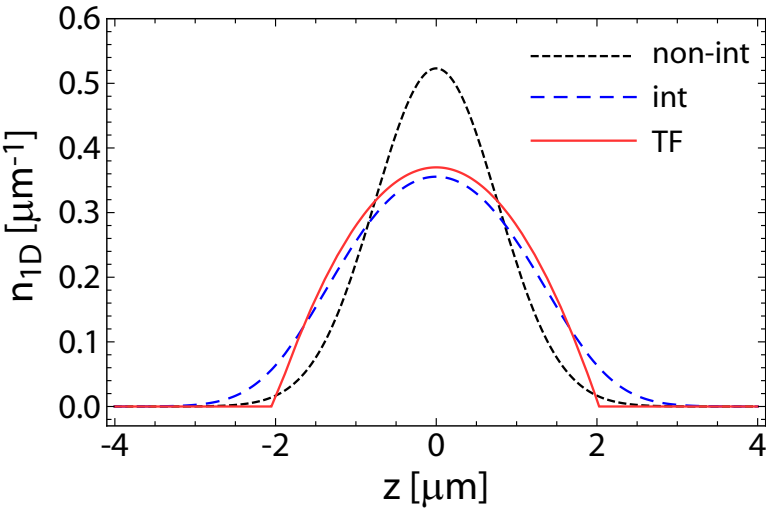

Figure 2.1: Condensate density profiles with and without atomic interactions. The 1D density profiles $n_{1D}(z)$ of condensates are shown for the case of no interactions (black, small dashing), with interactions (blue, dashed) as determined using Eq. 2.10, and with interactions in the Thomas–Fermi approximation (red, solid). Details of the assumed trapping potential and interaction coupling can be found in the text.

note that the Thomas–Fermi approximation gives a slightly different relation of the radius to atom number in one dimension than in three, which can be determined by normalizing the total atom number as

$$N = \frac{1}{g_{1D}} \int [\mu - m\omega^2 z^2/2]\Theta[\mu - m\omega^2 z^2/2]\mathrm{d}z \ , \tag{2.16}$$

where $\Theta[x]$ is the Heaviside function. This can then be solved as

$$\frac{2g_{1D}N}{m\omega^2} = \int \left[\frac{2\mu}{m\omega^2} - z^2\right]\Theta\left[\frac{2\mu}{m\omega^2} - z^2\right]\mathrm{d}z = \frac{4}{3}\left(\frac{2\mu}{m\omega^2}\right)^{3/2} , \tag{2.17}$$

where then using $\mu = m\omega^2 R^2/2$ as before leads to the 1D Thomas–Fermi radius $R = (3g_{1D}N/2m\omega^2)^{1/3}$.

2.2 Atom-light interaction

Neutral atoms interact with electromagnetic light fields in both a dissipative and conservative manner. The former relates to transitions to excited elec-

tronic states by photon absorption (followed by spontaneous emission), as used for laser-cooling and magneto-optical trapping of atoms [86]. The conservative interaction of atoms with light involves a "dressing" or modification of the energy levels of the atom in the presence of the light field. Physically, this comes about due to interaction of the light field with the field-induced dipole moment in the atom, which leads to a shift of the atomic energy levels (ac-Stark shift). For spatially inhomogeneous light fields, such energy shifts can be used for trapping [101, 102] or anti-trapping ground state atoms in attractive or repulsive potentials (analogous to dispersive trapping of refractive objects). Here we consider the simplified case of a two-level atom, however we will treat the topic of atom-light interactions more rigorously in Chapter 8 with respect to state-dependent optical potentials involving multiple excited-state transitions.

We consider a two-level atom with ground state $|g\rangle$ and excited state $|e\rangle$, separated energetically by $\hbar\omega_0 = E_e - E_g$. We also consider a single-frequency light field $\mathbf{E} = E_0\hat{\epsilon}\cos(\omega t - kz)$ with propagation along the direction z (E_0 the electric field amplitude, $\hat{\epsilon}$ the unit polarization vector), which has an angular frequency $\omega = 2\pi\nu$ (wave number $k = \omega/c$ and wavelength $\lambda = 2\pi/k$), and is detuned from the atomic resonance by an amount $\Delta = \omega - \omega_0$. This light field has a local intensity $I = \epsilon_0 c E_0^2/2$ (vacuum permittivity ϵ_0). Absent the atom-light interaction term, the Hamiltonian describing the atom and the light field is

$$\hat{H}_0 = \hbar\omega_0|e\rangle\langle e| + \hbar\omega(\hat{a}^\dagger\hat{a} + 1/2) \ , \tag{2.18}$$

where $\hat{a}^\dagger$ ($\hat{a}$) is the light field creation (annihilation) operator. We shall assume a macroscopic population of the light field $\langle\hat{a}^\dagger\hat{a}\rangle = N \simeq N - 1$.

We now consider the interaction term of the Hamiltonian that describes coupling between the atom and the light field in the dipole approximation (neglecting spatial variations of the light field on the length scale of the atom's electronic wavefunctions) of the form $\hat{H}_{int} = -\mathbf{d}\cdot\mathbf{E}$. In terms of the atomic ground and excited levels and the light field operators, the interaction term can then be expressed as [103]

$$\hat{H}_{int} = \left(|e\rangle\langle g|e^{i\omega_0 t} + |g\rangle\langle e|e^{-i\omega_0 t}\right)\left(\frac{\hbar\Omega^*(z)}{2}\hat{a}^\dagger e^{i\omega t} + \frac{\hbar\Omega(z)}{2}\hat{a}e^{-i\omega t}\right) . \tag{2.19}$$

Here, $\Omega(z) = \Omega e^{-ikz}$ (z-dependence of $\Omega(z)$ dropped from here on), $\hbar\Omega \equiv |\mu|E_0$ defines the Rabi frequency, where $\mu = e\langle e|\mathbf{r}|g\rangle$ is the dipole moment of the atom, and $\langle e|\mathbf{r}|g\rangle$ is the dipole matrix element describing overlap of the ground and excited state orbitals, where $\mathbf{r}$ is the electron coordinate. The Rabi frequency of light-atom coupling will thus be given by $\Omega = (eE_0/\hbar)|\langle e|\mathbf{r}|g\rangle|$.

We now make the rotating wave approximation (RWA), where we neglect the cross-terms with rapidly oscillating phase $e^{\pm i(\omega_0+\omega)t}$, which is valid for near-resonant light fulfilling $|\Delta| \ll \omega_0$. The interaction Hamiltonian can then be reduced to

$$\hat{H}_{int} \approx |e\rangle\langle g| \frac{\hbar\Omega\hat{a}e^{-i\Delta t}}{2} \; + \; |g\rangle\langle e| \frac{\hbar\Omega\hat{a}^\dagger e^{i\Delta t}}{2} \; , \tag{2.20}$$

where the first (second) term describes excitation (de-excitation) of the atom accompanied by absorption (emission) of a photon. Starting in the ground state, the probability of occupying the excited state oscillates at the effective Rabi frequency $\Omega' = \sqrt{\Omega^2 + \Delta^2}$, with a maximum value of $P_e^{max} = |\Omega/\Omega'|^2$. For large detunings $|\Delta| \gg \Omega$ the population remains within the ground state to a good approximation.

In the case of such large detunings, coupling to the light field still has the effect of shifting the energy levels of the ground and excited states. These energy shifts can be determined by second-order perturbation theory, or by direct solution of the Hamiltonian in a rotating frame [86], to be

$$\Delta E_{g,e} = \pm \frac{\hbar\Omega^2}{4\Delta} = \frac{3\pi c^2}{2\omega_0^3} \frac{\Gamma_e}{\Delta} I \; , \tag{2.21}$$

when the counter-rotating term can be neglected. At the right hand side we have related the shifts back to the local intensity of the light field I, and the excited state decay rate

$$\Gamma_e = \frac{\omega_0^3 \mu^2}{3\pi\epsilon_0 \hbar c^3} \; . \tag{2.22}$$

Thus, for red detunings $\Delta < 0$, corresponding to laser light with a frequency less than the atomic transition, the ground-state energy is lowered, proportional to the light intensity. For spatially inhomogeneous light fields, the atoms will then be attracted to the energy potential minima, located at positions of maximum light intensity. The atoms we study are typically confined to an attractive optical dipole potential, formed at the focus of far red-detuned Gaussian laser beams (Hermite–Gauss HG_{00} transverse modes) with intensity distributions

$$\frac{I(\rho, z)}{I_{max}} = \frac{w_0^2}{w^2(z)} e^{-2\rho^2/w^2(z)} \; , \tag{2.23}$$

with peak intensity $I_{max} = 2P/\pi w_0^2$, where P is the total laser power, w_0 the minimum $1/e^2$ radius. The beam-radius expands along the propagation direction of the beam as $w(z) = w_0\sqrt{1 + (z/z_R)^2}$, where $z_R = \pi w_0^2/\lambda$ is the beam's Rayleigh range.

In addition to the conservative potential experienced by the ground-state

atoms, small effects of spontaneous photon (Rayleigh) scattering remain, leading to a residual scattering rate

$$\Gamma_{sc} = \frac{3\pi c^2}{2\hbar\omega_0^3}\left(\frac{\Gamma_e}{\Delta}\right)^2 I \ . \tag{2.24}$$

This effect can be understood by the fact that the states with shifted energy levels are actually "dressed" states, with contributions from the ground and excited levels (excited-state "contamination"). We note that this scattering rate can be obtained simply by multiplying the time-averaged excited-state population with the excited state decay rate Γ_e. A rigorous derivation of Γ_{sc} in the context of multi-level atoms will be given in Chapter 8.

2.3 Optical lattices and band-structure

In addition to using Gaussian-beam optical dipole potentials for the trapping of neutral atoms, we also use optical lattice potentials to confine the atoms to periodic "light crystals". Optical lattices are formed by interfering two or more laser beams with well-defined relative phase. In the case of a 1D lattice, this is simply done by full retro-reflection of a Gaussian laser beam from a mirror, which creates an optical standing wave. The potential along the direction z of the beam will then be a periodic function, with spatial periodicity $d = \lambda/2$, and modulation depth V_{latt}. In the case of unequal local intensities in the forward and back-reflected beams, there will also be an offset potential. We assume that the transverse dependence of the beam intensity, due to the overall Gaussian profile, is negligible over the size of the atomic distribution being addressed, so that the beams forming the periodic potential can be considered to be plane-waves. The motion along z is transformed from the case of free particle dispersion to one described with an energy band structure, which we now describe in detail, following the descriptions in Refs. [104, 105].

We consider the fate of a particle of mass m moving within some lattice potential $V(z)$ with spatial periodicity $d = \lambda/2$ (spatial frequency $k = \pi/d$), subject to the Hamiltonian $H = \hat{p}^2/2m + V(z)$. Solutions to this problem are given by Bloch wavefunctions [106], which are products of plane-waves $\exp(iqz/\hbar)$ and periodic functions

$$\phi_q^{(n)}(z) = e^{iqz/\hbar} \cdot u_q^{(n)}(z) \tag{2.25}$$

with the same periodicity as the lattice potential, where the Bloch eigenstates $u_q^{(n)}$ have energies $E_q^{(n)}$. This leads to a Schrödinger equation for the $u_q^{(n)}(z)$

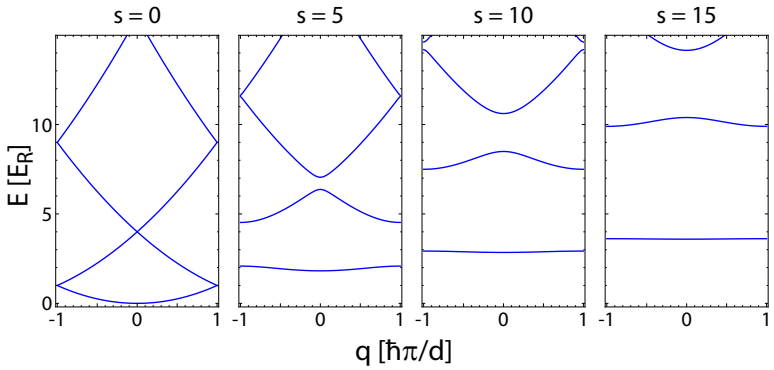

Figure 2.2: Energy band structure of a 1D lattice for varying lattice depths. We plot the band structure energies (in units of E_R, folded within the first Brillouin zone) as a function of quasimomentum q (in units of $\hbar\pi/d$) for lattice depth values of $s = V_{latt}/E_R = \{0, 5, 10, 15\}$.

of the form

$$H_B u_q^{(n)}(z) = E_q^{(n)} u_q^{(n)}(z) \qquad \text{with} \qquad H_B = \frac{1}{2m}(\hat{p}+q)^2 + V(z)\ . \quad (2.26)$$

For the generic periodic potential $V(z)$, we can write both the lattice potential and the functions $u_q^{(n)}(z)$ as discrete Fourier sums

$$V(z) = \sum_r V_r e^{i2rkz} \qquad \text{and} \qquad u_q^{(n)}(z) = \sum_l c_l^{n,q} e^{i2lkz}\ , \quad (2.27)$$

with integers r and l. The potential and kinetic energy terms of Eq. 2.26 respectively become

$$V(z)u_q^{(n)}(z) = \sum_r \sum_l V_r e^{i2(r+l)kz} c_l^{n,q} \qquad \text{and} \quad (2.28)$$

$$\frac{(\hat{p}+q)^2}{2m} u_q^{(n)}(z) = \sum_l \frac{(2l\hbar k + q)^2}{2m} c_l^{n,q} e^{i2lkz}\ . \quad (2.29)$$

For purely sinusoidal potentials of the form

$$V_{latt}(z) = \frac{sE_R}{2}\cos(2kz)\ , \quad (2.30)$$

where s is the lattice depth in units of the recoil energy $E_R = \hbar^2 k^2/2m$, only two Fourier terms of Eq. 2.27 survive, $V_{r=\pm 1} = sE_R/4$.

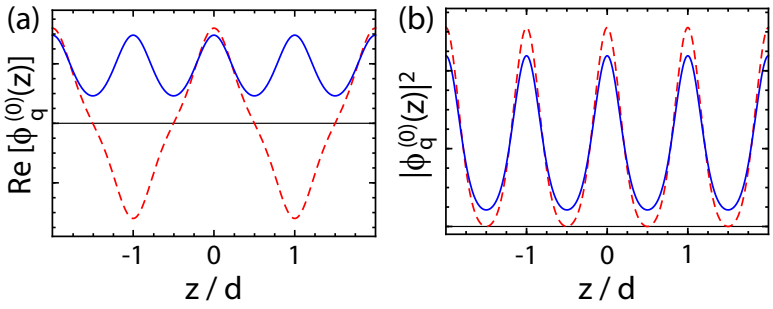

Figure 2.3: Spatial wave functions of the lowest-band Bloch eigenstates, for a lattice depth of $s = 5$. (a) Real part of the Bloch wave functions $\phi_q^{(n)}(z)$ in the lowest band ($n = 0$) for quasimomenta of $q = 0$ (blue solid line) and $q = \hbar k$ (red dashed line), i.e. at the band center and band-edge, respectively. (b) Density of the Bloch wave functions for the same two cases as in (a).

The Schrödinger equation for the coefficients $c_l^{n,q}$ can then be written in matrix form as

$$\sum_l H_{l,l'} \cdot c_l^{(n,q)} = E_q^{(n)} c_l^{(n,q)} \ . \tag{2.31}$$

The matrix $H_{l,l'}$ has diagonal kinetic energy contributions $(2lq/\hbar k)^2 E_R$, as well as off-diagonal elements for $|l - l'| = 1$ of weight $sE_R/4$. Here, q is the quasimomentum within the first Brillouin zone of the lattice, running from $q = -\hbar k$ to $\hbar k$. For a lattice of infinite extent, q will be continuous, while for a finite lattice with N sites it will have spacing $2\hbar k/2N$. For a given quasimomentum q, $E_q^{(n)}$ is the eigenenergy in the n-th energy band of the lattice (below we use the convention $n = 0$ for the ground band, $n = 1$ for first-excited, etc.) and the eigenvector $c^{(n,q)}$ defines the Bloch wave function of this state.

For illustration, we show a few calculations of the band energy structure and the Bloch wave functions (limits of l taken out to $|l| \leq 5$) for a 1D lattice. Fig. 2.2 displays band structure energies for varying lattice depth values, illustrating the transition from a quadratic free-particle dispersion for low lattice depths to one of flat bands with nearly uniform spacing (as in a harmonic oscillator) for very deep lattices.

Fig. 2.3 illustrates the spatial wave functions of the Bloch eigenstates of the lowest band ($n = 0$), at the center of the Brillouin zone ($q = 0$) and at the band-edge ($q = \hbar k$). From Fig. 2.3 (a), we see from the real part of the wave functions that, while the lowest band $q = 0$ Bloch wave function has a uniform phase distribution, those at the band-edge have a π phase inversion between adjacent sites (leading to a shift of the momentum peaks when projected onto

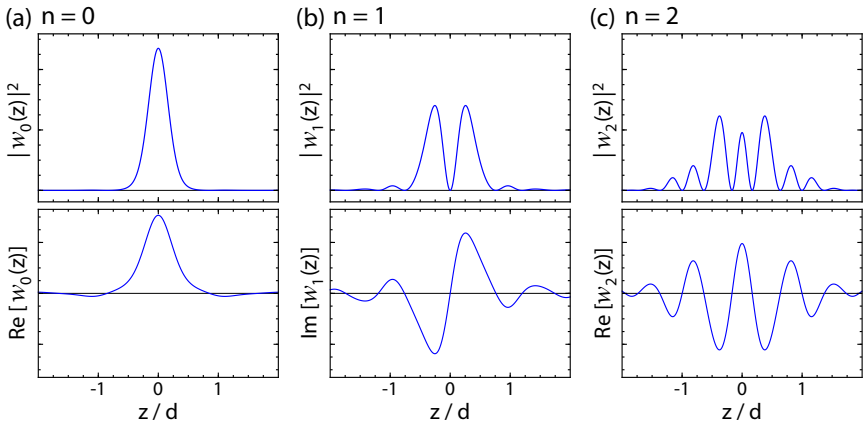

Figure 2.4: Spatial wave functions of the localized Wannier functions in the 3 lowest energy bands, for a lattice depth of $s = 5$: (a) Density of the central-site Wannier function $w_0(z)$ at top, as well as the real part of the wave function at bottom, for the lowest band ($n = 0$). (b) The first-excited band ($n = 1$) density and imaginary part of the Wannier function $w_1(z)$. (c) The second-excited band ($n = 2$) density and real part of the Wannier function $w_2(z)$.

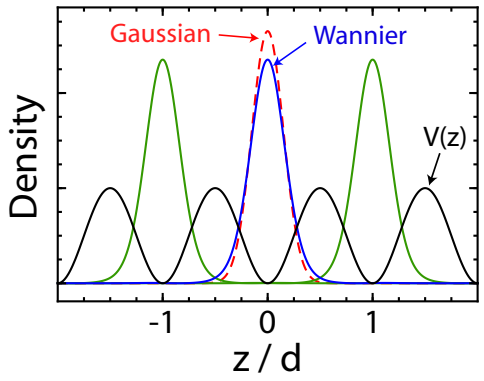

Figure 2.5: Localized Wannier functions at different sites. For a lattice of depth $s = 5$, we show the density distributions of localized lowest band ($n = 0$) Wannier functions at the central site (blue solid line) and the neighboring sites (green solid lines). For comparison, we show the central-site atomic wave function in the harmonic approximation to the lattice site potential (red dashed line). For clarity, we also show the lattice potential $V(z)$ as a black solid line.

plane-wave states, as for time-of-flight imaging). The rather similar density distributions ($|\phi_q^{(n)}(z)|^2$) of these same Bloch states are plotted in Fig. 2.3 (b).

So far, we have considered a basis of Bloch states, which are delocalized over the lattice sites. This is very suitable for the description of atomic wave func-

tions for non- and weakly-interacting Bose gases, where the coherence length (or spatial extent) of the atoms spans the system size. However, in many cases an equivalent description in terms of localized wavefunctions is more appropriate. This holds especially true for the case of strongly-interacting gases, where repulsive interactions can force atomic wave functions to become localized onto individual sites. A basis of localized Wannier functions of a particular energy band is constructed by superpositions of the different delocalized Bloch waves of that band. For a finite-size lattice composed of N sites, a summation over the $2N$ Bloch states of the n-th band (with $q \in \{-\hbar k, \hbar k\}$), of the form

$$w_n(z - z_j) = \mathcal{N}^{-1/2} \sum_q e^{-iqz_j/\hbar} \phi_q^{(n)}(z) \ , \tag{2.32}$$

is used to create a localized Wannier function at site position z_j, where $\mathcal{N}$ is a normalization constant. In Fig. 2.4, we show the constructed Wannier functions at the central lattice site $z_0 = 0$ for the three lowest bands, both the densities $|w_n(z)|^2$ and the relevant (non-zero) real/imaginary parts of the wave functions. In the limit $s \to \infty$ where the band structure resembles that of a harmonic potential, these Wannier orbitals map onto the Hermite–Gauss orbitals HG_0, HG_1, and HG_2, where the n-th such wave function has n nodes (relating to phase-inversions).

Finally, in Fig. 2.5 we plot lowest-band Wannier functions on three adjacent sites. As will be discussed in Chapter 6, the nearest-neighbor tunneling energy of the n-th band is determined by the overlap of adjacent Wannier functions $w_n(z)$ and $w_n(z + d)$,

$$t_n = -\int w_n^*(z) \left[-\frac{\hbar^2 \partial_z^2}{2m} + V_{latt}(z) \right] w_n(z + d) dz \ . \tag{2.33}$$

For the ground band, a harmonic approximation to the lattice potential is typically made for deep lattices $s \gg 1$, which yields an effective width of the wave functions $\sigma/d = s^{-1/4}/\pi$ and tunneling energy $t/E_R = (4/\sqrt{\pi}) s^{3/4} e^{-2\sqrt{s}}$ [107].

Chapter 3

Weakly interacting Bose gases II: experimental probes

In this chapter, we briefly discuss the apparatus used to produce and study systems of ultracold atoms in our experiments. We also discuss some commonly used techniques used for characterizing these systems.

3.1 Experimental setup

3.1.1 Laser cooling and evaporative cooling

As detailed in Refs. [45, 108–111], our experiments begin with the loading and laser-cooling of ^{87}Rb atoms from background vapor into a six-beam magneto-optical trap (MOT). The optical transitions used for the primary cycling ($F = 2 \rightarrow F' = 3$), repumping ($F = 1 \rightarrow F' = 2$), and depumping ($F = 2 \rightarrow F' = 2$) to accumulate population in the $F = 1$ ground state are displayed in Fig. 3.1. Over a course of about 10 s, during which light-induced atomic desorption (LIAD) [112] is used to enhance the MOT-loading rate, a cloud of $\sim 1 \times 10^{10}$ atoms is loaded and cooled to a temperature below 1 mK. The magnetic field of the MOT is then turned off for a brief optical molasses stage, by which the atoms are cooled to around 25 μK. From the mixture of trappable hyperfine states ($|F, m_F\rangle = |1, -1\rangle, |2, 1\rangle$, and $|2, 2\rangle$), the atoms are then optically pumped into the $|F, m_F\rangle = |1, -1\rangle$ hyperfine ground state. The magnetic quadrupole trap, which uses the coils of the MOT, is then turned on at a higher magnetic field gradient (40 G/cm) to catch the cooled cloud of atoms, yielding around 2.2×10^9 atoms at around 150 μK.

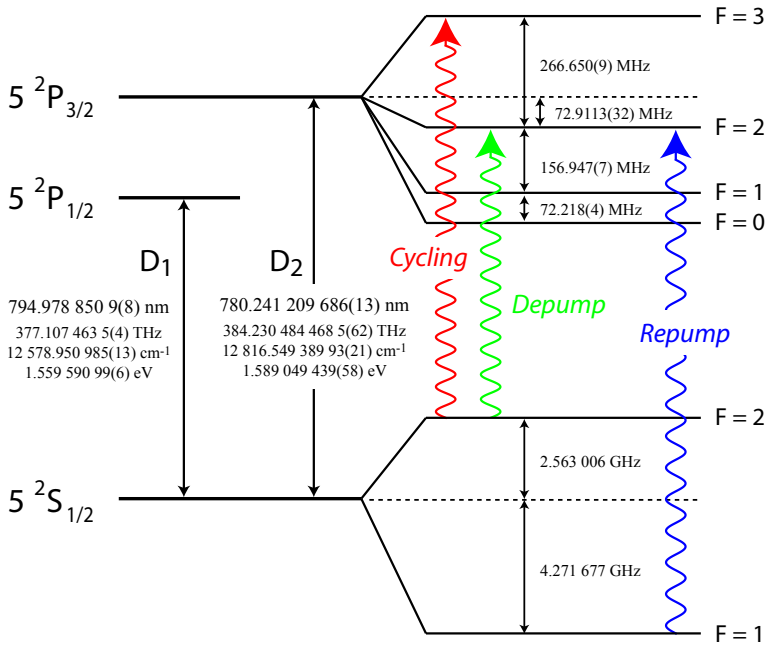

Figure 3.1: Relevant energy level-structure of ^{87}Rb showing transitions used for laser-cooling and imaging. Transition data is taken from Ref. [113].

Because of the relatively high background pressure of Rb atoms in the vapor cell ($\sim 10^{-9}$ torr), losses due to background gas collisions severely limit the lifetime of the trapped atoms. To reach quantum degeneracy, at higher density and lower temperature, we first move the atoms to a lower-pressure region before performing evaporative cooling. For the purpose of transporting the atoms, the Helmholtz coil pair forming the quadrupole trap is mounted onto a two-axis mechanical translation stage, as described in Ref. [111]. This allows for the atomic cloud to be moved from the vapor cell MOT chamber into a separate low-pressure chamber (at $\lesssim 10^{-11}$ torr, with differential pumping between the two chambers), and then into a connected glass cell (hereafter referred to as the "science cell") that provides almost unobstructed optical access. As the trap is first moved, it is also stiffened to a field gradient of $B'_z = 350$ G/cm to avoid losses and heating. This compression results in an adiabatic heating of the cloud to a temperature of about 450 μK. After a transport time of about 3 s, around 1.6×10^9 atoms remain, serving as a starting point for the evaporative cooling to quantum degeneracy. The first stage of evaporative cooling occurs in the linear quadrupole potential, until the temperature becomes low enough for spin-flip Majorana losses to become noticeable. At this point, we convert the magnetic quadrupole trap into a

harmonic (near the trap minimum) time-averaged, orbiting potential (TOP) trap [90], by adding a rotating magnetic bias field in the $x-y$ plane that is produced by two pairs of bias-field coils in Helmholtz configuration. In the TOP trap the magnetic field is offset from zero at the trap center, avoiding Majorana losses.

After reaching temperatures and densities near degeneracy in the TOP trap, we then transfer a thermal cloud of atoms into a crossed-beam optical dipole trap (ODT), formed at the intersection of two far red-detuned laser beams, as discussed in more detail in the following section. As the magnetic trap is slowly turned off, a magnetic bias field along the z-axis on the order of a few Gauss is left on, serving to define a quantization axis and preserve the spin orientation ($|F, m_F\rangle = |1, -1\rangle$). A final stage of evaporative cooling in the ODT is achieved by lowering the intensity of the trapping beams, thus decreasing the trap depth. Evaporation resulting in essentially pure condensates with no discernable thermal fraction is used to define the starting point for all of the experiments discussed in this thesis.

3.1.2 Optical dipole trap and optical lattices

As detailed in Refs. [45, 111, 114], we produce an attractive optical dipole trap at the intersection of two far-detuned laser beams of wavelength $\lambda = 1064$ nm, with beam-waists ($1/e^2$ radius) of ~ 135 μm at the BEC position and around $1.5-2$ W of power in each beam. The laser light comes from a single-frequency (line-width $\sim$ 70 kHz) ytterbium fiber laser (IPG YLR LP-SF series). To avoid interferences between the two trapping beams, they have orthogonal linear polarizations, and also a relative frequency offset of 20 MHz to average out residual interferences. The beams are separately fiber-coupled (single-mode TEM_{00}) to the position of the science cell, with PID-controlled intensity stabilization. As depicted in Fig. 3.2, in the area of the science cell the two laser beams, which are referred to as optical dipole trap beams 1 and 2 (ODT1 and ODT2), are oriented along the lab axes x and y, respectively (note a different convention of lab coordinates than in Refs. [45, 109, 114]). In addition to the attractive Gaussian potentials of the two laser beams, in general the atoms are also subject to the linear gravitational potential along z, such that the trap center is offset considerably from the center of the two laser beams due to gravitational sag.

Along with the weak optical trapping of the Bose-condensed atomic clouds, many of our experiments make use of optical standing waves to further confine the atoms. Depending on the number of lattices used (in a cubic geometry with 3 orthogonal axes), this confinement can result in a one-dimensional array of two-dimensional "pancake" gases (disc-shaped systems), a two-dimensional

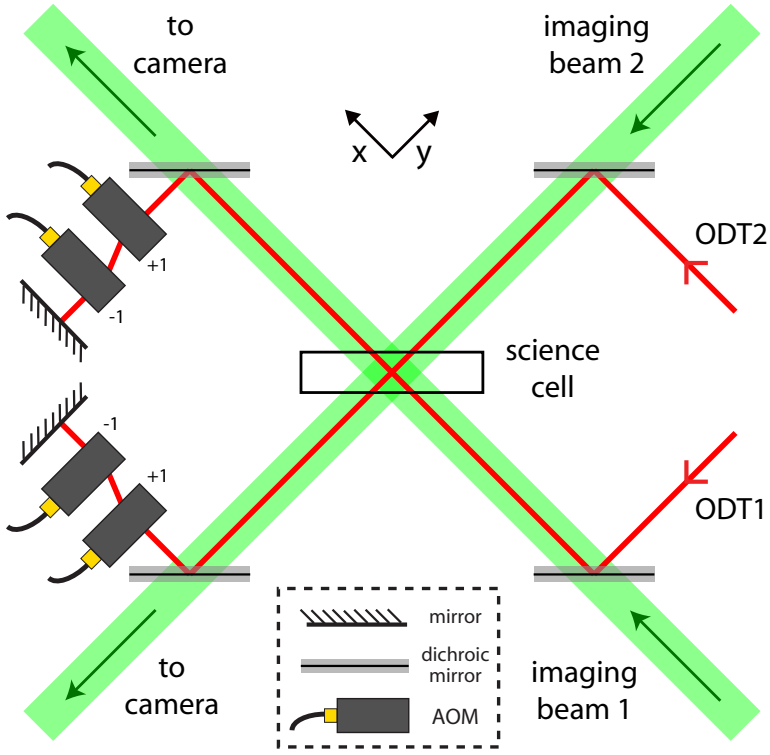

Figure 3.2: Configuration of laser beam paths in the $x-y$ plane, as used for imaging, optical trapping, and (x and y) optical lattices. The optical dipole trap (ODT) is formed by two crossed laser beams (ODT1 and ODT2) of wavelength $\lambda = 1064$ nm. Lattices along the directions of these beams, x and y, are formed through partial retroreflection of the beams ODT1 and ODT2, controlled by acousto-optic modulators (AOMs). Near-resonant laser beams used for absorption imaging of the atoms are combined onto the ODT beam path by transmission through dichroic mirrors, and removed from this path for imaging onto a CCD camera by use of dichroic mirrors as well.

array of one-dimensional "tube" gases (rod-shaped systems), or a fully three-dimensional array of zero-dimensional sites (restriction to a single spatial mode per site). This allows for the study of atoms in the Hubbard regime, where effects of atomic interactions become important. The optical lattices can be used not just for confinement, but also for the diffraction of BECs in order to split them up into a number of plane-wave momentum states.

The introduction of optical lattices along the lab axes x and y is effected by retroreflecting the beams that create the optical dipole trap (ODT). It is important to have no optical lattice present during evaporation in the ODT, to allow for efficient thermalization of the sample. Thus, we implement a retrore-

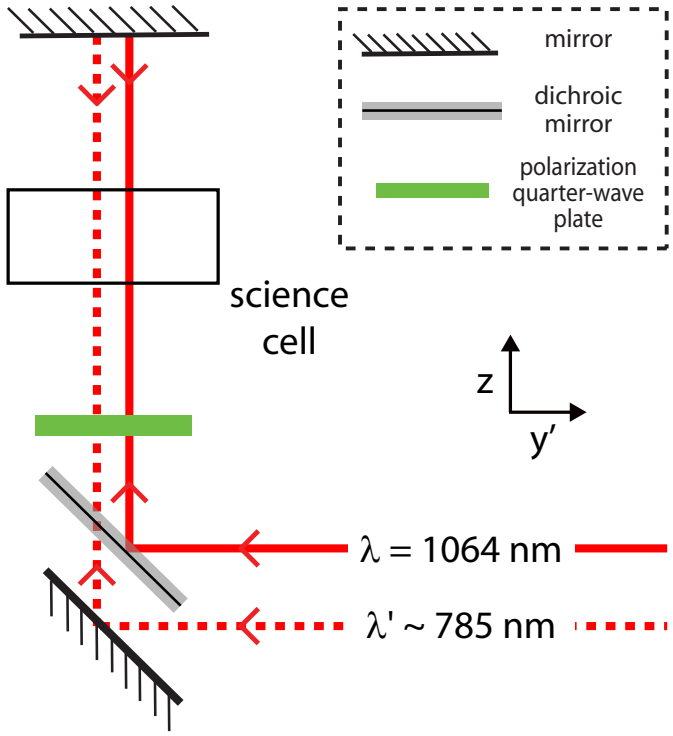

Figure 3.3: Configuration of optical lattice laser beam paths along the z-axis. The beam paths for the $\lambda = 1064$ nm laser light and $\lambda' \sim 785$ nm light are combined by use of a dichroic mirror, which is transmissive for λ'. Both lattices are formed by full retroreflection from a mirror above the science cell.

flection scheme as in Refs. [76, 111], by which the amount of light reflected back can be attenuated over seven orders of magnitude in a controlled way, from essentially no light reflected to $\sim 10 - 20\%$. As depicted in Fig. 3.2, each of the optical trapping beams pass through two acousto-optic modulators (AOMs), each driven at 80 MHz, in the $+1$ and -1 diffraction orders, respectively. The light is then reflected back by a mirror at normal incidence, passing back through the AOMs upon return. This results in no net frequency shift or variation in alignment of the retroreflected beam.

In addition to these optical lattices oriented along x and y, we also have two optical lattices that are both oriented along the z axis. One of the lattice beams at $\lambda = 1064$ nm is derived from the same laser light as for the ODT1 and ODT2 beams. The second, co-propagating lattice laser beam has a tunable wavelength operated in the ranged $\lambda' \in \{770, 800\}$ nm, typically at $\lambda' \sim$ 785 nm. This beam is derived from a Titanium-Sapphire (Ti-Sapph) ring laser (Coherent 899) pumped by a 10 W solid-state laser at 532 nm (Coherent Verdi

V10); more details of its spectral properties can be found in Ref. [114]. The output of the Ti-Sapph is fiber-coupled and exits the fiber near the position of the science cell, subject to intensity stabilization after passing through a polarizing element. As with the imaging light, the lattice laser beam at λ' is made to co-propagate with the 1064 nm z-beam upon passing through a dichroic mirror, as depicted in Fig. 3.3. The polarization of the beams is set by a quarter-wave plate phase retarder below the science cell. As discussed in Chapter 8, this is important for the relatively near-detuned λ' light, as the strength of the induced dipole potential is strongly dependent on polarization. After passing through the science cell, each of these two laser beams is then typically retroreflected by a dielectric mirror at normal incidence to form the optical standing wave lattices along z. As discussed in Chapter 8, additional beam manipulation above the science cell is used to construct a moving lattice along z, for the experiments described in Chapters 8 and 10.

3.1.3 Imaging of the atoms

To access the atomic column density distribution, we typically perform absorptive imaging in time-of-flight (TOF) after turning off all confining potentials rapidly ($\lesssim 1$ μs for optical potentials and $\lesssim 2$ ms for the magnetic traps) and allowing the atoms to freely evolve for $10 - 20$ ms. For our trapping frequencies, this time scale allows us to image the far-field momentum distribution of the atoms (neglecting the influence of interactions on TOF expansion). As depicted in Fig. 3.2, TOF imaging paths are available along both the x and y axes. The beams used for imaging co-propagate with the optical dipole trapping beams, entering and exiting through dichroic mirrors that are transmissive for the imaging light. As described in Ref. [108, 109], we image the shadow cast by the atoms, due to absorption of resonant imaging light, onto a CCD camera (Princeton Instruments PIXIS 1024B). A typical absorption image along x of atoms released from a 3D optical lattice is shown in Fig. 3.4 (a). The x direction is the primary TOF imaging path used for characterizing the momentum distributions of the atomic ensembles, while y is predominantly used for diagnostic purposes. The imaging is performed on the $F = 2 \rightarrow F' = 3$ cycling transition, concurrent with optical pumping from $F = 1 \rightarrow F' = 2$, with imaging timescales between 25 and 100 μs. For experiments with hyperfine state mixtures, as discussed in Chapter 8, a Stern–Gerlach pulse of a magnetic field gradient is first used to separate the different hyperfine states in time-of-flight.

In addition to time-of-flight absorption imaging of momentum-space distributions, we have also implemented *in-situ* imaging to provide real-space column density distributions. For this we utilize a different imaging beam-path -

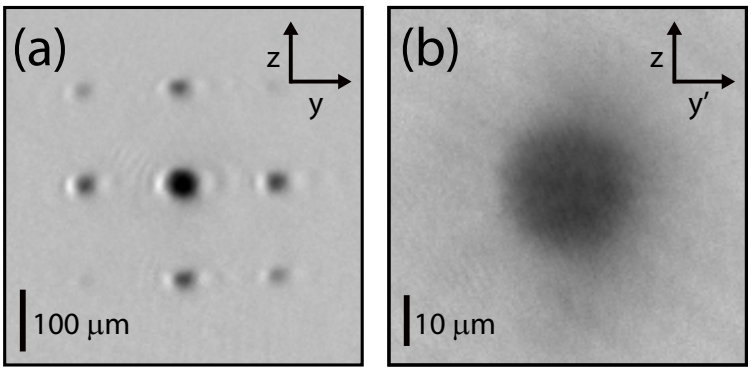

Figure 3.4: Absorption images of atoms in time-of-flight and in-trap. (a) After 18 ms of time-of-flight free expansion, atoms released from a cubic optical lattice are imaged, providing a picture of the momentum-space distribution. (b) Atoms imaged in-trap with no time-of-flight.

achieving higher magnification and a resolution ~ 1 μm - that interrogates the atomic cloud at 45° with respect to the time-of-flight imaging path along x, i.e. along the axis $x' = (x+y)/\sqrt{2}$ (not shown in Fig. 3.2). An aspheric lens with relatively high numerical aperture NA = 0.49 is used at close distance from the science cell for imaging light collection. Real-space absorption images of the atomic clouds are taken with the same laser light as for the TOF imaging, and the optical trapping and lattice beams are kept on prior to and throughout the imaging. A typical *in-situ* absorption image is shown in Fig. 3.4 (b).

3.2 Experimental characterization methods

3.2.1 External trapping potential

In the absence of direct *in situ* imaging capabilities, details of the atomic density distributions prior to release in TOF may be estimated based on knowledge of the total atom number and details of the confining potential. While the optical dipole trap is formed at the intersection of two Gaussian beams, often in the presence of a linear potential gradient due to gravity, we may approximate the potential as harmonic close to the trap minimum. As discussed in the previous chapter, a Thomas–Fermi description can be used to describe the density distribution of interacting Bose-condensed atoms in a harmonic trap. To estimate the BEC's chemical potential μ, as well as the spatial extent (Thomas–Fermi radius) of the gas along the three coordinate axes $R_{\{x,y,z\}} = (2\mu/m\omega^2_{\{x,y,z\}})^{1/2}$, we measure the harmonic trapping frequencies $\omega_{\{x,y,z\}}$ that characterize the

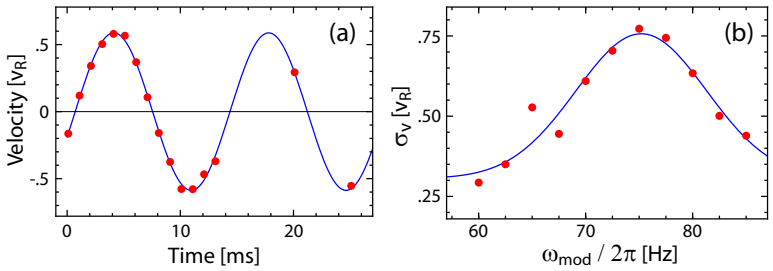

Figure 3.5: Measurement of optical trap frequencies. (a) Center-of-mass dipole oscillations (in velocity-space) of a trapped cloud along the z direction, after an abrupt displacement of the trap center. The blue line is a sinusoidal fit to the data yielding a trap frequency $\omega_z/2\pi = 73$ Hz. (b) Resonant excitation (heating) via sinusoidal modulation of the trap position. The rms velocity-width σ_v of the clouds is determined after a fixed time of excitation and thermalization. The peak response of the atomic gases to the modulation corresponds to resonant excitation at the trap frequency. The blue line is a Gaussian fit to the data. For each case, the velocity is given in units of $v_R = h/m\lambda$, with $\lambda = 785$ nm.

trapping potential [3] (for a discussion of our atom number determination see Ref. [109]).

In general, we determine the harmonic trapping frequencies using two methods: by observing center-of-mass dipole oscillations of the cloud in TOF and by excitation of the BEC via sinusoidal modulation of the trap position. Data obtained by these two methods are shown in Fig. 3.5. To induce center-of-mass dipole oscillations, we shift the atoms from the trap center with an added linear potential (magnetic field gradient), which is then quickly (in ~ 100 μs) extinguished. The atoms oscillate back and forth about the trap center at an angular frequency ω, which we observe through oscillations in their TOF velocity. The data shown in Fig. 3.5 (a) are for oscillations along z in an array of 1D gases – such that damping of the dipole oscillations by coupling to motion along x and y is suppressed – but the method is generically applicable.

For the case of excitation by sinusoidal modulation of the trap position, we begin with an array of harmonically trapped 1D BECs as in the case above. We then add a weak linear potential along z, whose amplitude is sinusoidally modulated with a Gaussian envelope as $A\sin(\omega_{\rm mod}t)\exp[-(t-t_0)^2/2\Delta_t^2]$, for a "wiggling time" of $2\Delta_t \sim 100$ ms. After driving the atoms, we allow for 500 ms of thermalization time before measuring the velocity-width of the distributions along z, to characterize the amount of energy deposited into the gas.

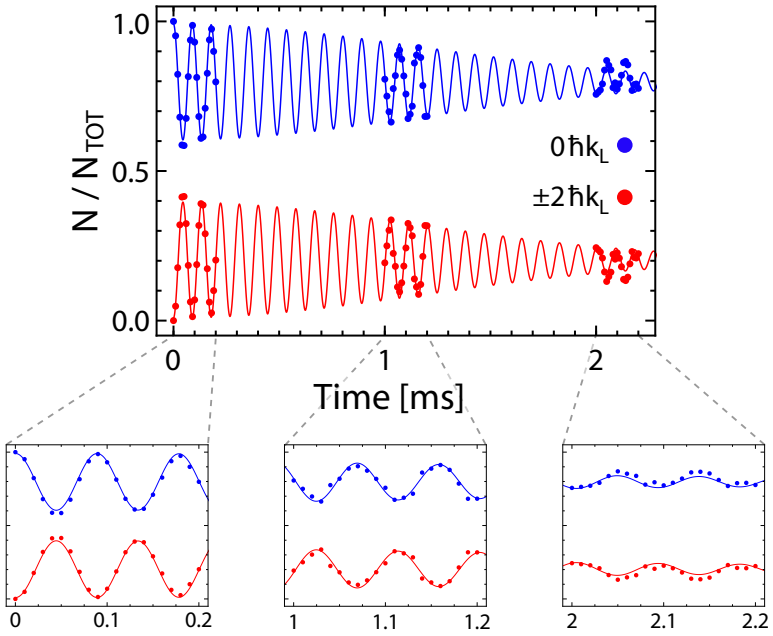

Figure 3.6: Pendellösung oscillations of momentum-mode populations in an optical lattice. For weak pulses, only the lowest few momentum orders are coupled by the applied optical lattice field, leading to Rabi-like oscillations of the momentum-mode populations. The solid lines are fits of sinusoidal oscillations with a Gaussian decay, observed to occur on the timescale of a few milliseconds.

Because of parity, we expect resonant excitation for $\omega_{\mathrm{mod}} \approx \omega_z$. As shown in Fig. 3.5 (b), the response shows a maximum around $\omega_{\mathrm{mod}}/2\pi \approx 75$ Hz, in approximate agreement with the dipole oscillation measurement.

3.2.2 Optical lattices

Precise knowledge of the optical lattice depth is often crucial for proper interpretation of observed physical effects, as well as for faithful modeling of the experimental situation. Here, we discuss a few experimental methods used to determine lattice depths for this purpose.

The first method that we use for lattice depth determination is based on matter-wave dynamics in the long-pulse or channeling regime [115] of Kapitza–Dirac diffraction [116, 117]. Beginning with a BEC at rest (quasimomentum $q = 0$), a stationary optical lattice is turned on abruptly for a variable time T. The atomic density focuses in towards the lattice potential minima, and then defocuses back out, undergoing so-called Pendellösung oscillations [115, 118].

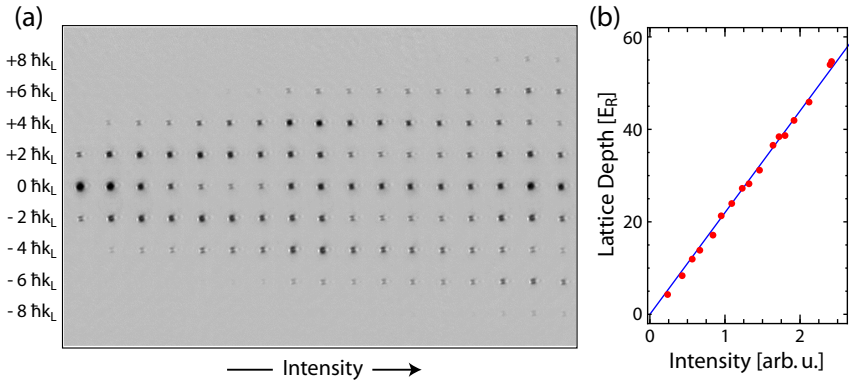

Figure 3.7: Lattice depth calibration by Kapitza–Dirac diffraction. (a) Time-of-flight diffraction patterns of BECs after pulsing by an optical lattice for a pulse duration $\tau = 10$ μs. With increasing optical intensity, higher momentum orders are populated (shown in multiples of $2\hbar k_L$, with $k_L = 2\pi/\lambda_L$ and $\lambda_L = 785$ nm). (b) Dependence of the fit-determined optical lattice depth (in units of $E_R = \hbar^2 k_L^2/2m$) on the optical intensity of the lattice's laser beams.

A simple way to understand the temporal evolution of the state is to project the initial state, essentially a $q = 0$ plane wave, onto eigenstates of the Hamiltonian in the presence of the lattice. By virtue of the symmetry of the situation, the decomposition is only onto $q = 0$ states of even lattice bands (index $n = 0, 2, 4 \ldots$). For sufficiently weak lattices, essentially only the lowest two such bands contribute, and the initial population can then be written as a superposition of the states $|n = 0, q = 0\rangle$ and $|n = 2, q = 0\rangle$, with energies $E_0(q = 0)$ and $E_2(q = 0)$. As a function of time T, these two states acquire a difference in phase of $\exp[i[E_2(q = 0) - E_0(q = 0)]T/\hbar]$. Upon projecting the band-states back onto a basis of plane-wave states by release in TOF, this differential phase evolution is converted into population oscillations. We thus expect that the frequency of the Pendellösung oscillations, for weak lattice depths, should occur at a frequency $[E_2(q = 0) - E_0(q = 0)]/\hbar$. From here, one can make a comparison to band-structure energy calculations to determine the lattice depth. We show in Fig. 3.6 an example of such Pendellösung oscillations in a lattice along z of wavelength $\lambda_z = 1064$ nm. From the observed oscillation frequency $\omega/2\pi \approx 11.2$ kHz, we determine the lattice depth to be $s_z = 5.68(2)$ E_R. We remark that the oscillations are observed to decay on the timescale of about 1-2 milliseconds, for which dissipation through atomic interactions [119] and higher-band tunneling are the most likely causes.

The second, related method investigates the response of atoms to lattice pulses in the short-pulse or phase-grating regime [115, 117], also known as

the Raman–Nath regime. In this short pulse limit, the atom's motion during the duration of the pulse can be ignored. Therefore, the dominant effect of the applied pulse is to imprint a spatially varying phase pattern onto the condensate, of the form $\exp[iV_L \cos^2(k_L z)\tau/\hbar]$, where $k_L = 2\pi/\lambda_L$ is the wave number and λ_L is the wavelength of the lattice light, τ is the duration of the pulse, and V_L is the depth of the lattice. Expanding the wavefunction in a plane-wave basis of states with momenta $p_n = 2n\hbar k_L$ [120–122], starting with a stationary condensate at $p = 0$, one finds that the coefficients of the different plane-wave orders after application of the pulse can be approximated as $c_n = (-i)^n e^{-iV_L\tau/2\hbar} J_n(V_L\tau/2\hbar)$, where the J_n are Bessel functions of the first kind. Thus, from populations of the form $P_n = |J_n(V_L\tau/2\hbar)|^2$, one can determine the lattice depth V_L. More generally, effects of finite pulse length – covered more in the following Chapter – can be accommodated through a simple solution of the Schrödinger equation for a $p = 0$ initial state, solving a set of coupled equations of the form

$$\dot{c}_n = -i\frac{4n^2 E_R}{\hbar}\, c_n \; - i\frac{V_L}{4\hbar}\left(c_{n-1} + c_{n+1}\right) \;, \tag{3.1}$$

where $E_R = \hbar^2 k_L^2/2m$ is the recoil energy. In Fig. 3.7, we show data for a typical calibration of lattice depth (as a function of laser beam intensity) based on comparisons of experimental momentum distributions and solutions of Eq. 3.1 for a fixed pulse duration of $\tau = 10\ \mu$s.

Each of the methods described thus far relies on starting with all of the atoms in a single quasimomentum state. For certain systems, in particular those consisting of spin-polarized fermions, these methods fail. The last method we explore is based on lattice amplitude modulation spectroscopy, which can be used in systems that lack matter-wave coherence. Here, we start with atoms loaded into very deep optical lattices, such that the lowest bands of the lattice are essentially flat. We then sinusoidally modulate the depth of the lattice, which near to the lattice minima performs an even parity z^2 perturbation. This perturbation can directly couple lattice bands whose indices are separated by even integers. The excitation can also be viewed as a two-photon Raman process, in which the modulation effectively adds frequency sidebands onto the laser beams. When the frequency of modulation matches the the frequency spacing between such sets of bands (in the atomic limit for deep lattices one can think of the spacing between lattice orbitals $s, p, d, f, g, \ldots$), resonant (and parity-conserving) excitation of population to higher bands can occur.

To directly detect the population of atoms in different lattice bands, a standard procedure known as band-mapping [123] can be used. Here, a rela-

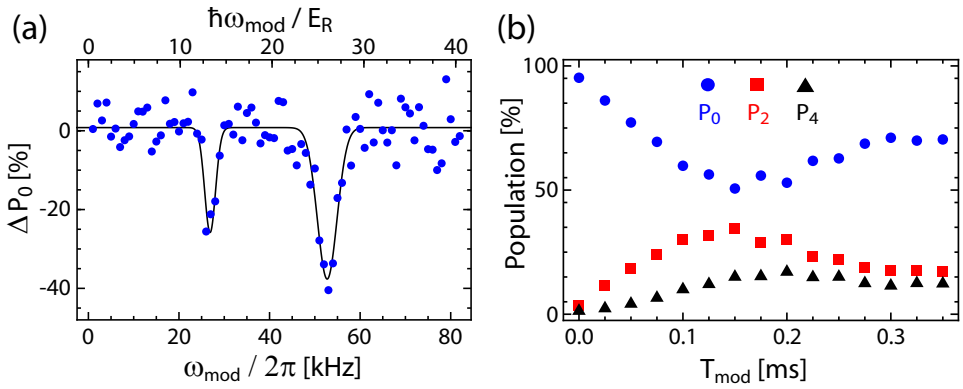

Figure 3.8: Lattice amplitude modulation spectroscopy of band-structure. (a) Even excitations can be made to higher bands, preserving parity of the atomic orbital wavefunctions (i.e. $s \to d$ and $d \to g$ allowed, $s \to p$ disallowed). By scanning the frequency ω at which we sinusoidally modulate the lattice amplitude, and monitoring the percentage change of ground-band atoms (following a band-mapping procedure), we can spectroscopically determine the transition frequencies to higher lattice orbitals. Plotted at the top is the modulation energy scale in units of E_R. By comparison to band-structure calculations, we determine the lattice depth to be 54 E_R. The dip at ~ 53 kHz is a direct (two-photon Raman) transition to the second-excited band, while the feature at ~ 27 kHz is due to a higher-order processes (with odd-parity excitation ruled out by an absence of population in the first-excited band). (b) For stronger amplitude of modulation at resonance, we can leave the linear-response regime and observe partially coherent dynamics in the band populations P_0, P_2, P_4 (s, d, and g orbitals) as a function of modulation time.

tively fast ramp-down of the lattice is performed, typically on the timescale $\tau_{\mathrm{BM}} \sim 1$ ms, slow enough to prevent redistribution of population between bands, fulfilling $\hbar/\tau_{\mathrm{BM}} \ll \Delta_{\mathrm{gap}}$, with Δ_{gap} the bandgap. Once the lattice is ramped off and there is a free-particle dispersion, the atoms originally residing in different bands will have momenta such that different Brillouin zones are populated in TOF. In Fig. 3.8 (a), we plot as a function of modulation frequency the fraction of atoms remaining in the lowest band ($n = 0$), following 10 ms of lattice amplitude modulation (at $\pm 5\%$, after a 0.85 ms bandmap). In the frequency range explored, the population removed from the lowest band is observed to populate the $n = 2$ band. We also note that these measurements are performed with amplitude modulation of the lattice along the y-axis, starting from a Mott insulator of atoms confined along all three axes (lattice depths $V_{\{x,z\}} = \{40, 30\}$ E_R along the other axes) with a lattice wavelength

of $\lambda = 1064$ nm along all axes. From the modulation spectra, we determine an energy spacing between the ground and 2nd-excited band of 26 E_R ($\omega_{\mathrm{mod}}/2\pi \approx 53$ kHz), corresponding to a lattice depth along y of $V_y = 54\ E_R$.

While this data is taken for relatively small amplitude of modulation, for larger amplitude "wiggling" we can drive the system well out of the linear response regime. In Fig. 3.8 (b), we show data for on-resonance modulation of the y-lattice amplitude [for slightly different conditions than in Fig. 3.8 (a)], which shows slightly coherent evolution of the population within the lowest and the second- and fourth-excited bands. More fully coherent dynamics should result for phase modulation ("shaken" lattice), which couples the lowest and the first-excited band, where the lower natural linewidth (tunneling rate) of the excited state provides for a more fully closed transition.

Chapter 4

Analysis of Kapitza–Dirac diffraction patterns beyond the Raman–Nath regime

In this chapter, we report on an experimental study of Kapitza–Dirac diffraction of matter waves from (temporally) short and not so short optical lattice pulses. We find that when pulse area is conserved, a longer pulse leads to less matter-wave diffraction. We find that for sufficiently weak pulses, the usual analytical short-pulse prediction for the Raman–Nath regime continues to hold for longer times, however with a reduction of the apparent modulation depth of the standing wave. We quantitatively relate this effect to the Fourier width of the pulse, and draw analogies to the Rabi dynamics of a coupled two-state system. Our findings, combined with numerical modeling for stronger pulses, are of practical interest for the calibration of optical lattices in ultracold atomic systems. This chapter reproduces our publication *Analysis of Kapitza–Dirac diffraction patterns beyond the Raman–Nath regime*, Opt. Express **17**, 19173 (2009) [122].

4.1 Introductory discussion

The diffraction of matter-waves from a standing light wave is a fundamental concept in atom optics [124, 125]. Originally predicted by Kapitza and Dirac [116] for electrons more than 75 years ago (and recently also observed for these [126]), it was first demonstrated in the 1980s with an atomic beam [117], a decade later with cold atoms [127], and has since become a standard tool in atom interferometry for the coherent mixing of momentum modes [125, 128]. The advent of Bose-Einstein condensates in the 1990s [95] has made it possible

to directly observe the dynamics of matter-wave diffraction in time-of-flight images [115, 129, 130]. Moreover, the diffraction of condensate atoms from standing light waves finds applications in high-resolution spectroscopy [131] and metrology [132, 133], and plays a fundamental role in superradiance [134, 135].

When atoms diffract from a standing light wave, each two-photon (absorption / stimulated emission) scattering event changes the atomic momentum along the standing wave by either zero or two photon momenta, which for multiple such events results in a series of evenly spaced atomic momenta. Two scenarios can generally be distinguished, depending on the presence of a resonant coupling. In the Bragg case, the atoms oscillate between two resonantly coupled momentum states, depending on the strength and duration of the interaction with the light field [136]. If the Bragg condition is not met (off-resonant case), atoms can nevertheless be diffracted into a number of momentum states, provided that the interaction is sufficiently short and strong [117]. In accordance with a common convention in atom optics [137] we refer to this case as Kapitza–Dirac diffraction, but we extend it to include times beyond the Raman–Nath regime. In this context, it is interesting to note a similar discussion for the diffraction of light from sound waves in acousto-optic devices [120].

In the Raman–Nath regime, i.e. when atomic motion during the interaction with the light field can be neglected, the populations of the diffracted states exclusively depend on the product of the strength V_0 and the duration τ of the interaction, i.e. the area of the applied pulse [117]. Outside the Raman–Nath regime, the diffraction dynamics exhibits collapses and revivals for constant interaction strength [115, 129, 130]. We now specifically analyze the case of a pulsed interaction of variable duration but constant pulse area. This allows for a study of the breakdown of the Raman–Nath prediction and, in particular, for a quantification of deviations when the system is close to, but not deep into, the Raman–Nath regime. The findings of our study are of direct interest for the elimination of systematic errors in calibration measurements for experiments with ultracold atoms in optical lattices [18, 26] when the lattice depth is determined via Kapitza–Dirac diffraction.

This Chapter is organized as follows: Section 4.2 reviews general aspects of the matter-wave diffraction from a one-dimensional optical lattice, while Section 4.3 briefly describes our experimental system. In Section 4.4 we analyze diffraction patterns for weak pulses, and give an analytical modification to the Raman–Nath diffraction formula, which is motivated by a comparison of the diffraction dynamics with that of a coupled Rabi system, as well as by considering the spectral properties of the pulse. Section 4.5 discusses the more

complicated dynamics of strong pulses, and Section 4.6 deals with calibration methods for the depth of optical lattices, comparing numerical simulations with single-shot diffraction patterns not restricted to the Raman–Nath regime.

4.2 Raman–Nath regime

We first briefly review general aspects of the diffraction of a condensate from a standing light wave with wavenumber $k = 2\pi/\lambda$ that is switched on for a duration τ. The standing wave gives rise to a sinusoidal optical potential $V_0 \cos^2 kz$ [18]. The evolution of the condensate in the standing wave can then be modeled [121, 138] (neglecting mean-field interactions) as that of a matter wave ψ subject to the Hamiltonian

$$\hat{H} = -(\hbar^2/2m)\partial_z^2 + V_0 \cos^2 kz \tag{4.1}$$

where m is the atomic mass. Expanding the condensate wave function in the basis of plane waves populated by diffraction from a standing wave as $\psi(t) = \sum_n c_n(t)\ e^{i2nkz}$ (where $n = 0, \pm1, \pm2, \ldots$ and $c_n(t = 0) = \delta_{n,0}$) and introducing the dimensionless parameters

$$\alpha = (E_r^{(2)}/\hbar)\ \tau \tag{4.2}$$

$$\beta = (V_0/\hbar)\ \tau, \tag{4.3}$$

(where $E_r^{(n)} = (n\hbar k)^2/2m$ denotes the n-photon recoil energy, with $E_r^{(1)} \equiv E_r$), transforms the time-dependent Schrödinger equation into a set of coupled differential equations

$$i\frac{\mathrm{d}c_n}{\mathrm{d}t} = \frac{\alpha\ n^2}{\tau}\ c_n + \frac{\beta}{4\tau}\left(c_{n-1} + 2c_n + c_{n+1}\right) \tag{4.4}$$

for the amplitudes $c_n(t)$ of the diffracted orders n. For a given lattice depth, the highest momentum order ($\pm 2n\hbar k$) capable of being populated is given by the cutoff

$$\bar{n} = \sqrt{\beta/\alpha} \tag{4.5}$$

for which the potential energy is fully converted into kinetic energy (cf. [130]). Note that in these equations, α is the pulse duration τ in units of the 2-photon recoil time $\tau_r^{(2)} = \hbar/E_r^{(2)}$, and β measures the area of the pulse.

The dynamics of the condensate in the standing wave depends on the ratio between αn^2 and β, i.e. between the kinetic energies acquired during diffraction and the depth of the potential. The Raman–Nath approximation

consists of neglecting the αn^2 terms in Eqs. (4.4), which is justified if τ is much shorter than the harmonic oscillation period in a potential well [115], such that $\tau\omega_{ho} \ll 1$, with $\omega_{ho} = [V_0 E_r^{(2)}]^{1/2}/\hbar$, or equivalently $\beta\alpha \ll 1$. In this case, the solution of Eqs. (4.4) is $c_n(t) = (-i)^n e^{-i\beta t/2\tau} J_n(\beta t/2\tau)$, such that the population $P_n = |c_n|^2$ of the nth diffracted order after application of the pulse is given by

$$P_n = J_n^2\left(\frac{\beta}{2}\right), \tag{4.6}$$

where the J_n are Bessel functions of the first kind.

4.3 Experimental procedure

In the experiments described in this Chapter, we subjected an optically trapped ^{87}Rb Bose-Einstein condensate to a vertically-oriented, pulsed standing light wave at 1064 nm, for which the 2-photon recoil time $\tau_r^{(2)} \approx 20$ μs. In brief, in a nearly isotropic crossed-beam optical dipole trap we produced condensates typically containing 5×10^5 atoms in the $|F = 1, m_F = -1\rangle$ hyperfine ground state without a discernible thermal fraction. The standing light wave, with a Gaussian $1/e^2$ radius of 130 μm at the position of the condensate, was derived from a single-frequency ytterbium fiber laser with a linewidth of 70 kHz and could be switched off within 1.5 μs using an acousto-optic modulator. Immediately after application of the pulse, the atoms were released from the optical trap and allowed 15 ms time-of-flight. They were then, in 100 μs, simultaneously repumped to $F = 2$ manifold and imaged on the cycling transition using near-resonant absorption imaging.

A series of images taken for pulses of variable duration τ but with constant pulse area $\beta = 4.5$ is shown in Fig. 4.1. Based on a naive invocation of Eq. (4.6) for the Raman–Nath regime one would expect the same diffraction pattern in all the images. Instead, the number of diffracted orders is seen to generally decrease with the duration of the pulse, with an oscillatory decay of the first diffracted orders for long pulse durations.

The populations of the $0\hbar k$ and $\pm 2\hbar k$ momentum orders in the series of Fig. 4.1 are shown in Figs. 4.2 (a) and (b), together with corresponding data for a weaker standing wave with $\beta = 1.5$, for which diffracted orders $2n\hbar k$ with $|n| > 1$ are not populated over the full range of pulse durations. For the larger area pulse with $\beta = 4.5$, this is only the case for pulse durations of at least 90 μs, due to contributions of the $\pm 4\hbar k$ orders, as shown in inset (c).

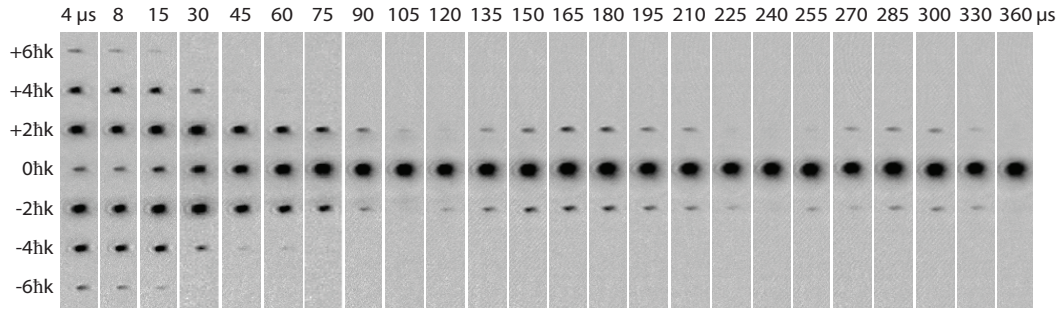

Figure 4.1: Time-of-flight (TOF) absorption images of a condensate diffracted from a 1064 nm standing-wave optical pulses of constant area $\beta = V_0\tau/\hbar = 4.5$, and varied durations, ranging from $\tau = 4$ μs ($\alpha = \tau/\tau_r^{(2)} \approx 0.2$) to 360 μs ($\alpha \approx 18$). For the data with durations $\tau \gtrsim 90$ μs (for which $[\beta/\alpha]^{1/2} \lesssim 1.0$), the apparent modulation depth of the standing wave undergoes an oscillatory decay consistent with the form $(\beta/2)\mathrm{sinc}(\alpha/2)$, as described in the text.

4.4 Weak-pulse dynamics

For sufficiently weak pulses with a cutoff $\bar{n} \approx 1$ for which only the lowest orders $\pm 2\hbar k$ are populated, Eqs. (4.4) can be reduced to three coupled equations; this approximation is valid for shallow potentials $V_0 \lesssim 4E_r$. The solutions c_0 and $c_{\pm 1}$ to Eqs. (4.4), which can be obtained in a straightforward way, then lead to

$$P_{\pm 1} = \frac{\beta^2}{2\beta^2 + 4\alpha^2} \sin^2\left(\frac{\sqrt{\beta^2/2 + \alpha^2}}{2}\right) \tag{4.7}$$

and $P_0 = 1 - 2P_{\pm 1}$. This can be cast into the standard form of a Rabi oscillation

$$P_{\pm 1} = \frac{1}{2}\left(\frac{\chi}{\Omega}\right)^2 \sin^2\left(\frac{\Omega}{2}\tau\right) \tag{4.8}$$

with generalized Rabi frequency $\Omega = [\chi^2 + \Delta^2]^{1/2}$, resonant coupling $\chi = V_0/\sqrt{2}\hbar$ and detuning $\Delta = E_r^{(2)}/\hbar = \omega_r^{(2)}$ between the atomic momentum states $0\hbar k$ and $\pm 2\hbar k$. Another way to interpret this result is the following: each scattering event that changes the atomic momentum from 0 to $\pm 2\hbar k$ by energy conservation leads to a frequency mismatch of the scattered photon by Δ with respect to the standing wave, requiring a corresponding Fourier width of the pulse for stimulated scattering to be able to occur. Consequently, the drop-off of populations in higher orders with increasing α can be seen as resulting from the decrease in the Fourier width of the square pulse which, in

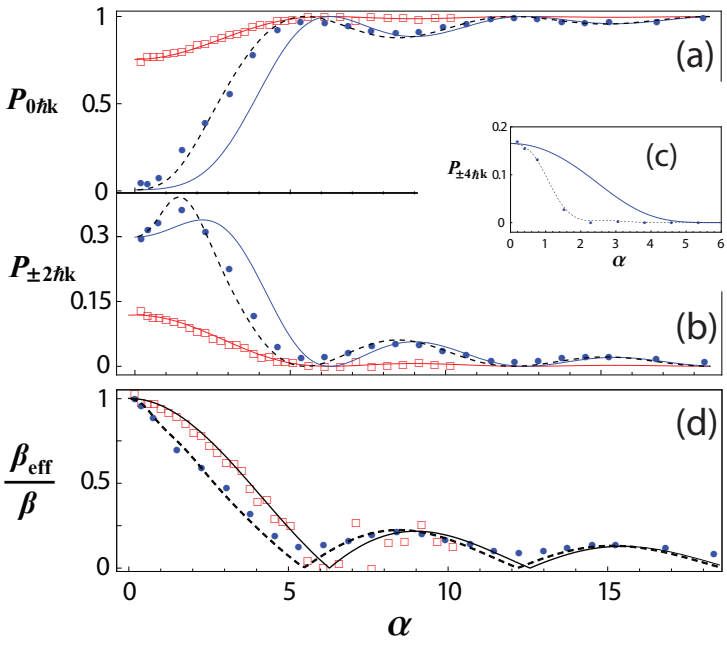

Figure 4.2: Suppression and revival of atomic diffraction from a constant-area standing wave light pulse with increasing pulse length. (a and b) Relative populations of the central condensate $0\hbar k$ and orders $\pm 2\hbar k$ vs. normalized pulse duration $\alpha = \tau/\tau_r^{(2)} \sim \tau/20$ μs. Filled blue dots and open red squares refer to pulses of area $\beta = 4.5$ (cf. Fig. 1) and 1.5, respectively, and the solid lines plot the function $J_n^2[(\beta/2)\mathrm{sinc}(\alpha/2)]$. The dashed black lines correspond to numerical fits for $\beta = 4.5$. (c) Decay of the $\pm 4\hbar k$ orders in the $\beta = 4.5$ data set, with the numerical simulation (dashed line) as well as the function $J_2^2[(\beta/2)\mathrm{sinc}(\alpha/2)]$. (d) Behavior of $\beta_{\mathrm{eff}}/\beta$, where the atomic diffraction patterns are fit with the distribution $J_n^2(\beta_{\mathrm{eff}}/2)$. The black solid line is the analytical form $\mathrm{sinc}(\alpha/2)$, and the dashed black line corresponds to a numerical solution of Eqs. (4.4) using $\beta = 4.5$.

some analogy to the treatment of sound-wave diffraction in [138], results in a more general modification of Eq. (4.6) to

$$P_n = J_n^2\left(\frac{\beta}{2}\,\mathrm{sinc}\frac{\alpha}{2}\right), \tag{4.9}$$

where the sinc function arises from the Fourier transform of the square pulse. Indeed, the populations $P_{0,\pm 1}$ predicted by Eq. (4.9) agree with those of Eq. (4.7) up to $O(\alpha^2\beta^2)$, independent of the pulse duration α or pulse area β.

For $[\beta/\alpha]^{1/2} \leq 1$, the agreement of Eq. (4.9) with the experimentally observed patterns is excellent, as can be seen in Figs. 4.2 (a) and (b).

It is interesting to note the connection of Eq. (4.9) to the resonant case of nth order Bragg diffraction from a moving standing wave (with a relative detuning $\delta\omega = n^2\Delta$ between the two beams). In this case, the Fourier transform of the applied potential $V_0 \cos^2(kz + \delta\omega\ t/2)$ with duration τ would lead to a frequency distribution $\propto \mathrm{sinc}[(\omega - \delta\omega)\tau/2]$ (i.e. identical to that of the standing wave case, but shifted by $\delta\omega$) making available the resonant frequency component, independent of the pulse duration.

The form of Eq. (4.9) shows that although the populations P_n in a spectrum may follow a Bessel distribution as predicted by the Raman–Nath Eq. (4.6), a fit will not necessarily return the correct modulation depth. The apparent pulse area in Eq. (4.9) is given by $\beta_{eff}/2 = (\beta/2)\mathrm{sinc}(\alpha/2)$, which means that for a pulse of duration τ, the apparent modulation depth of the standing wave extracted from a diffraction spectrum is reduced from its short-pulse value $V_0 = \hbar\beta/\tau$ to $V_{0,\mathrm{eff}} = \hbar\beta_{eff}/\tau$, i.e.

$$V_{0,\mathrm{eff}} = V_0\ \mathrm{sinc}\left(\tau/2\tau_r^{(2)}\right)\ . \tag{4.10}$$

The apparent pulse area returned by a fit of Eq. (4.6) to the diffraction patterns is shown in Fig. 4.2 (d) for both the $\beta = 4.5$ and $\beta = 1.5$ data sets. For the latter, the fit results agree with Eq. (4.10) over the full range, consistent with the fact that orders $|n| > 1$ are not populated. The first-order revivals can thus be interpreted as arising from a sampling of the Fourier transform of the pulse. For $\beta = 4.5$, the observed behavior still shows qualitative agreement with revivals from sampling of the sinc-shaped frequency distribution with increasing pulse duration τ, but clearly exhibits deviations when higher-order momentum states are present.

4.5 Strong-pulse dynamics

For more intense pulses with $\bar{n} = [\beta/\alpha]^{1/2} > 1$, the simple generalization of Eq. (4.9) no longer holds, as is evident by the large discrepancies in Fig. 4.2 for $\alpha < 4.5$ ($\tau < 90\ \mu$s) in the $\beta = 4.5$ data set.

The presence of higher diffraction orders leads to population decays that are faster than those determined by the two-photon timescale in Eqs. (4.9) and (4.10). This is shown in inset (c) of Fig. 4.2 for the $\pm 4\hbar k$ ($n = 2$) orders, which require the exchange of four photons in the transition from $0\hbar k$. In general, the presence of many higher momentum orders will complicate analytic descriptions of the diffraction dynamics.

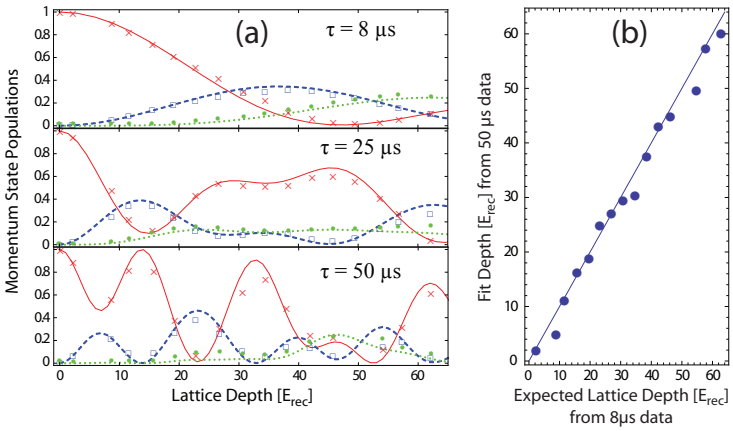

Figure 4.3: (a) Comparison of experimental diffraction spectra and numerical fits. For each data set, numerical simulations [using Eqs. (4.4)] of the momentum state distribution are shown as solid, dashed, and dotted curves for the $0\hbar k$, $\pm 2\hbar k$, and $\pm 4\hbar k$ diffraction components, respectively. The red crosses are data for the $0\hbar k$ order, and the blue open squares (green filled dots) are data averaged for the $\pm 2\hbar k$ ($\pm 4\hbar k$) orders. (b) Comparison of numerical lattice depth calibrations [using Eqs. (4.4)] from relatively short (8 μs) and long (50 μs) optical lattice pulses for various intensities of the standing light wave. The results for numerically-fit lattice depths agree to within 4% (the solid line has a slope of 1).

Nevertheless, it is possible to accurately describe the observed dynamics by numerical integration of the coupled differential Eqs. (4.4), truncated for unpopulated higher orders beyond $\bar{n}$. This is shown in Fig. 4.2 and Fig. 4.3 (a).

4.6 Single-shot calibration of optical lattices

In experiments with ultracold atoms in optical lattices, the tunneling rate depends exponentially on the lattice depth V_0 [18], for which an accurate knowledge thus is essential. Unlike most other methods (cf. [18]), applying a "short" Kapitza–Dirac diffraction pulse can conveniently reveal the lattice depth in a single-shot measurement. However, the application of well-defined pulses that are short enough to be deeply in the Raman–Nath regime, yet strong enough to yield significant diffraction, can be technically challenging. Our study quantified how the results of such a calibration measurement need to be corrected if pulses of finite length are used.

In Fig. 4.3 we present the comparison of experimentally observed mo-

mentum state distributions to numerical simulations, for three different pulse lengths (8, 25, and 50 μs), as the lattice depth is varied from 0 to 65 E_r. While the observed momentum state distributions are close to the typical Raman–Nath form Eq. (4.6) for the 8 μs pulses, this is no longer the case for longer pulses. For all pulse lengths, numerical simulations agree well, as can be seen in Fig. 4.3 (a). The lattice depth calibrations for the three pulse durations, determined by comparison of experimental data to numerically simulated patterns, agree to within 4%, as can be seen in Fig. 4.3 (b) for the extreme cases of 8 and 50 μs. Despite the complicated form the dynamics take, one can thus obtain a reliable lattice depth calibration even with longer pulse durations. We have independently verified the method described here with another single-shot calibration method for deep lattices (adiabatic lattice rampup, followed by a sudden projection of the ground band population onto the $\pm 2\hbar k$ plane-wave states [139]), for which we found comparable agreement to within 10%.

4.7 Concluding remarks

We have studied Kapitza–Dirac diffraction of a Bose-Einstein condensate in a pulsed standing light wave, considering the case that the pulse area remains constant as the pulse duration is varied. We find that for sufficiently weak pulses exciting only the $\pm 2\hbar k$ orders, the usual analytical short-pulse prediction continues to hold for longer times, albeit with a modification of the apparent modulation depth of the standing wave. We relate this effect to the frequency spread of the square-wave pulse, and also draw analogies to the Rabi dynamics of a coupled two-state system. Our findings are of practical interest for the calibration of optical lattices in ultracold atomic systems, and we show that for a general length and strength pulse, relatively simple (neglecting mean-field effects) numerical modeling can be used well outside the Raman–Nath regime to accurately determine the lattice depth.

Chapter 5

Quantum dynamics of matter waves in a pulsed incommensurate lattice

In this Chapter, we experimentally study the dynamical response of weakly-interacting atomic matter waves to a periodically pulsed optical lattice formed by two standing-waves of incommensurate spatial periodicity. While periodic driving with a single standing wave results in ballistic spreading of momentum wavepackets at quantum resonances and dynamical localization otherwise, we observe radically different behavior with the pulsed incommensurate lattice. Here, the spatial quasidisorder causes a suppression of momentum growth at resonance, and delocalization in momentum space for off-resonant driving. The observed breakdown of quantum interference effects can be explained by a mapping to a system of coupled kicked rotors, which has been predicted to display classical-like behavior even for a purely quantum evolution. This chapter is partially based on our manuscript *Quantum dynamics of matter waves in a pulsed disordered lattice*, arXiv:1203.3177v1 (2012) [50].

5.1 Introductory discussion

In isolated ultracold atomic systems, the quantum nature of matter can be made manifest in striking ways. One example arises in the dynamics of *quantum chaotic* systems, i.e. systems whose classical counterparts are chaotic, and in which destructive interference can suppress the onset of chaos [140]. The δ-kicked rotor model [140] has found particular relevance in experimental studies of driven quantum particles, as realized with cold neutral atoms periodically kicked by trains of optical standing wave pulses [82]. Whereas regimes

of fully chaotic behavior with diffusive growth of the momentum variable can be found in the classical system, the quantum analog generically displays dynamical localization due to quantum interference [140–142], which is analogous to one-dimensional (1D) Anderson localization [143] in real space [83]. Foundational experiments on quantum chaos in driven atomic vapors have demonstrated such dynamical localization [82, 144]. In recent years, the use of coherent rather than thermal sources of atoms has allowed for the observation of ballistic spreading in momentum space [145, 146], relating to a quantum walk [147, 148], when the frequency of δ-kicking corresponds to a discrete energy resonance.

Studies of the contrasting dynamics of classical and quantum systems [149], in particular those addressing how classical behavior arises in the presence of noise [150–153] and nonlinearities [84, 154–157], are central to the understanding and control of quantum decoherence [158]. Such a transition towards classical behavior was observed in early studies of δ-kicked rotors under the influence of random noise and decoherence [159–161]. Remarkably, classical behavior has also been predicted to already emerge in a simple driven quantum system consisting of two coupled kicked rotors [84], providing hope that the disparate behavior of quantum and classically chaotic systems may be reconciled in the macroscopic limit.

Here, we have explored the influence of controlled spatial quasidisorder on the dynamics of a quantum kicked rotor, which was realized with ultracold atomic matter waves in a periodically pulsed optical lattice. We observe that the addition of a second, incommensurate optical destroys hallmark behavior of the kicked rotor system, namely ballistic momentum spreading at quantum resonances and dynamical localization for off-resonant driving. We show that our configuration effectively realizes a system of two *coupled* kicked rotors, where the coupling suppresses transport at resonance and induces transport away from it. In addition to a direct connection to the field of quantum chaos, studies of wave propagation in disordered media (as with those in photonic lattices [162, 163]) may also provide insight into the influence of disorder on transport in solid materials.

5.2 Experimental procedure and kicked rotor system

Our system consists of a nearly-pure, optically-trapped Bose–Einstein condensate (BEC) of $(1.4 \pm 0.4) \times 10^5$ ^{87}Rb atoms in the $|F, m_F\rangle = |2, -2\rangle$ hyperfine ground state. The atoms are driven by pulsed optical lattices oriented along

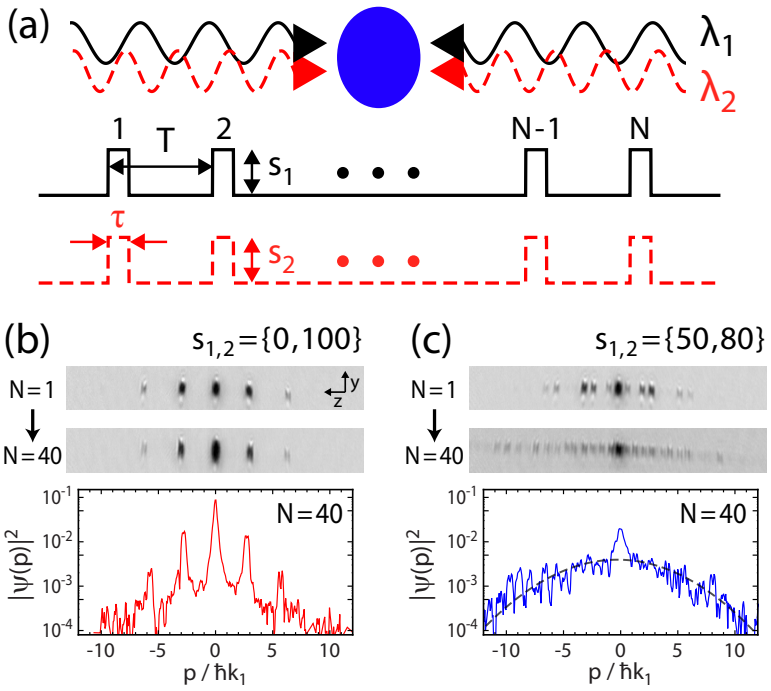

Figure 5.1: Atomic matter waves in a periodically-pulsed optical lattice potential. (a) A Bose–Einstein condensate is exposed to a train of N pulses (duration τ, separation T) of two incommensurate standing waves with wavelengths $\lambda_{1,2}$ and lattice depths $s_{1,2}$. (b) Time-of-flight diffraction spectra (averaged over 3-4 images) of atoms released after $N = 1$ and 40 kicks, for driving with a single lattice (lattice depths $s_{1,2} = \{0, 100\}$). The momentum distribution along z (integrated along y) after $N = 40$ kicks is shown below. (c) As in (b), but for driving with two incommensurate lattices ($s_{1,2} = \{50, 80\}$). The dashed black line at the bottom of (c), which serves as a guide to the eye, is a Gaussian profile corresponding to diffusive spreading.

the z-axis, as depicted in Fig. 5.1 (a). We perform simultaneous pulsing by two lattices of wavelengths $\lambda_1 = 1064$ nm and $\lambda_2 = 782$ nm, with wave numbers $k_{1(2)} = 2\pi/\lambda_{1(2)}$. The lattice depths are characterized as $V_{1(2)} = s_{1(2)}E_R$ (where $E_R = \hbar^2 k_1^2/2M$ is the recoil energy of the first lattice and M the atomic mass), and are calibrated via Kapitza–Dirac diffraction [122]. Subsequently, we use pulses of duration $\tau = 2$ μs (Raman–Nath regime), spaced at a variable period T. After applying N pulses, we immediately release the atoms and allow them to freely evolve in time-of-flight for 16 ms before performing absorptive imaging of momentum distributions, as displayed in Figs. 5.1 (b,c).

The system subject to a train of N lattice pulses is approximately described

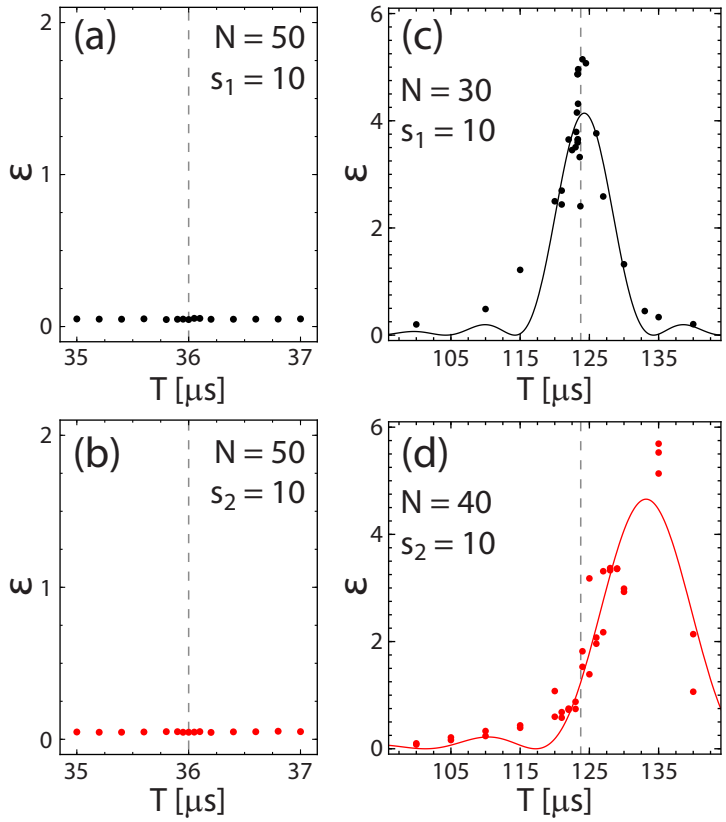

Figure 5.2: Scan of the pulse-period T revealing resonant and off-resonant behavior. The average energy per particle, ε (in units of E_R), is measured for clouds of atoms that are subject to a train of N pulses of a standing-wave optical lattice, of wavelength λ_1 and lattice depth $s_1 E_R$. (a,b) Results for a pulse period of $T \sim 36$ μs, which is off-resonant for both the first and second lattice ($\lambda_1 = 1064$ nm, $\lambda_2 = 782$ nm). (c) For a pulse period of $T \sim 124$ μs, driving with the lattice of wavelength λ_1 fulfills the first Talbot resonance, such that $\kappa/4\pi = 1$. (d) For this same value of T, driving with the second lattice (λ_2) is off-resonant. A nearby higher-order quantum resonance is seen for $T \sim 133$ μs, with $\eta^2\kappa/4\pi = 2$. The solid lines (sinc^2 functionals, motivated by the square-pulse shape) serve only as guides to the eye. The dashed lines in each plot refer to the pulse periods that were used for off-resonant and resonant driving.

by the 1D Hamiltonian

$$H = -\hbar^2\partial_z^2/2M + S(t)E_R/2\ , \tag{5.1}$$

with

$$S(t) = [s_1 \cos(2k_1 z) + s_2 \cos(2k_2 z)] \sum_{j=1}^{N} \sqcap(t/\tau - jT/\tau) \ , \tag{5.2}$$

where $\sqcap$ is the normalized boxcar function. The approximation ignores effects of the trapping potential ($\omega_z/2\pi \approx 30$ Hz along the axis of kicking and mean frequency $\bar{\omega}/2\pi \approx 20$ Hz) and interactions (chemical potential $\mu/h \approx 0.3$ kHz), which is justified if the total pulsing duration is kept less than both $2\pi/\omega_z$ and h/μ. Also, the actual intensity profiles are slightly smoother than the assumed rectangular shape, but with an equivalent area. Further, approximating the pulses as δ-functions allows us to write $S(t) = [s_1\tau \cos(2k_1 z) + s_2\tau \cos(2k_2 z)] \sum_{j=1}^{N} \delta(t - jT)$, which for pulsing with a single lattice corresponds to the standard δ-kicked rotor [82]. To make the connection to this well-studied problem, we reexpress the Hamiltonian in dimensionless form as

$$H' = \rho^2/2 + K(\phi) \sum_{j=1}^{N} \delta(t' - j) \ , \tag{5.3}$$

with

$$K(\phi) = K_1 \cos(\phi) + K_2 \cos(\eta\phi) \tag{5.4}$$

and η defined by the ratio $\eta = k_2/k_1 \sim 1.36$, and rescaled quantities $t' = t/T$, $H' = (8T^2/\hbar T_R)H$, $\phi = 2k_1 z$, $\rho = (2k_1 T/M)p$ (recoil time $T_R = \hbar/E_R$). Here, the conjugate variables ϕ and ρ obey the commutation relation $[\phi, \rho] = i\kappa$, with an effective Planck constant $\kappa = 8T/T_R$. The so-called stochasticity parameters $K_{1(2)} = 4s_{1(2)}\tau T/T_R^2$ serve to delineate regimes of classically regular and chaotic motion. Resonant driving by the first (second) lattice is achieved when $\kappa/4\pi$ ($\eta^2\kappa/4\pi$) is equal to a rational number [or in the parlance of Talbot interference [146], when T matches a rational multiple of the Talbot time $T_T = T_R\pi/2$ ($T_R\pi/2\eta^2$)]. In Fig. 5.2, we plot experimental results of scans of the pulse period T, which demonstrate growth on resonance and a lack thereof away from it.

5.3 A system of coupled kicked rotors

In general, we may expect that adding the incommensurate lattice causes deviations from behavior typical to the δ-kicked rotor. For example, the scenario of incommensurate and irrational values of η corresponds to a quasirandom real-space lattice [164], where the sets of momentum modes $|m\rangle$ and $|n\rangle$ coupled by each of the two light fields have no intersection (and only sparse overlap for most incommensurate values). The absence of direct coupling between these

modes allows us to describe the Hamiltonian as that of an effectively 2D system. Of course, this assumes that the momentum width of the distribution is negligible compared to the spacing between populated modes, necessitating spatially coherent samples as in a BEC. In the discrete plane wave basis of the lattice, $|m,n\rangle = |m\rangle \bigotimes |n\rangle$ with momenta $p_{m,n} = 2(m+n\eta)\hbar k_1$, the Hamiltonian can then be written as

$$H = H_T + \hbar\phi_V \sum_{j=1}^{N} \delta(t - jT) \ , \tag{5.5}$$

where the kinetic and potential terms are, respectively,

$$H_T = 4E_R \sum_{m,n} (m^2 + 2\eta mn + \eta^2 n^2)\hat{n}_{m,n} \qquad \text{and} \tag{5.6}$$

$$\phi_V = (T_R/8T) \sum_{m,n} [K_1(\hat{a}^\dagger_{m-1,n} + \hat{a}^\dagger_{m+1,n}) + K_2(\hat{a}^\dagger_{m,n-1} + \hat{a}^\dagger_{m,n+1})]\hat{a}_{m,n} \ . \tag{5.7}$$

Here $\hat{n}_{m,n}$ is the number operator and $\hat{a}^\dagger_{m,n}$ ($\hat{a}_{m,n}$) is the creation (annihilation) operator for the mode $|m,n\rangle$.

In a stroboscopic description [83], the parameters $K_{1,2}$ control the strength of tunneling within each of the two sets of non-overlapping modes, $|m\rangle$ and $|n\rangle$, whose quasienergies (phase accrual between kicks) are given by the distributions $4E_R T m^2 \mathrm{mod}(2\pi)$ and $4E_R T \eta^2 n^2 \mathrm{mod}(2\pi)$, which are pseudorandom for irrational $\kappa/2\pi$ ($\eta^2\kappa/2\pi$). While the absence of mode overlap guarantees a higher effective dimensionality, there is a *coupling* between the two dimensions in the momentum variables, in the form of the kinetic energy cross term $8\eta mnE_R$, which arises from the fact that the system (with quadratic dispersion) is still physically 1D. Systems of coupled kicked rotors have been shown to have a quantum-to-classical transition [84] even for the simplest possible case of only two rotors. In the following, we experimentally investigate in detail how this coupling influences the kicked rotor dynamics in our system, both away from and at quantum resonance.

5.4 Off-resonant dynamics

We first investigate the influence of an incommensurate lattice on dynamical localization [82], using a pulse period of $T = 36\ \mu$s that is off-resonant for either of the two lattices. When kicking with a single lattice only ($K_{1,2} = \{0, 4.6\}$), the atomic population remains localized in the lowest momentum orders, as can be seen from the TOF images in Fig. 5.1 (b). For increasing N, we observe in

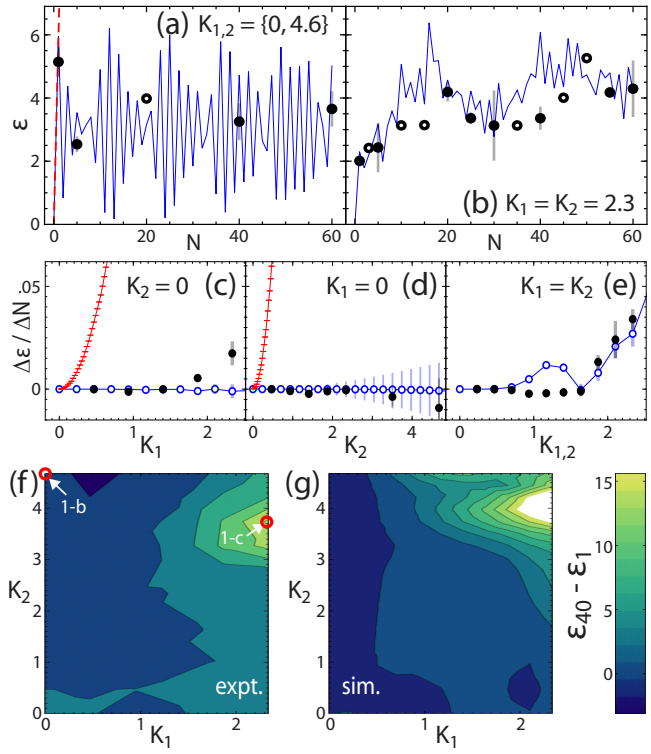

Figure 5.3: Dynamics of a BEC under off-resonant kicking in the presence of disorder. (a) Kicking by a single lattice, with stochasticity parameter $K_2 = 4.6$. Shown is the per-particle energy ε as a function of kick number N. The blue solid and red dashed lines are simulated quantum and classical trajectories, while the black points are experimental data with statistical error bars (empty circles for individual runs). (b) Off-resonant kicking with two incommensurate lattices ($K_1 = K_2 = 2.3$). (c,d,e) Rate of energy growth, $\Delta\varepsilon/\Delta N$, as determined from linear fits to data and simulated points in (a,b). Filled black points are experimental, open blue disks are numerical, and error bars represent the standard error of the linear fits. Shown are the cases of (c) only the first lattice, (d) only the second lattice, and (e) both lattices present with the same strength of kicking $K_1 = K_2$. Red points in (c,d) are classical growth rates. (f,g) Measured and simulated change in the mean energy ε between $N = 1$ to 40 kicks as a function of K_1 and K_2 (8-9 sampled points in each direction). The circles labeled 1-b and 1-c highlight data derived from the distributions of Figs. 5.1 (b,c).

Fig. 5.3 (a) that the per-particle energy ε (in units of E_R) shows no net increase over 60 pulses. This previously observed [157] behavior is unique to the use of degenerate gases occupying a single momentum mode, and is distinct from the

case of dynamical localization in laser-cooled samples of atoms in magneto-optical traps (MOTs), where the initial momentum distribution spans all of the relevant phase-space, and where the energy growth saturates after a "quantum break time" ($t_B = K^2/4\kappa^2$, in units of T), with exponential localization in momentum-space [82, 159]. In our experiments, the pulse period ($\kappa \approx 3.7$) and kicking strengths ($K_{1,2}$) are such that t_B is less than one pulse period for all the cases considered, such that localization sets in immediately.

A theoretical comparison based on numerical simulations, without free parameters and accounting for finite pulse length, shown in Fig. 5.3 (a), confirms the absence of growth. We start with all population in the zeroth momentum order $|\psi_0\rangle = |m = 0, n = 0\rangle$, and then describe the total evolution from one pulse to the next by a unitary "kick" operator $\hat{U} = \hat{R}^{-1}\hat{E}_L\hat{R}\hat{E}_0$, where $\hat{E}_0$ accounts for free evolution for a time $T - \tau$. More explicitly,

$$\langle m', n'|\hat{E}_0|m, n\rangle = \delta_{m,m'}\delta_{n,n'}e^{-i4(m+n\eta)^2(T-\tau)/T_R} \ . \tag{5.8}$$

Likewise, $\hat{E}_L$ describes evolution of the lattice eigenstates (as determined by numerical diagonalization) during the pulse for a time τ. $\hat{R}$ maps the free-particle eigenstates onto those of the lattice. After a train of N pulses, the atomic wavefunction is then given by $|\psi_N\rangle = \hat{U}^N|\psi_0\rangle$. From the simulated momentum distributions, we calculate both the mean per-particle energy ε and the rms momentum width σ_p (in units of $\hbar k_1$). While typically considering up to $\pm$15-20 momentum orders for each lattice, we restrict the determination of ε and σ_p to $|p|/\hbar k_1 \leq 15$, which corresponds to the experimentally observed momenta. We note that the experimental data in Fig. 5.3 (a) differ greatly from a computed classical trajectory (averaged over 10^5 individual trajectories), which after 60 pulses has an energy of $\varepsilon \sim 200$. This rules out the possibility that classical localization (due to Kolmogorov-Arnol'd-Moser [KAM] barriers separating classically chaotic regions [165]) causes the observed localization. We describe briefly at the end of this chapter the determination of the averaged classical trajectories.

We next address the effects of adding the second, incommensurate lattice. For the case of off-resonant kicking with two deep lattices ($K_{1,2} = \{2.3, 3.7\}$), as shown in Fig. 5.1 (c), the observed atomic population clearly delocalizes in momentum space, and the momentum distribution after 40 kicks has a nearly Gaussian distribution, which is consistent with diffusive spreading. Fig. 5.3 (b) shows the dependence of ε on N for a similar situation with slightly weaker kicking ($K_1 = K_2 = 2.3$). Consistently, both experiment and the simulated quantum trajectories reveal that the energy increases with N, and that dynamical localization is destroyed.

To gain insight into the disorder-driven crossover from localization to delo-

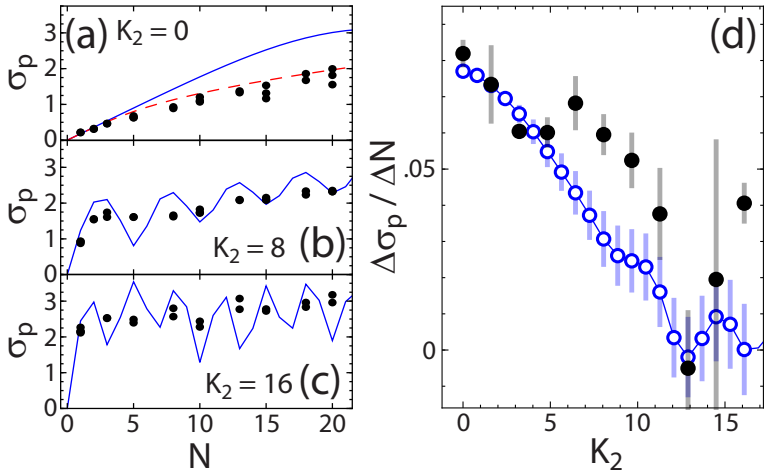

Figure 5.4: Dynamical evolution of resonantly kicked matter waves ($K_1 = 1.6$) in the presence an additional off-resonant drive (K_2). (a,b,c) Momentum-width σ_p of the atomic distribution as a function of kick number N, for a pulse period $T = 124$ μs ($\kappa/4\pi \approx 1$), and $K_2 = 0, 8, 16$. Black points are data from individual experimental runs, the blue line is a numerical calculation for an initial plane-wave, and the dashed red curve takes into account finite-size corrections. (d) Growth rate of the momentum width $\Delta\sigma_p/\Delta N$, determined by a linear fit to the N-dependence, as a function of K_2. The simulated growth rates (open blue circles) are scaled by a factor of 1/2 to account for effects of finite size.

calization, we characterize the energy-growth per kick $\Delta\varepsilon/\Delta N$ using a simple linear fit to the energy evolution (for $1 \leq N \leq 60$, allowing an energy offset at $N = 1$). The rates of growth as a function of K_1 and K_2 are plotted in Figs. 5.3 (c–e) for the cases $K_1 = 0$, $K_2 = 0$, and $K_1 = K_2$. In particular, Figs. 5.3 (c,d) show the absence of sustained growth for either of the single-lattice cases. When simultaneously kicking with both lattices, however, we observe in Fig. 5.3 (e) a transition to a regime of growth (a region of weak transient growth near the transition is seen in the simulation but not in experiment). Signatures of this crossover between dynamical localization and delocalization are confirmed through a time-independent analysis of the single-kick operator $\hat{U}$, based on a stroboscopic Floquet state analysis [83, 166], as described in more detail at the end of this Chapter. Along the line $K_1 = K_2$, such an analysis reveals a transition to delocalized states at a value $K_{1,2} \sim 2.2$, in approximate agreement with the observations of Fig. 5.3 (e).

To obtain a more complete picture of the dependence of dynamical localization on the two lattice strengths, we now more fully sample the parameter-

space of K_1 and K_2. Figs. 5.3 (g,f) show results for the change in ε between 1 and 40 kicks, with good qualitative agreement between data and simulations. As expected, the population remains localized when only a single lattice is used, while significant growth results when strongly kicking with two lattices simultaneously. We note that our observations are in contrast to the case of a single-lattice driven along 1D at incommensurate *temporal* frequencies [41, 152, 167, 168], where similar delocalization is expected only for effectively three or more dimensions [152, 169], as opposed to weak localization in 2D [170].

5.5 Suppression of resonant growth

We now turn to study the influence of the incommensurate lattice on a resonantly kicked quantum rotor, where atoms undergo ballistic transport in momentum space ($\sigma_p \propto N$). The use of a BEC precludes trivial decoherence from a rapid loss of spatial overlap between the momentum wavepackets. We set the pulse period to $T = 124$ μs, which realizes a resonance condition for the first lattice ($\kappa/4\pi \approx 1$), while the driving with the second lattice remains off-resonant. In Fig. 5.4 (a), we observe a (nearly) linear increase in the momentum width for up to $N = 20$ for weak resonant kicking ($K_{1,2} = \{1.6, 0\}$).

The measured growth rate is a factor of two off from what is expected based on plane-wave simulations. This deviation can be explained through the initial rms momentum spread $\Delta p/\hbar k_1 \approx 0.03$ of the trapped atomic distribution, which is limited by its finite size (Thomas–Fermi radius ~ 9 μm along z). Fig. 5.4 (a) also plots the expected on-resonance momentum growth, averaged over the initial momentum distribution of the sample. More explicitly, we assume a Gaussian distribution with momentum width $\sigma = 0.03\hbar k_1$, and employ the analytical formula describing the mean energy per particle (in units of E_R) after N lattice pulses for particles with initial quasimomentum $\beta = p/2\hbar k_1$

$$\varepsilon(\beta, N) = \frac{s_1^2 E_R^2 \tau^2}{2\hbar^2} \left[\frac{\sin^2(2\pi\beta N)}{\sin^2(2\pi\beta)} \right] , \tag{5.9}$$

which is used in and appears as Eq. (2) in Ref. [146], taken from Eq. (13) of Ref. [171].

With the addition of a deep incommensurate lattice [with $K_2 = 8$ and 16, Figs. 5.4 (b,c)] the momentum growth is markedly reduced with respect to the single-lattice case, despite a large effect of the initial kick. We again characterize the growth rate $\Delta\sigma_p/\Delta N$ by a simple linear fit in the range $1 \leq N \leq 20$, which reveals that this rate decreases with the strength of the incommensu-

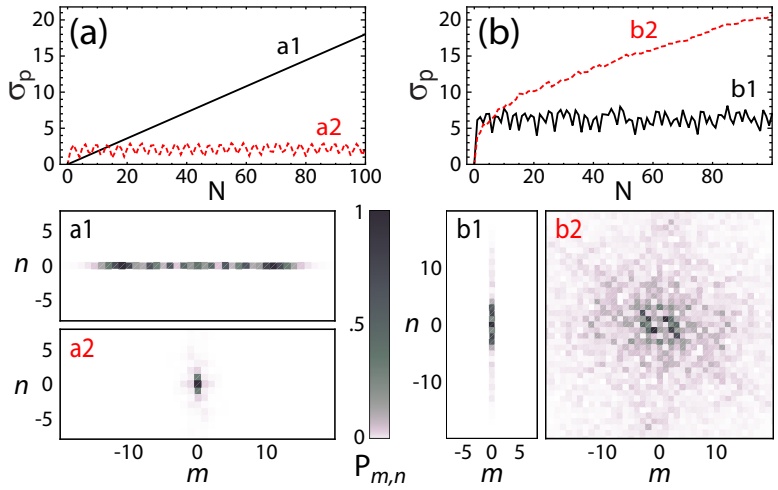

Figure 5.5: Simulated effective-2D dynamics of a coupled δ-kicked rotor system. (a) Dependence of the momentum width σ_p on kick number N, for the case of resonant kicking ($\kappa/4\pi = 1$; $\tau = 10$ ns) with a single lattice ($K_{1,2} = \{1.6, 0\}$, black solid line a1), and with an added deep incommensurate lattice ($K_{1,2} = \{1.6, 12.8\}$, red dashed line a2). (b) Dependence of σ_p on N for off-resonant kicking ($T = 36$ μs ; $\tau = 10$ ns) with a single lattice ($K_{1,2} = \{0, 11.7\}$, black solid line b1), and for off-resonant kicking with two lattices ($K_{1,2} = \{5.8, 5.8\}$, red dashed line b2). The lower panels show the 2D momentum distributions ($\mathrm{P}_{m,n} = |\langle m, n|\psi_N\rangle|^2$) at $N = 100$ for all trajectories, decomposed with respect to the two standing waves.

rate lattice K_2, as shown in Fig. 5.4 (d). A simulation for a wider range of kicks (and for more ideal δ-kicking exactly at resonance) suggests that the inhibition of ballistic transport is due not to a crossover to classical diffusion as in the off-resonant case, but rather to the onset of dynamical localization in the strong incommensurate lattice. This becomes even more apparent upon examining the distributions in the 2D space of modes with indices m and n of the two lattices, c.f. Fig. 5.5 (a).

5.6 2D representation

Naturally, we expect that the mechanism underlying the suppression of resonant growth should again be due to the coupling term $8\eta mnE_R$. It is clear that when the atoms have non-zero momenta from the second lattice ($n \neq 0$), this additional term destroys coherent phase revival of all modes of the first lattice [integer $4E_R T m^2/2\pi$]. Surprisingly, however, a complete suppression

of resonant growth is found, even though the atomic population spends a significant amount of time in the $n = 0$ subspace. The suppression of coherent growth due to strong coupling into and out of $n = 0$ is somewhat reminiscent of the physics of the Kapitza pendulum [172] and of ponderomotive potentials for charged particles, where strong off-resonant driving dynamically suppresses transport.

Depiction of the momentum distributions in the 2D space spanned by the two lattices also helps us to visualize the breakdown of dynamical localization for the case of off-resonant driving. Fig. 5.5 (b) shows simulated dynamics similar to the experimental situation in Fig. 5.3, however for couplings $K_{1,2}$ exceeding those attainable in experiment. The dynamics of σ_p show that dynamic localization occurs for kicking with a single lattice only ($K_{1,2} = \{0, 11.7\}$), while kicking off-resonantly with two lattices ($K_{1,2} = \{5.8, 5.8\}$, same total strength) gives rise to a dramatic delocalization in the 2D m-n space.

5.7 Concluding remarks

In conclusion, we have studied the dynamics of a BEC subject to a periodically kicked quasidisordered optical lattice that is formed by two incommensurate standing waves. We find that the addition of the second, incommensurate lattice leads to radically different behavior from that of the standard kicked rotor (occuring for a single lattice), characterized by a suppression of resonant momentum spreading at quantum resonance and diffusive transport instead of dynamical localization for off-resonant kicking. We relate these observations to the emergence of classical behavior in a system of two *coupled* kicked rotors. A possible extension of our study would be the realization the kicked Harper model [173, 174], for kicked harmonic oscillators, with a strong nonlinear coupling term. This could be studied, for example, by examining the single-site orbital (band population) dynamics of a periodically-tilted Mott insulator, where the nonlinear term may be controlled through either a tunable on-site filling or via the interaction strength with a Feshbach resonance. Additionally, a natural extension in our system would be to study a "spinful" kicked rotor, i.e. by using atoms in a superposition of different spin states and driving them with a state-dependent lattice beam. It has recently been proposed [175] that such a system might allow for a study of the anomalous quantum Hall effect with driven cold atoms. A simple scenario of spinful kicking, leading to classical diffusion in momentum-space, is discussed in Appendix A.

5.8 Supporting considerations

5.8.1 Classical dynamics

It is well known that classical localization can occur in kicked-rotor systems for small values of the stochasticity parameter, where the classical system is not globally chaotic but supports bounded orbits due to KAM barriers [83]. To demonstrate that this effect does not contribute to the observed localization in momentum space in Fig. 2 (a,c,d) of the main text (i.e. for atoms kicked by only a single optical lattice), we compare the experimental data and the simulated quantum trajectories of the per-particle energy ε as a function of kick number N to simulated classical dynamics, averaged over 10^5 classical trajectories. To briefly detail the determination of the averaged classical dynamics, each individual classical trajectory is determined by probabilistically projecting out the particle's momentum space wavefunction after each application of the kick operator $\hat{U}$. We show in FIG. 5.6 (i-iv) the classical dynamics of ε, as averaged over $n = 10$, 10^2, 10^3, and 10^5 individual trajectories, for the same system parameters as used in Fig. 2 (a) of the main text [$T = 36$ μs ; $\tau = 2$ μs ; $K_2 = 4.6$ ($s_2 = 100$) ; $K_1 = 0$]. For large sample sizes, the classical growth rate is found to be in fair agreement with the expected classical diffusion constant [166],

$$\Delta\varepsilon/\Delta N \sim \eta^2 V_2^2 \tau^2/2\hbar^2 = 2\eta^2 K_2^2/\kappa^2 \ , \tag{5.10}$$

for the second lattice ($2K_1^2/\kappa^2$ for the case of only using lattice 1). It is observed that for large kick numbers, the simulated classical trajectories grow more slowly than one would expect from the classical diffusion constant. This deviation is due to the finite pulse length ($\tau = 2$ μs) of the applied kicks [122], and in FIG. 5.6 (iv) we also plot the simulated trajectories for the same pulse area but for $\tau = 1$ μs and 0.1 μs, showing that better agreement is reached in the limit of δ-like pulses.

5.8.2 Floquet eigenstate analysis of $\hat{U}$

To gain a deeper insight into the expected response of the matter waves to a given kick operator $\hat{U}$ (i.e. for given pulse lengths, lattice depths, and pulse period), we analyze the properties of the matrix $\hat{U}$ in a time-independent manner. While monitoring the response of the matter waves as a function of the kick number N makes a direct connection to experiment and can discern between regimes of localization and delocalization in momentum space, at short times it may be subject to transient behavior and small-scale fluctu-

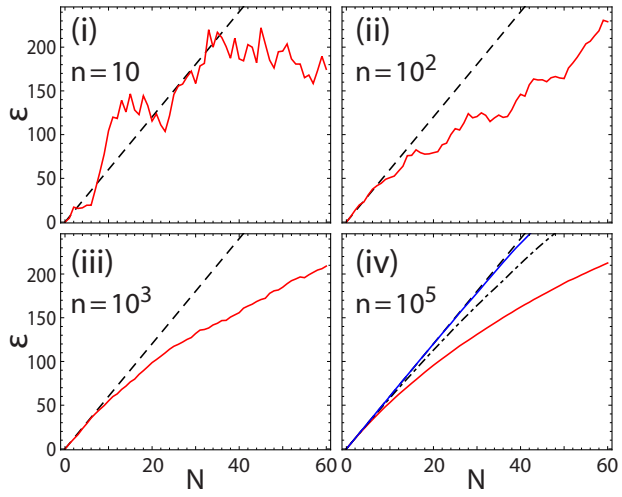

Figure 5.6: Averaged classical dynamics of the energy ε as a function of kick number N for different sample sizes consisting of n trajectories, for off-resonant kicking with the second lattice [$K_2 = 4.6$ ($s_2 = 100$) ; $K_1 = 0$; $\tau = 2$ μs]. (i-iv) Averaged trajectories are shown for the cases of $n = 10$, 10^2, 10^3, and 10^5 as solid red lines. In all plots, we also show as a dashed black line the expected classical diffusion for delta-function kicks. In (iv), we also show classical trajectories for the cases in which the pulse area is the same, but with smaller pulse durations of $\tau = 1$ μs (black dashed-dotted line) and 0.1 μs (blue solid line).

ations. We are experimentally restricted to a modest number of kicks in order to maintain a near-field treatment (i.e. assuming identical, overlapped spatial wavefunctions for all the matter-wave fields) and to minimize contributions from nonlinear atom-atom interactions. Motivated by pioneering work that made a stroboscopic connection between the quantum δ-kicked rotor model and the 1D Anderson model on a lattice [83], we study the properties of the Floquet (or Bloch–Floquet) quasi-energy eigenstates of the kick operator $\hat{U}$. For regimes in which the growth dynamics result in dynamical localization, these Floquet eigenstates should all be localized in momentum space, while they are delocalized in the case of diffusive growth.

We first investigate the case of kicking off-resonantly with two lattices of equal strength (stochasticity parameter $K_1 = K_2 \equiv K_{1,2}$), using the same parameter values as in Fig. 5.3 (e). In Fig. 5.7 (i,ii), we plot the momentum space distribution of the lowest energy Floquet eigenstates of $\hat{U}$, $|\psi_0^U\rangle$, for $K_{1,2} = 2.15$ and 2.34. The plotted distributions are shifted by the mean momentum $\bar{p} = \langle\psi_0^U|\hat{p}|\psi_0^U\rangle$ to $p' = p - \bar{p}$. While the distribution is localized

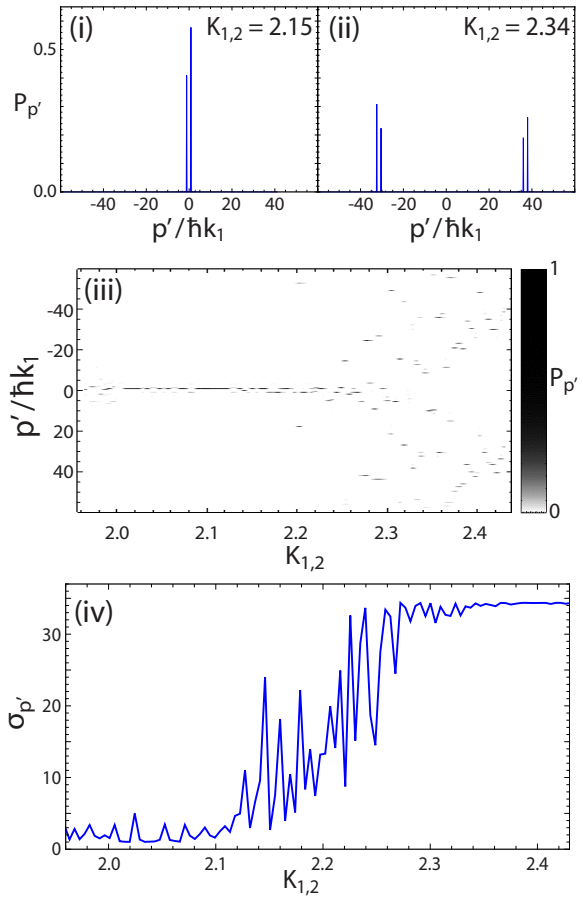

Figure 5.7: Time-independent analysis of the kick operator $\hat{U}$ for off-resonant kicking ($T = 36$ μs) by both lattices, with equal kicking strengths $K_{1,2}$ for each. (i,ii) Momentum distribution of the lowest energy Floquet eigenstate of $\hat{U}$, $|\psi_0^U\rangle$, in the plane-wave basis. The momenta p are shifted by the mean value $\bar{p} = \langle\psi_0^U|\hat{p}|\psi_0^U\rangle$ to $p' = p - \bar{p}$. For low values of the kicking strength, as in (i), the eigenstates are localized in momentum space, while for larger values they became delocalized as in (ii). (iii) Momentum distributions as in (i,ii) as a function of the stochasticity parameter $K_{1,2}$. Beyond a value of $K_{1,2} \sim 2.2$ a bifurcation and delocalization of the momentum distributions is observed. (iv) For the same range of stochasticity parameter values as in (iii), we plot the rms momentum width $\sigma_{p'}$ of the lowest energy eigenstates of $\hat{U}$, which exhibits a sharp increase across a value $K_{1,2} \sim 2.2$.

for the weaker kicking strength, it is delocalized into two regions for the larger strength. In fact, in Fig. 5.7 (iii) we observe a bifurcation of the eigenstate distributions as the stochasticity parameter $K_{1,2}$ is increased. We can readily

calculate the rms momentum width $\sigma_{p'}$ of these distributions, and as shown in Fig. 5.7 (iv) there is a sharp rise in the width across a value of $K_{1,2} \sim 2.2$. Not surprisingly, this value is in general agreement with the observed onset of non-zero energy growth versus kick number in Fig. 2 (e) of the main text.

There exist certain superficial analogies between our experiment involving atoms driven with two *spatial* frequencies and experiments performed with multiple *temporal* frequencies, which result in an effectively higher-dimensional localization when the frequencies are incommensurate. In order to explore this connection, we perform a Floquet eigenstate analysis in the full parameter space of K_1 and K_2. In Fig. 5.8 (i), we plot as white the regions in which the Floquet eigenstates are localized in momentum space and as dark blue the regions in which they are delocalized, with the criterion for delocalization being that more than 10% of the population resides further than 5.5 momentum units ($\hbar k_1$) away from the most populated mode. This plot shows localization along either axis, where dynamical localization is expected for any value of the kicking strength when only a single lattice is used, while delocalization generally occurs beyond some line in the parameter space spanned by K_1 and K_2. Much as in the case of driving with multiple temporal frequencies, delocalization only occurs when the strengths of each of the incommensurate frequency components are significant. We also show in Fig. 5.8 (ii) the simulated change in ε between one and $N = 40$ kicks, as in Fig. 3 (b) of the main text but over a larger range of K_1 values. This plot demonstrates that qualitatively similar regions of localization and delocalization are also observed in the energy growth dynamics.

5.8.3 Lattice incommensurability

In a theoretical treatment of the quantum kicked-rotor model with two spatial frequencies [153], the incommensurability of the two frequencies is found to be a necessary condition for inducing a quantum-to-classical transition in the dynamical behavior. Moreover, this incommensurability is a well-known condition for realizing higher dimensional localization in multi-frequency driving in the temporal domain [41, 152, 166, 168], as well as for achieving quasi-random lattices in configuration space with multiple standing-waves [33, 46]. While experimentally we work with a fixed commensurability parameter $\eta \sim 1.36$, here we investigate the role of this condition through simulations of the off-resonant and resonant dynamics.

In Fig. 5.9 (a), for $T = 36$ μs and $\tau = 2$ μs, we show the expected energy growth rate $\Delta\varepsilon/\Delta N$ (determined for $N = 1$ to 60 kicks) for atoms kicked by two lattices of equal depth $V_1 = V_2 = 100\ E_R$ as a function of the parameter η. A minimum in the induced growth can be seen for $\eta = 1$, as expected. However,

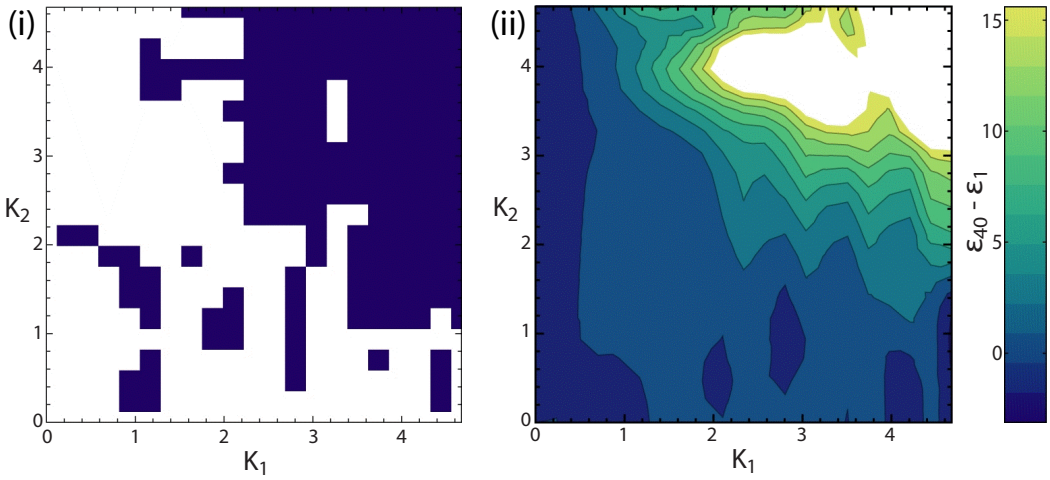

Figure 5.8: Localization-delocalization transition in the K_1-K_2 plane. (i) As a function of the stochasticity parameters K_1 and K_2, we plot as white the regions in which the Floquet eigenstates of $\hat{U}$ are localized in momentum space and as blue the regions in which they are delocalized, as detailed in the text. A general trend of delocalization for strong kicking with both lattices, and localization when kicking with only a single lattice, is observed. (ii) Here we replot the simulation data from Fig. 5.3 (g), showing the change in energy ε from the first to $N = 40$ kicks, but over a larger range of K_1 values. Behavior qualitatively similar to the localization-delocalization plot in (i) can be observed in this dynamical response data.

the dependence of the growth rate on the commensurability condition becomes somewhat intertwined with other η-dependent effects. Most importantly, while the wavelength of the first lattice is kept fixed at 1064 nm, the second lattice's wavelength varies with η, such that full or fractional quantum resonances [146] are encountered whenever $4\eta^2 T E_R/h$ equals a rational number. To disentangle these two contributions, we show in Fig. 5.9 (b) the growth rate dependence on η, averaged over a large sample of pulse periods to smooth out effects of quantum resonances. Specifically, we average over the randomly chosen set of values $T = \{36, 32, 59, 67, 98, 68, 62, 86, 84, 82, 76, 85, 48, 88, 41, 87, 99, 90, 55\}$ μs. Here, we observe a much clearer minimum at $\eta = 1$ for the case of full commensurability.

Now we investigate the dependence of resonant dynamics on the commensurability of the two lattices. It was observed in Fig. 5.4 of the main text that the addition of an incommensurate lattice reduces the growth of the rms momentum width as a function of kick number, $\Delta\sigma_p/\Delta N$. In Fig. 5.9 (c) we show the dependence of the growth rate on η for the case $V_1 = V_2 = 10\ E_R$ with

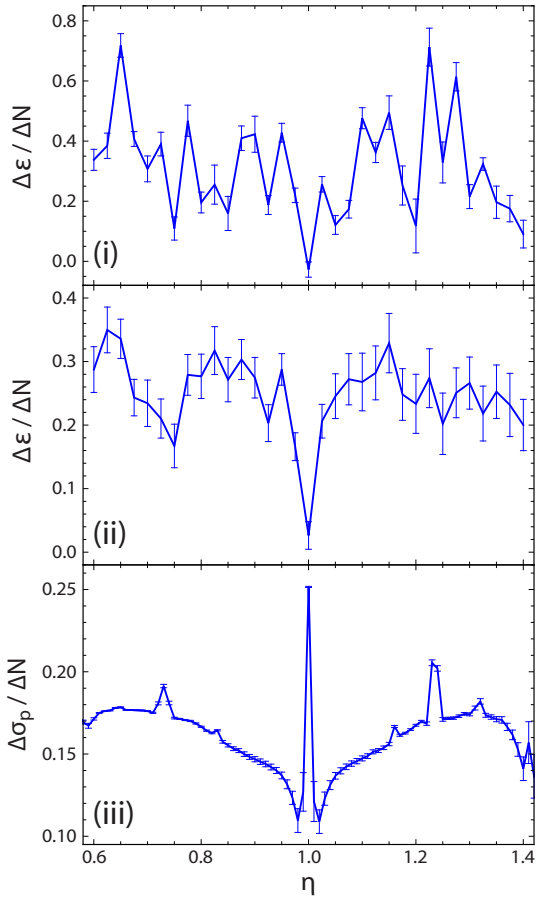

Figure 5.9: (a,b) Dependence of induced energy growth for off-resonant driving by two lattices on the commensurability parameter η. In (a) the growth rate $\Delta\varepsilon/\Delta N$ is shown as a function of $\eta = \lambda_1/\lambda_2$, for kicking with two lattices of equal strength ($V_1 = V_2 = 100\ E_R$ for $\tau = 2\ \mu$s) and a pulse period of $T = 36\ \mu$s. The wavelength of the first lattice is kept fixed at $\lambda_1 = 1064$ nm, while the second is varied with η. A local minimum at $\eta = 1$ can be observed, while other features may be due to full or fractional quantum resonances of the second lattice. (b) Same dependence of $\Delta\varepsilon/\Delta N$ on η, but averaged over a number of pulse periods T to smooth out features due to quantum resonances of the second lattice. (c) Effect of commensurability parameter η on the breakdown of momentum growth for on-resonant kicking. The pulse period is set to $T = 123.3\ \mu$s ($\kappa/4\pi = 1$) to be resonant with the first lattice, with pulse widths of $\tau = 2\ \mu$s and lattice depths of $V_1 = V_2 = 10\ E_R$. For values of $\eta \neq 1$ there is a strong suppression of the growth rate $\Delta\sigma_p/\Delta N$, while local maxima appear at $\eta^2 \sim 0.5$ and 1.5, i.e. when $\eta^2\kappa/4\pi$ is near a rational number.

timings $T = 123.3$ μs and $\tau = 2$ μs. A clear maximum is observed for $\eta = 1$, as both lattices contribute to the resonant growth, while a general suppression is observed otherwise. Smaller resonances can be observed for $\eta^2 \sim 0.5$ and 1.5, when the second lattice fulfills a fractional quantum resonance.

Chapter 6

Strongly interacting Bose gases I: theoretical concepts

In this chapter, we discuss some fundamental concepts for the study of strongly interacting, lattice-confined atomic gases, where effects of atom-atom interactions are of central importance. Theoretical descriptions are given both for the case of deep lattice confinement, where a basis of localized atomic wavefunctions is appropriate, and the case of strongly-interacting 1D gases in a weak (or vanishing) longitudinal optical lattice.

6.1 Bose–Hubbard model

A few years after the achievement of BEC [4, 5], it was realized [29] that ultracold bosons confined to an optical lattice potential could be an ideal experimental implementation of the Bose–Hubbard model (BHM) [28]. As the simplest description of interacting bosons in a period potential that fully maintains quantum correlations, the BHM is important for describing a number of experimental systems, including that of superfluid ^{4}He in porous media, Josephson junction arrays, and strongly-coupling BCS pairs. The experimental realization of the BHM several years later [123, 176], and the observation of a quantum phase transition between superfluid and an insulator of bosons, has thus been of great importance, not only with respect to study of bosonic systems, but in paving the way for quantum emulation of non-trivial systems with highly-controllable ensembles of ultracold atoms [27]. Here, we discuss concepts relevant to implementation of the Bose–Hubbard model with ultracold neutral atoms.

Let us first recall the second quantized Hamiltonian describing a system of interacting (via elastic two-body collisions) scalar bosonic particles in a potential $V_{pot}(\mathbf{x})$, as introduced in Chapter 2,

$$\hat{H} = \int d\mathbf{x}\hat{\psi}^\dagger(\mathbf{x})\Big[-\frac{\hbar^2\nabla^2}{2m} + V_{pot}(\mathbf{x})\Big]\hat{\psi}(\mathbf{x}) + \frac{1}{2}\int\int d\mathbf{x}d\mathbf{x}'\hat{\psi}^\dagger(\mathbf{x})\hat{\psi}^\dagger(\mathbf{x}')V_{at}(\mathbf{x}-\mathbf{x}')\hat{\psi}(\mathbf{x})\hat{\psi}(\mathbf{x}') \ , \quad (6.1)$$

where $\hat{\psi}^\dagger(\mathbf{x})$ and $\hat{\psi}(\mathbf{x})$ are the bosonic field creation and annihilation operators. The cold atom-atom collisions are described by the interatomic potential $V_{at}(\mathbf{x}) = g\delta(\mathbf{x})$, where the coupling constant g is given by $g = 4\pi\hbar^2 a_s/m$, with a_s the s-wave scattering length.

To faithfully describe the correlations in a system of strongly interacting bosons, it is necessary to forgo a mean-field description – as adopted in Chapter 2 in introducing the Gross–Pitaevskii equation – and maintain field quantization. For the case of an optical lattice potential, and allowing for a slowly-varying external potential, $V_{pot}(\mathbf{x}) = V_{latt}(\mathbf{x}) + V_{ext}(\mathbf{x})$, a more approximate description of the Hamiltonian for strongly-coupled lattice bosons can be found. We first expand the field operator $\hat{\psi}^\dagger(\mathbf{x})$ in the basis of localized Wannier states as

$$\hat{\psi}(\mathbf{x}) = \sum_{i,n}\hat{a}_i^{(n)}w_n(\mathbf{x}-\mathbf{x}_i) \ , \quad (6.2)$$

where $\hat{a}_i^{(n)}$ is the annihilation operator for a boson in the n-band Wannier orbital located on site i.

Under typical experimental conditions, a great simplification of the Hamiltonian is achieved through the tight-binding approximation, by considering only ground band Wannier orbitals ($n = 0$) and by neglecting off-site interactions. Furthermore, direct tunneling beyond the nearest neighbor can usually be neglected. These conditions require that the atomic samples be of sufficiently low temperature not to populate higher bands, and that the lattices be of sufficient depth such that the energy gap to the first-excited band is much larger than either the tunneling or on-site energies.

With these conditions fulfilled, the Hamiltonian can then be recast as

$$\hat{H}_{\mathrm{BH}} = -t\sum_i(\hat{a}_i^\dagger\hat{a}_{i+1} + \hat{a}_{i+1}^\dagger\hat{a}_i) + \frac{U}{2}\sum_i\hat{n}_i(\hat{n}_i - 1) + \sum_i\hat{n}_i(\varepsilon_i - \mu) \ . \quad (6.3)$$

Here, $\hat{a}_i^\dagger$ and $\hat{a}_i$ are the creation and annihilation operators for atoms at site i, obeying the standard bosonic commutation relations $[\hat{a}_i, \hat{a}_j^\dagger] = \delta_{ij}$, and

$\hat{n}_i = \hat{a}_i^\dagger \hat{a}_i$ is the number operator. The chemical potential μ serves as a Lagrangian multiplier to fix the mean atom number of the system in the grand canonical ensemble. The nearest-neighbor tunneling matrix element t, the on-site interaction energy U, and the site-dependent energy offset ε_i, are respectively defined in relation to the Wannier orbital wavefunctions and the applied potentials as

$$t = t_i = -\int d\mathbf{x} w_0^*(\mathbf{x} - \mathbf{x}_i)\Big[-\frac{\hbar^2\nabla^2}{2m} + V_{latt}(\mathbf{x})\Big] w_0(\mathbf{x} - \mathbf{x}_{i+1}) \ , \tag{6.4}$$

$$U = \frac{4\pi a_s \hbar^2}{m}\int d\mathbf{x}|w_o(\mathbf{x})|^4 \ , \text{ and} \tag{6.5}$$

$$\varepsilon_i = \int d\mathbf{x} w_0^*(\mathbf{x} - \mathbf{x}_i)\big[V_{ext}(\mathbf{x})\big] w_0(\mathbf{x} - \mathbf{x}_i) \approx V_{ext}(\mathbf{x}_i) \ . \tag{6.6}$$

For fixed chemical potential, a quantum phase transition between superfluid to Mott insulator is encountered as a function of t/U, due to a competition between kinetic and interaction energy. Here, superfluid refers to a state of atoms with non-zero number variance, a continuous spectrum of excited states, and supporting mass currents, i.e. density response to variations of the chemical potential. Mott insulator refers to a state that has zero number variance, has a gapped excitation spectrum, which makes it insensitive to small changes in the chemical potential, suppressing mass currents. In practice, AMO systems allow for a dynamical tuning of these parameters over a wide range, and provide access to a large range of the phase diagram. The on-site interaction U may be directly tuned via a Feshbach resonance [19], where the magnitude of a_s can be controlled over orders of magnitude, and the sign may even be inverted [177]. In our system, we control both the tunneling t and the on-site energy U through change of the optical lattice depths sE_R (recoil energy $E_R = \hbar^2k^2/2m$, lattice wavevector $k = 2\pi/\lambda$). We plot in Fig. 6.1 the dependence of t and U on the depth s, based on band-structure calculations, for the case of an isotropic 3D lattice of wavelength $\lambda = 1064$ nm and a s-wave scattering length of 100 a_0. For comparison with the numerically determined parameter values, we also provide analytical forms for t and U applicable for deep lattices $s \gg 1$, based on analytical solutions of the Mathieu equation and on the approximation of Gaussian wavefunctions in harmonic potentials, respectively [107]. For deep lattices, the tunneling parameter t is approximately given as $t/E_R = (4/\sqrt{\pi})s^{3/4}e^{-2\sqrt{s}}$, and the on-site interaction between two atoms for the case of isotropic lattice depths is given as $U/E_R = 4ka_s s^{3/4}/\sqrt{2\pi}$, or as $U = 2\hbar\omega(a_s/\sigma)/\sqrt{2\pi}$ in terms of the harmonic oscillation frequency $\omega = 2E_R\sqrt{s}/\hbar$ and harmonic oscillator length

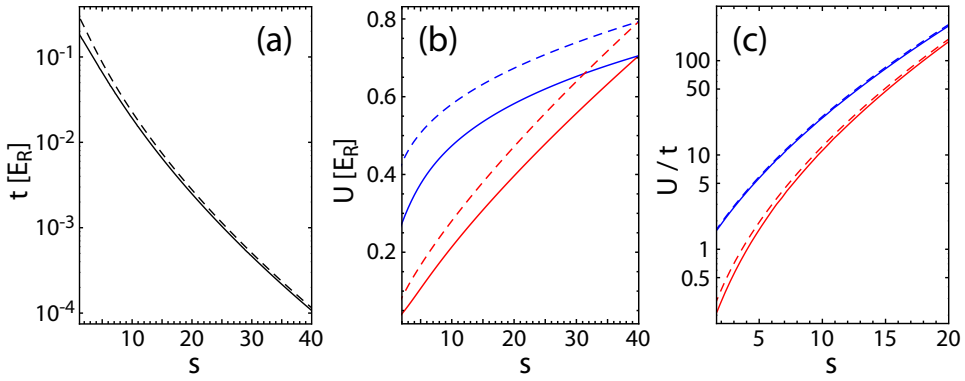

Figure 6.1: Bose–Hubbard model parameters t and U as a function of the lattice depth sE_R. (a) Magnitude of the tunneling matrix element t/E_R obtained from the width of the lowest lattice band $t = \Delta E/4$. (b) On-site interaction energy U/E_R for a 3D geometry (red), with an assumed s-wave scattering length $a_s = 100\ a_0$ and wavelength $\lambda = 1064$ nm. Also shown in blue is U/E_R for a 1D geometry, with lattice depths of $s_\perp = 40$ along the transverse axes. (c) Ratio of t/U as a function of lattice depth sE_R, for the 3D and 1D geometries, in red and blue. For all cases, the dashed lines represent approximate analytical forms as discussed in the text.

$\sigma = \sqrt{\hbar/m\omega}$. In the case of unequal lattice depths or spacings along different axes, the on-site energy is given as $U = 2\hbar\bar{\omega}(a_s/\bar{\sigma})/\sqrt{2\pi}$, where the bars refer to geometric means of the different axes. The distribution of site-dependent energy offsets ε_i is usually determined by the slowly-varying Gaussian envelope of the optical dipole trapping beams. However, as will be discussed in subsequent chapters, a more active control over the ε_i distribution – which can be implemented, e.g., with additional optical potentials [46, 68, 69, 75] or with atomic potentials in the two-component BHM [44, 46, 47, 66, 67, 71] – can be used to study phases of the disordered BHM.

A qualitative understanding of the BHM phase diagram can be obtained by examining the extreme limits of the competition between kinetic (t) and interaction (U) energies, which promote delocalization and localization the single-particle wavefunctions, respectively. In the limit of vanishing interactions $U/t \to 0$, the problem reduces to that of non-interacting bosons in a lattice band-structure. The lowest energy eigenstate in the ground-band is at $q = 0$, and all the particles will Bose condense into this lowest energy Bloch state. We can express the state of N particles condensed into this Bloch state, delocalized across a system of M sites with uniform phase, in the Wannier

orbital basis as

$$|\psi_{SF}\rangle \propto \left(M^{-1/2} \sum_{j=1}^{M} \hat{a}_j^\dagger \right)^N |0\rangle \ . \tag{6.7}$$

This pure superfluid (SF) state is a coherent number state, and it can be written as a product state of uncorrelated single-atom wavefunctions. We note that, although we use the standard terminology of a "superfluid", in the complete absence of interactions the typical hallmarks of superfluidity – the possibility of creating vortices, a linear phonon branch of the dispersion relation at low quasimomentum, etc. – are not present in the system.

In the opposite limit of negligible tunneling and/or strong interactions ($t/U \to 0$), repulsive interactions between atoms cause the position of a given atom to depend on the positions of the other atoms. The total energy of the Hamiltonian is minimized by reducing the sum of non-linear interaction energies on each site, which is achieved by having uniform site occupancies across the sample. This strongly-correlated state may be written in the occupation basis of Wannier states as

$$|\psi_{MI}\rangle \propto \prod_{j=1}^{M} (\hat{a}_j^\dagger)^{N/M} |0\rangle \ , \tag{6.8}$$

and is referred to as the Mott insulator (MI) state (assuming an integer value of N/M relating to a commensurable density). The MI state has a minimized variance in the number distribution (number-squeezed), and a maximized variance in the relative phase distribution, characterized by a loss of phase coherence across the sample. For more general ratios of t/U, the ground-state and excitations may be determined either by solving the system exactly, or through approximate theoretical techniques, as described below. In these intermediate regimes, even when the superfluid density is non-zero and the state may be characterized as a superfluid, it can display strong many-body correlations [178].

6.1.1 Mean-field treatment of the BHM

One approach used to approximately determine the state of a system for a given set of parameter values is to make a mean-field approximation [29, 179–181] that neglects the correlations between the individual particles. Similarly to the approach used to describe mean-field interactions in the Gross–Pitaevskii equation, we introduce a superfluid order parameter defined as $\psi = \sqrt{\langle \hat{n}_i \rangle} = \langle \hat{a}_i^\dagger \rangle = \langle \hat{a}_i \rangle$, which reflects the mean value of a spatially homogeneous condensate field (with ψ chosen to be a real number). The creation and

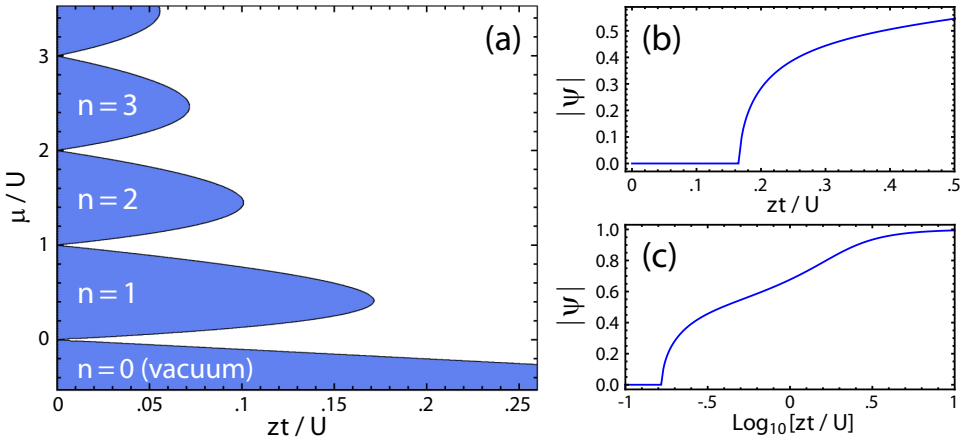

Figure 6.2: Mean-field phase diagram of the Bose–Hubbard model (BHM). (a) Areas of zero (blue) and non-zero (white) superfluid order parameter are shown, delineating the superfluid and insulating regions of the BHM. The phase diagram is plotted as a function of the chemical potential scaled by the interaction energy, μ/U (where the mean occupancy is $\langle n \rangle = \mu/U + 1/2$), and the scaled tunneling energy zt/U (with z the number of nearest neighbors). The insulating regions are characterized by a fixed atom number per site. (b) Superfluid order parameter $|\psi|$ (normalized), across the phase-transition boundary for variable zt/U and fixed average filling of unity ($\mu/U = 0.5$). (c) Over a larger range of zt/U values (in log-scale), a fuller growth of the superfluid order parameter can be seen.

annihilation operators are then given by their mean values and a fluctuation term about the mean, as $\hat{a}_i = \psi + \Delta\hat{a}_i$ and $\hat{a}_i^\dagger = \psi + \Delta\hat{a}_i^\dagger$. We may then insert the expression

$$\hat{a}_i^\dagger \hat{a}_j = (\psi + \Delta\hat{a}_i^\dagger)(\psi + \Delta\hat{a}_j) \approx \psi^2 + \psi(\hat{a}_i^\dagger - \psi) + \psi(\hat{a}_j - \psi) = -\psi^2 + \psi(\hat{a}_i^\dagger + \hat{a}_j) \ , \tag{6.9}$$

where we have neglected second-order fluctuations, into the Bose–Hubbard Hamiltonian. The Hamiltonian then reduces to a set of decoupled single-site Hamiltonians of the form [181]

$$\hat{H}_i' = -\frac{zt}{U}(\hat{a}_i^\dagger + \hat{a}_i)\psi - \frac{\mu}{U}\hat{n}_i + \frac{1}{2}\hat{n}_i(\hat{n}_i - 1) + \frac{zt}{U}\psi^2 \ , \tag{6.10}$$

where we have rescaled all terms by the on-site energy U. Here, $z = 2d$ is the number of nearest neighbors for a lattice of dimensionality d.

To find the ground state for a given set of parameters z, t, U, and μ, we variationally minimize the total energy as a function of ψ. Fig. 6.2 (a) plots

the variationally determined phase-diagram depicting regions in which the expectation value of $\hat{H}_i$ is minimized by either a zero or a non-zero superfluid order parameter, relating to insulating and superfluid regions. The value of the superfluid order parameter ψ becomes non-zero outside of the Mott insulator lobes, as shown in Fig. 6.2 (b,c) for fixed chemical potential $\mu/U = 0.5$, and approaches its maximum value in the limit $zt \gg U$. In nearly all experimental realizations, the system has a fixed total atom number but a spatially varying chemical potential μ, as defined by the inhomogeneous trapping potential. For a uniform value of zt/U about a sample in the atomic limit, this results in so-called "wedding cake" or "ziggurat" density structures [29, 76–78, 182, 183]. in which domains of different quantum phases - here SF and MI - coexist within the same inhomogeneous sample, as determined by the local density.

6.1.2 Exact solutions of the BHM for small systems

For systems of relatively small size, one can also perform exact numerical diagonalization of the BHM (Eq. 6.3) for fully soft-core bosons (i.e. no restrictions on site occupancy). For a fixed atom number N and fixed number of lattice sites M, the number of possible states of the system (of the form $|n_1, n_2, \cdots, n_{M-1}, n_M\rangle$ with a total of $\sum_{j=1}^{M} n_j = N$ particles) is given by $N_s = (N + M - 1)!/N!(M - 1)!$, growing exponentially with the system size. Here, we examine the case of commensurate filling $N/M = 1$ for $N = 6$ particles, assuming a uniform site-dependent offset energy $\varepsilon_i = 0$ and working with periodic boundary conditions $i \equiv M + i$.

To start, we shall consider only the ground state of the system $|\phi_g\rangle$, which should change character as a function of t/U. To study the transition between the superfluid and the Mott insulator regimes, we examine the overlap of the exact ground state with the superfluid and Mott insulator ground states, $|\psi_{SF}\rangle$ and $|\psi_{MI}\rangle$, which are exact only in the respective limits $t/U = \infty$ and $t/U = 0$. The overlap between two pure quantum states $|\phi_A\rangle$ and $|\phi_B\rangle$ can be characterized by the fidelity $F = |\langle\phi_A|\phi_B\rangle|$. In Fig. 6.3 (a), we plot the square of the fidelity of the ground state with the SF and MI ground states, i.e. $F_{SF}^2 = |\langle\phi_g|\psi_{SF}\rangle|^2$ and $F_{MI}^2 = |\langle\phi_g|\psi_{MI}\rangle|^2$, as a function of t/U. Another way to characterize the overlap between two pure quantum states $|\phi_A\rangle$ and $|\phi_B\rangle$ is through the statistical *distance* [184] between them, given as $D^2 = 4(1 - |\langle\phi_A|\phi_B\rangle|^2)$. In Fig. 6.3 (b), we plot the distance D between the exact ground state and the SF and MI ground states, as a function of t/U.

While studying the fidelity and statistical distance of the ground state with respect to some prototypical many-body states can be instructive, it is a bit detached from experiment, where one does not typically have information about the full quantum state of the system (as through quantum state tomog-

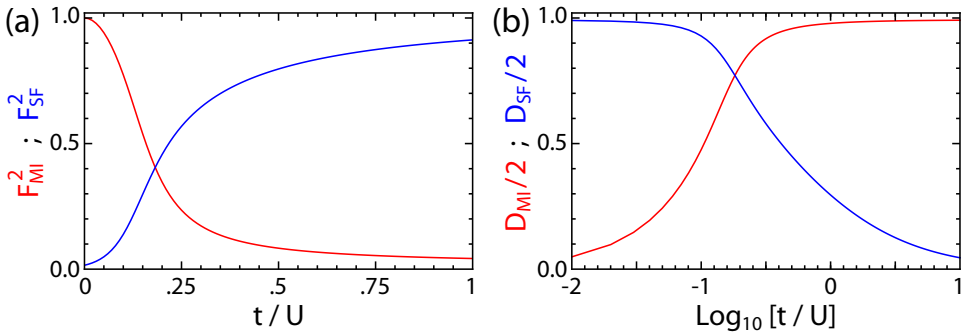

Figure 6.3: Tuning the ground state from a Mott insulator to a superfluid. (a) As a function of the ratio of tunneling to interaction energies t/U, we plot the square of the fidelity F of the ground state with respect to a perfect Mott insulator (MI, red) and perfect coherent state or superfluid (SF, blue), characterizing the degree of overlap with these two delineating distributions. (b) Over a larger range of t/U and in log-scale, we plot the statistical distance of the ground state from the MI and SF quantum states, with the same color code as in (d).

raphy). Thus, we now focus more on some properties of the system that have a connection to experimental measures, and which can provide signatures of a transition between different quantum phases. One common experimental technique is to study the excitation spectrum of a system [27, 185]. Here, one perturbs the system in some way at a controlled frequency or energy, and examines an observable of the system – relating to susceptibility, for example – as a function of the perturbation frequency or energy. This can yield information about the excited state spectrum of the system [186, 187].

Going back to the extreme limits of $t \ll U$ and $t \gg U$, excitations of the system can be easily visualized. In the atomic limit ($t/U = 0$), the excitations are those of particle-hole pairs, in which there is a *holon* (or 1 atom less than for uniform density) on one site and a *charge-on* (or 1 atom more than for uniform density) on another. For commensurate filling, this leads to doublon-holon pairs, with 2 particles on a given site and 0 particles on another, and other variations of vacancies and multiple occupancies. In the delocalized SF limit ($t/U = \infty$), the energy spectrum should be exactly as in the case for non-interacting atoms as studied in Chapter 2. As the BHM restricts particles to the lowest band, one would thus expect a band of energies with width $4t$, with quasimomenta ranging from $-\pi/d$ to π/d in steps of $\pi/2Nd$, continuous in the limit of large M. In Fig. 6.4, we plot the numerically determined eigenergy spectra as a function of t/U. In Fig. 6.4 (a), we see

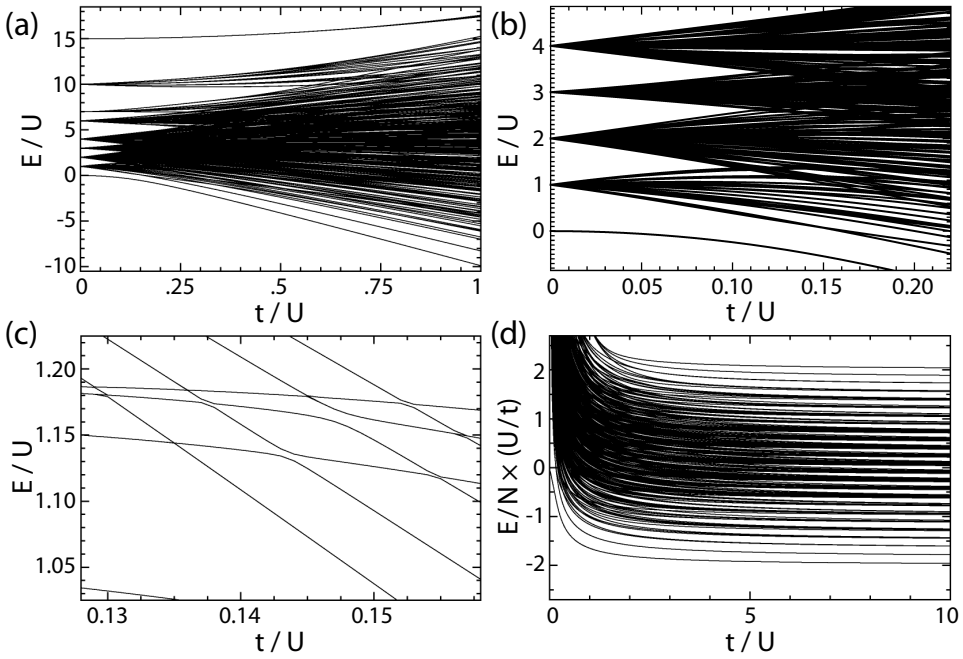

Figure 6.4: Ground and excited state energies of the Bose–Hubbard Hamiltonian. (a) We plot the eigen-energy distribution (scaled by U) of a six-site commensurate BHM, as a function of t/U. In the atomic limit ($t \ll U$), the energy spectrum is gapped with a typical energy spacing $\sim U$, and with particle-hole excitations (doublon-holon, 2 doublon-holons, triplon-biholon, etc.). In the limit of delocalized particles ($t \gg U$), a nearly continuous distribution of excited state energies can be seen. (b) As in (a), but plotted over a small range to highlight the lowest excitations. (c) Zooming in on some avoided many-body crossings as t/U is increased. (d) Distribution of eigen-energies scaled by the tunneling t and particle number N, relating to a single-particle band-width of $4t$ in the limit of weak interactions ($t \gg U$).

that for vanishing t/U the spectra are gapped, relating to discrete particle-hole excitations (doublon-holon, triplon-biholon, etc). The low-energy features for small t/U are highlighted in Fig. 6.4 (b). As the tunneling energy is increased, the eigenenergies spread out and form essentially continuous spectra. Avoided many-body energy crossings can be observed in the transition between the two regimes, as highlighted in Fig. 6.4 (c). Finally, in the limit $t \gg U$, we see in Fig. 6.4 (d) that the single-particle energy spectra indeed have the expected width $4t$ (eigenergies scaled by the total particle number N).

We now discuss some other experimentally relevant measures, which are better aimed at detecting (non-local) correlations in the system. The contrast

of time-of-flight interference patterns [27, 188, 189] is a standard observable used to distinguish a coherent superfluid state from a number-squeezed, phase-incoherent Mott insulator state. This is in analogy to observing the far-field interference pattern from a laser-illuminated grating, such that when the phase across the slit-pattern is uniform, sharp interference peaks are seen, and the pattern is washed out if the phase is randomized. Ignoring effects of interactions, the far-field time-of-flight single-particle interference pattern reveals the in-trap momentum distribution of the atoms [188],

$$S(k) \propto \sum_{j,j'=1}^{M} e^{i(j-j')kd} \langle \phi_g | \hat{a}_j^\dagger \hat{a}_{j'} | \phi_g \rangle \ . \tag{6.11}$$

Here, we have neglected an additional term, the Fraunhofer or Wannier envelope function $W(k)$, given by the Fourier transform of the on-site wavefunctions. For completely delocalized wavefunctions, the distribution of k-vectors is in complete analogy to the laser-illuminated slit, with $S(k) \propto N^{-2} \sin^2\big(Nkd/2\big)/\sin^2\big(kd/2\big)$. The on-site repulsion serves to reduce the spatial coherence length of the single-particle wavefunctions, and leads to a decreasing contrast of the interference pattern. For a 1D distribution of atoms, with only $N = M = 4$ atoms and sites, we plot in Fig. 6.5 the visibility contrast of the momentum distribution, defined as $C = S_-/S_+$ with $S_\pm = S(2\pi/d) \pm S(\pi/d)$. The visibility contrast serves to characterize the first-order, single-particle coherence of the sample. Higher-order correlations can be measured through higher moments of the matter-wave field, such as through noise-correlation measurements [190, 191] or through elastic diffraction experiments [49, 192].

Under certain conditions, such as at finite temperature or in reduced dimensions, the contrast of the interference pattern is not a particularly good observable to characterize correlations in a system [188, 193, 194], while the momentum peak-width serves as a better indicator [188]. The width of the interference peak is inversely proportional to the in-trap correlation length of the single-particle wavefunctions, i.e. the typical length scale over which the off-diagonal coherences of the single-particle density matrix decay. As a function of site distance r, the off-diagonal coherence from a site j is given by [188]

$$D_j(r) \propto \langle \phi_g | \hat{a}_j^\dagger \hat{a}_{j+r} | \phi_g \rangle / \sqrt{\hat{n}_j \hat{n}_{j+r}} \ , \tag{6.12}$$

which in the homogeneous system is independent of j. In the superfluid regime, these coherences decay algebraically as $D(r) \propto A|r|^{-K/2}$, while in the Mott insulator regime the decay is exponential as $D(r) \propto Be^{-|r|/\xi}$, with ξ the correlation length. Across the superfluid-to-insulator transition, the peak-width

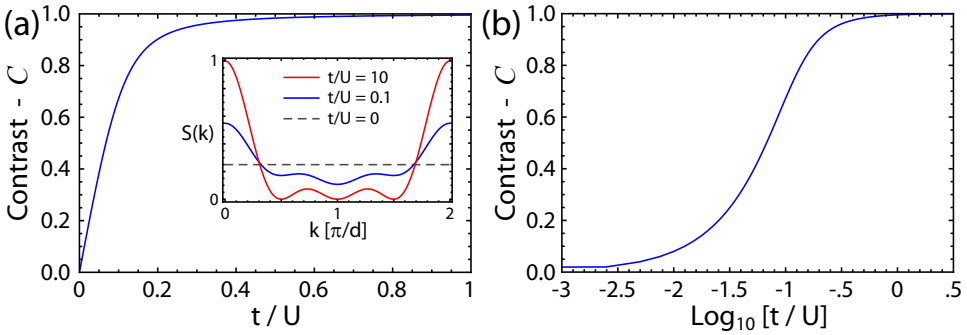

Figure 6.5: Momentum-distribution contrast of lattice gases. (a) As shown in the inset, the momentum wavevector distribution $S(k)$ of a lattice-modulated gas displays interference peaks at multiples of $k = 2\pi/d$, akin to the far-field interference pattern from an illuminated grating. For perfectly coherent samples [as shown for $t/U = 10$ (red)], the momentum distribution has a large contrast, defined as $C = S_-/S_+$ with $S_\pm = S(2\pi/d) \pm S(\pi/d)$. For more strongly interacting gases ($t/U = 0.1$ in blue and $t/U = 0$ as dashed grey) the contrast of the pattern decreases. In the greater graph, we plot the contrast C as a function of t/U. (b) The contrast C plotted as a function of t/U, over a larger range and in log-scale.

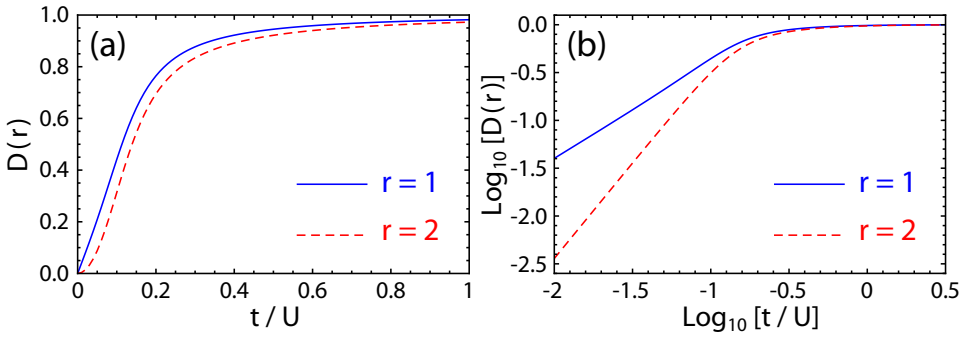

Figure 6.6: Decay of off-site correlations as a function across the superfluid-to-insulator transition. (a) The off-site correlator $D(r) \propto \sum_j \langle \hat{a}_j^\dagger \hat{a}_{j+r} \rangle$ is plotted as a function of t/U for both off-site distance $r = 1$ (solid blue) and $r = 2$ (dashed red). (b) Log-Log dependence of $D(r)$ on t/U.

increases abruptly from $w \propto L^{-1}$, where L is the system size for an inhomogeneous system, to $w \propto \xi^{-1}$ [188]. In Fig. 6.6, with plot the off-site correlator $D(r)$ for nearest-neighboring and next-nearest neighboring sites (for a small system of $N = M = 4$).

Finally, we recall the limits of validity for the BHM model, which consid-

ers only a single-band of the lattice, local on-site interactions, and nearest-neighbor tunneling. Of particular relevance to the remaining chapters are the limitations of this model at weak lattice depths in systems of strongly interacting one-dimensional (1D) Bose gases. In the following, we discuss some theoretical descriptions of interacting bosons in one dimension.

6.2 Theoretical descriptions of 1D Bose gases

6.2.1 General considerations

A system of bosonic atoms with motion restricted to one dimension (1D) can be realized by tight radial confinement in an array of "tubes" that are formed using deep lattices along the two transverse directions x and y. We may describe this system with an effective 1D Hamiltonian. To describe such a system, one can start from the description introduced in Chapter 2 based on the non-linear Schrödinger equation (Gross–Pitaevskii equation) describing bosonic fields with interactions, which are characterized by a 3D coupling constant $g = g_{3\mathrm{D}} = 4\pi\hbar^2 a_s/m$ (a_s the s-wave scattering length). We can then introduce an effective 1D coupling constant $g_{1\mathrm{D}}$ to describe boson-boson interactions in the 1D version of this equation. For this purpose, we assume that the wavefunctions of all the atoms are energetically restricted to the lowest radial mode ϕ_0. We can then factorize the wavefunctions in terms of radial and longitudinal coordinates (neglecting any azimuthal variation), as $\Psi(\mathbf{r}) = \phi_0(\rho)\psi(z)$, where $\phi_0(\rho) = 1/\sqrt{2\pi\sigma_\perp}e^{-\rho^2/2\sigma_\perp^2}$, with $\rho = \sqrt{x^2+y^2}$ and $\sigma_\perp = \sqrt{\hbar/m\omega_\perp}$, where $\omega_\perp$ is the radial harmonic frequency [195, 196]. The transverse degrees of freedom may then be integrated out, so that one arrives at an effective 1D description of the system, where the typical 3D atom-atom interaction potential $V_{at}(\mathbf{r}-\mathbf{r}') \approx g_{3\mathrm{D}}\cdot\delta(\mathbf{r}-\mathbf{r}')$ is replaced by the 1D interaction potential $V_{at,1\mathrm{D}}(z-z') \approx g_{1\mathrm{D}}\delta(z-z')$. The 1D coupling strength $g_{1\mathrm{D}}$ may then be described in terms of that for 3D by the relation [195]

$$g_{1\mathrm{D}} = g_{3\mathrm{D}}|\phi_0(0)|^2\left(1 - C\frac{a_s}{\sqrt{2}\sigma_\perp}\right) \approx g_{3\mathrm{D}}|\phi_0(0)|^2 = \frac{g_{3\mathrm{D}}}{2\pi\sigma_\perp^2}, \tag{6.13}$$

where C is a constant with value ~ 1.46, and where we neglect the second term in the parentheses as $Ca_s \ll \sqrt{2}\sigma_\perp$ for typical experimental conditions. The 1D coupling strength may also be reexpressed in terms of the transverse harmonic oscillator frequency as $g_{1\mathrm{D}} \approx 2a_s\hbar\omega_\perp$.

For non-interacting and weakly-interacting trapped gases of bosons in 1D, much is the same as in 3 dimensions. Absent interactions (and at $T = 0$) all

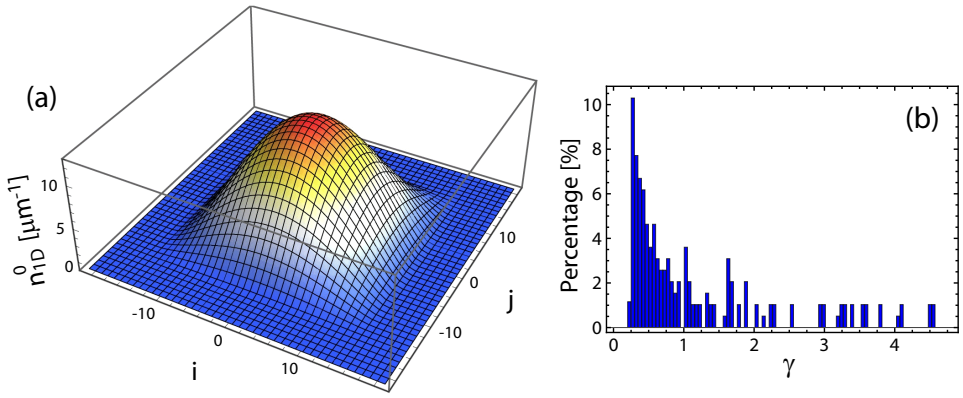

Figure 6.7: Characterizing the inhomogeneous two-dimensional array of the 1D systems. (a) Distribution of central densities of individual 1D systems (or tubes), $n_{1D}(z = 0)$, as a function of site indices i and j. (b) Binned percentages of tubes that are characterized by a given Lieb–Liniger parameter of value γ. The characteristic value, taken as a weighted (by tube population) average over the entire distribution, is $\gamma_{\text{eff}} \approx 0.6$.

the atoms will occupy the single-particle ground state. For weak interactions, a mean-field description can be retained, with an approximately Thomas–Fermi profile [197] as in 3D, albeit with increased density due to the transverse confinement [198]. For very strong repulsive interactions, however, even in the absence of a lattice potential, correlations between 1D bosons can have a large influence on a system's spectral properties and spatial distribution. To minimize interaction energy, repulsive bosons seek to minimize the spatial overlap of their wavefunctions. In the limit of infinite interactions, an effective *fermionization* of bosons takes place in 1D [199], where interacting bosons can be described as non-interacting fermions, with Pauli-blocking mimicked by the infinite repulsion (similar as to the case of non-identical fermions [200]). In this limit, the atoms form a Tonks–Girardeau gas [197, 201] where the single-particle coherence length decays on the length scale of the typical interparticle spacing, and higher-order correlations vanish at short length scales (anti-bunching). An effective Fermi wavevector can also be defined as for non-interacting fermions, with $k_F = \pi n_{1D}$, where n_{1D} is the 1D density (locally defined in a trapped system).

For the most general case, the state of a system of interacting 1D bosons can be described by the Lieb–Liniger parameter, which compares their interaction and kinetic energies, as $\gamma \sim E_{int}/E_{kin}$ [202]. For a lattice-free gas of bosons described by an effective 1D coupling strength g_{1D} and a 1D density n_{1D}, this is given as $\gamma = \frac{g_{1D} n_{1D}}{\hbar^2 n_{1D}^2/m}$. In terms of the Lieb–Liniger parameter, a general

rule of thumb is that a mean-field description is applicable for $\gamma \ll 1$, while for $\gamma \gg 1$ the Tonks–Girardeau regime is reached [197]. In the intermediate regime $\gamma \sim 1$, which characterizes most of our 1D gases in the absence of a z-lattice, correlations are important but coherent and superfluid behavior can still be observed. In our experiments, we typically populate ~ 1000 one-dimensional tubes of bosons from an initially three-dimensional BEC, with around 100 atoms per tube on average. Due to the external confinement, the 1D density $n_{1\mathrm{D}}$ varies amongst the 1D tubes and also within each 1D tube, such that it is a function of z as $n_{1\mathrm{D}}(z)$. To characterize our collection of 1D gases, we use 2/3 of the central density $n_{1\mathrm{D}}(z=0)$ as representative value for $n_{1\mathrm{D}}$ in each tube (this value $(2/3)n_{1\mathrm{D}}(z=0)$ is equal to $N/2R_{TF}$ in the Thomas–Fermi approximation). We then characterize the entire system by a mean-γ parameter, that is weighted by the population in each tube. Fig. 6.7 (a) plots a typical distribution of central densities in our array of 1D tubes. The resulting distribution of γ values is plotted in Fig. 6.7 (b), for a typical sample that is characterized by a mean value $\gamma_{\mathrm{eff}} = 0.6$.

6.2.2 Theoretical description of interacting 1D bosonic fields

So far we have attempted to give some qualitative insight as to how 1D bosons behave for weak and strong interactions, and how a system of these particles can be parameterized in experiment. We now discuss some commonly used theoretical descriptions of 1D Bose gases at low temperatures, with short-range δ-like interaction potentials, in weak or completely absent longitudinal lattice potentials, following the descriptions in Refs. [203, 204]. While for deep lattices a Bose–Hubbard model description can be used, as described in earlier sections, localized on-site wavefunctions are not a priori an appropriate description in the absence of deeply modulated lattice potentials. For a low-energy description of 1D quantum fluids, we again begin with a quantized Hamiltonian as in Eq. 6.1,

$$\hat{H} = \int dz \hat{\psi}^\dagger(z) \left[-\frac{\hbar^2 \nabla^2}{2m} - \mu \right] \hat{\psi}(z) + \frac{1}{2} \int dz dz' \hat{\psi}^\dagger(z) \hat{\psi}^\dagger(z') g_{1\mathrm{D}} \delta(z-z') \hat{\psi}(z) \hat{\psi}(z') \,, \tag{6.14}$$

here neglecting any additional external potentials, either slowly-varying as in $V_{ext}(z)$ or with short modulation length as for an added lattice. The density ρ (equal to $n_{1\mathrm{D}}$) is controlled through the Lagrangian multiplier μ. In the case of trapped gases the local density ρ will vary within the 1D system due to the external trapping potential.

We now follow the bosonization approach for a collective field description

of Tomonaga–Luttinger liquids, taking the bosonic field operator as [203–205]

$$\hat{\psi}^{\dagger}(z) = [\hat{\rho}(z)]^{1/2} e^{-\hat{\theta}(z)} \ , \tag{6.15}$$

where conjugate density and phase operators, $\hat{\rho}$ and $\hat{\theta}$, obey the commutation relation $[\hat{\rho}(z), \hat{\theta}(z')] = i\delta(z - z')$. Again, we assume a homogeneous system with average density $\langle \hat{\rho}(z) \rangle = \bar{\rho} = \mu / g_{1\mathrm{D}}$, which is also given by N/L for N particles in a uniform system of length L. The density operator can then be described to lowest order as $\hat{\rho}(z) \simeq \bar{\rho} - \partial_z \hat{\phi}(z)/\pi$, where $\hat{\phi}(z)$ is a slowly varying quantum field.

The Hamiltonian containing only kinetic and interaction contributions, Eq. 6.14, may then be expressed in the form of the Tomonaga–Luttinger (TL) Hamiltonian [206, 207]

$$\hat{H}_{TL} = \frac{\hbar \upsilon}{2\pi} \int dz \left[K (\partial_z \hat{\theta}(z))^2 + K^{-1} (\partial_z \hat{\phi}(z))^2 \right] \ . \tag{6.16}$$

Here, the system has a linear dispersion relation $\omega = \upsilon |k|$ at low energies, where υ is the speed of sound in the gas. The Luttinger parameter K serves to describe the correlation properties of the system, and is related to the earlier-used Lieb–Liniger parameter γ. In the limit of vanishing interactions ($\gamma = 0$) the Luttinger parameter takes a value $K = +\infty$, while in the limit of infinite zero-range interactions ($\gamma = +\infty$) it takes a value $K = 1$. Approximate forms can be found near these limits, with $K(\gamma) = \pi/\sqrt{\gamma} - 1/2$ for $\gamma \ll 1$ and $K(\gamma) = 1 + 4/\gamma^2 + O(\gamma^{-3})$ for $\gamma \gg 1$, and a sound velocity given by $\upsilon(\gamma) = \hbar \pi \bar{\rho} / m K(\gamma)$ [204].

Finally, the effect of weak periodic perturbations, as due to a longitudinal lattice, may be taken into account. We assume a lattice potential $V_{latt}(z) = V_0 \cos^2(kz)$, with small depth $V_0 \ll \mu$ such that it only weakly modulates the density distribution. The total Hamiltonian may then be written as $\hat{H}_{eff} = \hat{H}_{TL} + \hat{H}_V$, where the contribution due to the lattice potential is [204]

$$\hat{H}_V = \frac{\tilde{g}_u}{\pi} \int dz \cos \left[2p\hat{\phi}(z) + z\delta \right] \ . \tag{6.17}$$

Here, p is a parameterizing integer describing the density of atoms with respect to the lattice, where for $p = 1$ there is one particle per site, and for $p = 2$ there is one particle for every 2 sites, and so on. The second term relates to the incommensurability of the lattice potential with respect to the bosonic density, with $\delta = nk - 2p\pi\rho_0$, where n is an integer chosen such that δ takes its smallest value. The coupling strength is then given by $\tilde{g}_u \approx \pi \bar{\rho} V_0 (V_0/\mu)^{n-1}$ [204]. The added lattice potential can lead to a number of interesting ordered quantum

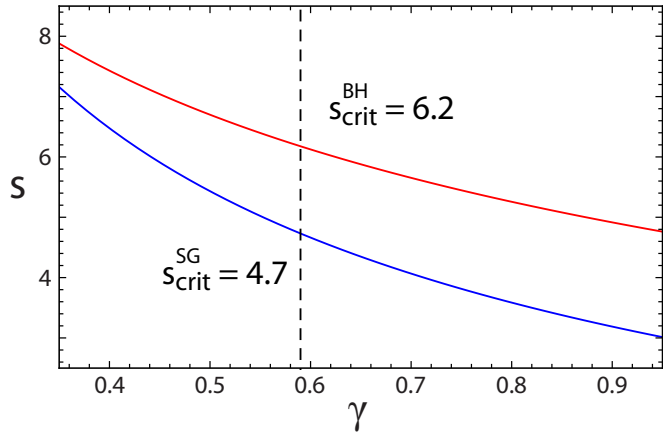

Figure 6.8: Analytical estimates of the transition point to insulating behavior in 1D Bose gases. As a function of the Lieb–Liniger parameter γ, the critical lattice depth that induces insulating behavior in 1D Bose gases, based on the sine-Gordon model and Bose–Hubbard models, are plotted in blue and red, respectively. At a typical value for our 1D gases of $\gamma \sim 0.6$, we expect to observe insulating behavior beyond critical depths of 4.7 and 6.2, based on the sine-Gordon and Bose–Hubbard models, respectively.

phases for a scalar bosonic field, including Mott-insulating phases for commensurate potentials and charge-density wave states for incommensurate ones.

For a fully commensurate lattice potential ($\delta = 0$), the addition of the lattice term $\hat{H}_V$ leads to the so-called *sine-Gordon* model. This model describes a superfluid to Mott insulator transition, with n/p bosons per site on average, as a function of the Luttinger parameter K. The value of the Luttinger parameter at the transition point for fixed filling is given by $K^* = 2/p^2$, and thus $K = 2$ for unit filling.

Based on the sine-Gordon model, analytical estimates for the superfluid to Mott-insulating transition point as a function of lattice depth $s = V_0/E_R$ have been determined for relatively strong interactions and weak potentials [31]. For values $\gamma \lesssim 10$, the Luttinger parameter may be approximated as $K(\gamma) \approx \pi/\sqrt{\gamma - \gamma^{3/2}/(2\pi)}$ [31], and the critical value for insulating behavior as $K_c = 2 + |s|K/2$ [107], reexpressed as a critical lattice depth in terms of γ as

$$s_{crit} = 2\left[\frac{\pi}{\sqrt{\gamma - \gamma^{3/2}/2\pi}} - 2\right] . \tag{6.18}$$

This can be compared to analytical estimates based on the Bose–Hubbard model, which apply in the limit of deep lattices and for weaker interactions.

In Ref. [107], a transcendental equation defining the $s-\gamma$ phase boundary to the insulating state was derived as

$$s = \frac{1}{4}\ln^2\left[\frac{2\sqrt{2}\pi}{\gamma}(U/t)_{crit}\sqrt{s}\right] , \tag{6.19}$$

with a critical ratio of the interaction to hopping parameter $(U/t)_{crit} \approx 3.85$. The critical depths for insulating behavior, based on these two analytical forms, are plotted in Fig. 6.8 as a function of the Lieb–Liniger parameter γ.

Chapter 7

Strongly interacting Bose gases II: experimental probes

In this chapter, we review some common experimental techniques used to characterize strongly interacting quantum gases.

7.1 Visibility

For weakly interacting, degenerate lattice gases, in which all the atoms may approximately be described as having the same wavefunction, the time-of-flight (TOF) far-field momentum distribution contains the full information about the spatial wavefunction of the atoms [18]. As a sum of many identical single-particle interference patterns after release from the lattice, a Fourier-transformed image of the BEC's spatial distribution builds up atom by atom. For strongly-interacting quantum gases, in which the atoms are no longer all Bose–condensed into the same quantum state, but rather have wavefunctions that are spatially anti-correlated, the loss of single-particle phase coherence across the lattice sites leads to a washed-out TOF interference pattern. Here, we shall first show how TOF spectra can provide evidence for a loss of global phase coherence in the superfluid-to-Mott insulator transition [27]. After this, we discuss limitations to using this technique as the sole diagnostic tool, and failures as a useful observable in reduced dimensions.

We typically operate with a system of $\sim 7 \times 10^4$ atoms of ^{87}Rb in the $|1, -1\rangle$ hyperfine state that are slowly loaded into a 3D optical lattice. The lattice is symmetric with respect to both the lattice wavelength ($\lambda_{\{x,y,z\}} \equiv \lambda = 1064$ nm) and the lattice depth (sE_R, with $E_R = h^2/2m\lambda^2$). Shortly after

ramping up the lattice to its final depth s, we suddenly turn off all confining potentials and release the atoms in time-of-flight. After 18 ms, we absorptively image the atomic distribution along the x axis. We then measure the *visibility* contrast C of the time-of-flight momentum distribution $P(k)$ [27, 189], as defined in Fig. 7.1. Unlike in the simple 1D example of the previous Chapter, here we measure the number of atoms in different regions about a ring of constant $k_y^2+k_z^2$ values (integrated over all k_x values by imaging along this axis). Specifically, we measure at and directly in between the first (and minus first) reciprocal lattice vectors along these two axes [189]. For a completely coherent cloud of atoms, we expect a visibility contrast of $C = 1$, while for a completely incoherent sample – e.g. due to either thermal or quantum depletion – we expect to measure $C = 0$. Fig. 7.1 (a) plots the contrast C as a function of the final lattice depth s, and reveals a steep decline of C beyond values of $s \sim 14$. In Fig. 7.1 (b) we plot the numerical derivative of the visibility, i.e. the difference between successive s-values, which has a sharp feature centered around $s \sim 15$ (with negative values first appearing around $s \sim 14$). We note that upon ramping back down to low s-values from a deep lattice, a high-visibility interference pattern is recovered, with little indication of heating. This reversible loss of phase coherence with increasing lattice depth s (and increasing U/t), is an indicator of the well-studied superfluid-to-Mott insulator transition in 3D.

In the 3D case, visibility contrast appears to be a reasonably accurate observable for detecting the SF-MI transition; the observed transition at a value of $U/t \sim 36$ for $s = 14$ is realistic for our distribution of local densities. However, in the more general situation, visibility contrast is not the best indicator for the loss of superfluidity. It has been shown that at zero temperature, measurement of the visibility contrast is not the most direct method for observing the superfluid-to-insulator transition in a system of Hubbard-regime bosons [188] (alternative measures discussed later). Moreover, visibility contrast can even be a *false* indicator if used as a proxy for superfluidity. It has been shown that thermal gases of atoms in the normal phase [193, 194] can exhibit sharp peaks in their time-of-flight momentum distribution.

In experiments with quantum-degenerate gases, the unsuitability of visibility contrast as an indicator of the SF-MI transition is most severe in low-dimensions. To emphasize this point, we show data for the visibility contrast as a function of lattice depth for an array of 1D Bose gases. Instead of using a symmetric 3D lattice as above, to create the 1D gases we first load the atoms into very deep transverse lattices along the axes x and y, with wavelength $\lambda = 1064$ nm and depth $s_\perp = 40\ E_R$. This results in a collection of isolated 1D gases, which can be characterized by a mean Lieb–Liniger parameter

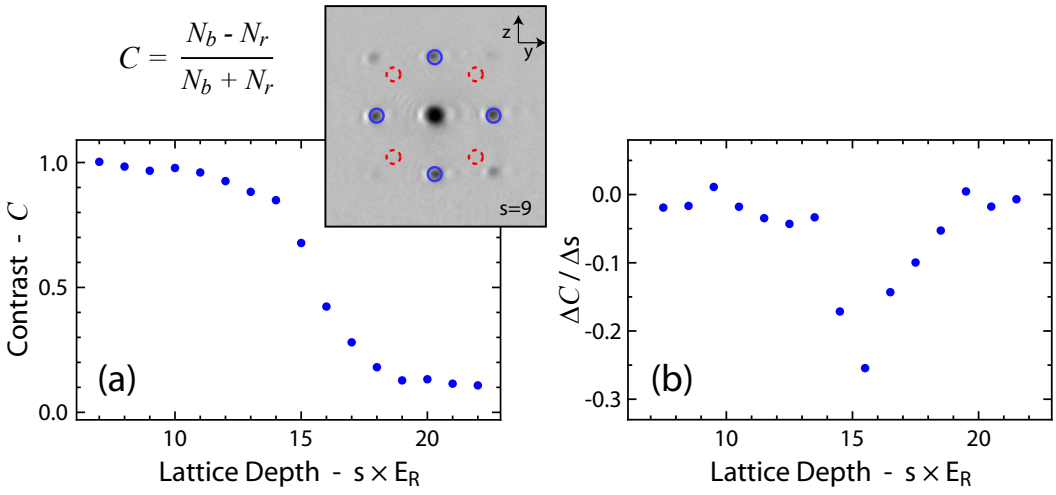

Figure 7.1: Loss of matter-wave coherence across the superfluid-to-insulator transition in 3D. (a) Visibility contrast C as a function of the lattice depth $V = sE_R$, symmetric along all axes. The inset illustrates the determination of C (shown for $s = 9$). (b) The numerical derivative (difference between successive points) of the contrast shows a distinct minimum near the expected position of the SF-MI transition in 3D.

$\gamma_{\text{eff}} = 0.6$. We then slowly ramp up a lattice of wavelength $\lambda = 1064$ nm and variable depth $s_z E_R$ along z. Due to the stronger interactions in 1D (from the enhanced density) and the smaller coordination number $z = 2$, we expect that the transition to a Mott-insulating state should occur at a smaller value of the lattice depth as compared to in 3D. For the characteristic density of the 1D systems, estimates based on the sine-Gordon [SG; Eq. 6.18] and Bose–Hubbard [BH; Eq. 6.19] models predict that the transition should occur at critical lattice depths of $s_c = 4.7$ and 6.2, respectively.

After releasing an array of interacting 1D Bose gases, no distinguishing momentum features are found along the axes of tight confinement (here x and y), due to the lack of phase coherence between the independent 1D systems. Thus, we use a slightly modified visibility contrast measure for the case of 1D gases. First, to ensure that the atoms always have the same projection onto Bloch states prior to release, we quickly (in 50 μs) load the lattice to the same depth $s_z = 20$ [185]. Then we perform a π phase-shift between adjacent lattice sites (half a Bloch oscillation, by turning off the ODT for ~ 450 μs while leaving the z-lattice on), which shifts the velocity envelope of the diffraction pattern by 1 v_R, resulting in symmetric peaks along z [27]. Finally, we measure the visibility contrast of the time-of-flight interferences as

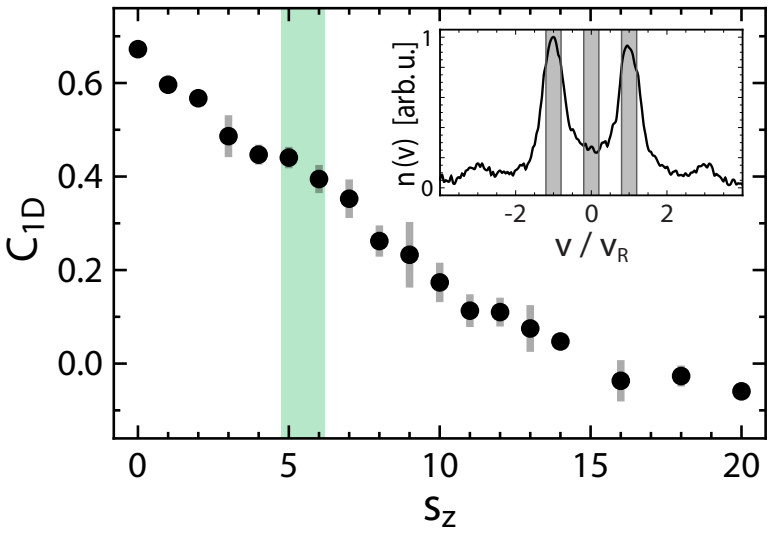

Figure 7.2: Time-of-flight visibility contrast C_{1D} as a function of lattice depth for an array of 1D Bose gases ($\gamma \approx 0.6$) as a function of the longitudinal lattice depth s_z. Inset: Time-of-flight velocity distribution (along z).

$C_{1D} = \eta_-/\eta_+$ [44], with $\eta_\pm = n_{v=+1} + n_{v=-1} \pm 2n_{v=0}$; $n_{v=0,\pm1}$ apertures shown in the inset of Fig. 7.2. We note that unlike the symmetric measure in Fig. 7.1, here the overall shape of the Wannier envelope (having greatest intensity at $n_{v=0}$) results in a visibility contrast not bounded by 1 and 0, but rather 1 and some slightly negative value (typically $\sim -.2$) that depends on the width of the envelope.

We now measure this 1D visibility contrast as a function of s_z. In contrast to the 3D case, we observe a continuous, slow decrease of C_{1D}, with no abrupt changes that might signal a transition between a coherent and phase-incoherent state. In the proximity of lattice depths for which we expect the transition to an insulating state ($s_c \sim 4.7 - 6.2$, shown in green), no significant changes in the visibility measure can be discerned. The lack of any sharp change in the visibility measure for 1D gases across the expected SF-IN transition is consistent with theoretical predictions [208] and previous observations [68, 185] (based on the measured coherent fraction or peak fraction in time-of-flight), which indicated that the measurement of sharp visibility fringes is not an appropriate stand-in for the detection of superfluidity in a generic system. This limitation notwithstanding, visibility contrast may still be used as a complementary observable to characterize the state of a system. As is seen in Fig. 7.2, the contrast still changes monotonically with the lattice depth s_z (and thus U/t), and the same may be said for the temperature dependence [209].

As a brief aside, we illustrate how visibility measurements in a system of 1D Bose gases can be used to estimate important parameters of the Bose–Hubbard Hamiltonian, based on collapse-and-revivals of the interference of a matter-wave field [178, 210, 211]. Starting from a lattice depth of $s_{z,i} = 6\ E_R$ along z, near the SF-MI transition (with $s_\perp = 40\ E_R$), we quickly (in 50 μs) linearly ramp the lattice depth to a value deep within the 1D Mott-insulating regime, $s_{z,f} = 18$. The lattice ramp speed is adiabatic with respect to the excitation of higher lattice bands, but fast enough to essentially freeze out tunneling in the system on relevant timescales. We then vary the amount of hold time τ in this deep lattice prior to release in time-of-flight, and monitor the visibility contrast of the released 1D Bose gas array as a function of τ.

To paint a simplified picture of how we expect the visibility contrast to evolve in time, we imagine the fate of a single particle interacting with a sea of other bosons (in reality all are indistinguishable, so it makes no sense to pick one out from the others). Since the freeze-out of the tunneling happened while the atoms were still in the 1D superfluid regime, it is fair to assume that the particle's spatial wavefunction is delocalized over several lattice sites. With tunneling frozen out, the particle's site-dependent temporal phase evolution will depend on the local site-dependent energy ε_i, as well as the on-site interaction energy $Un_i(n_i - 1)/2$. If only interaction terms contributed, we would expect phase evolution at multiples of U/h (1, 3, 6, etc. for double, triple, and quadruple occupancies). Somewhat similar to Bloch oscillations in a linear gradient, we thus expect that the particle's wavefunction on different sites will rephase with a characteristic times h/U (~ 0.87 ms for the $s_{z,f} = 18$). Taking the inhomogeneous trapping potential into account, however, we also expect that the different sites will phase evolve at an additional rate reflecting the local potential ε_i, of which there is a broad distribution, leading to an overall dephasing across the sample.

In Fig. 7.3, we plot the measured visibility contrast $C_{1\mathrm{D}}$ as a function of τ. We indeed see revivals of the interference pattern's contrast at times relating to the expected on-site interaction energy $U/E_R = 0.56$, however due to the external trapping potential these oscillations die out rather quickly. In more homogeneous external potentials, which allow for the observation of more than a few cycles, such collapse-and-revival measurements have been used as a spectroscopic tool for measuring site occupation statistics [210], observing number-squeezed superfluids upon approaching the MI regime [178, 210], and observing deviations from the single-band Hubbard Hamiltonian due to atom-atom interactions [210].

We shall now discuss some additional observables that may be used to characterize an ultracold lattice-gas system, in particular for the signaling of

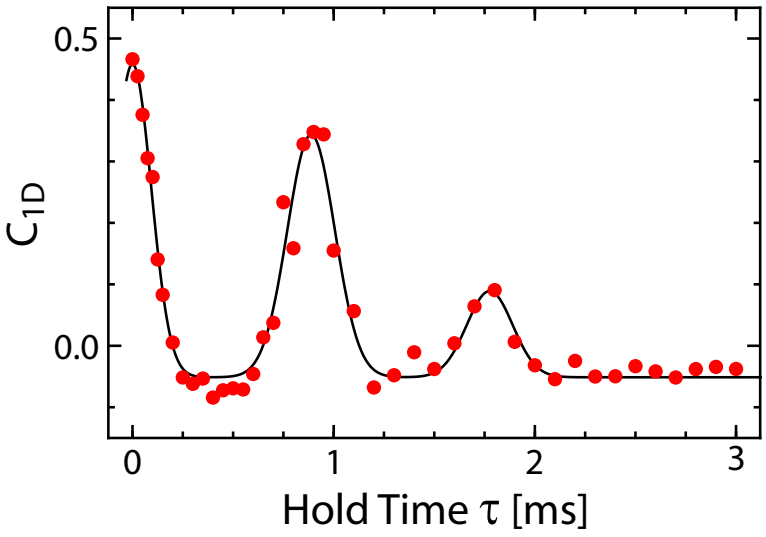

Figure 7.3: Collapse-and-revival in the matter-wave coherence of 1D Bose gases. For a cloud of 1D Bose gases ($s_\perp = 40$), the lattice confinement along z is quickly ramped up in 50 μs from an initial depth of $s_{z,i} = 6$ to $s_{z,f} = 18$. Oscillations in the contrast of time-of-flight interference patterns (quantified by the 1D visibility measure C_{1D}) at a frequency of 1.13(1) kHz are in good agreement with the expected on-site interaction energy $U/h = 1.15$ kHz.

a transition between superfluid and Mott-insulating states.

7.2 Momentum peak width

We recall the earlier discussion regarding what information about a system can be deduced from typical TOF momentum-space images. The number of momentum peaks, as well as their relative weights, is simply given by the Fraunhofer envelope function (or Wannier envelope, analogous to the Debye–Waller function for material crystals) that reflects the size of the atomic wavefunctions on individual lattice sites. The width of these peaks, on the other hand, reflects the number of sites that coherently contribute to the interference pattern. For a fully degenerate sample of bosons in a lattice, the width σ of the peaks just scales inversely with the system size L, as $\sigma \propto L^{-1}$. As soon as repulsive interactions cause the onset of quantum depletion, i.e. when atoms cease to exclusively occupy the single-particle ground state, the single-particle coherence length (decay length of Green's function, single-particle density matrix, etc.) becomes smaller than the system size (the same holds for thermal depletion [212]). Deep in the Mott-insulating regime, single-particle coherence does

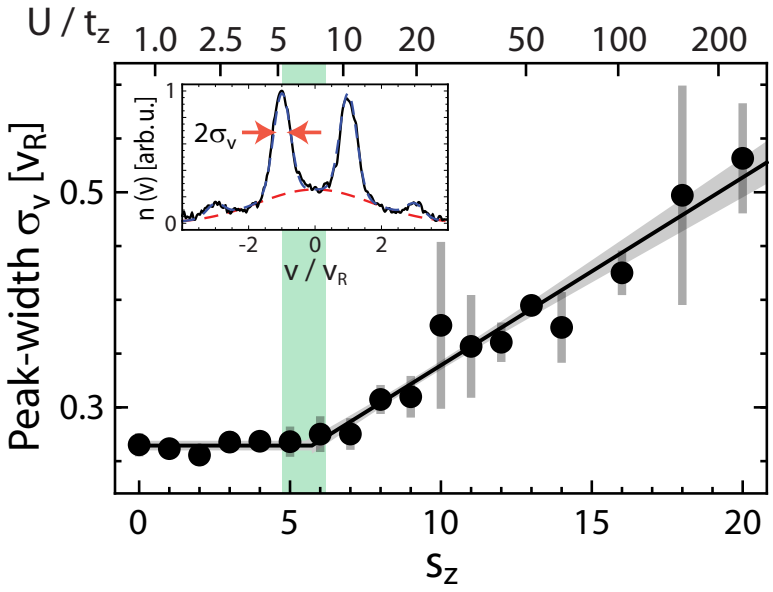

Figure 7.4: Momentum peak width in time-of-flight across the superfluid-to-insulator transition in 1D. As illustrated in the inset, the momentum-peak width σ ($1/\sqrt{e}$ half-width) is determined by a symmetric multi-Gaussian fit to time-of-flight interference patterns. The dependence of σ on s_z is plotted, along with the fit of a linear increase beyond a critical depth s_c.

not extend off-site. The width of the TOF momentum peaks increases when the coherence length in the system becomes smaller. Moreover, it has been demonstrated that the momentum peak-width is a good indicator of the SF-MI phase transition, showing a sudden change about the critical point [185, 188].

Here, using the same set of time-of-flight images that produced the 1D visibility measurements shown in Fig. 7.2, we instead determine the width of the momentum peaks. We do this by performing a symmetric multi-Gaussian fit to the integrated density profiles as shown in the inset of Fig. 7.4, consisting of symmetric diffraction peaks (in blue) on top of a broad background (dashed red). From such fits, we determine the peak-width σ_v ($1/\sqrt{e}$ half-width) as a function of the lattice depth s_z along z, as plotted in Fig. 7.4. To the dependence of peak-width on lattice depth, we fit a function that is constant below a critical value s_c, and then increases linearly beyond this point (fitting to the range of data with $s_z \leq 13$). The fit (plotted along with the 1 standard deviation confidence regions in Fig. 7.4) returns a value of $s_c = 5.7 \pm 0.5$, which is in good agreement with the expected region for the transition to insulating behavior, as shown in green and discussed in the previous section.

7.3 Impulse-response

Another way to observe the superfluid-to-insulator transition in lattice-confined atomic gases is through transport measurements [213], such as by monitoring the response of the atoms to an applied force. For repulsive 1D Bose gases in particular, it has been observed that collective motion in response to applied potential gradients is inhibited in weak optical lattice potentials [185, 214]. In the strongly-correlated regime, the redistribution of density between lattice sites costs a discrete energy $\sim U$, and for weak gradients (weak with respect to U) that do not bring adjacent sites into resonance, response to impulse is suppressed [27, 186]. In recent years, the response to weak impulses has been used as an experimental diagnostic to signal the superfluid-to-insulator transition in 1D [31, 215] and in 3D [75, 215].

To make things explicit, the measurement of impulse-response in its idealized form does not probe physical transport in the lattice (i.e. mass currents or density redistribution); rather it probes the coherence of the atomic wavefunctions. To explain how this works, we consider the extreme case of a superfluid BEC, with quasimomentum $q = 0$, in a deep lattice with essentially zero tunneling (as can be encountered in non-interacting gases), such that physical transport is *a priori* disallowed. Just as we wrote the localized Wannier states as superpositions of delocalized Bloch functions in Chapter 2, we can also represent the Bloch states as superpositions of localized Wannier orbitals. The delocalized Bloch wave function $\phi_q^{(n)}(z)$, of the nth lattice band and with quasimomentum q, can be written as

$$\phi_q^{(n)}(z) = \mathcal{N}^{-1/2} \sum_j e^{iqz_j/\hbar} w_n(z - z_j) \ , \tag{7.1}$$

where we recall that $w_n(z-z_j)$ is the Wannier orbital of the nth band, localized at position z_j, and that $\mathcal{N}$ is a normalization constant. Our $q = 0$ Bloch state thus represents an equal-phase superposition of all localized Wannier states. If we apply a weak potential gradient $U(z) = Fz$ onto the sample for some time T_{imp}, a site-dependent phase is accrued of the form $\varphi_j = Fz_jT_{imp}/\hbar$, which means that the Bloch state will be transformed from $q = 0$ to $q = FT_{imp}$. This evolution in quasimomentum space (and in momentum space after band-mapping) comes about solely due to interference between contributions of the wavefunction on different sites (with Bloch oscillations occurring at long times, or Josephson oscillations in the two-site case). In contrast to this linear evolution of quasimomentum for the delocalized Bloch state, a single particle localized to one site of the lattice will be unresponsive to applied gradients. We thus expect that if we transform the ground state of the system,

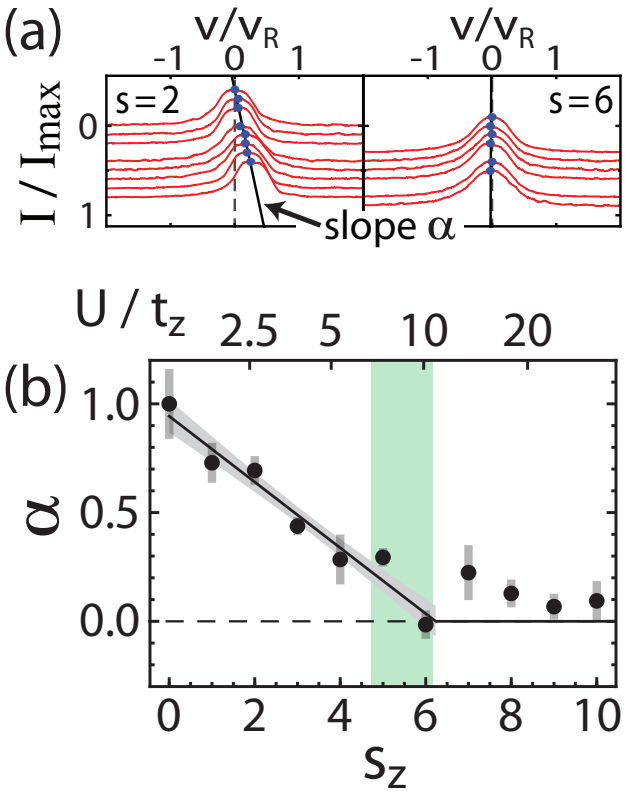

Figure 7.5: Impulse response of 1D bosons as a function of lattice depth. (a) The response to impulse is determined by a straight-line fit (with slope α, normalized to the case of free atoms) to the dependence of velocity on applied impulse I (recoil velocity $v_R = h/m\lambda$). (b) The dependence of α on the lattice depth s_z. The lines and surrounding shaded regions are fits to the data with confidence regions (1 s.d.) of a linearly decaying response, with no response ($\alpha = 0$) beyond a critical lattice depth s_c.

by control over t and U, from a superfluid (with delocalized, algebraically decaying single particle wavefunctions) to a Mott insulator (with exponentially localized single particle wavefunctions), that the response to applied impulse will go to zero across the quantum phase transition, serving as a good indicator for the superfluid-to-insulator transition [31, 75].

Here, we study impulse-response in a system of 1D Bose gases as in the above examples, again characterized by a tube-averaged value of $\gamma_{\text{eff}} = 0.6$ ($s_\perp = 40$ as above). We apply weak magnetic-field gradients along z, briefly pulsed on for a duration $T = 1.2$ ms, which applies forces of variable strength F ranging from 0 to $F_{max}/m = 1.2$ m/s^2 (the atoms are in the $|F, m_F\rangle = |2, -2\rangle$ state). A corresponding impulse $I = F \times T$ is applied to the atoms. The

magnitude of the strongest impulses are such that the final quasimomentum reached by nearly-free atoms is far from the band-edge, avoiding excitations that can occur for velocities in excess of some critical value v_{crit} (with low values of v_{crit} in 1D [213, 215]). After impulse, we monitor the response of the atomic cloud in time-of-flight, by measuring the center-of-mass velocity of the distribution along z, after a brief ($\sim$1 ms) ramp-off of the z-lattice (band-mapping). As illustrated in Fig. 7.5 (a), we characterize the response as a function of the impulse strength I (with slope α). As plotted in Fig. 7.5 (b), we observe a nearly linear decrease of the atomic response to impulse as a function of the optical lattice depth s_z. We determine the critical point at which the atoms become unresponsive to impulse by fitting a linear decay to the response α as a function of lattice depth, quenched beyond a critical depth s_c. The fit-determined critical depth of $s_c = 6.2 \pm 0.5$ is in good agreement with the peak-width measurement of Fig. 7.4, and with the expected position of the SF-MI transition in our 1D bosonic gases (shown in green in the plot). We note that the observed suppression of transport is due to many-body correlations, as over this range of weak lattice depths the modification of the atoms' effective mass alone does not explain the observed suppression.

7.4 Excitation spectra

Lastly, we discuss lattice amplitude modulation spectroscopy [185], which is a commonly used technique for characterizing the energy spectrum of excited states in systems of lattice-confined ultracold atoms, based on a sinusoidal modulation of the optical lattice depth. Similar to the methodology used in Chapter 3 for exciting higher lattice bands, in weakly-interacting samples or at large energies this method can provide access to the single-particle excitation spectrum, revealing band-gap energies and band-widths, etc. To study excitations relevant to gases in the Hubbard regime, however, we now concentrate on excitations with energy below the single-particle band-gap. For non-interacting gases, the spectrum simply reflects the structure of the zeroth energy band. In the atomic limit ($t \ll U$), there is a charge gap with energy U relating to the creation of a particle-hole pair (doublon-holon). Additional interaction bands, all with typical bandwidth on the order of t, appear around energies of $2U$ (2 doublon-holons), $3U$ (either 3 doublon-holons or a triplon-biholon), and so on, as plotted in Fig. 6.4 (a). The emergence of an energy gap has been used as an indicator of the transition between superfluid and Mott insulator in ultracold atom systems [27, 31, 185].

In lattice amplitude modulation spectroscopy, the lattice depth is varied sinusoidally in time as $s(T) = s_0 + \delta s \sin(\omega T)$. Thus, the tunneling energy

t and the on-site interaction strength U, which both depend on the lattice depth s, are also modulated in time. The time-varying perturbation to the system allows coupling to excited states at a spectroscopically defined energy $\hbar\omega$ (to lowest order in the linear response regime [31, 187]). The excitation mechanism itself [185, 187] can be related to a symmetric two-photon Bragg process [131] involving the lattice laser beams, in which the modulation effectively introduces frequency sidebands. Typically, the state of the system is characterized by observing how much energy is deposited at a particular modulation frequency (with fixed modulation time T_{mod} and modulation amplitude δs). We note that there is a wealth of additional techniques used to characterize excitations, including phase modulation spectroscopy [205], direct Bragg spectroscopy [216, 217], coupling to excited states via applied gradients [27], and photon-assisted tunneling in a gradient [218].

In the experiment, we investigate the excitation spectrum of a sample of 1D Bose gases, having the same properties as in the above examples ($s_\perp = 40$, $\gamma_{\text{eff}} = 0.6$), for a variable depth s_z of an applied lattice (wavelength $\lambda = 1064$ nm) along z. After slowly ramping up the lattice to a depth s_z, we sinusoidally modulate its amplitude by $\pm 15\%$ for $T_{mod} = 80$ ms. We then ramp down the depth to $s_z = 4$ in 5 ms, and allow for 15 ms of thermalization. We do not directly measure the energy deposition rate, or the energy increase of the system for fixed T_{mod}, but rather we release the atoms from this lattice in time-of-flight (following a π phase-shift as before) and measure the visibility contrast as a proxy for the amount of thermal energy in the system. We plot the excitation spectra for lattice depths of $s_z = 4$, 9, and 14 in Fig. 7.6, with energies normalized to the value of U for $s_z = 14$ (U is only slowly varying with lattice depth). For the lowest depth of $s_z = 4$, which is expected to be in the superfluid regime (same transition region as in the preceding sections), we observe an essentially continuous dependence of the visibility on the excitation frequency ω. For $s_z = 9$ however, a non-monotonic dependence of the visibility on ω is observed, and for a depth of $s_z = 14$ well into the Mott-insulating regime ($U/t \approx 66$), resonant peaks at energies of $\sim U$ and $\sim 2U$ are observed. The emergence of these excitation features with increasing s_z thus signal a transition to gapped excitations of particle-hole pairs. We note that the production of a doublon excitation relies on nearest-neighbor tunneling, and thus in an inhomogeneous system also depends on the difference between the site-dependent energy offsets $\Delta_i = \varepsilon_i - \varepsilon_{i+1}$, with excitation at energies at roughly $U \pm \Delta$ [218]. Thus, neglecting the small spread in the values of U and t due to the slowly varying envelope of the lattice beams, the large widths of the observed excitation peaks in Fig. 7.6 (b,c) are due to the inhomogeneous external trapping potential, and the resultant spread of the local resonance

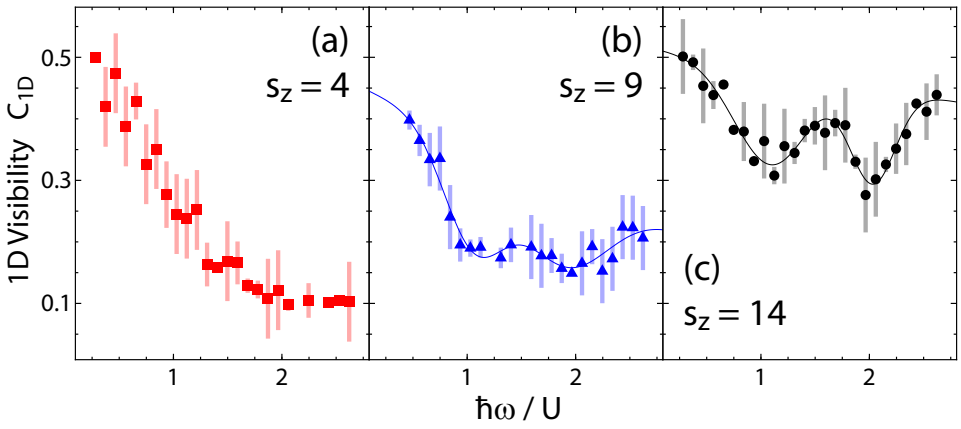

Figure 7.6: Excitation spectra across the superfluid-to-insulator transition in 1D. (a) Visibility as a function of amplitude modulation frequency (normalized to $U/E_R = 0.53$ for $s_z = 14$), for a lattice depth of $s_z = 4$. (b) Similar data, but for a lattice depth along z of $s_z = 9$. Fit lines are two Gaussians on a linear slope. (c) Similar data, but for $s_z = 14$. The emergence of peak-like structure in (b) and (c) reflect the appearance of a charge gap in the system in the Mott-insulating regime.

condition for nearest neighbor tunneling.

Here, we have used measurements of the excitation spectrum to highlight the transition from a superfluid state to a Mott-insulating state. Furthermore, excitation spectra characteristic of different quantum phases – such as gapped and ungapped – are also important for the detection of different states of quantum matter in disordered bosonic systems [28, 46, 48, 68].

Chapter 8

Atomic mixtures in state-dependent lattices

More Is Different.

– P. W. Anderson, Science ***177****, 393–396 (1972)*

In this chapter, we discuss the generation of hyperfine state mixtures in our experiment and briefly review our method for implementing state-dependent optical potentials. We include a discussion of areas of experimental study that are made possible with these techniques, and briefly highlight two such studies that we have performed. These deal with nonlinear atom-optical four-wave mixing and implementation and study of the two-component bosonic Hubbard model, as based on our publications *Collinear Four-Wave Mixing of Two-Component Matter Waves*, Phys. Rev. Lett. **104**, 200402 (2010) [219] and *Superfluidity of interacting bosonic mixtures in optical lattices*, Phys. Rev. Lett. **105**, 045303 (2010) [44], which have been discussed in detail in Ref. [45].

8.1 Introductory discussion

Nearly a decade ago, the experimental study of scalar bosons in ordinary (single-frequency and stationary) three-dimensional (3D) optical lattices [27] allowed for realization of the 3D Bose–Hubbard model with ultracold atoms [29], with later studies in 2D [220] and 1D [31, 185]). While the study of scalar particles in optical lattices is a wide-ranging field in and of itself (especially with the inclusion of dynamical effects, superlattice structures, and higher-orbital physics), the introduction of a (pseudo)spin degree-of-freedom (not restricted

to 1/2) in the particles' internal state greatly enlarges the number of physical phenomena that can be studied.

For the situation of having two types of bosons in an optical lattice, which are both in the Hubbard regime, the system can generally be described by the two-component Bose–Hubbard model [60–62] (2BHM). One interest is in studying exotic quantum ground states particular to this Hamiltonian. Inter-species pairing phenomena – in some analogy to the BCS mechanism – can be studied in the emergence of so-called pair and counterflow (anti-pair) superfluidity [60, 221], in systems in which the single-particle charge excitations are gapped. Furthermore, the 2BHM can be used to study quantum magnetism and spin Hamiltonians [59], with state-dependent lattices allowing for the control of spin-exchange coupling constants. Spin dynamics in these systems can be used to directly engineer entangled-state resources for quantum computing [222]. Additionally, more direct methods with spin-dependent potentials may be used for the generation of many-particle entanglement and squeezing in lattices [223, 224] and in bulk systems [225]. As a matter of practical importance, studies of the 2BHM may also provide insight into the mechanism underlying the observed loss of decoherence in mixture experiments with pseudospin-asymmetric tunneling, both for boson-boson [51, 52] and boson-fermion [54–57] mixtures.

In a recent work of ours [44, 45], we have implemented the 2BHM with a homonuclear mixture of bosonic particles moving in a 3D lattice with state-dependence along one lattice axis. Compared to studies of heteronuclear mixtures in far-detuned lattices, study of the 2BHM with homonuclear particles allows for a species-specific tunneling that is not fixed by the mass ratio and respective polarizabilities of the two species, but rather is tunable through the wavelength or polarization of the state-dependent lattice potentials. This has allowed us to span our system across different regimes of the 2BHM. One likely contribution to the observed coherence loss in atomic mixture experiments occurs when the tunneling of one of the species is much weaker than that of the other species, and in fact is nearly frozen out: loading mixtures into a lattice with these tunneling characteristics can result in the dynamical formation of disorder, so-called quantum emulsions [47, 70]. These quantum emulsions effectively result from the probabilistic projection of the slower-tunneling atoms' density onto sites of the lattice. While this comes about somewhat naturally in multi-species mixtures with species-specific tunneling, there have also been a number of proposals [66, 67, 71] for the controlled generation of disorder using localized *impurity* atoms. One key motivation for implementing disorder in this way is the small length scale over which atoms can be localized, leading to a rather small correlation length of the disordered landscape. As

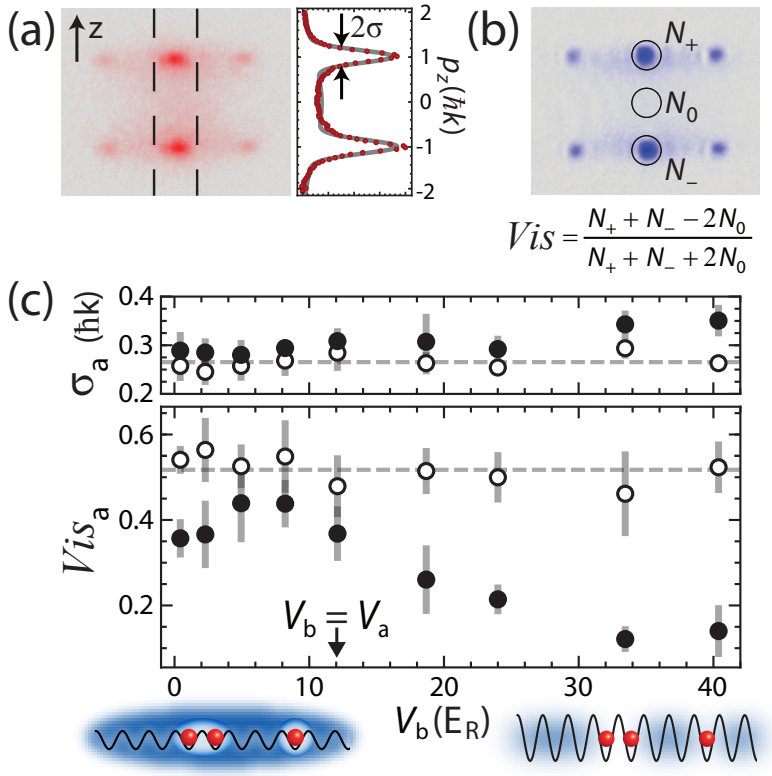

Figure 8.1: Two-component mixture in a state-dependent optical lattice [44, 45]. (a) Single-axis momentum-peak width measurement σ. The $1/e$ half-width σ of the diffraction peaks is determined by a symmetric multi-Gaussian fit to the integrated (within the dashed region) 1D momentum profiles, following a π phase-shift of the diffraction envelope. (b) Single-axis visibility measurement *Vis*, determined by the contrast of time-of-flight interference patterns. (c) Visibility *Vis* and peak width σ_a of the $|a\rangle$ component (filled circles), with fixed lattice depths of $V_a = 12\ E_R$ and $V_\perp = 12\ E_R^\perp$, in the presence of $|b\rangle$ atoms [$f_b \approx 3/4$, $N_a + N_b = (3.7 \pm 0.2) \times 10^5$] as V_b is increased. Here, the recoil energies of the transverse and z lattices, with wavelengths $\lambda_\perp = 1064$ nm and $\lambda_z = 785$ nm, respectively, are $E_R^\perp = h^2/2m\lambda_\perp^2$ and $E_R = h^2/2m\lambda_z^2$. In reference data taken without $|b\rangle$ atoms and with $N_a = (1.0 \pm 0.1) \times 10^5$ (open circles), the visibility and peak width are roughly constant at 0.52(3) and 0.26(2), shown as the dashed lines. Data points are averaged over 3-5 runs, with statistical error bars shown. Cartoons at bottom demonstrate the regimes in which polaron and quantum emulsion effects can be expected. For an extended discussion of this experiment, see Refs. [44, 45].

shown in Fig. 8.7 we have measured the coherence properties [visibility and momentum-peak width as detailed in Fig. 8.7 (a,b)] of one species (called $|a\rangle$) in contact with a second species ($|b\rangle$) whose tunneling was tunable through its lattice depth V_b. The properties of the $|a\rangle$ species were kept constant throughout, and by itself the $|a\rangle$ species was a strongly interacting superfluid near the Mott insulator transition. For large lattice depths for the $|b\rangle$ atoms V_b, i.e. in a regime where one would expect the formation of quantum emulsion states, we indeed observe in Fig. 8.7 (c) greatly reduced coherence of the $|a\rangle$ species.

A second possible contribution to observed coherence loss in mixture experiments occurs in the opposite limit, when one of the species is very mobile. Indeed, a reduction of the $|a\rangle$ component's coherence can also be observed in this regime, as seen in Fig. 8.7 (c) for very small values of V_b. The mechanism that can lead to reduced spatial coherence in this regime is that of a polaronic coupling between the $|a\rangle$ atoms in the lattice and the highly superfluid background of mobile $|b\rangle$ atoms. In this scenario, the slower-tunneling atoms couple to density deformations of the faster-tunneling species, represented as phonon excitations. This coupling between lattice-based atoms and phonon modes of a superfluid background leads to quasiparticles known as polarons [63] consisting of atoms surrounded by a density deformation (a dip for repulsive coupling and a bulge for attractive coupling), described by a coherent cloud of phonons. The effects of the background on the lattice-confined atoms can be approximately described through a renormalization of tunneling (effective mass [226]) and on-site interactions, and the coupling can in fact induce a premature (in terms of lattice depth) transition to an insulating state as compared to the single-species case. In dynamical studies of multi-species mixtures [227, 228], the coupling of the motional state of one species to density excitations of another might be used to study the phenomenon of Bloch-phonon coupling [229–231], which is relevant to condensed matter systems.

Polaronic coupling can also induce long-range off-site interactions between the lattice-confined atoms [63, 64]. For atoms that are mobile, enough to be able to reconfigure their density distribution through hopping, induced nearest-neighbor attraction can lead to the formation of polaron clusters, which minimize the kinetic energy of density deformations in the bath. In the regime in which the tunneling of the lattice-confined atoms is completely frozen out, the coupling of the localized atoms to the delocalized bath can be used to study the spin-boson model [232], which is fundamental to the study of decoherence and the dissipative dynamics of qubits coupled to an environment. The qubit may be represented by a number of possible states of the localized atom - such as its internal state [233], site-occupancy [234, 235], or orbital wavefunction [119] - with coupling governed by collisional interaction with the atoms of the bath.

In recent years, a number of proposals have been presented that suggest using bath-induced dissipation as a mechanism for cooling atoms in a bath [236], and more generally for quantum state engineering through dissipation [237].

As a final example, we mention that in the extreme case of one species confined to a lattice and the other unconfined and behaving as an ideal gas, the use of contact thermometry has been proposed for the characterization of temperature in strongly-correlated lattice gases [238] [however the equilibration time between atoms with large ratios of (effective) mass may be prohibitively long in practice due to a mismatch in their dispersion relations [49, 219]]. Also in this limit, the scattering of free massive particles [49, 80] may be used for measurement of the dynamic and static structure factors of strongly-correlated lattice gases, in analogy to photon scattering [131, 192, 239–241].

8.2 Hyperfine-state mixtures

We now discuss the specific internal state structure that allows for atoms to be in different (pseudo)spin states in our experiments. We consider atoms in the electronic ground state of ^{87}Rb, the state $^2\mathrm{S}_{1/2}$ [86]. With a spin angular momentum of $S = 1/2$ and no fine structure splitting of the $L = 0$ ground-state, there is a total electron angular momentum $J = 1/2$. Inclusion of the nuclear spin I ($I = 3/2$ for ^{87}Rb) then leads to the total angular momentum $\mathbf{F} = \mathbf{I}+\mathbf{J}$, with allowed values within $|J-I| \leq F \leq I+J$. Thus, interaction of the nuclear spin and the electron total angular momentum leads to hyperfine splitting of the ground-state into the $F = 1$ and $F = 2$ manifolds, by a frequency $\Delta_{\mathrm{hfs}} \sim 6.8$ GHz. Each manifold is split into different Zeeman sublevels, defined by their projection along the magnetic field quantization axis m_F, with allowed values of $|m_F| \leq F$. The Zeeman effect shifts the internal state energies with applied magnetic field B, and as shown in Fig. 8.2 (a) at low fields, the separation between adjacent Zeeman sublevels $|F, m_F\rangle$ is roughly proportional to field, as $\Delta E = g\mu_B m_F B$ (here $\mu_B = e\hbar/2m_e c$ is the Bohr magneton and g is the Landé g-factor, with $g_{F=\{1,2\}} = \{-1/2, +1/2\}$ for the ground-state hyperfine manifolds). A more general dependence of the internal state energy levels on magnetic field B is plotted in Fig. 8.2 (b), based on the so-called Breit–Rabi formula [242]. This is based on a combination of the Zeeman shifts for a given magnetic moment of the electron $\mu_J = g_J\mu_B\mathbf{J}/\hbar$ and of the nucleus $\mu_I = g_I\mu_B\mathbf{I}/\hbar$, described by the Hamiltonian $H_{Zeeman} = -(\mu_J + \mu_I)\cdot\mathbf{B}$, and the coupling of these magnetic moments via the hyperfine interaction $H_{hf} = A_{hf}\mathbf{I}\cdot\mathbf{J}$.

For magnetic fields that are spatially inhomogeneous, conservative potentials can be constructed for atoms in a given internal state, as used in magnetic

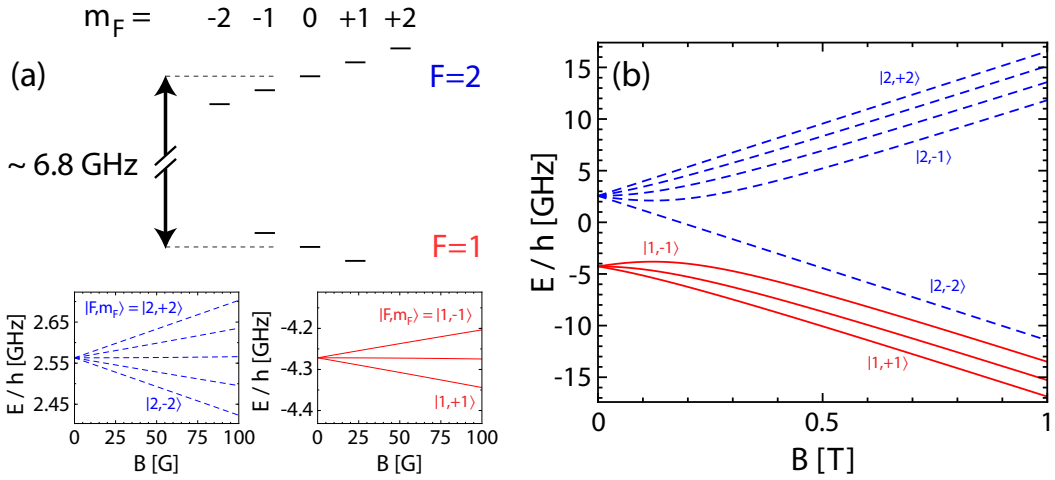

Figure 8.2: Hyperfine energy level structure. (a) Hyperfine state structure of ^{87}Rb electronic ground state, with energy dependence of the Zeeman sublevels ($|F, m_F\rangle$ states) at low magnetic fields B. (b) Ground-state energies as a function of magnetic field B, at high fields (in Tesla, T = 10^4 G).

trapping potentials (quadrupole trap and time-orbiting potential (TOP) trap used for the BEC production, c.f. Chapter 3). The introduction of forces via spatially-varying magnetic fields is also used for Stern–Gerlach separation of the different internal states in our experiments. Shortly after releasing the atoms for time-of-flight expansion, we apply a magnetic field gradient pulse, which "kicks" the atoms in a state-dependent way. After a suitable duration, the different "spin"-components fully separate in time-of-flight, and can be separately imaged onto different regions of the camera's field of view.

To create mixtures of atoms in different hyperfine states, we need to address the atoms with an oscillatory field with frequency matching the hyperfine splitting. For this, we use microwave radiation resonant with the hyperfine splitting, at a tunable frequency of ~ 6.8 GHz (with the microwave-frequency source and antenna used to address the atoms are described in detail in Ref. [45]). In Fig. 8.3, we display two methods used for populating different mixtures of internal states. The first method, as shown in Fig. 8.3 (a), is simply to address the atoms with microwave radiation of constant intensity ($\propto V$) and with a fixed frequency that is resonant only between two states, shown here for $|r\rangle = |1, -1\rangle$ and $|b\rangle = |2, -2\rangle$. For the two-state system with resonant driving, the ground and excited state populations will display an oscillatory dependence with 100% contrast, so-called Rabi-flopping. This method of internal state control is ideally suited to rapidly transfer population, and for creating coherent superpositions of different internal states. The

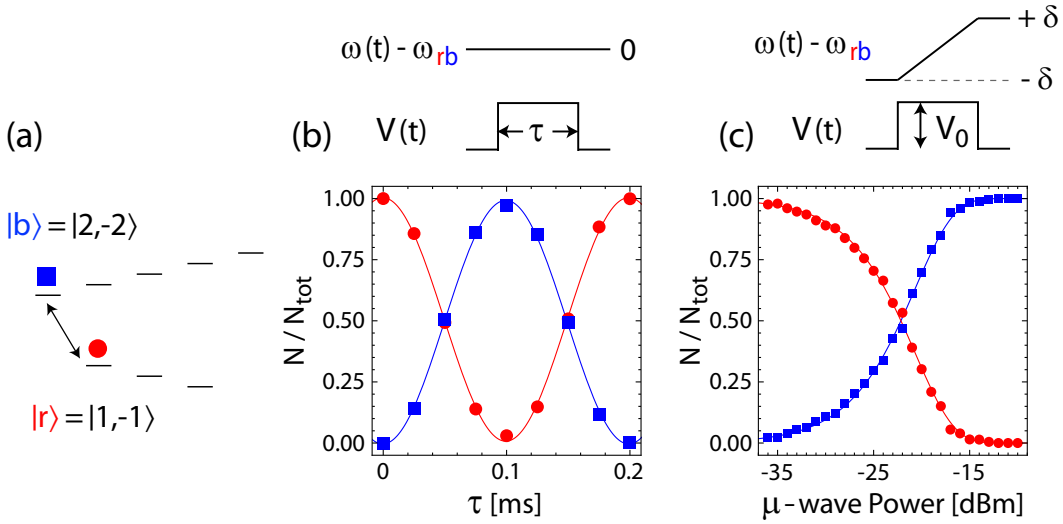

Figure 8.3: Transitions between different internal states of the atoms. (a) We drive coherent Rabi oscillations in the internal state populations, using microwave radiation that is on resonance with a transition between two internal states, shown here as red ($|r\rangle = |1,-1\rangle$) and blue ($|b\rangle = |2,-2\rangle$). (b) We perform Landau–Zener sweeps of the microwave frequency across the resonance, enabling a well-controlled probability of transition between the two states. The transition probability can be tuned through the microwave power.

second method is displayed in Fig. 8.3 (b), and is based on the Landau–Zener protocol [243]. Here, population initially resides solely in the ground-state level $|r\rangle$, and the frequency of the microwave field is ramped linearly across the transition frequency ω_{rb}. Either the speed of the ramp or the intensity of the microwave field may be adjusted to control the probability that the population "tunnels" to the excited state $|b\rangle$. In Fig. 8.3 (b), we plot final state populations as a function of the microwave power. This method is especially well suited to provide highly controllable mixture ratios, with little sensitivity to variations in the magnetic fields.

In addition to these microwave transitions, we can also make intramanifold transitions to different states via radiofrequency radiation [109]. Note that, at low fields the near degeneracy in the energy-splittings between different pairs of states prohibits a two-level description. However, as seen in Fig. 8.2 (b), at higher fields this restriction is lifted as the linear description of the Zeeman shift breaks down. At low magnetic fields, the degeneracy can also be lifted by "dressing" the energy levels - i.e. shifting the levels in a non-uniform, state-specific way - by applying microwave fields that are off-resonant with respect to the hyperfine structure splitting [244, 245]. For homogeneous microwave fields,

this technique has become an important tool for manipulating internal state dynamics [246, 247]. In the following section, we shall discuss an analogous technique of applying off-resonant light fields to shift energy levels in a state-specific way. However, the applied light fields will in general be spatially inhomogeneous, and thus can be used to exert forces, including trapping.

8.3 State-dependent optical potentials

We now describe the general methodology used to create state-dependent optical potentials [248–250] in our experiments, using laser beams with tunable wavelength λ and polarization $\hat{\epsilon}$. Firstly, when trying to create completely state-selective potentials, we need to achieve a cancellation of trapping and anti-trapping potentials. As described in Chapter 2, depending on the sign of the detuning of a laser frequency ω from an excited-state transition at frequency ω_0, a far-detuned optical potential can either create an attractive trap (red-detuned, $\omega < \omega_0$) or a repulsive anti-trap (blue-detuned, $\omega > \omega_0$). To create such a cancellation with a single-frequency laser beam, we need to tune between two different excited-state transitions, such that the laser frequency is red-detuned with respect to one and blue-detuned with respect to the other. For alkali atoms there are two strong optical transitions from the electronic ground state, the D_1 and D_2 lines. For ^{87}Rb these transitions occur at wavelengths 795 nm and 780 nm, respectively, and the wavelength of our state-dependent laser light is tunable within this range. In Fig. 8.4 (a), we show how light with wavelength between the D_1 and D_2 lines leads to red- and blue-detuned contributions from different excited-state transitions.

Secondly, we need to create an optical potential that is particular to a given internal state of the atom. This is based on the conservation of angular momentum, which for a given polarization state of light only allows transitions between certain sets of $|m_F\rangle$ sublevels. Here, certain ground states may only experience optical coupling via either the D_1 or D_2 transitions. In Fig. 8.4 (a,b) we illustrate how this takes place for the specific case of σ^- circularly polarized light, with a wavelength of $\lambda = 787.56$ nm. The $|1,-1\rangle$ state couples to excited states via the D_1 and D_2 lines, while the $|2,-2\rangle$ state is only coupled to the $P_{3/2}$ level by the D_2 line. Thus, the $|1,-1\rangle$ experiences a light-shift cancellation (with *zero* net potential for the given λ and $\hat{\epsilon}$), while the $|2,-2\rangle$ does not and experiences an attractive potential.

We now demonstrate how such a state-selective potential can be used in practice. In Fig. 8.5 (a,b) we show diffraction patterns for two different hyperfine states of atoms that are (separately) subject to a state-dependent optical lattice. One of the species exhibits diffraction peaks, due to coupling to the

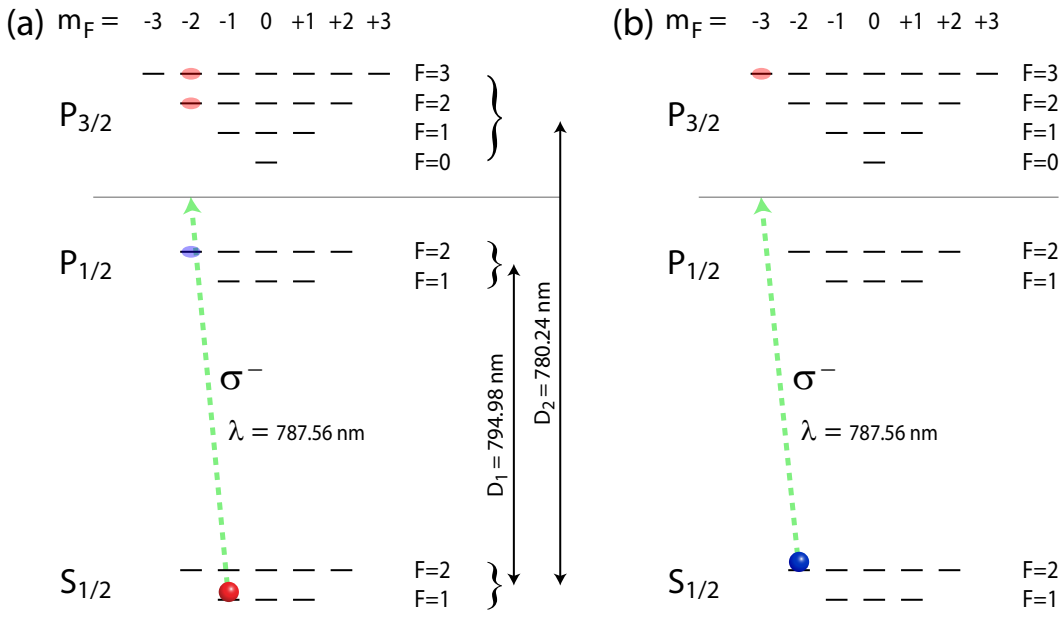

Figure 8.4: Basic scheme for creating state-dependent optical potentials. (a) For certain internal states (shown for $|F, m_F\rangle = |1, -1\rangle$), σ^- polarized light with a wavelength halfway between the D_1 and D_2 optical transitions leads to zero net light-shift, i.e. no optical dipole potential. This effect is due to a complete cancellation of negative and positive light-shifts, from the light being red-detuned with respect to the D_2 line and blue-detuned with respect to the D_1 line. (b) For a different internal state, $|2, -2\rangle$, only coupling to excited states via the D_2 transition is allowed for σ^- polarized light, such that no light-shift cancellation occurs and this state experiences an attractive optical dipole potential.

light-field, while the other does not. Interesting effects can take place when both species are present, leading to diffraction peaks being observed for each of the states, as in Fig. 8.5 (c). As studied in detail in Ref. [219], pair-wise momentum-exchanging collisions between the two species lead to the appearance of diffraction peaks for the species that experienced no optical potential [cf. Fig. 8.5 (d)], due to nonlinear atomic four-wave mixing.

After having introduced the general idea behind the method we employ for producing state-dependent optical potentials, and after discussing some practical examples, we explain in a bit more detail how one can calculate such state-dependent light-shifts [45, 114, 248, 250, 251]. We again consider the dispersive effect of off-resonant laser light acting on neutral single-electron atoms [102], but now a bit more rigorously than in Chapter 3. For light

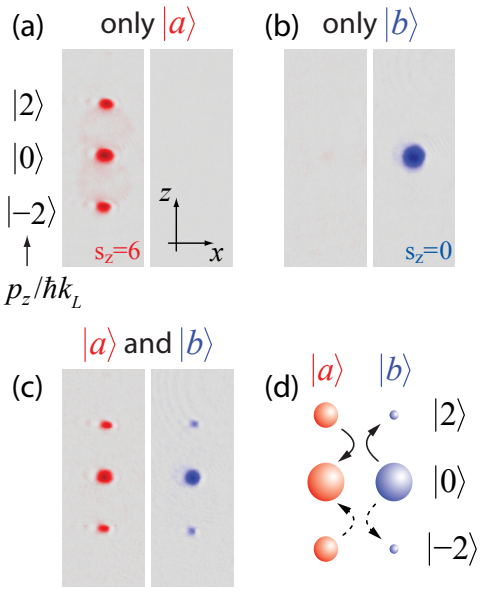

Figure 8.5: State-dependent lattices and atomic four-wave mixing [45, 219]. (a) Diffraction pattern of $|a\rangle$ atoms from an optical lattice of wavelength $\lambda = 785$ nm and σ^+ polarization, pulsed on briefly for $\tau = 25$ μs. Calibration of the lattice reveals a depth $V_a = 6\ E_R$, with recoil energy $E_R = h^2/2m\lambda^2$. (b) Same for $|b\rangle$ atoms only, with no observable diffracted population. The lattice is fully state-selective, with $V_b = 0\ E_R$. (c) When both species are present and subject to the state-selective lattice, atoms of the $|b\rangle$ species appear in the diffracted momentum modes. (d) The mechanism for this apparent diffraction is a pair-wise momentum redistribution between the two hyperfine states, i.e. nonlinear four-wave mixing of matter-wave fields. For an extended discussion of this experiment, see Refs. [45, 219].

fields far from resonance, for which direct transitions to excited states can be ignored (for a detuning $|\Delta/\Gamma| \gg 1$), the effect of the atom-light interaction $H_{int} = -\mathbf{d} \cdot \mathbf{E}$ (with $\mathbf{d}$ the dipole operator and $\mathbf{E}$ the local electric field) on the ground state energy can be treated in second-order perturbation theory. For some state $|i\rangle$, coupling to excited states $|j\rangle$ by $\mathbf{E}$ induces an energy-level shift

$$\Delta E_i = \sum_{j \neq i} \frac{|\langle j|\mathbf{d} \cdot \mathbf{E}|i\rangle|^2}{E_i - E_j} \ , \tag{8.1}$$

with the assumption of a defined quantization axis. For a light field with intensity $I(\mathbf{r}, t)$ possibly varying both spatially and temporally (with $I = \epsilon_0 c E_0^2/2$ and E_0 the electric field amplitude), with frequency ω, and of uniform

polarization $\hat{\epsilon}$, this can be reexpressed (now including both the rotating and counter-rotating terms) as

$$U_i(\mathbf{r},t) = \frac{1}{2\epsilon_0 c}\sum_{j\neq i}\left[\frac{|\langle j|\mathbf{d}\cdot\hat{\epsilon}|i\rangle|^2}{\hbar(\omega-\omega_{ji})} - \frac{|\langle j|\mathbf{d}\cdot\hat{\epsilon}|i\rangle|^2}{\hbar(\omega+\omega_{ji})}\right] I(\mathbf{r},t)\ , \tag{8.2}$$

where $\hbar\omega_{\alpha\beta} = E_\alpha - E_\beta$. Due to dipole selection rules stemming from conservation of angular momentum and symmetry considerations [86], only transitions satisfying $\Delta L = \pm 1$, $|\Delta J| \leq 1$, $|\Delta F| \leq 1$, and $\Delta m_F \leq 1$ are allowed, such that typically only a few excited states will contribute to the level shift for a given polarization of the light field.

We now focus more narrowly on the system at hand, ^{87}Rb atoms within the $^2\mathrm{S}_{1/2}$ ground state, either in the $F = 1$ or 2 manifold, coupled to the $^2\mathrm{P}_{1/2}$ and $^2\mathrm{P}_{3/2}$ excited states by the D_1 and D_2 transitions, respectively. Here we can, ignoring counter-rotating terms, approximate the induced dipole potential as

$$U_i(\mathbf{r},t) = \frac{3\pi c^2}{2}\left[\frac{\Gamma_{\mathrm{D}_1}}{\omega_{\mathrm{D}_1}^3}\sum_{j\in{}^2\mathrm{P}_{1/2}}\frac{|c_{ji}|^2}{\omega-\omega_{ji}} + 2\frac{\Gamma_{\mathrm{D}_2}}{\omega_{\mathrm{D}_2}^3}\sum_{j\in{}^2\mathrm{P}_{3/2}}\frac{|c_{ji}|^2}{\omega-\omega_{ji}}\right] I(\mathbf{r},t) \tag{8.3}$$

for a given polarization of the light field $q = 0, \pm 1$ ($q = 0$ corresponding to linear π polarization and $q = \pm 1$ to circular $\sigma^\pm$), with the factor of two coming from the different line strength factors of the D_1 and D_2 lines. Here $\Gamma_{\mathrm{D}_\alpha}$ and $\omega_{\mathrm{D}_\alpha}$ are the natural line-width and transition frequency of the D_α transition ($\alpha \in \{1,2\}$), respectively. The term c_{ji} is the Clebsch–Gordon coefficient for a given polarization q and set of states $|i\rangle = |F, m_F\rangle$ and $|j\rangle = |F', m_F'\rangle$, defining the angular part of the dipole matrix element as $c_{ji} = \langle F'\ m_F'|F\ 1\ m_F\ q\rangle$ [113].

For detunings $\Delta_{1,2} = \omega - \omega_{\mathrm{D}_{1,2}}$ that are small compared to the fine structure splitting Δ_{fs} ($\Delta_{\mathrm{fs}}/2\pi \sim 7$ THz for ^{87}Rb) but large compared to the excited-state hyperfine structure splittings Δ'_{hfs} (with the largest being $\sim 2\pi \times 800$ MHz), small differences in the transition frequencies ω_{ji} can be neglected. After also setting the nearly equal quantities $\Gamma_{\mathrm{D}_1}/\omega_{\mathrm{D}_1}^3 \approx \Gamma_{\mathrm{D}_2}/\omega_{\mathrm{D}_2}^3$ to Γ/ω_0^3, we then arrive at a much simplified form of the dipole potential experienced by the state $|i\rangle \equiv |F, m_F\rangle$ for a given polarization q of the light field [250, 251]

$$U(\mathbf{r},t) = \frac{\pi c^2\Gamma}{2\omega_0^3}\left[\frac{1 - g_F m_F q}{\Delta_1} + \frac{2 + g_F m_F q}{\Delta_2}\right] I(\mathbf{r},t)\ . \tag{8.4}$$

One serious consideration to keep in mind when using state-dependent optical potentials, given their relatively small detuning from excited-state transitions, is the effect of spontaneous photon scattering or Rayleigh scatter-

ing. By ignoring the counter-rotating term in Eq. 8.2 and incorporating the earlier used form of the scattering rate for far off-resonant dipole potentials $\Gamma_{\text{scatt}} = \Gamma U_{\text{dipole}}/\hbar\Delta$, we can describe the total scattering rate for a state $|i\rangle$ from coupling to excited states $|j\rangle$ as

$$\Gamma_i(\mathbf{r},t) = \frac{1}{2\epsilon_0 c}\sum_{j\neq i}\left[\frac{\Gamma_j|\langle j|\mathbf{d}\cdot\hat{\epsilon}|i\rangle|^2}{\hbar^2(\omega-\omega_{ji})^2}\right] I(\mathbf{r},t)\ . \tag{8.5}$$

Alternatively, we can apply the expression for Γ_{scatt} separately to the D_1 and D_2 line contributions of Eq. 8.4, yielding the approximate form

$$\Gamma_i(\mathbf{r},t) = \frac{\pi c^2\Gamma}{2\hbar\omega_0^3}\left[\Gamma_1\frac{1-g_F m_F q}{\Delta_1^2} + \Gamma_2\frac{2+g_F m_F q}{\Delta_2^2}\right] I(\mathbf{r},t)\ . \tag{8.6}$$

For the typical laser intensities used in our studies with state-dependent optical lattices, heating due to Rayleigh scattering becomes the main limitation on the lifetime of the experiments, on the order of a few 100 ms. While these timescales allow for the study of many interesting effects as discussed in the following chapters, processes occurring at rates of a few Hz or requiring very low temperatures, such as those based on engineered spin-exchange [59], will likely be hard to observe due to this incoherent photon scattering.

Having introduced the essentials for calculating light shifts and scattering rates for the most general of situations, we now plot in Fig. 8.6 calculated dipole potentials and scattering rates (using Eqs. 8.2 and 8.6) as a function of wavelength in the vicinity of the D_1 and D_2 transitions (using ^{87}Rb transition line data from Ref. [113]). Our experiments incorporate in some capacity optical potentials with wavelengths in this range. We note that laser light fields in general will not be restricted to either linear or circular polarizations, but may be represented as a coherent superposition of σ^+ and σ^- contributions. Fig. 8.7 shows the experimentally measured polarization dependence of the state-dependent optical lattice depth, in a fully retro-reflected geometry using light with wavelength $\lambda = 785$ nm. The induced lattice depth due to a state-dependent coupling to excited states is measured with respect to the states $|a\rangle = |1,-1\rangle$ and $|b\rangle = |2,-2\rangle$.

8.4 A moving state-dependent optical lattice

Here, we briefly also detail the implementation of a moving state-selective lattice potential. A standard method for the generation of a moving optical lattice is through the interference of two laser beams of the same wavelength

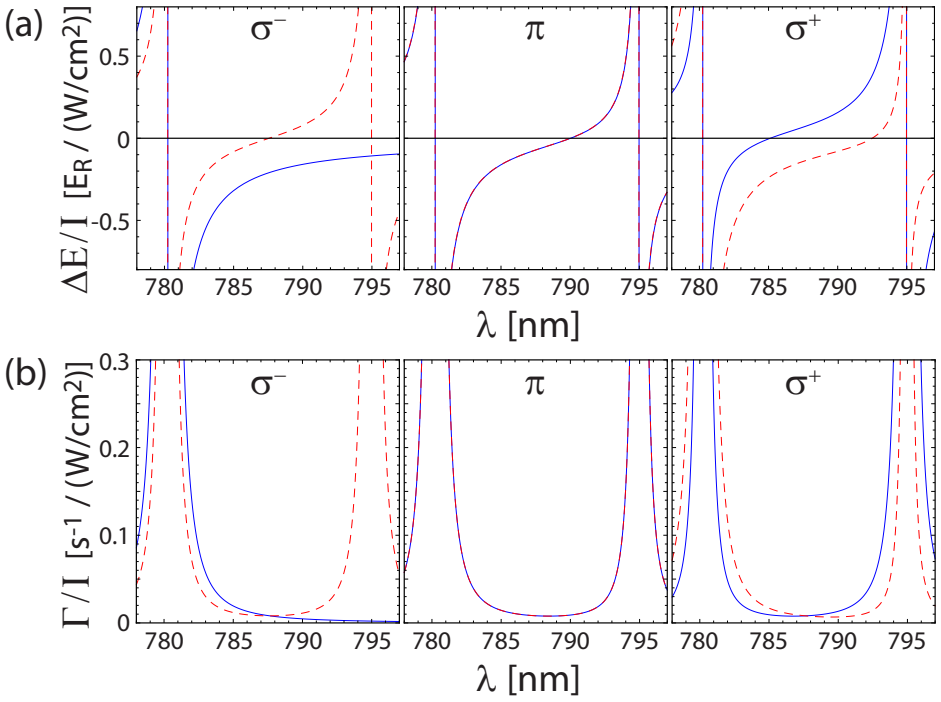

Figure 8.6: Energy shifts and scattering rates as a function of optical wavelength. (a) Ratio of energy level shift ΔE to light intensity I, shown for σ^-, π, and σ^+ polarizations and for the hyperfine states $|a\rangle = |1, -1\rangle$ (red dashed line) and $|b\rangle = |2, -2\rangle$ (blue solid line). (b) Ratio of incoherent scattering rate Γ to light intensity I, for polarizations and internal states as in (a).

λ, but with a slight frequency difference δf [215, 252, 253]. For fixed frequency detuning δf, the optical interference pattern moves with a constant velocity $v_L = \delta f(\lambda/2)$. This frequency detuning may be experimentally achieved in many ways, such as by changing the optical path length in a fully retroreflected geometry - either by a moving mirror, a rotating dispersive element, or with a modulated electro-optical element - or by frequency-shifting with acousto-optic modulators (AOMs). Due to a greater stability and control of the frequency-shifts, we use radiofrequency-driven AOMs. We use a phase-stable setup shown in Fig. 8.8 (a). Some portion of the incident laser beam is reflected by a polarizing beam-splitter (with the transmitted pathway blocked off). The reflected light passes through two AOMs, driven by two frequencies different by δf, and is diffracted into the first $(+1)$ and minus-first (-1) orders respectively. This beam, frequency-shifted by δf, is then rotated in polarization and transmitted back through the polarizing beam splitter, nearly antiparallel to the forward-traveling beam. Finally, the light's polarization is

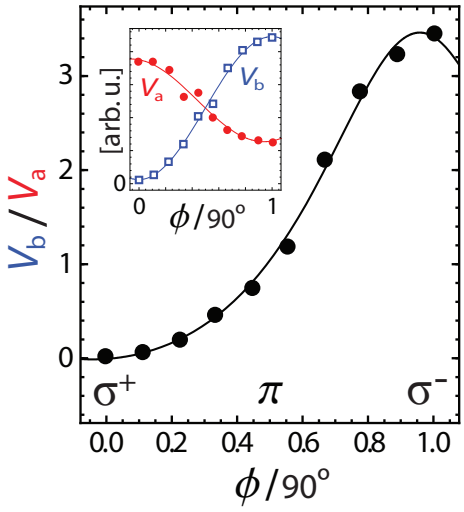

Figure 8.7: The polarization dependence of a fully retro-reflected optical lattice acting on atoms in two internal states, $|a\rangle = |1, -1\rangle$ and $|b\rangle = |2, -2\rangle$. The main plot shows the polarization dependence of the ratio of optical lattice depths experienced by the two states V_b/V_a, with the inset showing (in arbitrary units) the individual dependence of each of the two states on polarization. The polarization axis is parameterized by the rotation angle of a polarization $\lambda/4$ waveplate, which is used to change the polarization from linear π to circularly polarized, either σ^+ or σ^-. Data are determined from Kapitza–Dirac diffraction spectra.

again changed through use of quarter- and half-waveplates, so that at the position of the atoms the forward-going and backwards-going pathways have the same polarization. In Fig. 8.8 (b), we show time-of-flight images of expanded clouds of atoms from a moving lattice (originally loaded in a stationary lattice to form a deep Mott insulator state) for several velocities.

In Chapter 10, we shall use this moving state-selective lattice to study the scattering of free neutral atoms from crystals of localized atoms. In regard to characterizing strongly interacting systems, it can be also used as a tool for inelastic Bragg spectroscopy [131], phase-modulation spectroscopy [205], and, in the state-dependent case, for detecting the dynamic spin-response of bosonic mixtures [254]. Furthermore, arbitrary control over the phase-modulation [255] of a state-dependent lattice may also allow for the engineering of spin-dependent gauge potentials for ultracold mixtures, i.e. to create spin-orbit coupling [256] in lattice-dressed matter-wave mixtures.

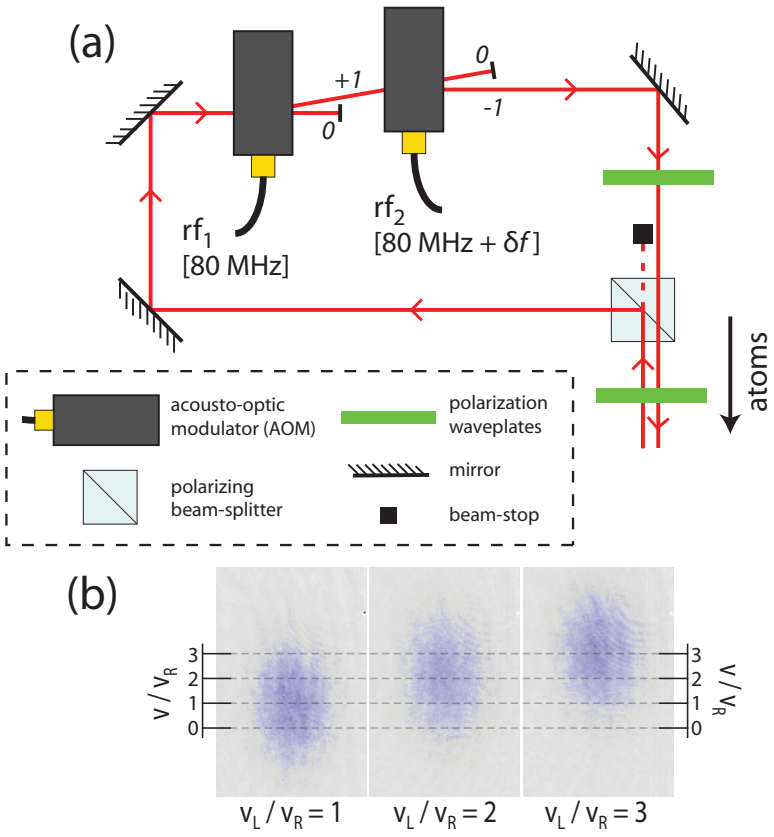

Figure 8.8: (a) Moving optical lattice setup. The interference of two laser beams, with equal polarization and wavelength λ, up to a slight frequency difference δf, creates optical lattices moving with a velocity $v_L = \delta f \lambda/2$. (b) Time-of-flight images of expanded clouds of atoms released from a moving optical lattice. The change in center-of-mass positions along z corresponds to the change in v_L, shown for frequency detunings of $\delta f = \{15, 30, 45\}$ kHz and corresponding lattice velocities $v_L/v_R = \{1, 2, 3\}$, with $v_R = h/m\lambda$ the recoil velocity and $\lambda = 785$ nm.

Chapter 9

Glassy behavior in a binary atomic mixture

In this chapter, we report on the experimental study of disordered one-dimensional (1D) Bose gases, where the disorder is generated with an incommensurate optical standing wave consisting of two spatial frequencies. The standing wave plays the role of a disordering agent, either directly through an associated optical lattice potential or by selectively pinning impurity atoms to the intensity maxima of one of the two constituent standing waves. We use such randomly distributed localized impurity atoms to study the effect of uncorrelated disorder on 1D lattice-modulated Bose gases. We then make comparisons to the case of correlated quasi-disorder, which is formed by an incommensurate lattice potential that acts directly on the 1D gas. While the effects of the two disorder realizations are comparable deeply in the strongly interacting regime, both showing signatures of Bose glass formation, we find a dramatic difference near the superfluid-to-insulator transition. In this transition region, we observe that random, uncorrelated disorder leads to a shift of the critical lattice depth for the breakdown of transport as opposed to the case of correlated quasi-disorder, where no such shift is seen. Our findings, which are consistent with recent predictions for interacting bosons in one dimension, illustrate the important role of correlations in disordered atomic systems. This chapter is based on our publication *Glassy behavior in a binary atomic mixture*, Phys. Rev. Lett. **107**, 145306 (2011) [46].

9.1 Introductory discussion

The presence of disorder is inherent to solid state systems, and it has profound effects on transport in a variety of contexts, ranging from electron conductivity

in metals to dirty superconductors [257]. Quantum gases in optical lattices [26] can, with a high degree of experimental control, elucidate the role played by disorder in a number of physical phenomena. Recently, Anderson localization of matter-waves in disordered potentials has been observed for non-interacting gases [33, 34], and additionally, the reemergence of superfluidity due to repulsive interactions [74]. Discerning the (at times) competing roles of disorder and interactions is key to the understanding of Bose-glass behavior [28, 48, 258] in strongly interacting disordered systems. Ultracold atomic systems [68, 69, 75] should provide a versatile testbed to aid in this endeavor [37].

Previous studies of ultracold atoms in disordered potential landscapes, generated by optical fields, have generally suffered from strong correlations of the disorder that decay over length scales greater than either the healing length of the superfluid or the lattice spacing. This is true for both speckle potentials [34, 69, 75] that are diffraction-limited to structures on the order of the generating laser field's wavelength, and quasi-disordered bichromatic lattices [33, 68, 74], which over large distances exhibit perfect correlations that may make them rather unsuitable for the realization of true disorder. To circumvent these limitations, recently it has been proposed [47, 66, 67, 71] to use atomic impurities, which can be confined to regions much smaller than a lattice spacing, to act as point-like defects.

The sudden quench of an atomic impurity field acting on mobile particles has been proposed [67, 71] for the study of dynamical, out-of-equilibrium response to disorder. Alternatively, theoretical studies [47, 70] have shown that even a slow "freeze-out" of the tunneling of one species from an initially homogenous mixture can lead to metastable "quantum emulsion" states, typified by local separation between frozen and mobile atoms (for repulsive interactions) and displaying properties similar to an equilibrium Bose glass. The study of quantum emulsions may help shed light on the coherence-loss mechanism in a number of experiments involving mass-imbalanced atomic mixtures, both for the boson-boson [51] and boson-fermion [54–56] cases.

In this chapter, we report on experimental studies of interacting 1D Bose gases in the presence of disorder. We have studied the effects of uncorrelated disorder formed by atoms of an auxiliary spin state "frozen" to sites of an incommensurate lattice, and compare to the case of correlated quasi-disorder from an incommensurate bichromatic optical lattice. While both disorder types drive strongly interacting samples into an apparent Bose glass state, a large difference is seen for intermediate interactions, where we find that uncorrelated disorder has a dramatic effect in driving the system towards an insulating state. Our observation of enhanced localization for a more random disorder is consistent with recent theoretical predictions for interacting bosons

in 1D [259].

9.2 Experimental procedure

To briefly describe our experimental procedure, we begin with an optically trapped Bose–Einstein condensate of ^{87}Rb atoms. In 200 ms we load an array of isolated, one-dimensional tubes formed by the intersection of two optical lattices. These lattices are of period $d = \lambda/2$ and depth 40 E_R (with $\lambda =$ 1064 nm, $E_R = (h/\lambda)^2/2m$, Planck's constant h, m the atomic mass). The atoms are trapped along the tube axis z by a nearly harmonic potential of trapping frequency $\omega_z/2\pi = 80$ Hz. A lattice along z, also of period d and with variable depth s (in units of the recoil energy E_R), is smoothly ramped up within 100 ms. This *primary* lattice will serve to define the sites (with index i) and parameter values (tunneling t, and on-site interaction U) of the the (disordered) Bose–Hubbard Hamiltonian we shall use to characterize the system.

Initially, the tubes contain only atoms in the $|F, m_F\rangle \equiv |2, -2\rangle$ hyperfine ground state. To create localized atomic impurities that act as uncorrelated disorder, a fraction (f_{imp}) of the total population of 8×10^4 atoms is transferred to the $|1, -1\rangle$ state via a microwave Landau–Zener sweep. The impurity atoms are loaded into a completely state-selective lattice [44] along z in 20 ms. This lattice has spacing $d' = \lambda'/2$, with $\lambda' = 785$ nm, and the impurity atoms are deeply localized at 20 E'_R (recoil energy $E'_R = (h/\lambda')^2/2m \sim 1.8E_R$). As we begin with an initially homogeneous spin-mixture (i.e. with no spatial dependence of the spin expectation value), and the lattice loading is fast with respect to global mass redistribution in our 1D system (but slow with respect to intra-site band dynamics), this situation has been shown in several theoretical studies to lead to a so-called "quantum emulsion" state [47, 70, 71], in which the localized or slow-tunneling atoms can serve as static disorder for the faster-tunneling atoms. When considering the case of impurity creation starting from a homogeneous spin mixture, the loading should lead to a superposition of many different random distributions or impurity atoms, i.e. to many different realizations of disorder. In fact, the use of atomic quantum fields in such a manner has been suggested because of this quantum parallelism [67, 71]. In the end, the measurement will show the response of the system to one such probabilistic spin projection (for each of the independent tubes). In what follows, we refer to the typically equal mixture used ($f_{\mathrm{imp}} = 0.5$, equal parts frozen and mobile atoms) as "the mixture".

The cartoon in Fig. 9.1 (a) qualitatively depicts such a one-dimensional system of lattice-trapped bosons with embedded impurities. It shows that, af-

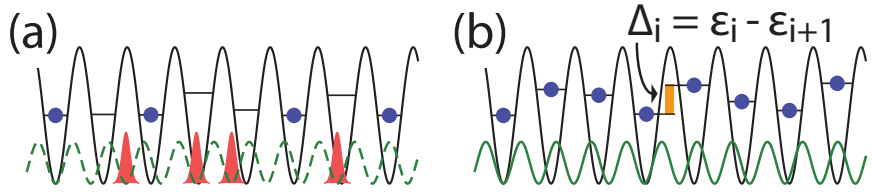

Figure 9.1: Disordered one-dimensional Bose gases. (a) To create a disordered impurity-field, half the atoms of a lattice-trapped Bose gas are converted to an auxiliary spin state (red) and localized to a state-selective incommensurate lattice (dashed green). (b) Alternatively, a weak incommensurate lattice (green) is superimposed onto a lattice-trapped Bose gas. In both cases, the secondary potential (atomic or optical) causes site-dependent energy shifts ε_i and site-to-site energy differences Δ_i. Here we show an average filling of 1 atom of either spin state per site, while in the experiment we have an inhomogeneous system with a typical central filling factor of $\overline{n} \sim 3$ (total) atoms per site.

ter creating a homogeneous spin mixture, we slowly freeze the impurity atoms (red) to a deep state-selective lattice (dashed green) of incommensurate spacing. For comparison to a well-studied case of correlated disorder, we also study bosons in an incommensurate bichromatic lattice system [33, 68, 74], as depicted in Fig. 9.1 (b). For this alternate disorder implementation, we begin with a sample of 4×10^4 atoms in the state $|2, -2\rangle$ (i.e. same number of mobile atoms as for the case of uncorrelated disorder). We then ramp up a secondary lattice in 20 ms, of spacing d' and variable depth $s' \times E'_R$, onto the $|2, -2\rangle$ atoms. In general, due to the external trapping potential, our system is not homogeneous but can be characterized by a typical central filling factor of $\overline{n} \sim 3$ (total) atoms per site. The depictions in Fig. 9.1 are intended to show the key aspects of the two schemes for disorder implementation, while they are not necessarily representative of our actual densities.

A brief note on the timescales of adiabaticity in our system, in relation to our experimental sequence: the timescale over which we "turn on" the disorder ensures that we are adiabatic with respect to local excitations (i.e. on-site band excitations for either of the species), however it strongly deviates from adiabaticity with respect to the global ground state of the system. In fact, the dynamical creation of disorder in a quantum emulsion relies on this non-adiabaticity, as the true ground-state in such a system will typically be characterized by global phase separation between the slow-tunneling and fast-tunneling species (assuming, as in our experiments, that interactions between slow-tunneling atoms are stronger than those between fast-tunneling atoms

and interspecies interactions, i.e. $U_{ss} > U_{sf} > U_{ff}$), with the more mobile atoms moving to the outer regions of the trap. This is a rather boring state, at least with regard to studies of disorder. The quantum emulsion state [47], on the other hand, is a metastable state characterized by a disordered arrangement of the densities of the two species. The pathways by which this metastable state may relax, such as by global mass redistribution of the two species, are effectively cut off by the insulating nature of the state.

9.3 Disordered Bose–Hubbard gas

In both cases, the dynamics of the mobile atoms can approximately be described by the Bose–Hubbard Hamiltonian (BHH) [28, 29]

$$\hat{H} = -t \sum_i (\hat{a}_i^\dagger \hat{a}_{i+1} + \hat{a}_{i+1}^\dagger \hat{a}_i) + \frac{U}{2} \sum_i \hat{n}_i(\hat{n}_i - 1) + \sum_i \hat{n}_i \varepsilon_i \ , \tag{9.1}$$

where t and U are the tunneling and interaction energies of the mobile atoms, and $\hat{a}_i$, $\hat{a}_i^\dagger$, and $\hat{n}_i = \hat{a}_i^\dagger \hat{a}_i$ are the annihilation, creation, and number operators for particles at lattice site i. While in a typical system the site-dependent energy shifts ε_i will take the slowly varying form $\varepsilon_i = m\omega_z^2 d^2 i^2/2$ due to harmonic trapping, here they will be largely determined by the added disordering potentials. Neglecting harmonic confinement, we consider the effect of disorder in generating random site-to-site energy differences $\Delta_i = \varepsilon_i - \varepsilon_{i+1}$, which define the resonance conditions for single-particle intersite tunneling. The disordering potentials, inhomogeneous over individual sites, will in general have a second (likely more minor) effect of modifying the local on-site wavefunctions of the atoms. For strong perturbations this will necessitate a multi-band treatment, and will lead to a spread of site-dependent values for both t and U, with the possibility of asymmetric tunneling. In the following and in Eq. 9.1, we consider only modifications of the Δ distribution and neglect the effects on t and U.

The introduction of random or pseudorandom ε (Δ) distributions leads to the *disordered* Bose–Hubbard model (dBHM), which has been important for the description of experimentally relevant systems [28, 37, 204], such as cold ^{4}He atoms in porous media and bosonic Cooper pairs in Josephson junction arrays. Aside from understanding better the physics of these analogous systems, experimental studies of the dBHM with ultracold atoms are important for several reasons. Currently, there is still active theoretical research aimed at detailing the phase diagram of the dBHM and understanding the nature of the superfluid-to-insulator transition [28, 260], and experimental efforts may

play a complementary role in this regard. These studies are also interesting as the dBHM displays a non-trivial many-body phase – the Bose glass – which to date has not been unambiguously observed in any cold atom experiment. The Bose glass phase is insulating, as in the Mott insulating state, however it has no discrete excitation gap and displays non-zero number fluctuations, i.e. non-zero compressibility. Study of disordered scalar bosons should also help pave the way for the study of disordered spin Hamiltonians and spin glass phases [37]. Lastly, the study of the dBHM in 1D is interesting as it examines the intersection of two fundamentally different localization phenomena in low-dimensional bosonic systems. In the absence of interactions, random disorder leads to localization of the one-dimensional bosonic wavefunctions for arbitrarily weak values of the disorder strength. At the opposing case, for fixed density but in the absence of any modulating potential - disordered or otherwise - strong repulsive interactions can mimic Pauli blocking and induce the localization of single-particle wavefunctions, through the so-called fermionization of bosons into a Tonks–Girardeau gas [199]. The physics of the Bose glass phase, which results from a competition between disorder and strong repulsive interactions, thus interpolates between these two extremes.

In general, the many-body ground state and excitations of the dBHM will be defined by the filling factor $\bar{n} = \mu/U + 1/2$, as well as by a competition between t, U, and $\widetilde{\Delta}$, where $\widetilde{\Delta}$ characterizes the scale of the random energy shifts. There will also be a dependence on the details of the Δ-distribution [28], e.g. quasirandom [259, 261] vs. random (including unbounded Gaussian noise [28], box-top distributions [28], random binary disorder [262], etc.). Here, we contrast the disordered Δ-distributions characteristic of randomly located impurity atoms and an incommensurate lattice potential, respectively, by showing histograms of site-to-site energy shifts (for 1000 sites). To calculate each distribution, we begin by assuming ground-state Wannier orbitals of the $|2\rangle \equiv |2,-2\rangle$ atoms in a three-dimensional lattice with isotropic lattice spacing d and with depths $s_{x,y,z} = \{40, 40, 6\}E_R$, $\omega_i(\mathbf{r})$ (with i the site index). For a generic disordering potential $V_{dis}(\mathbf{r})$ that is random across the lattice, the site-dependent energy shift is given by $\varepsilon_i = \int d^3r |\omega_i(\mathbf{r})|^2 V_{dis}(\mathbf{r})$ with the integral taken over site i ($\pm d/2$ along each axis). For the incommensurate lattice potential, we homogeneity along x and y (as the lattice beam has a 230 μm waist) and a form $V_{inc}(z) = s' E'_R \sin^2(k'z)$, where $k' = 2\pi/\lambda'$ and $s' = 1$. The histogram of Δ values for this quasiperiodic lattice is plotted in Fig. 9.2 (b). For the random impurity potential, $V_{imp}(\mathbf{r})$, we begin by assuming a fifty-percent mixture of impurity atoms (state $|1\rangle \equiv |1,-1\rangle$) that are localized to sites of the very deep state-selective lattice along z, of spacing d' and depth $s_z = 20E'_R$, with a corresponding Wannier orbital $\tilde{\omega}_j(\mathbf{r})$. The

site indices that play host to impurity atoms, j_k with index k ranging from 1 to 500, are determined by projecting out impurities from a distribution of hard-core bosons on the primary lattice, i.e. with no multiple occupancies per site and with positions forced to the nearest site of the secondary lattice. We then represent the total impurity potential as $V_{imp}(\mathbf{r}) = g_{12} \sum_k |\tilde{\omega}_{j_k}(\mathbf{r})|^2$, where g_{12} is the interspecies scattering length between $|1\rangle$ and $|2\rangle$ atoms, nominally taken as 100 a_0. A histogram of Δ values for the impurity potential is shown in Fig. 9.2 (a). We note that given our actual densities and the inhomogeneity of the system as discussed earlier, a more realistic representation of our Δ distributions would vary over the system and would support multiple impurity occupancies per site.

While both of these distributions are contiguous and extend beyond $\pm\Delta/U$, the details differ considerably. The impurity distribution is peaked about $\Delta/U = 0$ due to adjacent impurity-free sites, while the bichromatic lattice distribution is peaked at the outer-bounds of the distribution. In Fig. 9.2 (c,d) we plot the normalized autocorrelation function

$$\chi_j = \langle \Delta_i \Delta_{i+j} \rangle_i / \langle \Delta_i \Delta_i \rangle_i \ . \tag{9.2}$$

The perfectly regular correlations in Fig. 9.2 (d) are a known attribute of quasi-disordered incommensurate lattices [259, 261]. In contrast, for the atomic impurity field – which combines the irregular spacing of bichromatic lattices and the irregular, probabilistic filling of binary disorder – off-site correlations are strongly suppressed. This difference can have profound effects, as the localization properties of a system will generally depend on both the strength and correlation length of the disorder potentials [263, 264]. An extreme case can be found for non-interacting particles in 1D, where random disorder leads to Anderson localization for any finite disorder strength $\Delta \neq 0$, while incommensurate lattices induce localization only beyond a critical lattice depth [33, 204], i.e. in the Aubré–Andre transition [164]. One final, fairly natural way to characterize the two distributions is by their respective spatial frequency components. As is clear, the potential landscape of the quasi-disordered bichromatic lattice should have only two spectral components at spatial frequencies k_1 and k_2. This, however is not so for the case of impurity atoms that are randomly located at the sites of the incommensurate lattice. Here, random occupation (and thus vacancies) can lead to many more spatial frequency components. In Fig. 9.2 (e,f), we plot the spatial frequency power spectra (zoomed-in over a small scale) of the two distributions (random and quasi-disordered). Here, the spectra are for the continuous potential landscapes, and not discrete in terms of site indices. Both spectra contain dominant peaks at spatial frequencies $k/k_1 = 1$ and $k/k_1 = d_1/d_2 \sim 1.35$, due to the primary and secondary lattices,

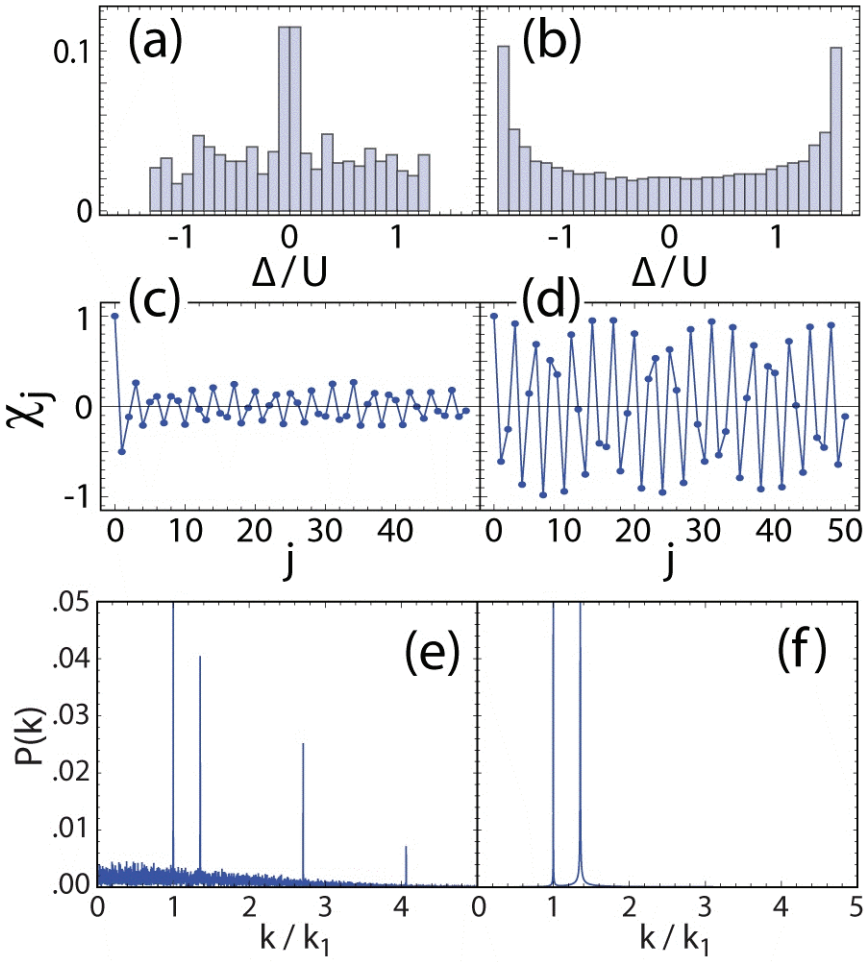

Figure 9.2: (a,b) Histograms of calculated Δ-distributions for the cases of the mixture (assuming either 0 or 1 impurities per site) and an incommensurate lattice of depth $s' = 1$. Both are for a primary lattice depth $s = 6$ ($U/E_R = 0.4$). (c,d) Autocorrelation function $\chi_j = \langle \Delta_i \Delta_{i+j} \rangle_i / \langle \Delta_i \Delta_i \rangle_i$ of the Δ-distributions in (a,b), as a function of the site-to-site distance j. The averaging is over 1000 sites. (e,f) Spatial frequency power spectra for the same distributions as above. Both spectra contain dominant peaks at spatial frequencies $k/k_1 = 1$ and $k/k_1 = d_1/d_2 \sim 1.35$, due to the primary and secondary lattices, respectively. In the case of impurity atoms, however, the probabilistic filling of $|1, -1\rangle$ atoms within the incommensurate lattice leads to higher harmonics at $k/k_1 \sim 2.7$ and 4, as well as to a broad continuum at low spatial frequencies, reminiscent of a "white noise" distribution.

respectively. In the case of impurity atoms, however, the probabilistic filling of $|1,-1\rangle$ atoms within the incommensurate lattice leads to higher harmonics at $k/k_1 \sim 2.7$ and 4, as well as a broad continuum at low spatial frequencies, reminiscent of a "white noise" distribution.

9.4 Results and discussion

9.4.1 Excitation spectra

We begin our investigation into the effects of disorder by measuring excitation spectra, which relate most directly to the distribution of site-to-site energy shifts. Along with a finite compressibility [265, 266], a gapless excitation spectrum is a characteristic feature distinguishing a disordered Bose glass state from a (homogenous) Mott insulator. We measure the excitation spectra by performing amplitude-modulation spectroscopy [31, 68, 185] of the primary z-lattice at driving frequencies $\omega_{\mathrm{mod}}/2\pi$. As described in Chapter 8, we sinusoidally modulate s by $\pm 15\%$ for 80 ms, ramp down to $s = 4$ in 5 ms, and allow 15 ms of thermalization. When used, the incommensurate lattice is turned on in 20 ms prior to modulation and off in 5 ms concurrent with primary lattice ramp-down. From time-of-flight interference we measure the visibility η_-/η_+ [44], with $\eta_\pm = N_{+1}+N_{-1}\pm 2N_0$; $N_{0(\pm 1)}$ apertures in Fig. 9.4 (d). For the disorder-free case ($\Delta_i \approx 0$) in Fig. 9.3 (a), with the sample chosen to be deep into the 1D Mott regime ($s = 14$, $U/t \approx 66$), the excitation spectrum exhibits resonant structure. The resonance positions are consistent with the excitation of particle-hole pairs at U/h [27, 185] (and $2U/h$ due to either higher-order processes or excitation at the edge of Mott domains [27, 185]). In contrast, for both the atomic impurity mixture (Fig. 9.3 (b)) and for an incommensurate lattice of depth $s' = 1$ (Fig. 9.3 (c)) having comparable Δ-distribution bounds, we observe flat excitation spectra (cf. [68]). These observations are expected [28] for broadly-filled Δ-distributions with bounds $\Delta_{\mathrm{max}} > U$, and are consistent with the system being in a Bose glass state (future compressibility measurements [266] should allow for the disambiguation between a true Bose glass [28, 48, 258] and a disordered Mott state [267]).

While the observed spectral properties are consistent with Bose glass formation, transport measurements are necessary to confirm insulating behavior. Here, we study the effects of disorder in the transition region between superfluid and insulator, determining the critical lattice depth at which the systems become insulating through the study of localization and transport. In regard to the former, the momentum-peak width of a released sample (related to the inverse correlation length ξ^{-1} of the sample in-situ [188]), exhibits a sudden

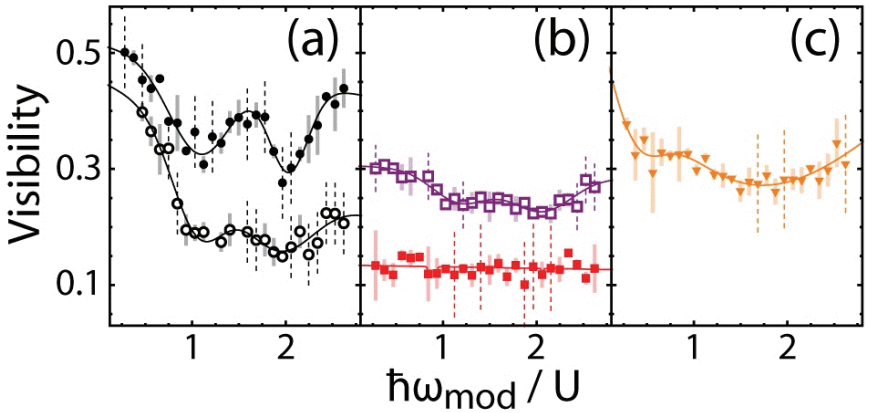

Figure 9.3: Disappearance of excitation gap due to disorder. (a) Visibility as a function of amplitude modulation frequency (normalized to $U/E_R = 0.53$ for $s = 14$), in the absence of disorder for $s = 9$ and $s = 14$ (open and filled black circles). Fit lines are two Gaussians on a linear slope. (b) For $s = 14$, with atomic impurities, open purple squares and filled red squares represent $f_{\text{imp}} = 0.1$ and 0.5, respectively. (c) For $s = 14$, with an incommensurate lattice of depth $s' = 1$ (orange triangles) and no impurities. Solid error bars are statistical over several runs, while dashed are estimated errors for individual runs (120% of maximum statistical error).

increase accompanying an abating superfluid fraction and loss of off-diagonal long-range order [212]. As for the latter, it has been shown [185, 214] that the response to an applied impulse dies away upon entering the strongly correlated regime, and can serve as a signature of insulating behavior [31, 75].

9.4.2 Transport and spatial coherence measurements

To study transport, we look at how the system evolves after an applied impulse. A magnetic-field gradient along z is pulsed on for a duration of $T = 1.2$ ms and applies a variable force F ranging from 0 to $F_{max}/m = 1.2$ m/s^2, resulting in an impulse $I = F \times T$. As illustrated in Fig. 9.4 (a), we characterize the response as a function of I (with slope α) by monitoring the center-of-mass velocity along z in time-of-flight absorption images following a brief ($\sim$1 ms) ramp-off of the z-lattice. As explained in Chapter 8, we access the momentum-peak width as in [68, 185] by releasing the atoms in time-of-flight following a 50 μs lattice ramp up to $s = 20$ and a gravitational phase-shift along z (without impulse or lattice ramp-off). We then determine the peak width σ by a fit to the profile of symmetric diffraction peaks on top of an incoherent background, as shown in Fig. 9.4 (d).

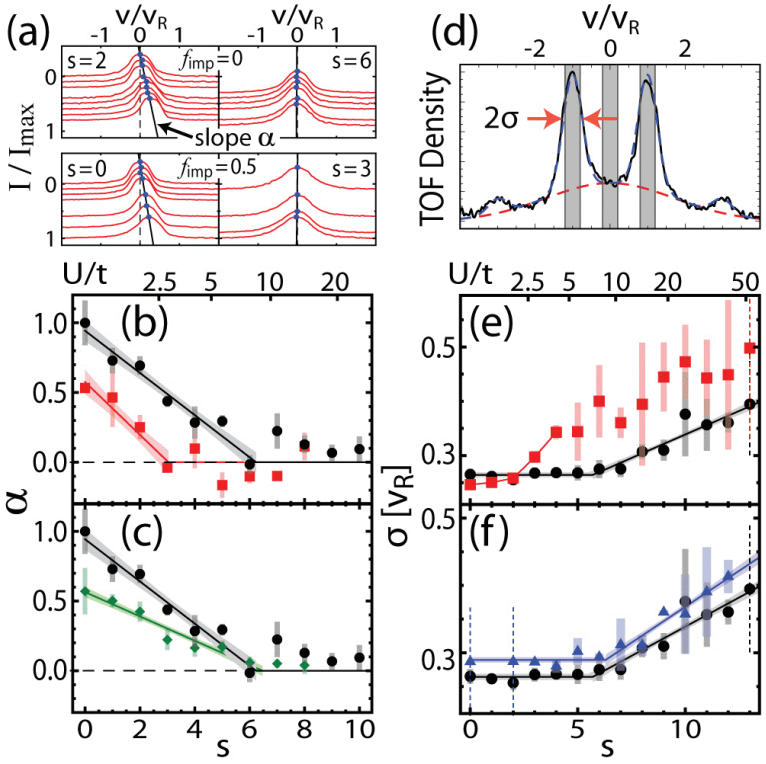

Figure 9.4: (a) The response to impulse is determined by a straight-line fit (with slope α, normalized to the case of free atoms) to the dependence of velocity on applied impulse I (profiles shown for disorder-free and impurity mixture cases; recoil velocity $v_R = h/2md$). (b) α versus lattice depth s for bosons without disorder (black circles) and with atomic impurities ($f_{\rm imp} = 0.5$, red squares). Lines and surrounding shaded regions are fits to the data with confidence regions (1 s.d.) of a linearly decaying response, with no response ($\alpha = 0$) beyond a depth s_c. (c) Similarly, but for an incommensurate lattice ($s' = 3$, green diamonds), with disorder-free data reproduced for comparison. (d) The momentum-peak width σ ($1/\sqrt{e}$ half-width) is determined by a symmetric multi-Gaussian fit to time-of-flight interference patterns. The shaded regions about $v/v_R = 0(\pm 1)$ are used to count $N_{0(\pm 1)}$ for visibility measurements of Fig. 9.3. (e) σ versus s for 1D bosons without disorder and for the mixture (colors/symbols as in (b)). The straight line for the disorder-free data is a fit of a linear increase beyond a depth s_c. The first few data points for the case of atomic impurities are connected as a guide to the eye. (f) Similarly, but for an incommensurate lattice with $s' = 2$ (blue triangles) and with disorder-free data reproduced.

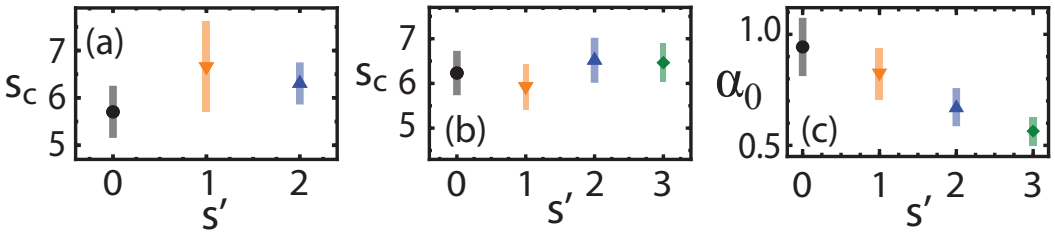

Figure 9.5: (a) Critical intercept s_c as a function of the incommensurate lattice depth s' from linear fits to momentum-peak-width data. (b) Critical intercept s_c as a function of s' from the impulse-response data. (c) The fit values of α_0 (y-axis intercept of linear fit to impulse-response data) as a function of the incommensurate lattice depth s'.

We find that for the impurity mixture, the mobile atoms are more easily driven towards insulating behavior. Similar to [31], we determine the critical point at which the atoms become unresponsive to impulse by fitting a linear decay to the response α as a function of lattice depth. As shown in Fig. 9.4 (b), this fit to the transport measurements yields a critical depth $s_c = 3.0 \pm 0.5$. While we do not fit the peak width data, a kink near $s_c \approx 2$ can be observed in Fig. 9.4 (e). These values are roughly half of those measured for the disorder-free case, with values of $s_c = 6.2 \pm 0.5$ and 5.7 ± 0.5 based on impulse response and peak width, respectively. The value of $s_c \approx 6$ is close to the expectation for our given densities and interaction strengths. For our sample of one-dimensional systems, which have a tube-averaged Lieb–Liniger parameter value of $\gamma = 0.6$, estimates (see Eqs. 6.19 & 6.18) based on the Bose–Hubbard and sine-Gordon models predict $s_c = 6.2$ and $s_c = 4.7$, respectively [31]. The Lieb–Liniger parameter is determined as $\gamma = mg_{1D}/\hbar^2 n_{1D}$ [204], with a 1D density n_{1D}, an effective 1D interaction strength $g_{1D} \approx 2\hbar\omega_\perp a$ [195], s-wave scattering length $a \approx 5.3$ nm, and transverse trapping frequency $\omega_\perp = 2\pi \times 26$ kHz.

For the incommensurate lattice, transport data for $s' = 3$ is shown in Fig. 9.4 (c). In this case no shift of the critical depth is seen. The momentum-peak width data mirrors this lack of a shift of the transition point, shown for a value of $s' = 2$ in Fig. 9.4 (f). Indeed, for the range of incommensurate lattice depths considered (we restrict to $s' E'_R / s E_R \lesssim 1$ in the transition region to keep the depth of the *secondary* lattice less than the first), no shift of the critical point can be seen for either of the two measures. We show in Fig. 9.5 (a) and (b) the fit-determined values of s_c as a function of s' from the peak-width and impulse-response measures, respectively. Although no shift of the critical point is seen, we do find that the incommensurate lattice has a detrimental effect on transport. The response to impulse is generally suppressed, characterized by

a reduced y-axis intercept α_0 (i.e. α for $s = 0$), as is plotted in Fig. 9.5 (c) as a function of s'.

While both incarnations of disorder resulted in an apparent Bose glass state for very deep lattices, a clear difference was seen in their effect on more weakly interacting samples. In attempting to account for the observed difference, a natural consideration is the disparity in their correlations [χ_j, cf. Fig. 9.2 (c,d)]. In general, one expects that the less correlated the disorder, the more enhanced is the localization [263, 264]. For interacting bosons in 1D, it has been shown theoretically [259] that the localization transition occurs for a more weakly interacting gas (larger values of the Luttinger exponent K or lower values of the Lieb–Liniger parameter γ [204]) in uncorrelated disorder than for correlated disorder. Our observations of a sizeable shift of the transition point for impurities and a negligible shift for an incommensurate lattice are thus in qualitative agreement with expectations based on their dissimilar correlation properties.

Also relevant to our observations is the reduction of phase-space density in the presence of localized impurities, as well as of the atomic density due to the dynamical formation of impurities from the mobile species. The first effect has been shown [268, 269] to be responsible for adiabatic heating and loss of coherence in recent Bose–Fermi mixture experiments [56], due to reduced entropy following a reduction in effectively occupiable sites, both for attractive and repulsive interactions. The second effect is more particular to "quantum emulsion" [44, 47, 71] experiments. Here, reduced density leads to more strongly correlated many-body states in 1D and thus favors increased localization and insulating behavior.

9.5 Concluding remarks

In conclusion, we have observed signatures of Bose glass formation in 1D Bose gases with superimposed disorder, both for atomic impurities and for quasi-disordered bichromatic lattices. The two disorder types have dramatically different effects in the transition region between superfluid and insulator, with atomic impurity disorder inducing localization in much more weakly interacting gases. Our observation that a more weakly correlated disorder leads to enhanced localization is in qualitative agreement with recent theoretical predictions for interacting 1D boson systems. Future experiments aimed at measuring a non-zero compressibility in insulating regions of our system may provide the "smoking gun" for Bose glass formation. Direct observation of compressibility through local number fluctuations [76] would be extremely difficult in our system, even provided an available *in-situ* imaging capability with resolution on the order of ~ 1 μm, due to a line-of-sight interrogation through

many planes of our overall 3D system. Some information may be gained however through measuring the overall response to trap compression [266].

Chapter 10

Probing an ultracold-atom crystal with matter waves

In this chapter, we report on the experimental study of the Bragg scattering of delocalized matter-waves from an ultracold atomic crystal, in which scattering centers are formed by lattice-trapped neutral atoms. In recent years, atomic quantum gases in optical lattices have served as a versatile testbed for important concepts of modern condensed-matter physics. The availability of methods to characterize strongly correlated phases is crucial for the study of these systems. Diffraction techniques to reveal long-range spatial structure, which may complement *in situ* detection methods, have been largely unexplored. Here we experimentally demonstrate that Bragg diffraction of neutral atoms can be used for this purpose. Using a one-dimensional Bose gas as a source of matter waves, we are able to infer the spatial ordering and on-site localization of atoms confined to an optical lattice. We also study the suppression of inelastic scattering between incident matter waves and the lattice-trapped atoms, occurring for increased lattice depth. Furthermore, we use atomic de Broglie waves to detect forced antiferromagnetic ordering in an atomic spin mixture, demonstrating the suitability of our method for the non-destructive detection of spin-ordered phases in strongly correlated atomic gases. In implementing the matter-wave crystallography of lattice-trapped gases, we make use of two techniques that are compared and contrasted in this chapter. This chapter is partially based on our publication *Probing an Ultracold-Atom Crystal with Matter Waves*, Nature Phys. **8**, 544–549 (2012) [49].

10.1 Introductory discussion

The diffraction of electron and neutron matter waves from crystalline structures is a standard tool in crystallography, complementing x-ray techniques [106]. The advent of quantum gases in optical lattices has introduced a new class of highly controllable systems that mimic the physics of solids at lattice constants that are three orders of magnitude larger [26], and it appears natural to ask about a possible role for atomic matter-wave diffraction in the characterization of these systems [80, 270].

Several approaches for detecting the spatial structure of strongly correlated phases of ultracold atoms in optical lattices have so far been taken. These include the analysis of noise correlations in momentum space [190, 191], accessible after release of the atoms from the lattice, as well as dedicated *in situ* detection methods based on optical imaging [76–78] and electron microscopy [79]. In this context, diffraction experiments have the potential to reveal important information on the existence of long-range order, such as spin-ordered phases in atomic mixtures [235, 271, 272], in a non-destructive manner and with substantially lower experimental requirements. Here, optical and atomic matter-wave diffraction are equivalent in the sense that scattering of photons and atoms can be sensitive to both the external and internal state of atomic scatterers. However, there are certain advantages to using matter-wave probes. The de Broglie wavelength of an atomic probe can be tuned freely by controlling its velocity, thus precluding limits on spatial resolution and also providing access to Bragg resonances without the need of varying the angle of incidence. As in the optical case [192, 273], matter-wave probes of high spectral brightness are readily available by using atoms from a Bose–Einstein condensate.

In this work we study the scattering of a *probe* species, consisting of one-dimensional Bose gases, from *target* atoms confined to an optical lattice. For weak confinement, we observe free-particle-like, one-dimensional (1D) collisions [195, 274] between the two species, corresponding to inelastic band-structure excitations of the target by the incident probe field. The inelastic scattering is suppressed for more deeply confined target atoms, giving way to elastic scattering and Bragg diffraction, from which the underlying crystalline order can be inferred. We use this matter-wave scattering technique to characterize the introduction of forced antiferromagnetic ordering [52] in the system.

10.2 Matter-wave probing of an atomic crystal

Our experiments begin with a virtually pure Bose–Einstein condensate of ^{87}Rb atoms in the $|F, m_F\rangle = |1, -1\rangle$ hyperfine ground state, prepared in an optical dipole trap (ODT) of nearly isotropic harmonic trapping frequency $2\pi \times 50$ Hz in the transverse (x and y) and vertical (z) directions. Along the transverse axes, far-detuned attractive optical lattices ($\lambda_\perp = 1064$ nm) are smoothly ramped up in 200 ms via partial retroreflection of the ODT's laser beams [111], resulting in an array of one-dimensional Bose gases, with trapping frequency $\omega_z/2\pi \approx 70$ Hz along z. The final depths of these transverse lattices, $s_\perp = 40$ (measured in units of the transverse recoil energy $(h/\lambda_\perp)^2/2m$, where m is the atomic mass), are sufficiently deep so as to suppress tunneling between the 1D tubes on our experimental timescales. Moreover, given a transverse oscillation frequency in each tube of $\omega_\perp/2\pi = 26$ kHz (in the harmonic approximation), and a corresponding energy spacing to the first allowed transverse excited mode of $2\hbar\omega_\perp \approx 14\ E_R$, all dynamics are energetically restricted to the lowest mode. For all the studies that follow, in the absence of additional lattice potentials along z, the 1D bosons are not deeply within the Tonks–Girardeau regime [199], and can be characterized by a Lieb–Liniger parameter value $\gamma \lesssim 1$ [197, 202].

After forming the array of 1D tubes, we next create a mixture of probe ($|p\rangle \equiv |2, -2\rangle$) and target ($|t\rangle \equiv |1, 0\rangle$ or $|1, -1\rangle$, see below) species through manipulation of the atoms' internal hyperfine state via microwave Rabi pulses and Landau–Zener sweeps at a magnetic bias field of 1.7 G. By adiabatically ramping up a magnetic field gradient, we then fully separate the probe and target atoms along the longitudinal (z) axis. We thereafter smoothly ramp up a state-selective lattice along z, formed by light of wavelength $\lambda_z = 785$ nm, between the D_1 and D_2 lines of ^{87}Rb. This allows ([44, 219, 248]; for more details see the end of the chapter) for a cancellation of light-shifts (and zero lattice depth) for the probe atoms, while the target atoms experience an attractive lattice along z, with period $d = \lambda_z/2$ and variable depth s_z (measured in units of the longitudinal recoil energy $E_R = (h/\lambda_z)^2/2m$). This allows for the target to be driven to a 1D Mott insulator state [185], while the probe species remains a superfluid 1D Bose gas. Finally, as detailed below, we examine scattering processes between probe and target at a well-defined relative velocity, v_{rel}, relating to a probe de Broglie wavelength of $\Lambda_{dB} = h/mv_{rel}$.

10.3 1D collisions and inelastic scattering

We begin by studying collisions between the two species, as the target atoms become localized to a state-selective lattice of increasing depth. In the limit of zero lattice confinement along z, the collisions occurring between the $|p\rangle$ and $|t\rangle$ atoms are essentially free-particle collisions, with all scattering restricted to the 1D tubes. Such binary collisions have previously been studied with a single species as a quantum analog of a "Newton's cradle" [274], and with a two-species mixture in the context of damped spin impurity transport [275]. Here, we realize such collisions by accelerating the probe atoms into an initially separated sample of target atoms, which is itself at rest.

As illustrated in Fig. 10.1 (a), we set the relative velocity of the collisions by controlling the magnetic field gradient along z that initially separates the two species. The probe atoms experience a longitudinal trapping potential shifted by a distance Δz, while the target atoms ($|F, m_F\rangle = |1, 0\rangle$, insensitive to the applied gradient) remain at the trap center. The magnetic field gradient is quickly extinguished, and after a quarter oscillation in the trap the probe atoms have accelerated to a nominal velocity of $v_p^0 \equiv \omega_z \Delta z$ upon interacting with the stationary ($v_t^0 = 0$) target atoms. At this point, we access their momentum distributions by turning off all confining potentials and separating them by applying a pulsed magnetic field gradient during time of flight (TOF), followed by absorption imaging.

Typical TOF absorption images are displayed in Fig. 10.1 (b), for the case of free (along z) target atoms and probe atoms incident at $v_{rel} = v_p^0 - v_t^0 = 2v_R$ (z-lattice recoil velocity $v_R = h/2md \simeq 5.8$ mm/s). Here, and also for weak z-lattice depths, two distinct velocity components at 0 and v_{rel} can be seen for both species. As the target atoms are initially at rest and the accelerated probe atoms are initially at v_{rel} before colliding with each other, the scattering spectra show energy- and momentum exchanging binary collisions between probe and target atoms, i.e. reflections in the center-of-mass frame of atomic pairs. Whereas reflection and transmission events are indistinguishable for colliding atoms of the same spin [274], a spin-mixture gives experimental access to the reflection probability [195]. The atoms collide with a high kinetic energy that far exceeds the mean-field energy of either species, such that the collisions have free-particle character. Using a slightly uneven mixture of the two species (3:2 target to probe atoms), we find that $11 \pm 1\%$ of the target atoms and $14 \pm 3\%$ of the probe atoms are reflected, in fair agreement with the calculated reflection probability of $R = 10\%$ [195] for our system parameters. Here, we have taken

$$R \approx 1 - |1 - 1/(1 + ik_z^{COM} a_{1D})|^2 \ , \tag{10.1}$$

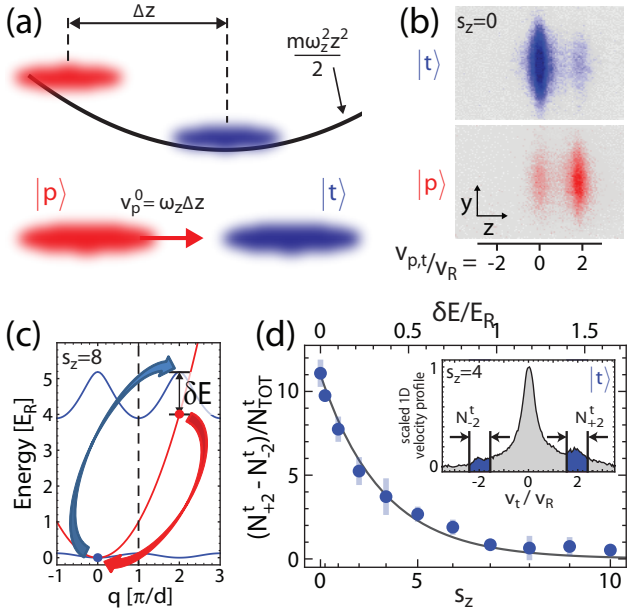

Figure 10.1: Interspecies collisions of one-dimensional bosons. (a) To study collisions between two bosonic species in one-dimensional systems, probe ($|p\rangle$) atoms of one species are displaced (by distance Δz) and then accelerated within a trap potential (trap frequency ω_z) to a final velocity $v_p^0 = \omega_z \Delta z$. The $|p\rangle$ atoms then interact with the stationary target ($|t\rangle$) atoms at the trap center. (b) Absorption images showing Stern–Gerlach separated TOF spectra for the target (top) and probe (bottom), with velocity components at $v_{p,t} = 0$ and $2v_R$, due to momentum-exchanging "Newton's cradle" (NC) collisions. (c) Illustration of momentum and energy exchange in the band structure of the optical lattice, shown for a lattice depth $s_z = 8$ (in units of the recoil energy E_R). (d) Percentage of target atoms that participate in NC-type collisions, as a function of the energy mismatch δE. The solid curve is an exponential fit with a decay constant of 0.35 E_R. The percentage is determined from the peak asymmetry in the TOF velocity distribution (after summation over the y direction) of the target species, as shown for $v_p^0 = 2v_R$ in the inset, with atom numbers $N^t_{\pm 2}$ (peaks) and N^t_{TOT} (total).

where the center-of-mass wavevector of the colliding particles is given by $k_z^{COM} = (v_{rel}/2v_R)\pi/d = \pi/d$, and the effective 1D scattering scattering length is

$$a_{1D} = -\frac{a_\perp^2}{2a}\left[1 - C\frac{a}{a_\perp}\right], \tag{10.2}$$

with constant $C \approx 1.4603$ and harmonic oscillator length, sometimes also

written as $\sigma_\perp$, $a_\perp = \lambda_\perp s_\perp^{-1/4}/2\pi \approx 67$ nm in the harmonic approximation for $s_\perp = 40$. As an aside, we mention that such probabilistic free-particle collisions between 1D bosons may find future use in generating atomic distributions with nonclassical correlations [276], much as in atomic four-wave mixing [219]. Indeed, population transferred to the unseeded modes via pairwise momentum-exchange should display properties akin to two-mode squeezed vacuum [277], and moreover these collisions can create atomic beams with non-separable spin-correlations [278].

As mentioned above, much effort has been devoted to studying collisions of lattice-free 1D Bose gases, both for the spin-polarized [274] and spin-mixed cases [275]. In our system, we now investigate what happens when the dispersion relations are qualitatively different, with one of the species subject to a longitudinal optical lattice. To discuss in simple terms our expectations for the case that the target atoms reside in a lattice of finite depth, we describe the momentum and energy exchange in the periodic zone scheme associated with the lattice. For zero lattice depth, the dispersion relations of target and probe atoms coincide, such that the momentum exchange is resonant. However, as illustrated in Fig. 10.1 (c), for non-zero lattice depth $s_z \neq 0$, each collision demotes an incident probe atom from the first band to the ground band, and vice versa for the target atom involved in the collision. With an energy mismatch δE that increases with s_z, the momentum-exchange becomes off-resonant, amounting to an inelastic band-structure excitation of the target. This process can occur as long as the energetic uncertainty $\Delta E \sim h/\tau$ associated with the finite interaction time τ is larger than δE.

The observed changes of the target's TOF spectra with increasing lattice depth are analyzed in Fig. 10.1 (d). In the absence of collisions, s_z-dependent, symmetric peaks due to optical diffraction are observed at $v_t = \pm 2v_R$ as expected (for up to $s_z \sim 20$). Collisions at the incident velocity $v_p^0 = 2v_R$ give rise to an asymmetry between the two peaks, depending on the depth of the lattice. The observed asymmetry decays with the mismatch δE, in qualitative agreement with our expectation. We estimate the time for probe atoms to traverse half of the target (at which point we switch off the lattice) to be $\tau \sim 10\mu\text{m}/2v_R \simeq 0.9$ms, giving an associated energy uncertainty $\Delta E \sim 0.3E_R$. This value is in good qualitative agreement with the observed $1/e$ exponential decay constant of $0.35E_R$. Our observation of the suppression of elastic two-body collisions due to band-structure mismatch should be of direct consequence for recently proposed thermometry schemes in strongly correlated systems that are based upon the use of a lattice-free spectator species in contact with lattice-modulated atoms [238].

10.4 Elastic Bragg diffraction of matter waves

While inelastic scattering events are seen to die off with increasing lattice confinement, we instead can expect to observe elastic scattering of probe matter waves from the crystal of target atoms. The distribution of elastically scattered probe atoms is determined by the static structure factor $S(q)$ of the target (where $\hbar q$ is the probe momentum transfer). As $S(q)$ is given by the square of the Fourier transform of the target's density, probe scattering can thus reveal information about the underlying spatial distribution of the target atoms. As a caveat, we briefly mention that the study of the dynamic structure factor through low-energy inelastic scattering, which could provide insight into correlations of the target atom array [80], is largely precluded in our system due to dominant reflection at low energies (described below), as well as our use of a superfluid probe gas, which itself supports low-energy collective excitations. Such a study may thus be more well-suited to energy-deposition measurements based on optical Bragg spectroscopy [216, 217].

The static structure factor, for a deeply modulated target, can be approximated as $S(q) = |\sum_j f_j(q) e^{iqz_j}|^2$, where the $f_j(q)$ are the amplitudes of isolated scatterers at positions $z_j = jd$, with j an integer. If one assumes them to be identical ($f_j(q) \equiv f(q)$), as in a Mott phase with uniform filling, the structure factor is a product of two terms, $|\sum_j e^{iqz_j}|^2$ and $|f(q)|^2 = |\langle \varphi_0 | e^{iqz} | \varphi_0 \rangle|^2$, where $\varphi_0(z)$ describes the on-site density distribution of each scatterer. The first term determines the positions of Bragg diffraction resonances, and reveals the periodicity of the array of scatterers. The second term, the atomic form factor $|f(q)|^2$ (or equivalently the single-scatterer or Fraunhofer envelope function) reveals information of the on-site density distribution.

In order to perform crystallographic measurements, we begin by introducing a controlled method to vary the relative velocity (de Broglie wavelength) of matter waves incident on a deeply-confined crystal. Such a wavelength scan is necessary to identify Bragg diffraction resonances, which are expected when a multiple of the probe's de Broglie wavelength coincides with the target's lattice spacing (i.e. $2d = n\Lambda_{dB}$, or $v_{rel} = nv_R$, with n the order of diffraction), and more generally it allows study of the dependence of scattering on the probe's de Broglie wavelength. As illustrated in Fig. 10.2 (a), the target atoms (here in the $|1, -1\rangle$ state) are loaded into a very deep state-selective lattice initially at rest in the lab frame. This lattice is then made to move at a well-defined velocity $v_L = \delta\omega(\lambda_z/4\pi)$ by detuning the relative frequency of the two interfering laser beams that create the lattice by an amount $\delta\omega$. The pinned target atoms, which are initially far-separated from the probe atoms, follow the moving lattice minima at a variable velocity v_{rel} for a total time T_{move}, in-

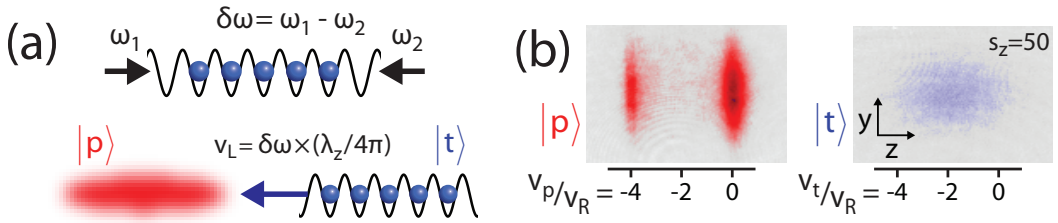

Figure 10.2: Diffraction from a moving atomic crystal. (a) Target ($|t\rangle$) atoms, strongly confined to a state-selective lattice, move towards a stationary cloud of probe ($|p\rangle$) atoms at a velocity $v_L = \delta\omega \times (\lambda/4\pi)$, by frequency detuning (by $\delta\omega$) the two lattice beams. (b) Absorption images show the $|t\rangle$ and $|p\rangle$ species after interaction and expansion in TOF.

cluding a set delay time before the probe and target make contact. The large initial separation helps to avoid the formation of a quantum emulsion [47], resulting when homogeneous mixtures are loaded into state-dependent lattice potentials, which can affect interspecies transport properties [44, 46].

In Fig. 10.2 (b), we show TOF absorption images of both species following interaction, taken for the case of deep confinement ($s_z = 50$) and a velocity $v_{rel} = 2v_R$. The target's velocity distribution is very broad, as expected for a deep 1D Mott state, and is centered around the velocity of the moving lattice ($-2v_R$). The velocity distribution of the probe, initially centered around $v_p = 0$, displays a peak of atoms transferred to $-4v_R$. A series of such scattering spectra (integrated along the transverse y axis) is shown in Fig. 10.3 (a), for a range of relative velocities v_{rel}. For each velocity, the time T_{move} is chosen so that the target crystal enters the probe and then moves for 1.4 ms (kept much less than the trap period $T_z = 2\pi/\omega_z \sim 14$ ms to avoid the dispersion of out-coupled atoms to different velocities due to propagation in the trapping potential). From the scattered probe spectra as in Fig. 10.2 (b) we observe that, in addition to the line of "transmitted" atoms at $v_p = 0$, some probe atoms are out-coupled (i.e. reflected) due to the target crystal. The reflection of probe atoms comes from two apparent elastic mechanisms - specular reflection and resonant Bragg diffraction. We note that both of these mechanisms are to be distinguished from observations of free-space four-wave mixing in two-component mixtures [219, 238], which does not persist when one species loses matter-wave coherence.

The specular contribution is due to the reflection of probe atoms from the potential "step" of the target crystal (energy mismatch outside and inside the crystal). This reflection is dominant at low velocities and gives way to transmission at larger probe velocities (kinetic energies), where the band structure

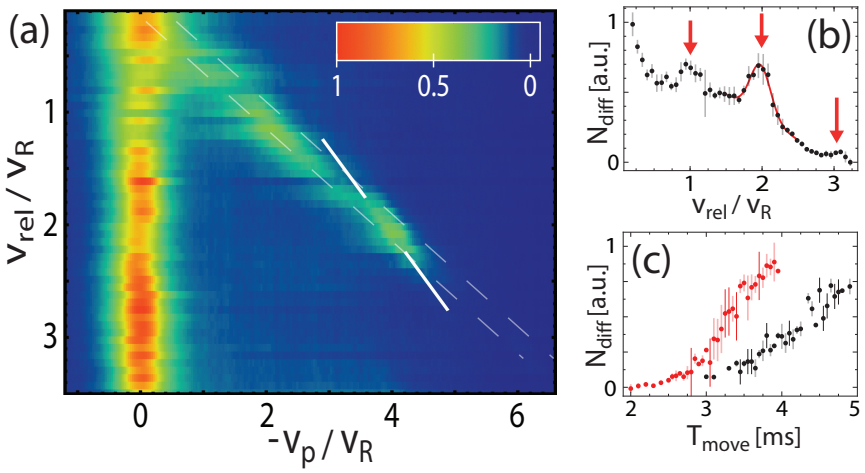

Figure 10.3: Probe scattering from a moving crystalline target. (a) Probe TOF spectra after interaction with a target at $s_z = 50$, at varied relative velocity v_{rel}. Each horizontal line is obtained from a yz spectrum as in Fig. 10.2 (b) by integrating along y and normalizing to the total $|p\rangle$ atom number. The solid white lines near $v_{rel}/v_R \sim 2$ illustrate the slope of the clearly visible second-order Bragg resonance, i.e. extrapolations of a linear fit to the positions of maximum out-coupling for $1.8 \lesssim v_{rel}/v_R \lesssim 2.2$. (b) Dependence of reflection from the crystal on v_{rel}. We count the number of atoms scattered to $v_p \sim -2v_{rel}$, i.e. within dashed lines of Fig. 10.3 (a). Bragg resonances of the $|t\rangle$ crystal are observed for $v_{rel}/v_R = 1, 2, 3$, on top of a background contribution due to specular reflection, which decays with increasing v_{rel}. (c) Reflected probe population as a function of the time during which the crystal is moved (T_{move}), for fixed velocities $v_{rel}/v_R = 1.5$ (black data) and $v_{rel}/v_R = 2$ (red data). The data fall off at long times due to the evolution in the trapping potential.

of the target "atomic crystal" is free-particle-like. The specular contribution leads to the transfer of probe atoms to $v_p = -2v_{rel}$ and shows no resonant structure. In contrast, Bragg reflection from scattering centers of the target crystal occurs at values $v_{rel}/v_R = n$ and results in the transfer of probe atoms to velocities $v_p = -v_{rel} - nv_R$. Such a "locking" to a Bragg resonance is observable through a change in the slope of the out-coupled branch of probe atoms. Results of the velocity scan, which displays these features, are shown in Fig. 10.3 (a).

In Fig. 10.3 (b) we count the number of probe atoms out-coupled to $v_p \approx 2v_{rel}$, and plot it as a function of v_{rel}/v_R. Three resonant peaks in the number of reflected atoms are observed for $v_{rel}/v_R = 1, 2, 3$, corresponding to first-,

second-, and third-order Bragg processes. In addition to these resonances, a significant non-resonant contribution due to specular reflection is observed, which as expected decays with increasing velocity v_{rel}. We fit the second-order resonance peak with a Gaussian on top of a linear slope [red line in Fig. 10.3 (b)], and extract a $1/\sqrt{e}$-width of $2\sigma_v = 0.3v_R$, reflecting the in-trap velocity width of the probe species. The width is a factor of two smaller than the directly observed TOF velocity width of the probe atoms [279], likely owing to effects of interaction-induced expansion during TOF [131].

Using our ability to vary the total time T_{move} that the target crystal moves at constant velocity, we can also study the temporal buildup of the out-coupled probe population. In contrast to optical scattering, this may in the future be used to provide "line-of-sight" information in matter-wave scattering experiments. In Fig. 10.3 (c), we plot the temporal buildup of probe population to $v_p \sim -2v_{rel}$, for the cases $v_{rel} = 1.5v_R$ and $2v_R$. The difference between incoherent (specular reflection) and coherent (Bragg) processes should lead to differences in the growth behavior. Indeed, there are some indications of a more nonlinear initial growth for $v_{rel} = 2v_R$ than for $v_{rel} = 1.5v_R$ case. However, since the relatively short coherence length of the probe [$L \sim \hbar/(m\sigma_v) = 0.8$ μm] precludes a fully coherent temporal evolution, the observed growth will be mostly determined by the time-dependent overlap of the inhomogeneous profiles of the probe and target.

Finally, we recall the dependence of the static structure factor $S(q)$ on the atomic form factor $|f(q)|^2$, in relation to the three Bragg resonances observed in Fig. 10.3 (b). In the harmonic approximation, the form factor is proportional to $\exp(-q^2\sigma_z^2/2)$, where σ_z is the harmonic-oscillator length characterizing the extent of the atomic distribution on each site. While the third-order peak ($q = 3$) is smaller than the second-order peak ($q = 2$), the expected momentum dependence is partially masked, owing to a fixed probe-target interaction time that results in the probe atoms of lower velocity (such as for the first-order peak) interacting with fewer scattering centers of the target crystal. However, we can directly probe the contribution from the atomic form factor, which can be seen to be formally identical to the Debye–Waller factor $W = \exp(-q^2\langle u^2\rangle/2)$ describing the reduction of elastic scattering due to position fluctuations $\langle u^2\rangle$ of scatterers in an ionic crystal [106]. The larger σ_z, the smaller $|f(q)|^2$, in analogy to the decrease of the Debye–Waller factor with temperature. We point out, however, that in our case these fluctuations are not thermal but arise from zero-point motion, and may be tuned through σ_z by varying s_z.

To extract the s_z dependent amount of elastic Bragg diffraction, we recall the experimental situation of Fig. 10.1, where the earlier described method

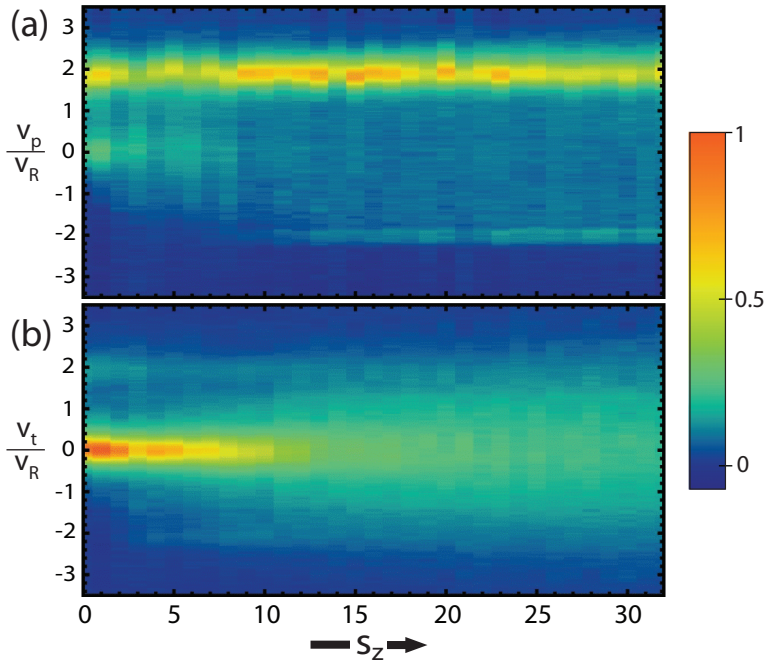

Figure 10.4: Scattering profiles as a function of target confinement. (a,b) Integrated TOF spectra of the $|p\rangle$ and $|t\rangle$ species, following collisions of incident probe atoms (at velocity $v_{rel}/v_R = 2$) from a stationary target of atoms confined to a lattice of varied depth s_z. With increasing depth, we observe the decay of pairwise momentum-exchanging collisions as studied in Fig. 10.1, which lead to the initial asymmetry in target population of the $\pm 2v_R$ diffraction peaks, as well as stationary probe atoms at $v_p = 0$. Accompanying this decay of energy-changing collisions is the appearance of an elastic Bragg reflection peak of probe atoms at $v_p/v_R = -2$.

of probe acceleration in the longitudinal trapping potential (with $|1,0\rangle$ target atoms) was employed. For a complete picture of probe-target scattering events in the crossover from localized-to-delocalized target atoms, we plot in Fig. 10.4 the integrated 1D scattering profiles of both species as a function of s_z. At very low depths, profiles consistent with Fig. 10.1 (b) are observed, owing to (nearly-)free-particle momentum- and energy-exchanging collisions between $|p\rangle$ and $|t\rangle$ atoms. As these collisional events cease to occur, as seen in both the peak of probe population at $v_p = 0$ and the asymmetry of the $v_t/v_R = \pm 2$ target peaks, a probe feature at $v_p = -v_{rel} = -2v_R$ becomes visible. This peak can be attributed to elastic second-order Bragg diffraction, and in Fig. 10.5 (a) we plot the percentage of diffracted atoms as a function of s_z. The percentage of second-order Bragg-reflected probe atoms N_{diff} is determined from a fit of

the TOF spectrum with Gaussian peaks for (i) the transmitted probe around $v_p \approx v_p^0$; (ii) a broad incoherent background centered at $v_p = 0$; (iii) Bragg-reflected atoms at $v_p = -2v_R$. N_{diff} is determined as the amount of Bragg-reflected atoms normalized with respect to the total probe population.

The data in Fig. 10.5 (a) reveal an increase of diffraction efficiency as the target atoms become more localized, and we find the data to be in good qualitative agreement with the calculated dependence of $|f(q)|^2$ on s_z (using Bloch wavefunctions, taken over a single site, for φ_0). We show cartoon depictions in Fig. 10.5 (b,c) of the atomic wavefunctions and the Fraunhofer diffraction envelope. While there is good general agreement, the observed signal saturates at large s_z while the expected curve does not, and a better agreement with the data can be obtained by taking into account s_z-dependent heating due to Rayleigh scattering from the laser beams forming the longitudinal lattice. We attribute this mostly to heating of the probe species, leading to reduced coherence and an increased spectral width, and thus less population at the velocity class that matches the Bragg resonance condition. Indeed, if for a fixed lattice depth of $s_z = 25.5$ we hold the species for a variable time prior to probe acceleration to $v_p^0 = 2v_R$, we observe such heating through a linear increase in the probe's TOF velocity-width, as seen in Fig. 10.5 (d). The ensuing Bragg diffraction signal exhibits a roughly exponential decay with hold time ($1/e$–time $t_{\text{heat}} \sim 150 - 200$ ms), slightly faster than what we should expect due to probe heating alone - i.e. expecting a $1/\sigma_v(t)$ decay, with time-dependent spectral width $\sigma_v(t)$. Assuming that all contributions from heating due to Rayleigh scattering (of either $|p\rangle$ or $|t\rangle$ atoms) should scale as the time integral over the lattice depth, we expect a correction factor of $\exp(-0.01 s_z)$ to modify the form factor. A fit to the data with $|f(q)|^2 \times \exp(\beta s_z)$ yields $\beta = -0.015$ [value used for the dashed curve in Fig. 10.5 (a)], consistent with the expected role of such heating.

10.5 Bragg diffraction spectra using accelerated probes

We now make a qualitative comparison between the spectrally well-resolved method of moving a crystal through a stationary probe, and the method of accelerating a displaced probe cloud into a stationary target crystal, at a relatively well-defined final velocity v_p throughout the time of probe-target interaction. In Fig. 10.6 (a), we show a relative velocity scan similar to that of Fig. 10.3 (a), however here the velocity is controlled by the initial displacement, Δz, of the probe species in the external trapping potential. We have here used

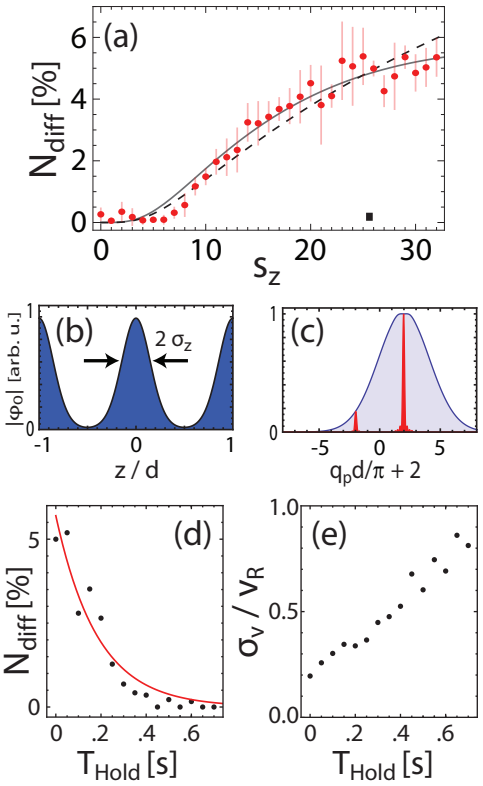

Figure 10.5: Measuring the on-site density profiles of atomic scattering centers. (a) Percentage of (second-order) Bragg-diffracted probe atoms as a function of s_z. The dashed curve is proportional to the form factor $|f(2 \times 2\pi/d)|^2$ calculated as a function of s_z; the solid curve accounts for additional heating effects as described in the text. The black square is a reference measurement without $|t\rangle$ atoms. (b) Plot of the modulated wavefunction of an array of target atoms in a lattice, with the extent on each site characterized by a harmonic-oscillator length σ_z. (c) Cartoon depiction of the Bragg reflection efficiency, as governed by the atomic form factor $|f(q)|^2$ (i.e. the Fraunhofer envelope of individual target scatterers, or quantum-limited Debye–Waller factor W). With $\hbar q_p$ referring to the momentum change of probe atoms after scattering from the target crystal, the Fraunhofer envelope of allowed probe momentum change is approximated by $e^{-q_p^2\sigma_z^2/2}$, determining the percentage of probe atoms that are reflected. (d) Dependence of the percentage of probe atoms, N_{diff} undergoing second-order Bragg diffraction, on the hold time prior to acceleration and target interrogation, T_{Hold}. The red line is a fit exponential decay, with a $1/e$ time constant of 185 ms. (e) Spectral width σ_v of the probe component, based on a fit to the transmitted peak, as a function of the T_{Hold}.

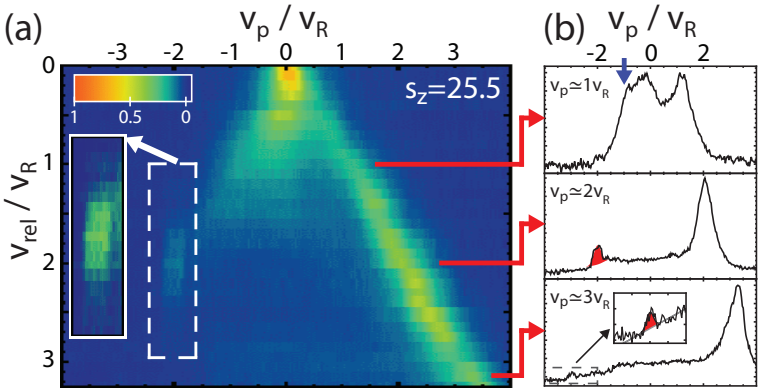

Figure 10.6: Scattering of an accelerated probe from a stationary crystal. (a) Probe TOF spectra from a crystal of atoms localized to a lattice of depth $s_z = 25.5$. The inset shows the second-order Bragg resonance (within the dashed line) with color enhanced. (b) Plots of integrated probe spectra, at $v_{rel}/v_R \simeq 1, 2, 3$. The arrow indicates the expected position of the first-order Bragg peak; Gaussian fits to the second- and third-order Bragg peaks are highlighted in red.

a crystal of target atoms that are slowly loaded into a state-selective optical lattice of depth $s_z = 25.5$. Broadly speaking, the two methods produce quite similar results, with similar observations of first-, second-, and third-order Bragg reflection peaks as shown in Fig. 10.6 (b). We note that the second-order Bragg reflection peak in Fig. 10.6 (a) is fixed at $v_p/v_R = -2$, as the Bragg condition is defined in the reference frame of the *stationary* target crystal. This difference in slope from the specular contribution is exactly related to the observed Bragg peak's slope in Fig. 10.3 (a), although in the case of a moving crystal the reference frame in fact changes with v_{rel}.

However, the method of using a moving target crystal, at an extremely well-defined velocity throughout the time of interaction, allows for a less ambiguous observation many of the features, especially at low impact velocities. This is owing to the methodology for achieving the relative probe-target velocity. At low v_{rel}, the method of probe acceleration begins with small displacements Δz. In fact, the separation between the center-of-mass positions of the two species can in general be less than their combined extents, i.e. the two species should overlap at the outer edges of their distributions up to a value of $v_{rel}/v_R \sim 1.2$, in the central-most 1D "tubes". As the two clouds are strongly-interacting, we should expect in general a significant deviation from the expected distributions based on the single-component scenario, with the likelihood of full phase-separation at low temperatures, even for very weak applied gradients [280].

Even without such deviations from the non-interacting case, the fact that the probe species is not at a fixed velocity, but is rather accelerating towards the trap minimum, will ensure that during the time of probe-target interaction a range of v_{rel} will be experienced. This issue is most severe at small v_{rel}, as both the absolute and relative (as a fraction of v_{rel}) range of velocities occurring throughout probe-target overlap decrease as a function of v_{rel}. We expect that these such effects, as well as possible interspecies instabilities [281] and effects of dispersion in the trap, may contribute to the obscuration and ambiguity of the first-order Bragg reflection peak in Fig. 10.6 (b). By dispersion effects, we mean the fact that specularly reflected atoms will experience a loss of energy and decrease in velocity they travel back up the dipole trap "hill", in the short time between reflection and release for TOF imaging. As discussed briefly earlier, the fact that the probe species is weakly-trapped not only leads to an increased spectral width, but limits the useful timescale of probe-target interaction [cf. Fig. 10.3 (c)].

Finally, there is one last effect that can occur when the two species are overlapped prior to loading of the state-selective lattice. This is the possibility that a *quantum emulsion*, as studied in the previous chapter and in Refs. [44, 46, 47, 70]), can be formed during the loading process. In the following section, we study low-energy scattering between probe and target atoms, with an emphasis on the transport of 1D probe gases through a crystal of target atoms, or in the reference frame of the gas, the dragging of impurities through 1D Bose gases.

10.6 Low energy scattering of free and trapped 1D bosons

We now turn our attention directly to the case of small values of v_{rel}/v_R (for accelerated probe atoms), depicted again in the top row of Fig. 10.7 (a). Naively, apart from the transmitted probe, one would expect to simply see a first-order Bragg peak around $v_{rel}/v_R = 1$. As mentioned earlier, a broad distribution of outgoing probe velocities with $|v_p| \leq v_{rel}$ is seen instead, obscuring the peak (see also Fig. 10.6 (b), top row). In this context, it is important to recall that $v_{rel} = \omega_z \Delta z$ is controlled by varying the initial probe displacement Δz. For small displacements with $v_{rel}/v_R \leq 1.2$, the target and probe never fully separate, encompassing most of the range of the expected Bragg resonance. It seems likely that the overlap contributes to the blurring of the distribution. In the following, we analyze these effects more closely.

In the range $v_{rel}/v_R \lesssim 0.5$, most of the $|p\rangle$ atoms remain near zero velocity,

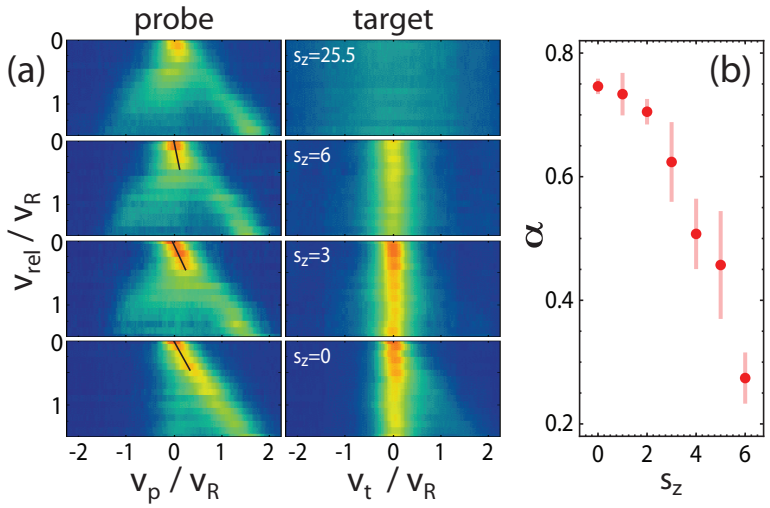

Figure 10.7: Low velocity impurity transport. (a) Probe $|p\rangle$ and target $|t\rangle$ velocity distributions for four values of s_z; for comparison the data of Fig. 10.6 (a) is partially reproduced. (b) Inhibition of probe transport due to interactions with the target. For low velocities ($v_{rel} < 0.5$) we fit a straight line [solid black lines in (a)] with slope α to the probe distribution's peak locations (the peak for a given v_{rel} is defined as the region around the maximum that comprises all points down to 50%; its location is then determined from a Gaussian fit). The error bars indicate the linear regression standard error of the fit.

despite the force exerted on them by the harmonic potential after switching off the gradient. In order to study this effect further, we take displacement scans at different target lattice depths s_z as shown in Fig. 10.7 (a). For $v_{rel}/v_R \lesssim 0.5$, we observe that the peak of the $|p\rangle$ distribution is at velocities that linearly scale as $v_p^{\max}/v_{rel} = \alpha < 1$. In the range considered ($s_z \leq 6$), the coefficient α decreases smoothly with s_z, as seen in Fig. 10.7 (b) (a reference run without $|t\rangle$ atoms at $s_z = 25.5$ yields $\alpha = 1.0 \pm 0.1$ as expected). Without attempting to quantitatively model this behavior, we note that in this range the depth of the effective *atomic* lattice increases nearly linearly with s_z, surpassing the probe's chemical potential $\mu \simeq 0.4\ E_R$ at $s_z = 3$. By atomic lattice we refer to the modulated potential landscape acting on the probe atoms due to repulsive interactions with the localized target atoms, with modulation depth given by $V_{tp} = \langle n \rangle g_{tp} |\varphi_\perp(0)|^4 (|\varphi_z(0)|^2 - |\varphi_z(d/2)|^2)$ [238]. Here, $g_{tp} = 4\pi\hbar^2 a_{tp}/m$ is the 3D probe-target coupling strength with probe-target s-wave scattering length a_{tp}, and $\varphi_z(z)$, $\varphi_\perp(x, y)$ are the target's Bloch wave functions (lowest band at $q = 0$), and $\langle n \rangle$ the mean site occupancy. This modulation is appreciable already at $s_z = 3$, $V_{tp}/\langle n \rangle \simeq 0.5\ E_R$, growing only modestly to $V_{tp}/\langle n \rangle \simeq$

1.4 E_R at $s_z = 25.5$. For our experimental parameters, we expect $\langle n \rangle = 1.7$ for the site occupancy in the center of the target.

We expect that the observed inhibition of transport for increasing s_z is likely the result of the increasing *atomic* lattice, with the possibility of added localization due to the formation of a quantum emulsion in the overlap region [44, 46, 47, 70]. Similar observations of greatly inhibited transport in one-dimensional Bose gases have also been made in purely corrugated optical potentials [31, 214]. At $s_z = 0$, for which the target is a superfluid 1D Bose gas just as the probe, the maximum of the probe distribution suffers appreciable retardation ($\alpha \simeq 0.75$), with momentum transfer to the $|t\rangle$ atoms (as seen in a corresponding shift of the center of mass). The slowdown of $|p\rangle$ atoms entering the target volume can be viewed as resulting from an increase in mean-field energy (i.e. with the target atoms acting as a repulsive potential "hill"), which can be expressed as a change of the refractive index for matter waves similar to the case of photons [133]. We note that this mean-field "slow-down" effect can also be observed (to a small extent) in the position of the transmitted probe peak at $v_p/v_R \sim 2$ in Fig. 10.4 (a). As the lattice depth s_z is increased, the induced "slow-down" in Fig. 10.4 (a) is seen to disappear.

Over the larger range of velocities considered in Fig. 10.7 (a), we observe a broad distribution of $|p\rangle$ atoms that is centered at negative velocities and bounded by retroreflection $v_p/v_{rel} = -1$. The observed broadening of the $|p\rangle$ spectra is consistent with the expected presence of dissipation for velocities near the speed of sound $\tilde{c}_s = (\sqrt{\mu/m})/v_R \simeq 0.4$ [282]. The presence of backscattered atoms (i.e. atoms with $v_p/v_R < 0$) does not depend much on the degree to which the $|t\rangle$ atoms are localized, but persists to low s_z. Remarkably, the velocity spectrum of the target does not contain atoms at the corresponding momentum change (which would violate energy conservation). This means that the momentum of the backscattered $|p\rangle$ atoms is collectively transferred to the optical lattice rather than to single $|t\rangle$ atoms, similar to the Mössbauer effect. An intuitive explanation for this surprising effect is that the backscattering originates from the target's density modulation, which is not free to move around but is spatially locked to the optical lattice potential. Indeed, when no lattice is present ($s_z = 0$), the probe spectrum does not contain atoms at negative velocities. In this case, it is bounded at v_{rel} while the target spectrum contains atoms with velocities up to $v_t = v_{rel}$, indicating the presence of energy- and momentum exchanging binary collisions between $|p\rangle$ and $|t\rangle$ atoms, as studied earlier.

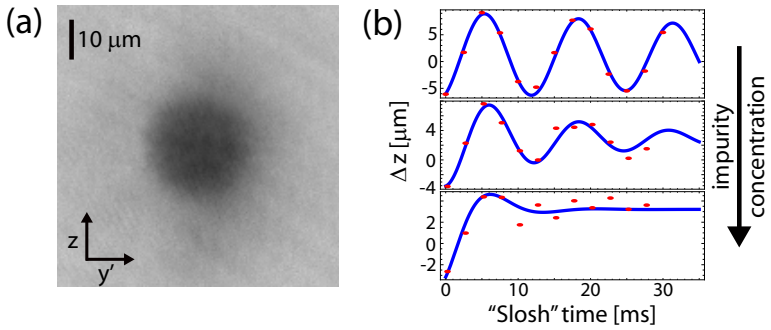

Figure 10.8: Low velocity impurity transport as observed *in-situ*. (a) Typical *in-situ* absorption image of an array of 1D Bose gases, oriented along z. (b) By taking images at different times after an abrupt displacement of the trap-center, dipole oscillations or "sloshing" of the center-of-mass displacement Δz can be observed for a gas of $|p\rangle$ atoms. With the addition of impurity $|t\rangle$ atoms, which are confined to a very deep state-selective lattice, we find a strong damping of the $|p\rangle$ species' dipole oscillations.

10.7 *In-situ* investigation of low-velocity impurity transport

In addition to investigating the influence of localized impurities on transport in momentum-space, we can also directly monitor the temporal evolution of the probe in-situ density profiles as the 1D Bose gases come in contact with an impurity-field. For this, we utilize the *in-situ* imaging beam path discussed in Chapter 3, having higher magnification than the TOF imaging path and with a resolution ~ 1 μm. A typical *in-situ* absorption image taken along the axis $x' = (x+y)/\sqrt{2}$ is shown in Fig. 10.8 (a).

We again use a mixture of hyperfine states, here $|t\rangle = |1,-1\rangle$ and $|p\rangle = |2,-2\rangle$, which are confined to an array of 1D tubes ($s_\perp = 40$), with on average ~ 80 total atoms per tube. By controlling the fractional amount of the two species, we can control the concentration of "impurity " $|t\rangle$ atoms within each tube. The impurity atoms experience a deep, state-selective lattice potential along z, while the $|p\rangle$ experience only the longitudinal trapping potential, with harmonic frequency $\omega_z/2\pi \approx 75-80$ Hz. To perform transport measurements, we begin by applying a relatively strong magnetic field gradient to the atomic mixture, displacing each of the species from the initial equilibrium trap position along z in opposite directions. Next, we first quickly (in 200 μs) ramp up a state-selective lattice to a depth of $s_z \sim 40$, and then quickly turn off the magnetic field gradient. When there are no impurity atoms present, we

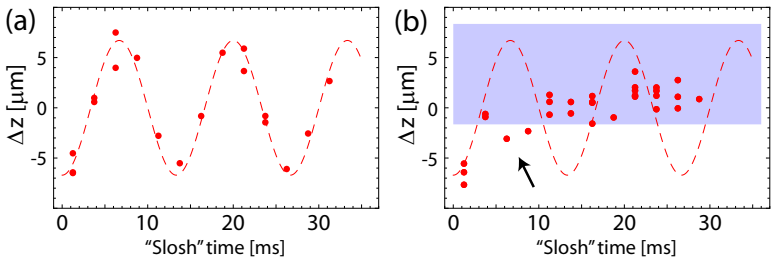

Figure 10.9: Direct *in-situ* evidence for specular reflection. (a) In the complete absence of impurities, undamped dipole oscillations of the center-of-mass position of the $|p\rangle$ species are observed following a trap displacement. After a hold time of about $6-7$ ms, the atoms have reached the outer turning point of the oscillation. (b) With added impurity atoms we observe a strong damping of these oscillations. We also observe evidence of specular reflection, in that the center-of-mass position reverses course at the impurity-field interface (mean extent of $|t\rangle$ atom distributions shown in blue) instead of reaching the outer turning point, as highlighted by the arrow.

observe that the $|p\rangle$ atomic distribution undergoes center-of-mass dipole oscillations following the gradient turn-off, as can be seen in the upper panel of Fig. 10.8 (b). Separately, we confirm that the $|t\rangle$ distribution remains fixed as a function of hold time, due to the deep lattice confinement.

Finally, we can investigate how the presence of an inhomogeneous impurity-field influences the dipole oscillation of the $|p\rangle$ atoms. For this, we image only atoms that are in the $F = 2$ hyperfine state. As shown in Fig. 10.8 (b), for an increasing amount of impurity atoms (for a few percent and for roughly 25 percent), a strong damping of the center-of-mass oscillations is observed. Due to the large extent of the atomic distributions as compared to the interspecies separation, as well as the optical interrogation through a number of 1D systems along x', the mechanism for the observed damping is not completely transparent. We expect that a combination of effects can contribute to the observed damping, including excitation of the 1D gases and possible localization within the impurity field [282], as well as an *apparent* damping of the COM position due to specular reflection at the interface of the impurity-field distribution. If the incoming atomic wave-packets split into transmitted and reflected components, the center-of-mass position may die off even if no energy is dissipated. We note that we only consider contributions of specular reflection, and not coherent Bragg diffraction, as the probe's maximum center-of-mass velocity is only ~ 3mm/s ($\sim 0.5\ v_R$).

Indeed, we observe some evidence for specular reflection in the dynamical evolution of the *in-situ* probe density profiles. In Fig. 10.9 (a), we plot the

center-of-mass displacement from the trap center of a cloud of $|p\rangle$ atoms, in the absence of impurities. In Fig. 10.9 (b), we plot again, as the dashed-line, the expected path of the COM position if there were no impurities. We also illustrate the position and extent of the impurity-atom distribution, in light blue. The center-of-mass trajectory of the $|p\rangle$ atoms – in addition to exhibiting a strong damping and slow "creep" into the impurity field at long times – actually appears to double-back on itself upon reaching the outer edge of the impurity field, corresponding to specular reflection at the boundary. These *in-situ* observations complement the earlier observations of a decaying (with v_{rel}) specular component to the elastic diffraction signal in Fig. 10.3 (b). In the future, the engineering of inhomogeneous atomic (or optical [283] for that matter, e.g. using projected 2D light patterns [77]) potential landscapes may be used for creating bandgap materials and tunnel junctions [284, 285] or resonators for propagating matter-waves.

10.8 Detecting forced checkerboard ordering

We now return to the spectrally well-resolved case of a moving target crystal, and we seek to further demonstrate that matter-wave diffraction may be used to probe non-trivial structure. Here, we show that it gives access to a clear signature of forced antiferromagnetic, or checkerboard, ordering [52] in a mixed-spin crystal. As before, we start with a mixture of atoms in one-dimensional tubes, with a probe that sees no longitudinal lattice along z ($|p\rangle$, here $|1,1\rangle$ atoms, with $\lambda_z \sim 788$ nm) and "crystal" atoms that are loaded into and then follow an optical lattice potential. However, instead of using only one additional species that experiences an attractive lattice along z, our target now consists of two species. The first one $|r\rangle \equiv |1,-1\rangle$ again experiences an attractive lattice potential, whereas for the second species $|b\rangle \equiv |2,-2\rangle$ the potential is repulsive. Thus, the $|r\rangle$ atoms will be drawn to the intensity maxima, while the $|b\rangle$ atoms will be forced to the minima, as illustrated in Fig. 10.10 (a). While we keep the total population of these two species fixed, we vary their relative population, which can be quantified by the net "polarization" of the crystal $P = \Delta N/N$, with $\Delta N = N_r - N_b$ and $N = N_r + N_b$.

When the target is "spin-polarized" consisting of either all $|r\rangle$ or all $|b\rangle$ atoms, the situation is as before, with a lattice constant of $d = \lambda_z/2 \sim 400$ nm. However, when both species are present, the new dominant length scale, between atoms of the two species sitting on distinct sets of sites, will be given by $d' = \lambda_z/4 \sim 200$ nm. This may be viewed as a crystal with the original periodicity and a two-atom basis, or as a new crystal structure having half the lattice period, given that the interactions of the probe with the $|r\rangle$ and $|b\rangle$ atoms are

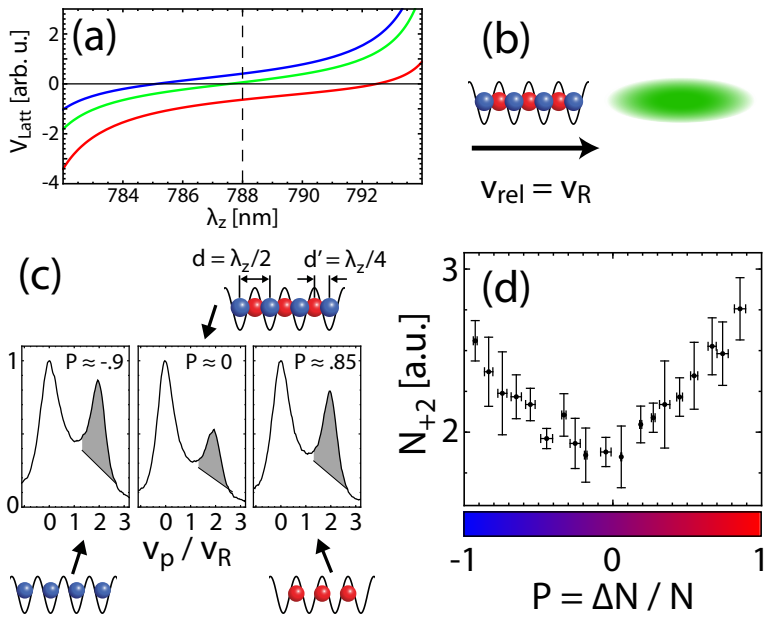

Figure 10.10: Detecting forced antiferromagnetic ordering via matter-wave scattering. (a) Calculated dependence of state-dependent optical lattice depth (in arbitrary units of energy, for σ^+ polarization), of the hyperfine states $|1,-1\rangle$ ($|r\rangle$, red line), $|2,-2\rangle$ ($|b\rangle$, blue line), and $|1,1\rangle$ (probe atoms, green line). Using a lattice of wavelength ~ 788 nm, and for slightly elliptical light, the $|1,1\rangle$ atoms experience a vanishing potential. (b) A stationary cloud of $|1,1\rangle$ atoms is used as a matter-wave probe for a moving crystal of $|r\rangle$ and $|b\rangle$ atoms, attracted to and repelled from intensity maxima of a state-dependent lattice, respectively. (c) Velocity distributions of scattered probe atoms following interaction with a crystal of atoms in a tunable spin-mixture of the $|r\rangle$ and $|b\rangle$ states, moving at a velocity $v_{rel} = -v_R$. Shown are the cases of spin-polarized crystals of nearly all $|r\rangle$ ($P \sim -1$) and $|b\rangle$ ($P \sim 1$) atoms, as well as for an even mixture of the two states ($P \sim 0$). (d) The number of reflected probe atoms [shaded regions in (c)], as a function of the spin imbalance of the target crystal, $P = \Delta N/N$. A distinct minimum is observed for $P = 0$, relating to the case of a spin-mixed crystal with maximal forced antiferromagnetic ordering at spacing $d' = \lambda_z/4$.

approximately the same. This change results in a different diffraction spectrum for the matter wave probes. With the addition of a second species, as scattering centers separated by d give way to those of a smaller spacing d', the original first-order diffraction peak at $v_{rel}/v_R = -1$ will become diminished, and entirely disappear if an equal mixture of the two species uniformly fills the

lattice, with a new first-order peak now occurring at half the momentum-space frequency, $v_{rel}/v_R = -2$.

To probe the mixed-spin crystal, we move it at a constant velocity of $v_{rel}/v_R = -1$ with respect to the probe atoms, for a fixed interaction time of 1 ms. In Fig. 10.10 (a), we show probe velocity distributions in TOF for the three cases $P \sim -1$, 0, and 1. As can be seen, the number of probe atoms out-coupled to $2v_R$ is much lower for the spin mixture ($P = 0$) than for either of the nearly spin-polarized cases. We note that an appreciable number of out-coupled atoms appears even for the balanced spin-mixture, which is most likely due to specular reflection as in the previously studied case, while the presence of unoccupied sites of either the attractive or repulsive lattices may also cause some Bragg diffraction consistent with the original lattice spacing.

To characterize how the crystal structure changes as the population imbalance is continuously tuned, we count the number of probe atoms transferred to a velocity region around $v_p \sim 2v_R$. As a function of the crystal "polarization", the transferred population shows a distinct minimum near $P = 0$ for a balanced mixture, as shown in Fig. 10.10 (b). This example readily demonstrates how matter-wave scattering can be used to detect changes to the crystal structure of an ultracold lattice gas, and through species-selective scattering may eventually be used to detect quantum-magnetic spin-ordered states. Finally, we point out that the full tunability of the wavelength for atomic matter waves should provide a distinct advantage over optical scattering in certain circumstances, namely in studying density structures not formed in optical lattice potentials, such as through self-organization or with magnetic trapping potentials. By using probes of small de Broglie wavelength, this could also include the study of novel quantum states realized at more easily attainable temperatures in systems with smaller characteristic length scales. For example, at fixed lattice depth s and fixed tunneling-to-interaction ratio $(t/U)_c$ (e.g., by control of the scattering length a_s), the Néel temperature T_N, marking the onset of antiferromagnetic ordering, scales with lattice wavelength λ as $T_N \propto \lambda^{-2}$ [286]. For fixed a_s and with variable lattice depth s, an even more favorable scaling is achieved for realistic system parameters, with $T_N \propto \lambda^{-3} \ln^{3/2}[\lambda^{-1}\sqrt{2}\pi a_s(t/U)_c] \sim \lambda^{-2.7}$ for $a_s = 100\ a_0$ and $(t/U)_c = 1/32$. For a more complete determination of the optimal conditions for stabilizing a desired quantum phase, entropy considerations and effects of lattice-cooling [287] should also be taken into account.

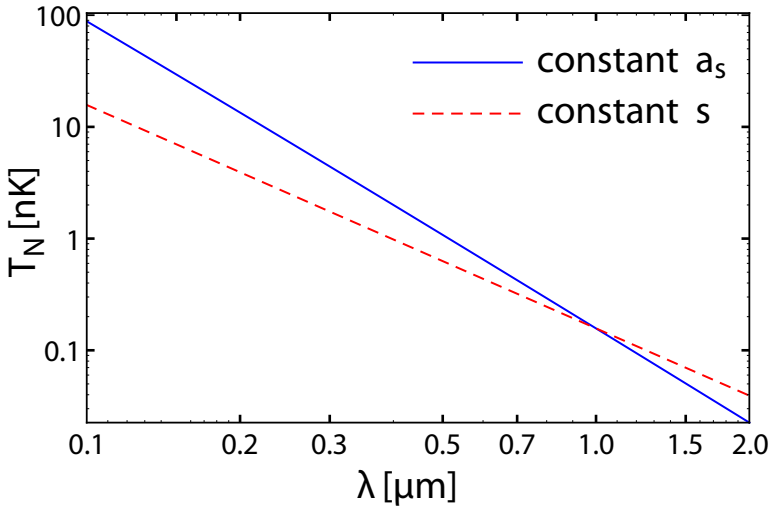

Figure 10.11: Scaling of Néel temperature T_N with lattice wavelength, λ, for fixed interaction-to-tunneling ratio $U/t = 32$. Shown are the cases of (blue line) fixed scattering length $a_s = 100\ a_0$ but variable lattice depth s and (red dashed line) fixed lattice depth $s = 13$ (in units of $E_R = h^2/2m\lambda^2$ but variable scattering length a_s). Scalings of $T_N \propto \lambda^{-2}$ and (roughly, see text) $T_N \propto \lambda^{-2.7}$ are found for the two methods.

10.9 Concluding remarks

In this work, we have demonstrated that matter-wave diffraction can be used to characterize the crystalline structure of strongly correlated atoms in an optical lattice. In the future, these techniques may be extended to the characterization of various novel states of ultracold matter, such as charge- and spin-density waves, magnetically-ordered ground states of quantum gas mixtures, and even self-assembled structures such as Tonks–Girardeau gases of fermionized bosons, Abrikosov vortex lattices [288, 289], and dipolar crystals [290].

10.10 Some experimental details

10.10.1 Hyperfine state mixtures

The initial two-species mixture of probe $|p\rangle \equiv |2,-2\rangle$ and target $|t\rangle \equiv |1,0\rangle$ atoms, used to study in Figs. 10.1, 10.4, 10.5, 10.6 & 10.7 the scattering dependence on s_z, contains a total of $(1.6\pm0.2)\times10^5$ atoms, with 60% of atoms in the target state. For this mixture, a final magnetic bias field of 7.4 G is employed

to suppress $|1,0\rangle \leftrightarrow |1,\pm 1\rangle$ spin-changing collisions. A second binary mixture of probe $|p\rangle \equiv |2,-2\rangle$ and target $|t\rangle \equiv |1,-1\rangle$ atoms is used in conjunction with the moving optical lattice [Figs. 10.2 & 10.3]. This mixture contains a total of $(2.8 \pm 0.5) \times 10^5$ atoms, with 33% target atoms. A three-species mixture of one probe species ($|p\rangle \equiv |1,1\rangle$) and two target species ($|2,-2\rangle$ and $|1,-1\rangle$) is used to study forced antiferromagnetic ordering [Fig. 10.10]. This mixture contains a total of $(1.5 \pm 0.2) \times 10^5$ atoms, with 50% of the atoms in the target. The target, consisting of two different species, has a fully tunable spin composition [c.f. Fig. 10.10 (b)]. The intra- and interspecies scattering lengths for all the states used are approximately equal to 5.3 nm, i.e. the background scattering length for ^{87}Rb atoms.

10.10.2 State-selective lattice potential

The state-selective lattices are formed by interfering two laser beams ($1/e^2$ radius ~ 230 μm , the same polarization) with tunable wavelength between the ^{87}Rb D_1 and D_2 lines to effect a light-shift cancellation for the probe atoms. In the case of a stationary target of $|1,0\rangle$ atoms, the lattice is loaded to a variable depth s_z with an s-shaped curve in 75 ms and held for an additional 5 ms prior to acceleration of the probe atoms. This lattice is made from fully retroreflected laser light of wavelength $\lambda = 785$ nm of σ^+ polarization. For the case of a moving target of $|1,-1\rangle$ atoms (wavelength and polarization as in the stationary case), the lattice is first smoothly loaded in 45 ms to a depth of $s_z = 10$, exceeding the critical depth of the 1D Mott insulator transition, and then loaded in 5 ms to a depth of $s_z = 50$ to freeze the atoms to the sites of the lattice. The lattice is then moved, by introducing a relative frequency detuning of $\delta\omega$ between the forward and retroreflected laser beams comprising the z-lattice, via two acousto-optic modulators driven by phase-locked function generators.

For the case of a spin-mixed crystal with forced antiferromagnetic ordering, the two species are quickly loaded into the state-dependent lattice in 2 ms following creation of the target mixture to avoid spatial separation in a small magnetic field gradient used to separate the probe. The lattice has modulation depths $s_z = 5$ and $s_z = 12$, for the $|b\rangle = |2,-2\rangle$ (repulsive lattice) and $|r\rangle = |1,-1\rangle$ (attractive lattice) atoms, respectively. This lattice is formed with light of wavelength $\lambda \sim 788$ nm, of slightly elliptical polarization. After loading, this lattice is moved at a fixed velocity as above, with a restriction to relatively low velocities to ensure that both target species faithfully follow the optical potential at these modest depths, as observed in the velocity distributions of the target species.

All the lattice depths are calibrated using Kapitza–Dirac atom diffrac-

tion [122], with a systematic uncertainty of about 3%. For probe atoms, the lattice potential is sufficiently "zeroed" even for greatest available optical potentials such that no diffraction is observed for a pulsed-on lattice or for application of a linear potential gradient while the lattice is present (i.e. no Bloch oscillations). To further "zero" the optical lattice, the probe atoms are loaded into 1D tubes, and we either minimize excitations of probe atoms undergoing dipole oscillations, or in the case of a moving lattice we move with velocity of $v_L = v_R$, with no observable transfer of probe atoms to non-zero velocities.

Chapter 11

Conclusion and outlook

In this thesis, I have detailed several experiments studying the equilibrium and dynamical properties of ultracold Bose gases in optical and atomic potentials. We have explored [44] phases of the two-component Bose–Hubbard model, using a binary mixture in a state-dependent optical lattice that allows for independent control of the species' tunneling and on-site interactions. Here, an apparent loss of spatial coherence of a given species was observed, most pronounced when the other species was either a delocalized superfluid or was made up of immobile impurity atoms, consistent with expected formation of polarons due to superfluid immersion [63] in one case, and of a quantum emulsions [47] in the other case. We further studied [46] such quantum emulsions in a fully one-dimensional geometry, and compared the effects of random ("white noise") impurity disorder to the quasi-disorder of a pseudorandom incommensurate lattice. In studying the transition from superfluid to an insulating Bose-glass-like state [28, 48], we found that the loss of superfluid behavior occurred for a much larger mobility (hopping) in the case of random impurity disorder. Moreover, we have introduced [49] a new technique for the characterization of atomic gases in optical lattices, based on the scattering of atomic de Broglie waves. Through inelastic and elastic scattering, we were able to study excitations and the spatial structure of lattice-modulated one-dimensional Bose gases, as well as to detect the introduction of forced antiferromagnetic ordering in an atomic crystal. Lastly, we observed [50] an unusual effect, namely that disorder can induce transport, when a Bose–Einstein condensate was pulsed by two incommensurate standing waves, corresponding to a quantum-to-classical transition in a system of two coupled, kicked quantum rotors [84].

In addition to the topics I have presented in this thesis, several lines of research are currently being undertaken in the laboratory. These include the dynamical screening of disordered potentials due to mean-field interactions (observed through the lifetime of coherent Bloch oscillations in applied

gradients), the use of low-field Feshbach resonances [291, 292] to tune the interspecies scattering length in one-dimensional bosonic mixtures, and the implementation of state-selective dynamical control over the particles' time-averaged band-structure [293] for modification of the tunneling [294–296] and creation of tunable gauge potentials [255].

Moreover, our experimental ability to independently control the localization of different species in an optical lattice lends itself to a number of directions of future research. In an earlier study [44], we observed some indications of possible polaronic coupling when atoms were immersed in a superfluid bath. More focused investigations along these lines, such as to measure directly the induced density "dips" (by modification of Franck-Condon overlaps) through rf spectroscopy [52] or to observe the clustering of polarons through Bragg spectroscopy [63], could be made to study polarons in this system. In a similar system, one can explore the physics of the spin-boson model [232, 297], where coupling of localized atomic "qubits" (with coherent control over e.g., some internal pseudospin or lattice orbital occupation) to a bosonic bath can lead to local dissipation and also long-range interactions between the "qubits". I certainly look forward to seeing the interesting physics that will come out of this lab for years to come.

Bibliography

[1] A. Einstein. Quantentheorie des einatomigen idealen Gases. *Sitzungsber. Preuss. Akad.*, pages 261–267, 1924.

[2] S. N. Bose. Plancks Gesetz und Lichtquantenhypothese. *Z. Phys.*, 26: 178–181, 1924.

[3] F. Dalfovo, S. Giorgini, L. P. Pitaevskii, and S. Stringari. Theory of Bose–Einstein condensation in trapped gases. *Rev. Mod. Phys.*, 71:463–512, 1999.

[4] M. H. Anderson, J. R. Ensher, M. R. Matthews, C. E. Wieman, and E. A. Cornell. Observation of Bose–Einstein condensation in a dilute atomic vapor. *Science*, 269:198–201, 1995.

[5] K. B. Davis, M. O. Mewes, M. R. Andrews, N. J. van Druten, D. S. Durfee, D. M. Kurn, and W. Ketterle. Bose–Einstein condensation in a gas of sodium atoms. *Phys. Rev. Lett.*, 75:3969–3973, 1995.

[6] C. C. Bradley, C. A. Sackett, J. J. Tollett, and R. G. Hulet. Evidence of Bose–Einstein condensation in an atomic gas with attractive interactions. *Phys. Rev. Lett.*, 75:1687–1690, 1995.

[7] C. C. Bradley, C. A. Sackett, and R. G. Hulet. Bose–Einstein condensation of lithium: Observation of limited condensate number. *Phys. Rev. Lett.*, 78:985–989, 1997.

[8] B. DeMarco and D. S. Jin. Onset of Fermi degeneracy in a trapped atomic gas. *Science*, 285:1703–1706, 1999.

[9] S. Giorgini, L. P. Pitaevskii, and S. Stringari. Theory of ultracold atomic Fermi gases. *Rev. Mod. Phys.*, 80:1215–1274, 2008.

[10] S. Jochim, M. Bartenstein, A. Altmeyer, G. Hendl, S. Riedl, C. Chin, J. Hecker Denschlag, and R. Grimm. Bose–Einstein condensation of molecules. *Science*, 302:2101–2103, 2003.

[11] M. Greiner, C. A. Regal, and D. S. Jin. Emergence of a molecular Bose-Einstein condensate from a Fermi gas. *Nature*, 426:537–540, 2003.

[12] M. W. Zwierlein, C. A. Stan, C. H. Schunck, S. M. F. Raupach, S. Gupta, Z. Hadzibabic, and W. Ketterle. Observation of Bose–Einstein condensation of molecules. *Phys. Rev. Lett.*, 91:250401, 2003.

[13] K.-K. Ni, S. Ospelkaus, D. Wang, G. Quemener, B. Neyenhuis, M. H. G. de Miranda, J. L. Bohn, J. Ye, and D. S. Jin. Dipolar collisions of polar molecules in the quantum regime. *Nature*, 464:1324–1328, 2010.

[14] S. Ospelkaus, K.-K. Ni, D. Wang, M. H. G. de Miranda, B. Neyenhuis, G. Quéméner, P. S. Julienne, J. L. Bohn, D. S. Jin, and J. Ye. Quantum-state controlled chemical reactions of ultracold potassium-rubidium molecules. *Science*, 327:853–857, 2010.

[15] A. L. Fetter. Rotating trapped Bose–Einstein condensates. *Rev. Mod. Phys.*, 81:647–691, 2009.

[16] W. Ketterle and S. Inouye. Collective enhancement and suppression in Bose–Einstein condensates. *C. R. Acad. Sci. Paris - Serie IV*, 2: 339–380, 2001.

[17] S. L. Rolston and W. D. Phillips. Nonlinear and quantum atom optics. *Nature*, 416:219–224, 2002.

[18] O. Morsch and M. Oberthaler. Dynamics of Bose-Einstein condensates in optical lattices. *Rev. Mod. Phys.*, 78:179–215, 2006.

[19] C. Chin, R. Grimm, P. Julienne, and E. Tiesinga. Feshbach resonances in ultracold gases. *Rev. Mod. Phys.*, 82:1225–1286, 2010.

[20] T. Kraemer, M. Mark, P. Waldburger, J. G. Danzl, C. Chin, B. Engeser, A. D. Lange, K. Pilch, A. Jaakkola, H.-C. Nägerl, and R. Grimm. Evidence for Efimov quantum states in an ultracold gas of caesium atoms. *Nature*, 440:315–318, 2006.

[21] M. Bartenstein, A. Altmeyer, S. Riedl, S. Jochim, C. Chin, J. Hecker Denschlag, and R. Grimm. Crossover from a molecular Bose–Einstein condensate to a degenerate Fermi gas. *Phys. Rev. Lett.*, 92:120401, 2004.

[22] J. Kinast, S. L. Hemmer, M. E. Gehm, A. Turlapov, and J. E. Thomas. Evidence for superfluidity in a resonantly interacting Fermi gas. *Phys. Rev. Lett.*, 92:150402, 2004.

[23] G. B. Partridge, K. E. Strecker, R. I. Kamar, M. W. Jack, and R. G. Hulet. Molecular probe of pairing in the BEC-BCS crossover. *Phys. Rev. Lett.*, 95:020404, 2005.

[24] M. W. Zwierlein, J. R. Abo-Shaeer, A. Schirotzek, C. H. Schunk, and W. Ketterle. Vortices and superfluidity in a strongly interacting Fermi gas. *Nature*, 435:1047–1051, 2005.

[25] M. Lewenstein, A. Sanpera, V. Ahufinger, B. Damski, Sen(De) A., and U. Sen. Ultracold atomic gases in optical lattices: mimicking condensed matter physics and beyond. *Adv. Phys.*, 56:243–379, 2007.

[26] I. Bloch, J. Dalibard, and W. Zwerger. Many-body physics with ultracold gases. *Rev. Mod. Phys.*, 80:885–964, 2008.

[27] M. Greiner, O. Mandel, T. Esslinger, T. W. Hänsch, and I. Bloch. Quantum phase transition from a superfluid to a Mott insulator in a gas of ultracold atoms. *Nature*, 415:39, 2002.

[28] M. P. A. Fisher, P. B. Weichman, G. Grinstein, and D. S. Fisher. Boson localization and the superfluid-insulator transition. *Phys. Rev. B*, 40: 546–570, 1989.

[29] D. Jaksch, C. Bruder, J. I. Cirac, C. W. Gardiner, and P. Zoller. Cold bosonic atoms in optical lattices. *Phys. Rev. Lett.*, 81:3108–3111, 1998.

[30] R. Jördens, N. Strohmaier, K. Günter, H. Moritz, and T. Esslinger. A Mott insulator of fermionic atoms in an optical lattice. *Nature*, 455: 204–207, 2008.

[31] E. Haller, R. Hart, M. J. Mark, J. G. Danzl, L. Reichsöllner, M. Gustavsson, M. Dalmonte, G. Pupillo, and H.-C. Nägerl. Pinning quantum phase transition for a Luttinger liquid of strongly interacting bosons. *Nature*, 466:597, 2010.

[32] J. Simon, W. S. Bakr, R. Ma, M. E. Tai, P. M. Preiss, and M. Greiner. Quantum simulation of antiferromagnetic spin chains in an optical lattice. *Nature*, 472:307–312, 2011.

[33] G. Roati, C. D'Errico, L. Fallani, M. Fattori, C. Fort, M. Zaccanti, G. Modugno, M. Modugno, and M. Inguscio. Anderson localization of a non-interacting Bose–Einstein condensate. *Nature*, 453:895, 2008.

[34] J. Billy, V. Josse, Z. Zuo, A. Bernard, B. Hambrecht, P. Lugan, D. Clément, L. Sanchez-Palencia, P. Bouyer, and A. Aspect. Direct observation of Anderson localization of matter waves in a controlled disorder. *Nature*, 453:891, 2008.

[35] K. Baumann, C. Guerlin, F. Brennecke, and T. Esslinger. Dicke quantum phase transition with a superfluid gas in an optical cavity. *Nature*, 464: 1301–1306, 2010.

[36] C. Trefzger, C. Menotti, B. Capogrosso-Sansone, and M. Lewenstein. Ultracold dipolar gases in optical lattices. *J. Phys. B: At. Mol. Opt. Phys.*, 44:193001, 2011.

[37] L. Sanchez-Palencia and M. Lewenstein. Disordered quantum gases under control. *Nature Phys.*, 6:87, 2010.

[38] J. Dalibard, F. Gerbier, G. Juzeliūnas, and P. Öhberg. *Colloquium*: Artificial gauge potentials for neutral atoms. *Rev. Mod. Phys.*, 83:1523–1543, 2011.

[39] S. Sachdev. Quantum magnetism and criticality. *Nature Phys.*, 4:173–185, 2008.

[40] A. Polkovnikov, K. Sengupta, A. Silva, and M. Vengalattore. *Colloquium*: Nonequilibrium dynamics of closed interacting quantum systems. *Rev. Mod. Phys.*, 83:863–883, 2011.

[41] G. Lemarié, H. Lignier, D. Delande, P. Szriftgiser, and J. C. Garreau. Critical state of the Anderson transition: Between a metal and an insulator. *Phys. Rev. Lett.*, 105:090601, 2010.

[42] X. Zhang, C.-L. Hung, S.-K. Tung, and C. Chin. Observation of quantum criticality with ultracold atoms in optical lattices. *Science*, 335:1070–1072, 2012.

[43] M. Endres, T. Fukuhara, D. Pekker, M. Cheneau, P. Schauß, C. Gross, E. Demler, S. Kuhr, and I. Bloch. The 'Higgs' amplitude mode at the two-dimensional superfluid-Mott insulator transition. *arXiv:1204.5183v2*, 2012.

[44] B. Gadway, D. Pertot, R. Reimann, and D. Schneble. Superfluidity of interacting bosonic mixtures in optical lattices. *Phys. Rev. Lett.*, 105: 045303, 2010.

[45] D. A. Pertot. *Two-Component Bosons in State-Dependent Optical Lattices*. PhD thesis, Stony Brook University, 2011.

[46] B. Gadway, D. Pertot, J. Reeves, M. Vogt, and D. Schneble. Glassy behavior in a binary atomic mixture. *Phys. Rev. Lett.*, 107:145306, 2011.

[47] T. Roscilde and J. I. Cirac. Quantum emulsion: A glassy phase of bosonic mixtures in optical lattices. *Phys. Rev. Lett.*, 98:190402, 2007.

[48] T. Giamarchi and H. J. Schulz. Anderson localization and interactions in one-dimensional metals. *Phys. Rev. B*, 37:325–340, 1988.

[49] B. Gadway, D. Pertot, J. Reeves, and D. Schneble. Probing an ultracold-atom crystal with matter waves. *Nature Phys.*, 8:544–549, 2012.

[50] B. Gadway, J. Reeves, L. Krinner, and D. Schneble. Quantum dynamics of matter waves in a pulsed disordered lattice. *arXiv:1203.3177v1*, 2012.

[51] J. Catani, L. De Sarlo, G. Barontini, F. Minardi, and M. Inguscio. Degenerate Bose-Bose mixture in a three-dimensional optical lattice. *Phys. Rev. A*, 77:011603, 2008.

[52] P. Soltan-Panahi, J. Struck, P. Hauke, A. Bick, W. Plenkers, G. Meineke, C. Becker, P. Windpassinger, M. Lewenstein, and K. Sengstock. Multi-component quantum gases in spin-dependent hexagonal lattices. *Nature Phys.*, 7:434–440, 2011.

[53] P. Soltan-Panahi, D.-S. Lühmann, J. Struck, P. Windpassinger, and K. Sengstock. Quantum phase transition to unconventional multi-orbital superfluidity in optical lattices. *Nature Phys.*, 8:71–75, 2012.

[54] S. Ospelkaus, C. Ospelkaus, O. Wille, M. Succo, P. Ernst, K. Sengstock, and K. Bongs. Localization of bosonic atoms by fermionic impurities in a three-dimensional optical lattice. *Phys. Rev. Lett.*, 96:180403, 2006.

[55] K. Günter, T. Stöferle, H. Moritz, M. Köhl, and T. Esslinger. Bose-Fermi mixtures in a three-dimensional optical lattice. *Phys. Rev. Lett.*, 96:180402, 2006.

[56] Th. Best, S. Will, U. Schneider, L. Hackermüller, D. van Oosten, I. Bloch, and D.-S. Lühmann. Role of interactions in ^{87}Rb-^{40}**K** Bose-Fermi mixtures in a 3D optical lattice. *Phys. Rev. Lett.*, 102:030408, 2009.

[57] S. Sugawa, K. Inaba, S. Taie, R. Yamazaki, M. Yamashita, and Y. Takahashi. Interaction and filling-induced quantum phases of dual Mott insulators of bosons and fermions. *Nature Phys.*, 7:642–648, 2011.

[58] A. V. Gorshkov, M. Hermele, V. Gurarie, C. Xu, P. S. Julienne, J. Ye, P. Zoller, E. Demler, M. D. Lukin, and A. M. Rey. Two-orbital SU(N) magnetism with ultracold alkaline-earth atoms. *Nature Phys.*, 6:289–295, 2010.

[59] L.-M. Duan, E. Demler, and M. D. Lukin. Controlling spin exchange interactions of ultracold atoms in optical lattices. *Phys. Rev. Lett.*, 91: 090402, 2003.

[60] A. B. Kuklov and B. V. Svistunov. Counterflow superfluidity of two-species ultracold atoms in a commensurate optical lattice. *Phys. Rev. Lett.*, 90:100401, 2003.

[61] E. Altman, W. Hofstetter, E. Demler, and M. D. Lukin. Phase diagram of two-component bosons on an optical lattice. *New J. Phys.*, 5:113, 2003.

[62] A. Isacsson, M.-C. Cha, K. Sengupta, and S. M. Girvin. Superfluid-insulator transitions of two-species bosons in an optical lattice. *Phys. Rev. B*, 72:184507, 2005.

[63] M. Bruderer, A. Klein, S. R. Clark, and D. Jaksch. Polaron physics in optical lattices. *Phys. Rev. A*, 76:011605, 2007.

[64] S. G. Söyler, B. Capogrosso-Sansone, N. V. Prokof'ev, and B. V. Svistunov. Sign-alternating interaction mediated by strongly correlated lattice bosons. *New J. Phys.*, 11:073036, 2009.

[65] L. Mathey, I. Danshita, and C. W. Clark. Creating a supersolid in one-dimensional Bose mixtures. *Phys. Rev. A*, 79:011602, 2009.

[66] U. Gavish and Y. Castin. Matter-wave localization in disordered cold atom lattices. *Phys. Rev. Lett.*, 95:020401, 2005.

[67] B. Paredes, F. Verstraete, and J. I. Cirac. Exploiting quantum parallelism to simulate quantum random many-body systems. *Phys. Rev. Lett.*, 95:140501, 2005.

[68] L. Fallani, J. E. Lye, V. Guarrera, C. Fort, and M. Inguscio. Ultracold atoms in a disordered crystal of light: Towards a Bose glass. *Phys. Rev. Lett.*, 98:130404, 2007.

[69] M. White, M. Pasienski, D. McKay, S. Q. Zhou, D. Ceperley, and B. DeMarco. Strongly interacting bosons in a disordered optical lattice. *Phys. Rev. Lett.*, 102:055301, 2009.

[70] P. Buonsante, S. M. Giampaolo, F. Illuminati, V. Penna, and A. Vezzani. Mixtures of strongly interacting bosons in optical lattices. *Phys. Rev. Lett.*, 100:240402, 2008.

[71] B. Horstmann, S. Dürr, and T. Roscilde. Localization of cold atoms in state-dependent optical lattices via a Rabi pulse. *Phys. Rev. Lett.*, 105: 160402, 2010.

[72] S. S. Kondov, W. R. McGehee, J. J. Zirbel, and B. DeMarco. Three-dimensional Anderson localization of ultracold matter. *Science*, 334: 66–68, 2011.

[73] F. Jendrzejewski, A. Bernard, K. Müller, P. Cheinet, V. Josse, M. Piraud, L. Pezzé, L. Sanchez-Palencia, A. Aspect, and P. Bouyer. Three-dimensional localization of ultracold atoms in an optical disordered potential. *Nature Phys.*, 8:398–403, 2012.

[74] B. Deissler, M. Zaccanti, G. Roati, C. D'Errico, M. Fattori, M. Modugno, G. Modugno, and M. Inguscio. Delocalization of a disordered bosonic system by repulsive interactions. *Nature Phys.*, 6:354, 2010.

[75] M. Pasienski, D. McKay, M. White, and B. DeMarco. A disordered insulator in an optical lattice. *Nature Phys.*, 6:677, 2010.

[76] N. Gemelke, X. Zhang, C.-L. Hung, and C. Chin. *In-situ* observation of incompressible Mott-insulating domains in ultracold atomic gases. *Nature*, 460:995–998, 2009.

[77] W. S. Bakr, A. Peng, M. E. Tai, R. Ma, J. Simon, J. I. Gillen, S. Fölling, L. Pollet, and M. Greiner. Probing the superfluid-to-Mott insulator transition at the single-atom level. *Science*, 329:547–550, 2010.

[78] J. F. Sherson, C. Weitenberg, M. Endres, M. Cheneau, I. Bloch, and S. Kuhr. Single-atom-resolved fluorescence imaging of an atomic Mott insulator. *Nature*, 467:68–72, 2010.

[79] T. Gericke, P. Würtz, D. Reitz, T. Langen, and H. Ott. High-resolution scanning electron microscopy of an ultracold quantum gas. *Nature Phys.*, 4:949–953, 2008.

[80] S. N. Sanders, F. Mintert, and E. J. Heller. Matter-wave scattering from ultracold atoms in an optical lattice. *Phys. Rev. Lett.*, 105:035301, 2010.

[81] N. Bohr. Über die Serienspektra der Elemente. *Zeitschrift für Physik*, 2:423–478, 1920.

[82] F. L. Moore, J. C. Robinson, C. F. Bharucha, Bala Sundaram, and M. G. Raizen. Atom optics realization of the quantum δ-kicked rotor. *Phys. Rev. Lett.*, 75:4598–4601, 1995.

[83] D. R. Grempel, R. E. Prange, and S. Fishman. Quantum dynamics of a nonintegrable system. *Phys. Rev. A*, 29:1639–1647, 1984.

[84] S. Adachi, M. Toda, and K. Ikeda. Quantum-classical correspondence in many-dimensional quantum chaos. *Phys. Rev. Lett.*, 61:659–661, 1988.

[85] F. London. The δ-phenomenon of liquid helium and the Bose–Einstein degeneracy. *Nature*, 141:643–644, 1938.

[86] H. J. Metcalf and P. van der Straten. *Laser Cooling and Trapping.* Springer-Verlag, New York, 1999.

[87] S. Chu. Nobel lecture: The manipulation of neutral particles. *Rev. Mod. Phys.*, 70:685–706, 1998.

[88] C. N. Cohen-Tannoudji. Nobel lecture: Manipulating atoms with photons. *Rev. Mod. Phys.*, 70:707–719, 1998.

[89] W. D. Phillips. Nobel lecture: Laser cooling and trapping of neutral atoms. *Rev. Mod. Phys.*, 70:721–741, 1998.

[90] W. Petrich, M. H. Anderson, J. R. Ensher, and E. A. Cornell. Stable, tightly confining magnetic trap for evaporative cooling of neutral atoms. *Phys. Rev. Lett.*, 74:3352–3355, 1995.

[91] N. Masuhara, J. M. Doyle, J. C. Sandberg, D. Kleppner, T. J. Greytak, H. F. Hess, and G. P. Kochanski. Evaporative cooling of spin-polarized atomic hydrogen. *Phys. Rev. Lett.*, 61:935–938, 1988.

[92] K. B. Davis, M.-O. Mewes, M. A. Joffe, M. R. Andrews, and W. Ketterle. Evaporative cooling of sodium atoms. *Phys. Rev. Lett.*, 74:5202–5205, 1995.

[93] E. A. Cornell and C. E. Wieman. Nobel lecture: Bose–Einstein condensation in a dilute gas, the first 70 years and some recent experiments. *Rev. Mod. Phys.*, 74:875–893, 2002.

[94] W. Ketterle. Nobel lecture: When atoms behave as waves: Bose–Einstein condensation and the atom laser. *Rev. Mod. Phys.*, 74:1131–1151, 2002.

[95] M. Inguscio, S. Stringari, and *eds.* C. Wieman. Bose–Einstein Condensation in Atomic Gases, Proceedings of the International School of Physics "Enrico Fermi" Course CXL. IOS Press, Amsterdam, 1999.

[96] C. J. Pethick and H. Smith. *Bose–Einstein Condensation in Dilute Gases*. Cambridge University Press, New York, 2008.

[97] T. D. Lee and C. N. Yang. Low-temperature behavior of a dilute Bose system of hard spheres. I. equilibrium properties. *Phys. Rev.*, 112:1419–1429, 1958.

[98] E. P. Gross. Structure of a quantized vortex in boson systems. *Nuovo Cimento*, 20:451, 1961.

[99] L. P. Pitaevskii. Vortex lines in an imperfect Bose gas. *Sov. Phys. JETP*, 13:451, 1961.

[100] E. A. Donley, N. R. Claussen, S. L. Cornish, J. L. Roberts, E. A. Cornell, and C. E. Wieman. Dynamics of collapsing and exploding Bose-Einstein condensates. *Nature*, 412:295–299, 2001.

[101] S. Chu, J. E. Bjorkholm, A. Ashkin, and A. Cable. Experimental observation of optically trapped atoms. *Phys. Rev. Lett.*, 57:314–317, 1986.

[102] A. Ashkin. Optical trapping and manipulation of neutral particles using lasers. *Proc. Natl. Acad. Sci. USA*, 94:48534860, 1997.

[103] C. Cohen-Tannoudji, J. Dupont-Roc, and G. Grynberg. *Atom - Photon Interactions: Basic Process and Appilcations*. Wiley-VCH Verlag GmbH, Weinheim, Germany, 2008.

[104] D. Jaksch. *Bose–Einstein condensation and Applications*. PhD thesis, Universität Innsbruck, 1999.

[105] M. Greiner. *Ultracold quantum gases in three-dimensional optical lattice potentials*. PhD thesis, Ludwig-Maximilians-Universität München, 2003.

[106] N. W. Ashcroft and N. D. Mermin. *Solid State Physics*. Holt–Saunders International Editions, London, 1976.

[107] W. Zwerger. Mott-Hubbard transition of cold atoms in optical lattices. *J. Opt. B: Quantum Semiclass. Opt.*, 5:S9–S16, 2003.

[108] S. G. Albert. Cooling, trapping, and transport of atom clouds in a new BEC apparatus. Master's thesis, Stony Brook University, 2007.

[109] D. G. Greif. Evaporative cooling and Bose–Einstein condensation of Rb-87 in a moving-coil TOP trap geometry. Master's thesis, Stony Brook University, 2007.

[110] D. E. Sproles. Laser spectroscopy and magneto-optical trapping of rubidium atoms. Master's thesis, Stony Brook University, 2008.

[111] D. Pertot, D. Greif, S. Albert, B. Gadway, and D. Schneble. Versatile transporter apparatus for experiments with optically trapped Bose–Einstein condensates. *J. Phys. B: At. Mol. Opt. Phys.*, 42:215305, 2009.

[112] B. P. Anderson and M. A. Kasevich. Loading a vapor-cell magneto-optic trap using light-induced atom desorption. *Phys. Rev. A*, 63:023404, 2001.

[113] D. A. Steck. Rubidium 87 D line data. available online at `http://http://steck.us/alkalidata`. (revision 2.1.4, 23 December 2010).

[114] R. H. Reimann. Quantum gases in state-dependent optical potentials. Master's thesis, Stony Brook University, 2009.

[115] Yu. B. Ovchinnikov, J. H. Müller, M. R. Doery, E. J. D. Vredenbregt, K. Helmerson, S. L. Rolston, and W. D. Phillips. Diffraction of a released Bose-Einstein condensate by a pulsed standing light wave. *Phys. Rev. Lett.*, 83:284–287, 1999.

[116] P. L. Kapitza and P. A. M. Dirac. The reflection of electrons from standing light waves. *Proc. Cambridge Phil. Soc.*, 29:297, 1933.

[117] P. L. Gould, G. A. Ruff, and D. E. Pritchard. Diffraction of atoms by light: The near-resonant Kapitza-Dirac effect. *Phys. Rev. Lett.*, 56: 827–830, 1986.

[118] S. Dürr, S. Kunze, and G. Rempe. Pendellösung oscillations in second-order Bragg scattering of atoms from a standing light wave. *Quantum Semiclass. Opt.*, 8:531, 1996.

[119] T. Müller, S. Fölling, A. Widera, and I. Bloch. State preparation and dynamics of ultracold atoms in higher lattice orbitals. *Phys. Rev. Lett.*, 99:200405, 2007.

[120] W. R. Klein and B. D. Cook. Unified approach to ultrasonic light diffraction. *IEEE Trans. Sonics and Ultrasonics*, 14:123, 1967.

[121] H. Batelaan. *Colloquium*: Illuminating the Kapitza-Dirac effect with electron matter optics. *Rev. Mod. Phys.*, 79:929–941, 2007.

[122] B. Gadway, D. Pertot, R. Reimann, M. G. Cohen, and D. Schneble. Analysis of Kapitza–Dirac diffraction patterns beyond the Raman–Nath regime. *Opt. Express*, 17:19173, 2009.

[123] M. Greiner, I. Bloch, O. Mandel, T. W. Hänsch, and T. Esslinger. Exploring phase coherence in a 2D lattice of Bose–Einstein condensates. *Phys. Rev. Lett.*, 87:160405, 2001.

[124] C. Adams, M. Sigel, and J. Mlynek. Atom optics. *Phys. Rep.*, 240:143, 1994.

[125] P. Meystre. *Atom Optics*. Springer-Verlag, New York, 2001.

[126] D. L. Freimund and H. Batelaan. Bragg scattering of free electrons using the Kapitza-Dirac effect. *Phys. Rev. Lett.*, 89:283602, 2002.

[127] S. B. Cahn, A. Kumarakrishnan, U. Shim, T. Sleator, P. R. Berman, and B. Dubetsky. Time-domain de Broglie wave interferometry. *Phys. Rev. Lett.*, 79:784–787, 1997.

[128] P. Berman. *Atom Interferometry*. Academic Press, San Diego, 1997.

[129] J. Hecker Denschlag, J. E. Simsarian, H. Häffner, C. McKenzie, A. Browaeys, D. Cho, K. Helmerson, S. L. Rolston, and W. D. Phillips. A Bose-Einstein condensate in an optical lattice. *J. Phys. B: At. Mol. Opt. Phys.*, 35:3095, 2002.

[130] J. H. Huckans, I. B. Spielman, B. Laburthe Tolra, W. D. Phillips, and J. V. Porto. Quantum and classical dynamics of a Bose-Einstein condensate in a large-period optical lattice. *Phys. Rev. A*, 80:043609, 2009.

[131] J. Stenger, S. Inouye, A. P. Chikkatur, D. M. Stamper-Kurn, D. E. Pritchard, and W. Ketterle. Bragg spectroscopy of a Bose-Einstein condensate. *Phys. Rev. Lett.*, 82:4569–4573, 1999.

[132] S. Gupta, K. Dieckmann, Z. Hadzibabic, and D. E. Pritchard. Contrast interferometry using Bose-Einstein condensates to measure h/m and α. *Phys. Rev. Lett.*, 89:140401, 2002.

[133] G. K. Campbell, A. E. Leanhardt, J. Mun, M. Boyd, E. W. Streed, W. Ketterle, and D. E. Pritchard. Photon recoil momentum in dispersive media. *Phys. Rev. Lett.*, 94:170403, 2005.

[134] S. Inouye, A. P. Chikkatur, D. M. Stamper-Kurn, J. Stenger, D. E. Pritchard, and W. Ketterle. Superradiant Rayleigh scattering from a Bose–Einstein condensate. *Science*, 285:571, 1999.

[135] D. Schneble, Y. Torii, M. Boyd, E. W. Streed, D. E. Pritchard, and W. Ketterle. The onset of matter-wave amplification in a superradiant Bose–Einstein condensate. *Science*, 300:457, 2003.

[136] P. J. Martin, B. G. Oldaker, A. H. Miklich, and D. E. Pritchard. Bragg scattering of atoms from a standing light wave. *Phys. Rev. Lett.*, 60: 515–518, 1988.

[137] S. Gupta, A. E. Leanhardt, A. D. Cronin, and D. E. Pritchard. Coherent manipulation of atoms with standing light waves. *C.R. Acad. Sci. Paris*, 2:497, 2001.

[138] R. J. Cook and A. F. Bernhardt. Deflection of atoms by a resonant standing electromagnetic wave. *Phys. Rev. A*, 18:2533–2537, 1978.

[139] M. Cristiani, O. Morsch, J. H. Müller, D. Ciampini, and E. Arimondo. Experimental properties of Bose-Einstein condensates in one-dimensional optical lattices: Bloch oscillations, Landau-Zener tunneling, and mean-field effects. *Phys. Rev. A*, 65:063612, 2002.

[140] G. Casati, J. Ford, B. Chirikov, and F. Izraelev. *Stochastic Behavior in Classical and Quantum* H*amiltonian Systems*, page 334. Springer, New York, 1979.

[141] T. Hogg and B. A. Huberman. Recurrence phenomena in quantum dynamics. *Phys. Rev. Lett.*, 48:711–714, 1982.

[142] S. Fishman, D. R. Grempel, and R. E. Prange. Chaos, quantum recurrences, and Anderson localization. *Phys. Rev. Lett.*, 49:509–512, 1982.

[143] P. W. Anderson. Absence of diffusion in certain random lattices. *Phys. Rev.*, 109:1492–1505, 1958.

[144] E. J. Galvez, B. E. Sauer, L. Moorman, P. M. Koch, and D. Richards. Microwave ionization of H atoms: Breakdown of classical dynamics for high frequencies. *Phys. Rev. Lett.*, 61:2011–2014, 1988.

[145] L. Deng, E. W. Hagley, J. Denschlag, J. E. Simsarian, Mark Edwards, Charles W. Clark, K. Helmerson, S. L. Rolston, and W. D. Phillips. Temporal, matter-wave-dispersion Talbot effect. *Phys. Rev. Lett.*, 83: 5407–5411, 1999.

[146] C. Ryu, M. F. Andersen, A. Vaziri, M. B. d'Arcy, J. M. Grossman, K. Helmerson, and W. D. Phillips. High-order quantum resonances observed in a periodically kicked Bose–Einstein condensate. *Phys. Rev. Lett.*, 96:160403, 2006.

[147] A. Romanelli, A. Auyuanet, R. Siri, G. Abal, and R. Donangelo. Generalized quantum walk in momentum space. *Physica A*, 352:409–418, 2005.

[148] A. Romanelli, R. Siri, and V. Micenmacher. Sub-ballistic behavior in quantum systems with Lévy noise. *Phys. Rev. E*, 76:037202, 2007.

[149] A. M. García-García and J. Wang. Anderson transition in quantum chaos. *Phys. Rev. Lett.*, 94:244102, 2005.

[150] D. L. Shepelyansky. *Physica*, 8D:208, 1983.

[151] E. Ott, T. M. Antonsen, and J. D. Hanson. Effect of noise on time-dependent quantum chaos. *Phys. Rev. Lett.*, 53:2187–2190, 1984.

[152] G. Casati, I. Guarneri, and D. L. Shepelyansky. Anderson transition in a one-dimensional system with three incommensurate frequencies. *Phys. Rev. Lett.*, 62:345–348, 1989.

[153] R. Graham and A. R. Kolovsky. Dynamical localization for a kicked atom in two standing waves. *Phys. Lett. A*, 222:47–49, 1996.

[154] F. Benvenuto, G. Casati, A. S. Pikovsky, and D. L. Shepelyansky. Manifestations of classical and quantum chaos in nonlinear wave propagation. *Phys. Rev. A*, 44:R3423–R3426, 1991.

[155] D. L. Shepelyansky. Delocalization of quantum chaos by weak nonlinearity. *Phys. Rev. Lett.*, 70:1787–1790, 1993.

[156] C. Zhang, J. Liu, M. G. Raizen, and Q. Niu. Transition to instability in a kicked Bose–Einstein condensate. *Phys. Rev. Lett.*, 92:054101, 2004.

[157] G. J. Duffy, A. S. Mellish, K. J. Challis, and A. C. Wilson. Nonlinear atom-optical δ-kicked harmonic oscillator using a Bose–Einstein condensate. *Phys. Rev. A*, 70:041602, 2004.

[158] W. H. Zurek. Decoherence and the transition from quantum to classical. *Physics Today*, 44:36–44, 1991.

[159] B. G. Klappauf, W. H. Oskay, D. A. Steck, and M. G. Raizen. Observation of noise and dissipation effects on dynamical localization. *Phys. Rev. Lett.*, 81:1203–1206, 1998.

[160] M. B. d'Arcy, R. M. Godun, M. K. Oberthaler, D. Cassettari, and G. S. Summy. Quantum enhancement of momentum diffusion in the delta-kicked rotor. *Phys. Rev. Lett.*, 87:074102, 2001.

[161] M. B. d'Arcy, R. M. Godun, M. K. Oberthaler, G. S. Summy, K. Burnett, and S. A. Gardiner. Approaching classicality in quantum accelerator modes through decoherence. *Phys. Rev. E*, 64:056233, 2001.

[162] T. Schwartz, G. Bartal, S. Fishman, and M. Segev. Transport and Anderson localization in disordered two-dimensional photonic lattices. *Nature*, 446:52–55, 2007.

[163] L. Levi, M. Rechtsman, B. Freedman, T. Schwartz, O. Manela, and M. Segev. Disorder-enhanced transport in photonic quasicrystals. *Science*, 332:1541–1544, 2011.

[164] S. Aubry and G. André. Analyticity breaking and Anderson localization in incommensurate lattices. *Ann. Israel Phys. Soc.*, 3:133–140, 1980.

[165] T. Geisel, G. Radons, and J. Rubner. Kolmogorov–Arnol'd-Moser barriers in the quantum dynamics of chaotic systems. *Phys. Rev. Lett.*, 57: 2883–2886, 1986.

[166] G. Lemarié, J. Chabé, P. Szriftgiser, J. C. Garreau, B. Grémaud, and D. Delande. Observation of the Anderson metal-insulator transition with atomic matter waves: Theory and experiment. *Phys. Rev. A*, 80:043626, 2009.

[167] J. Ringot, P. Szriftgiser, J. C. Garreau, and D. Delande. Experimental evidence of dynamical localization and delocalization in a quasiperiodic driven system. *Phys. Rev. Lett.*, 85:2741–2744, 2000.

[168] J. Chabé, G. Lemarié, B. Grémaud, D. Delande, P. Szriftgiser, and J. C. Garreau. Experimental observation of the Anderson metal-insulator transition with atomic matter waves. *Phys. Rev. Lett.*, 101:255702, 2008.

[169] C. Tian, A. Altland, and M. Garst. Theory of the Anderson transition in the quasiperiodic kicked rotor. *Phys. Rev. Lett.*, 107:074101, 2011.

[170] E. Abrahams, P. W. Anderson, D. C. Licciardello, and T. V. Ramakrishnan. Scaling theory of localization: Absence of quantum diffusion in two dimensions. *Phys. Rev. Lett.*, 42:673–676, 1979.

[171] S. Wimberger, I. Guarneri, and S. Fishman. Quantum resonances and decoherence for delta-kicked atoms. *Nonlinearity*, 16:1381, 2003.

[172] P. L. Kapitza. Dynamic stability of the pendulum with vibrating suspension point. *Sov. Phys. JETP*, 21:588–597, 1951.

[173] R. Lima and D. Shepelyansky. Fast delocalization in a model of quantum kicked rotator. *Phys. Rev. Lett.*, 67:1377–1380, 1991.

[174] I. Dana. Quantum suppression of diffusion on stochastic webs. *Phys. Rev. Lett.*, 73:1609–1612, 1994.

[175] J. P. Dahlhaus, J. M. Edge, J. Tworzydło, and C. W. J. Beenakker. Quantum Hall effect in a one-dimensional dynamical system. *Phys. Rev. B*, 84:115133, 2011.

[176] C. Orzel, A. K. Tuchman, M. L. Fenselau, M. Yasuda, and M. A. Kasevich. Squeezed states in a Bose–Einstein condensate. *Science*, 291:2386, 2001.

[177] M. J. Mark, E. Haller, K. Lauber, J. G. Danzl, A. Janisch, H. P. Büchler, A. J. Daley, and H.-C. Nägerl. Preparation and spectroscopy of a metastable Mott-insulator state with attractive interactions. *Phys. Rev. Lett.*, 108:215302, 2012.

[178] M. Greiner, O. Mandel, T. W. Hänsch, and I. Bloch. Collapse and revival of the matter wave field of a Bose-Einstein condensate. *Nature*, 419:51–54, 2002.

[179] W. Krauth, M. Caffarel, and J.-P. Bouchaud. Gutzwiller wave function for a model of strongly interacting bosons. *Phys. Rev. B*, 45:3137–3140, 1992.

[180] K. Sheshadri, H. R. Krishnamurthy, R. Pandit, and T. V. Ramakrishnan. Superfluid and insulating phases in an interacting-boson model: Mean-field theory and the RPA. *Europhys. Lett.*, 22:257, 1993.

[181] D. van Oosten, P. van der Straten, and H. T. C. Stoof. Quantum phases in an optical lattice. *Phys. Rev. A*, 63:053601, 2001.

[182] S. Fölling, A. Widera, T. Müller, F. Gerbier, and I. Bloch. Formation of spatial shell structure in the superfluid to Mott insulator transition. *Phys. Rev. Lett.*, 97:060403, 2006.

[183] G. K. Campbell, J. Mun, M. Boyd, P. Medley, A. E. Leanhardt, L. G. Marcassa, D. E. Pritchard, and W. Ketterle. Imaging the Mott insulator shells by using atomic clock shifts. *Science*, 313(5787):649–652, 2005.

[184] S. L. Braunstein and C. M. Caves. Statistical distance and the geometry of quantum states. *Phys. Rev. Lett.*, 72:3439–3443, 1994.

[185] T. Stöferle, H. Moritz, C. Schori, M. Köhl, and T. Esslinger. Transition from a strongly interacting 1D superfluid to a Mott insulator. *Phys. Rev. Lett.*, 92:130403, 2004.

[186] S. Sachdev, K. Sengupta, and S. M. Girvin. Mott insulators in strong electric fields. *Phys. Rev. B*, 66:075128, 2002.

[187] C. Kollath, A. Iucci, T. Giamarchi, W. Hofstetter, and U. Schollwöck. Spectroscopy of ultracold atoms by periodic lattice modulations. *Phys. Rev. Lett.*, 97:050402, 2006.

[188] C. Kollath, U. Schollwöck, J. von Delft, and W. Zwerger. Spatial correlations of trapped one-dimensional bosons in an optical lattice. *Phys. Rev. A*, 69:031601, 2004.

[189] F. Gerbier, A. Widera, S. Fölling, O. Mandel, T. Gericke, and I. Bloch. Phase coherence of an atomic Mott insulator. *Phys. Rev. Lett.*, 95: 050404, 2005.

[190] E. Altman, E. Demler, and M. D. Lukin. Probing many-body states of ultracold atoms via noise correlations. *Phys. Rev. A*, 70:013603, 2004.

[191] S. Fölling, F. Gerbier, A. Widera, O. Mandel, T. Gericke, and I. Bloch. Spatial quantum noise interferometry in expanding ultracold atom clouds. *Nature*, 434:481–484, 2005.

[192] C. Weitenberg, P. Schauß, T. Fukuhara, M. Cheneau, M. Endres, I. Bloch, and S. Kuhr. Coherent light scattering from a two-dimensional Mott insulator. *Phys. Rev. Lett.*, 106:215301, 2011.

[193] R. B. Diener, Q. Zhou, H. Zhai, and T.-L. Ho. Criterion for bosonic superfluidity in an optical lattice. *Phys. Rev. Lett.*, 98:180404, 2007.

[194] Y. Kato, Q. Zhou, N. Kawashima, and N. Trivedi. Sharp peaks in the momentum distribution of bosons in optical lattices in the normal state. *Nature Phys.*, 4:617–621, 2008.

[195] M. Olshanii. Atomic scattering in the presence of an external confinement and a gas of impenetrable bosons. *Phys. Rev. Lett.*, 81:938–941, 1998.

[196] T. Bergeman, M. G. Moore, and M. Olshanii. Atom-atom scattering under cylindrical harmonic confinement: Numerical and analytic studies of the confinement induced resonance. *Phys. Rev. Lett.*, 91:163201, 2003.

[197] V. Dunjko, V. Lorent, and M. Olshanii. Bosons in cigar-shaped traps: Thomas-Fermi regime, Tonks-Girardeau regime, and in between. *Phys. Rev. Lett.*, 86(24):5413–5416, 2001.

[198] P. Pedri, L. Pitaevskii, S. Stringari, C. Fort, S. Burger, F. S. Cataliotti, P. Maddaloni, F. Minardi, and M. Inguscio. Expansion of a coherent array of Bose–Einstein condensates. *Phys. Rev. Lett.*, 87:220401, 2001.

[199] M. Girardeau. Relationship between systems of impenetrable bosons and fermions in one dimension. *J. Math. Phys.*, 1(516):8, 1960.

[200] G. Zürn, F. Serwane, T. Lompe, A. N. Wenz, M. G. Ries, J. E. Bohn, and S. Jochim. Fermionization of two distinguishable fermions. *Phys. Rev. Lett.*, 108:075303, 2012.

[201] T. Kinoshita, T. Wenger, and D. S. Weiss. Observation of a one-dimensional Tonks–Girardeau gas. *Science*, 305:1125–1128, 2004.

[202] E. H. Lieb and W. Liniger. Exact analysis of an interacting Bose gas. I. The general solution and the ground state. *Phys. Rev.*, 130:1605–1616, 1963.

[203] T. Giamarchi. *Quantum Physics in One Dimension*. Oxford University Press, New York, 2003.

[204] M. A. Cazalilla, R. Citro, T. Giamarchi, E. Orignac, and M. Rigol. One dimensional bosons: From condensed matter systems to ultracold gases. *Rev. Mod. Phys.*, 83:1405–1466, 2011.

[205] A. Tokuno and T. Giamarchi. Spectroscopy for cold atom gases in periodically phase-modulated optical lattices. *Phys. Rev. Lett.*, 106:205301, 2011.

[206] S.-i. Tomonaga. Remarks on Bloch's method of sound waves applied to many-fermion problems. *Prog. Theor. Phys.*, 5:544–569, 1950.

[207] J. M. Luttinger. An exactly soluble model of a many-fermion system. *J. Math. Phys.*, 4:1154, 1963.

[208] R. Roth and K. Burnett. Superfluidity and interference pattern of ultracold bosons in optical lattices. *Phys. Rev. A*, 67:031602, 2003.

[209] E. Toth and P. B. Blakie. Thermally induced coherence in a Mott insulator of bosonic atoms. *Phys. Rev. A*, 83:021601, 2011.

[210] S. Will, Th. Best, U. Schneider, L. Hackermüller, D.-S. Lühmann, and I. Bloch. Time-resolved observation of coherent multi-body interactions in quantum phase revivals. *Nature*, 465:197–201, 2010.

[211] S. Will, Th. Best, S. Braun, U. Schneider, and I. Bloch. Coherent interaction of a single fermion with a small bosonic field. *Phys. Rev. Lett.*, 106:115305, 2011.

[212] S. Trotzky, L. Pollet, F. Gerbier, U. Schnorrberger, I. Bloch, N. V. Prokof'ev, B. Svistunov, and M. Troyer. Suppression of the critical temperature for superfluidity near the Mott transition. *Nature Phys.*, 6: 998, 2010.

[213] E. Altman, A. Polkovnikov, E. Demler, B. I. Halperin, and M. D. Lukin. Superfluid-insulator transition in a moving system of interacting bosons. *Phys. Rev. Lett.*, 95:020402, 2005.

[214] C. D. Fertig, K. M. O'Hara, J. H. Huckans, S. L. Rolston, W. D. Phillips, and J. V. Porto. Strongly inhibited transport of a degenerate 1D Bose gas in a lattice. *Phys. Rev. Lett.*, 94:120403, 2005.

[215] J. Mun, P. Medley, G. K. Campbell, L. G. Marcassa, D. E. Pritchard, and W. Ketterle. Phase diagram for a Bose–Einstein condensate moving in an optical lattice. *Phys. Rev. Lett.*, 99:150604, 2007.

[216] D. Clément, N. Fabbri, L. Fallani, C. Fort, and M. Inguscio. Exploring correlated 1D Bose gases from the superfluid to the Mott-insulator state by inelastic light scattering. *Phys. Rev. Lett.*, 102:155301, 2009.

[217] P. T. Ernst, S. Götze, J. S. Krauser, Karsten Pyka, D.-S. Lühmann, D. Pfannkuche, and K. Sengstock. Probing superfluids in optical lattices by momentum-resolved Bragg spectroscopy. *Nature Phys.*, 6(1):56–61, 2010.

[218] R. Ma, M. E. Tai, P. M. Preiss, W. S. Bakr, J. Simon, and M. Greiner. Photon-assisted tunneling in a biased strongly correlated Bose gas. *Phys. Rev. Lett.*, 107:095301, 2011.

[219] D. Pertot, B. Gadway, and D. Schneble. Collinear four-wave mixing of two-component matter waves. *Phys. Rev. Lett.*, 104:200402, 2010.

[220] I. B. Spielman, W. D. Phillips, and J. V. Porto. Mott-insulator transition in a two-dimensional atomic Bose gas. *Phys. Rev. Lett.*, 98:080404, 2007.

[221] A. Hu, L. Mathey, I. Danshita, E. Tiesinga, C. J. Williams, and C. W. Clark. Counterflow and paired superfluidity in one-dimensional Bose mixtures in optical lattices. *Phys. Rev. A*, 80:023619, 2009.

[222] H. J. Briegel and R. Raussendorf. Persistent entanglement in arrays of interacting particles. *Phys. Rev. Lett.*, 86:910–913, 2001.

[223] O. Mandel, M. Greiner, A. Widera, T. Rom, T. W. Hänsch, and I. Bloch. Coherent transport of neutral atoms in spin-dependent optical lattice potentials. *Phys. Rev. Lett.*, 91:010407, 2003.

[224] O. Mandel, M. Greiner, A. Widera, T. Rom, T. W. Hänsch, and I. Bloch. Controlled collisions for multi-particle entanglement of optically trapped atoms. *Nature*, 425:937–940, 2003.

[225] M. F. Riedel, P. Böhi, Y. Li, T. W. Hänsch, A. Sinatra, and P. Treutlein. Atom-chip-based generation of entanglement for quantum metrology. *Nature*, 464:1170–1173, 2010.

[226] J. Catani, G. Lamporesi, D. Naik, M. Gring, M. Inguscio, F. Minardi, A. Kantian, and T. Giamarchi. Quantum dynamics of impurities in a one-dimensional Bose gas. *Phys. Rev. A*, 85:023623, 2012.

[227] H. Ott, E. de Mirandes, F. Ferlaino, G. Roati, G. Modugno, and M. Inguscio. Collisionally induced transport in periodic potentials. *Phys. Rev. Lett.*, 92:160601, 2004.

[228] M. Bruderer, T. H. Johnson, S. R. Clark, D. Jaksch, A. Posazhennikova, and W. Belzig. Phonon resonances in atomic currents through Bose–Fermi mixtures in optical lattices. *Phys. Rev. A*, 82:043617, 2010.

[229] J. Hader, T. Meier, S. W. Koch, F. Rossi, and N. Linder. Microscopic theory of the intracollisional field effect in semiconductor superlattices. *Phys. Rev. B*, 55:13799–13807, 1997.

[230] T. Dekorsy, A. Bartels, H. Kurz, K. Köhler, R. Hey, and K. Ploog. Coupled Bloch-phonon oscillations in semiconductor superlattices. *Phys. Rev. Lett.*, 85:1080–1083, 2000.

[231] A. W. Ghosh, L. Jönsson, and J. W. Wilkins. Bloch oscillations in the presence of plasmons and phonons. *Phys. Rev. Lett.*, 85:1084–1087, 2000.

[232] A. J. Leggett, S. Chakravarty, A. T. Dorsey, M. P. A. Fisher, A. Garg, and W. Zwerger. Dynamics of the dissipative two-state system. *Rev. Mod. Phys.*, 59:1–85, 1987.

[233] A. Recati, P. O. Fedichev, W. Zwerger, J. von Delft, and P. Zoller. Atomic quantum dots coupled to a reservoir of a superfluid Bose–Einstein condensate. *Phys. Rev. Lett.*, 94:040404, 2005.

[234] P. P. Orth, I. Stanic, and K. Le Hur. Dissipative quantum Ising model in a cold-atom spin-boson mixture. *Phys. Rev. A*, 77:051601, 2008.

[235] I. de Vega, J. I. Cirac, and D. Porras. Detection of spin correlations in optical lattices by light scattering. *Phys. Rev. A*, 77:051804, 2008.

[236] A. Griessner, A. J. Daley, S. R. Clark, D. Jaksch, and P. Zoller. Dark-state cooling of atoms by superfluid immersion. *Phys. Rev. Lett.*, 97: 220403, 2006.

[237] S. Diehl, A. Micheli, A. Kantian, B. Kraus, H. P. Büchler, and P. Zoller. Quantum states and phases in driven open quantum systems with cold atoms. *Nature Phys.*, 4:878–883, 2008.

[238] D. McKay and B. DeMarco. Thermometry with spin-dependent lattices. *New J. Phys.*, 12:055013, 2010.

[239] G. Birkl, M. Gatzke, I. H. Deutsch, S. L. Rolston, and W. D. Phillips. Bragg scattering from atoms in optical lattices. *Phys. Rev. Lett.*, 75: 2823–2826, 1995.

[240] M. Weidemüller, A. Hemmerich, A. Görlitz, T. Esslinger, and T. W. Hänsch. Bragg diffraction in an atomic lattice bound by light. *Phys. Rev. Lett.*, 75:4583–4586, 1995.

[241] H. Miyake, G. A. Siviloglou, G. Puentes, D. E. Pritchard, W. Ketterle, and D. M. Weld. Bragg scattering as a probe of atomic wave functions and quantum phase transitions in optical lattices. *Phys. Rev. Lett.*, 107: 175302, 2011.

[242] G. Breit and I. I. Rabi. Measurement of nuclear spin. *Phys. Rev.*, 38: 2082–2083, 1931.

[243] M.-O. Mewes, M. R. Andrews, D. M. Kurn, D. S. Durfee, C. G. Townsend, and W. Ketterle. Output coupler for Bose-Einstein condensed atoms. *Phys. Rev. Lett.*, 78:582–585, 1997.

[244] J. Kronjäger, C. Becker, P. Navez, K. Bongs, and K. Sengstock. Magnetically tuned spin dynamics resonance. *Phys. Rev. Lett.*, 97:110404, 2006.

[245] F. Gerbier, A. Widera, S. Fölling, O. Mandel, and I. Bloch. Resonant control of spin dynamics in ultracold quantum gases by microwave dressing. *Phys. Rev. A*, 73:041602, 2006.

[246] E. M. Bookjans, A. Vinit, and C. Raman. Quantum phase transition in an antiferromagnetic spinor Bose–Einstein condensate. *Phys. Rev. Lett.*, 107:195306, 2011.

[247] C. Gross, H. Strobel, E. Nicklas, T. Zibold, N. Bar-Gill, G. Kurizki, and M. K. Oberthaler. Atomic homodyne detection of continuous-variable entangled twin-atom states. *Nature*, 480:219–223, 2011.

[248] I. H. Deutsch and P. S. Jessen. Quantum-state control in optical lattices. *Phys. Rev. A*, 57:1972–1986, 1998.

[249] D. Jaksch, H.-J. Briegel, J. I. Cirac, C. W. Gardiner, and P. Zoller. Entanglement of atoms via cold controlled collisions. *Phys. Rev. Lett.*, 82:1975–1978, 1999.

[250] L. J. LeBlanc and J. H. Thywissen. Species-specific optical lattices. *Phys. Rev. A*, 75:053612, 2007.

[251] R. Grimm, M. Weidemüller, and Y. B. Ovchinnikov. Optical dipole traps for neutral atoms. *Adv. At. Mol. Opt. Phys.*, 42:95, 2000.

[252] M. Ben Dahan, E. Peik, J. Reichel, Y. Castin, and C. Salomon. Bloch oscillations of atoms in an optical potential. *Phys. Rev. Lett.*, 76:4508–4511, 1996.

[253] L. Fallani, L. De Sarlo, J. E. Lye, M. Modugno, R. Saers, C. Fort, and M. Inguscio. Observation of dynamical instability for a Bose–Einstein condensate in a moving 1D optical lattice. *Phys. Rev. Lett.*, 93:140406, 2004.

[254] S. Hoinka, M. Lingham, M. Delehaye, and C. J. Vale. Dynamic spin response of a strongly interacting Fermi gas. *arXiv:1203.4657v1*, 2012.

[255] J. Struck, C. Ölschläger, M. Weinberg, P. Hauke, J. Simonet, A. Eckardt, M. Lewenstein, K. Sengstock, and P. Windpassinger. Tunable gauge potential for neutral and spinless particles in driven optical lattices. *Phys. Rev. Lett.*, 108:225304, 2012.

[256] Y.-J. Lin, K. Jiménez-Garcia, and I. B. Spielman. Spin-orbit-coupled Bose-Einstein condensates. *Nature*, 471:83–86, 2011.

[257] P. W. Anderson. Theory of dirty superconductors. *J. Phys. Chem. Solids*, 11:26, 1959.

[258] W. Krauth, N. Trivedi, and D. Ceperley. Superfluid-insulator transition in disordered boson systems. *Phys. Rev. Lett.*, 67:2307–2310, 1991.

[259] G. Roux, T. Barthel, I. P. McCulloch, C. Kollath, U. Schollwöck, and T. Giamarchi. Quasiperiodic Bose-Hubbard model and localization in one-dimensional cold atomic gases. *Phys. Rev. A*, 78:023628, 2008.

[260] L. Pollet, N. V. Prokof'ev, B. V. Svistunov, and M. Troyer. Absence of a direct superfluid to Mott insulator transition in disordered Bose systems. *Phys. Rev. Lett.*, 103:140402, 2009.

[261] T. Roscilde. Bosons in one-dimensional incommensurate superlattices. *Phys. Rev. A*, 77:063605, 2008.

[262] P. Buonsante, F. Massel, V. Penna, and A. Vezzani. Gutzwiller approach to the Bose-Hubbard model with random local impurities. *Phys. Rev. A*, 79:013623, 2009.

[263] P. Lugan, D. Clément, P. Bouyer, A. Aspect, M. Lewenstein, and L. Sanchez-Palencia. Ultracold Bose gases in 1D disorder: From Lifshits glass to Bose-Einstein condensate. *Phys. Rev. Lett.*, 98:170403, 2007.

[264] R. C. Kuhn, O. Sigwarth, C. Miniatura, D. Delande, and C. A. Müller. Coherent matter wave transport in speckle potentials. *New J. Phys.*, 9: 161, 2007.

[265] R. T. Scalettar, G. G. Batrouni, and G. T. Zimanyi. Localization in interacting, disordered, Bose systems. *Phys. Rev. Lett.*, 66:3144–3147, 1991.

[266] D. Delande and J. Zakrzewski. Compression as a tool to detect Bose glass in a cold atomic gas. *Phys. Rev. Lett.*, 102:085301, 2009.

[267] D. Heidarian and N. Trivedi. Inhomogeneous metallic phase in a disordered Mott insulator in two dimensions. *Phys. Rev. Lett.*, 93:126401, 2004.

[268] M. Snoek, I. Titvinidze, I. Bloch, and W. Hofstetter. Effect of interactions on harmonically confined Bose-Fermi mixtures in optical lattices. *Phys. Rev. Lett.*, 106:155301, 2011.

[269] M. Cramer. Interaction-dependent temperature effects in Bose-Fermi mixtures in optical lattices. *Phys. Rev. Lett.*, 106:215302, 2011.

[270] A. B. Kuklov and B. V. Svistunov. Testing quantum correlations in a confined atomic cloud by the scattering of fast atoms. *Phys. Rev. A*, 60: R769–R772, 1999.

[271] J. Javanainen and J. Ruostekoski. Optical detection of fractional particle number in an atomic Fermi-Dirac gas. *Phys. Rev. Lett.*, 91:150404, 2003.

[272] T. A. Corcovilos, S. K. Baur, J. M. Hitchcock, E. J. Mueller, and R. G. Hulet. Detecting antiferromagnetism of atoms in an optical lattice via optical Bragg scattering. *Phys. Rev. A*, 81:013415, 2010.

[273] J. M. Pino, R. J. Wild, P. Makotyn, D. S. Jin, and E. A. Cornell. Photon counting for Bragg spectroscopy of quantum gases. *Phys. Rev. A*, 83: 033615, 2011.

[274] T. Kinoshita, T. Wenger, and D. S. Weiss. A quantum Newton's cradle. *Nature*, 440:900–903, 2006.

[275] S. Palzer, C. Zipkes, C. Sias, and M. Köhl. Quantum transport through a Tonks-Girardeau gas. *Phys. Rev. Lett.*, 103(15):150601, 2009.

[276] S. Bose and V. Korepin. Quantum gates between flying qubits via spin-independent scattering. *arXiv:1106.2329v1*, 2011.

[277] M. D. Reid and P. D. Drummond. Quantum correlations of phase in nondegenerate parametric oscillation. *Phys. Rev. Lett.*, 60:2731–2733, 1988.

[278] L.-M. Duan, G. Giedke, J. I. Cirac, and P. Zoller. Inseparability criterion for continuous variable systems. *Phys. Rev. Lett.*, 84:2722–2725, 2000.

[279] N. Fabbri, D. Clément, L. Fallani, C. Fort, and M. Inguscio. Momentum-resolved study of an array of one-dimensional strongly phase-fluctuating Bose gases. *Phys. Rev. A*, 83:031604, 2011.

[280] D. M. Weld, P. Medley, H. Miyake, D. Hucul, D. E. Pritchard, and W. Ketterle. Spin gradient thermometry for ultracold atoms in optical lattices. *Phys. Rev. Lett.*, 103:245301, 2009.

[281] G. Barontini and M. Modugno. Instabilities of a matter wave in a matter grating. *Phys. Rev. A*, 80:063613, 2009.

[282] M. Albert, T. Paul, N. Pavloff, and P. Leboeuf. Dipole oscillations of a Bose–Einstein condensate in the presence of defects and disorder. *Phys. Rev. Lett.*, 100(25):250405, 2008.

[283] C. M. Fabre, P. Cheiney, G. L. Gattobigio, F. Vermersch, S. Faure, R. Mathevet, T. Lahaye, and D. Guéry-Odelin. Realization of a distributed Bragg reflector for propagating guided matter waves. *Phys. Rev. Lett.*, 107:230401, 2011.

[284] A. Micheli, A. J. Daley, D. Jaksch, and P. Zoller. Single atom transistor in a 1D optical lattice. *Phys. Rev. Lett.*, 93:140408, 2004.

[285] M. Bruderer and W. Belzig. Mesoscopic transport of fermions through an engineered optical lattice connecting two reservoirs. *Phys. Rev. A*, 85:013623, 2012.

[286] D. McKay and B. DeMarco. Cooling in strongly correlated optical lattices: prospects and challenges. *Rep. Prog. Phys.*, 74:054401, 2011.

[287] P. B. Blakie and J. V. Porto. Adiabatic loading of bosons into optical lattices. *Phys. Rev. A*, 69:013603, 2004.

[288] K. W. Madison, F. Chevy, V. Bretin, and J. Dalibard. Stationary states of a rotating Bose-Einstein condensate: Routes to vortex nucleation. *Phys. Rev. Lett.*, 86:4443–4446, 2001.

[289] C. Raman, J. R. Abo-Shaeer, J. M. Vogels, K. Xu, and W. Ketterle. Vortex nucleation in a stirred Bose-Einstein condensate. *Phys. Rev. Lett.*, 87:210402, 2001.

[290] G. Pupillo, A. Griessner, A. Micheli, M. Ortner, D.-W. Wang, and P. Zoller. Cold atoms and molecules in self-assembled dipolar lattices. *Phys. Rev. Lett.*, 100:050402, 2008.

[291] M. Erhard, H. Schmaljohann, J. Kronjäger, K. Bongs, and K. Sengstock. Measurement of a mixed-spin-channel Feshbach resonance in ^{87}Rb. *Phys. Rev. A*, 69:032705, 2004.

[292] A. Widera, O. Mandel, M. Greiner, S. Kreim, T. W. Hänsch, and I. Bloch. Entanglement interferometry for precision measurement of atomic scattering properties. *Phys. Rev. Lett.*, 92:160406, 2004.

[293] N. Gemelke, E. Sarajlic, Y. Bidel, S. Hong, and S. Chu. Parametric amplification of matter waves in periodically translated optical lattices. *Phys. Rev. Lett.*, 95:170404, 2005.

[294] H. Lignier, C. Sias, D. Ciampini, Y. Singh, A. Zenesini, O. Morsch, and E. Arimondo. Dynamical control of matter-wave tunneling in periodic potentials. *Phys. Rev. Lett.*, 99:220403, 2007.

[295] A. Zenesini, H. Lignier, D. Ciampini, O. Morsch, and E. Arimondo. Coherent control of dressed matter waves. *Phys. Rev. Lett.*, 102:100403, 2009.

[296] J. Struck, C. Ölschläger, R. Le Targat, P. Soltan-Panahi, A. Eckhard, M. Lewenstein, P. Windpassinger, and K. Sengstock. Quantum simulation of frustrated classical magnetism in triangular optical lattices. *Science*, 333:996–999, 2011.

[297] K. Le Hur. Entanglement entropy, decoherence, and quantum phase transitions of a dissipative two-level system. *Ann. Phys.*, 323:2208–2240, 2008.

[298] D. Witthaut. Quantum walks and quantum simulations with Bloch-oscillating spinor atoms. *Phys. Rev. A*, 82:033602, 2010.

[299] A. Ossipov, D. M. Basko, and V. E. Kravtsov. A super-Ohmic energy absorption in driven quantum chaotic systems. *Eur. Phys. J. B*, 42: 457–460, 2004.

[300] J. H. Bardarson, J. Tworzydło, and C. W. J. Beenakker. Stroboscopic model of transport through a quantum dot with spin-orbit scattering. *Phys. Rev. B*, 72:235305, 2005.

Appendix A

Delocalization of a spinful kicked rotor

In this chapter, we consider (in simulations) a problem similar to that addressed experimentally in Chapter 5, namely the dynamical response of a matter-wave field to time-dependent "kicking" with an optical lattice. However, instead of studying the influence of spatial quasidisorder on kicked rotor behavior, here we consider "spinful" δ-kicking of a quantum rotor system, for which the atoms are driven in a pseudorandom, aperiodic way by both lattice pulses and spin rotations. As we will show, this analogously leads to classical diffusion in momentum space.

A.1 Introductory discussion

Coherent spin-dependent transport of atomic matter-waves has been considered recently in several contexts, including the generation of entanglement [223] and for quantum simulation of charged particles [298]. Some recent proposals [175, 299, 300] have considered using spin-dependent "kicking" of cold atoms (in a kicked-rotor type experiment) to study the influence of spin-orbit coupling, i.e. broken time-reversal symmetry, on localization phenomena of charged particles. In the spirit of studying the effects of spin-orbit coupling on Anderson localization, here we consider a very simple case of the spinful kicked rotor, where non-interacting atoms are periodically kicked by a lattice that is completely state-selective (as described in Chapter 8), and couples different plane-wave momentum orders. Between each lattice kick, a variable spin-rotation is applied to the atoms, causing coherent transitions between two internal states. We find that for certain spin rotations applied, a breakdown of dynamical localization is achieved, leading to classical-like diffusion

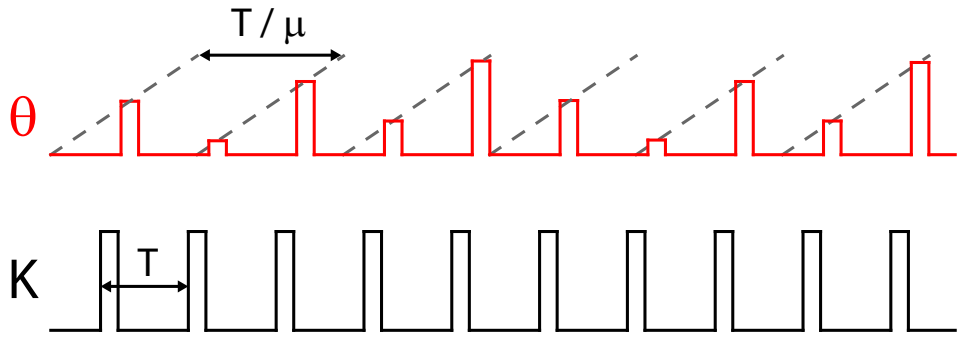

Figure A.1: Periodic driving of a matter-wave field by external (lattice pulse) and internal (spin rotation) state driving. Lattice pulses (at bottom) with kicking strength K occur with a frequency $2\pi/T$, and periodic spin rotations (at top, occurring with the same frequency) by an amount θ, where θ (modulo 2π) varies at a frequency $2\pi\mu/T$.

in momentum space, similar to the case of two incommensurate lattices in Chapter 5.

A.2 System under consideration

We consider a collection of non-interacting atoms beginning in the plane-wave state with zero momentum, approximately realized by a weakly-trapped Bose–Einstein condensate. We consider the case of two internal states of the atoms, $|a\rangle$ and $|b\rangle$ (e.g. as with hyperfine states $|1,-1\rangle$ and $|2,-2\rangle$), where the possibility of coherent internal state manipulation is assumed, for example by applying resonant microwave radiation. Furthermore, we consider an optical lattice oriented along one axis, with wavelength λ and wave number $k = 2\pi/\lambda$. This lattice is assumed to be state-selective, addressing only atoms in the internal state $|a\rangle$, with a depth measured as sE_R ($E_R = \hbar^2k^2/2M$ the recoil energy and M the atomic mass). A train of N pulses of this state-selective lattice act on the atoms, having duration τ and periodic spacing T, and the strength of the lattice is the same for each of the pulses (labeled $j \in \{1, N\}$).

For internal state manipulation we assume that some short fixed time ϵ after the j-th lattice-pulse, a δ-like (in time) microwave spin-rotation by an angle θ_j is performed (where a π rotation relates to a spin flip from $|a\rangle$ to $|b\rangle$, $|b\rangle$ to $-|a\rangle$), where the subscript j denotes that, unlike for the lattice-kicking, the rotation amount is not the same for each pulse. As shown in Fig. A.1, to realize the case of two-frequency driving (at frequencies $2\pi/T$ and $2\pi\mu/T$) we

define the j-dependent spin-rotation angles as

$$\theta_j = \theta_0 + 2\pi\mu j \ . \tag{A.1}$$

The rotation angle θ_j thus increases linearly with the pulse-number j, and modulo 2π it varies periodically (in the saw-tooth pattern shown in Fig A.1 with frequency $2\pi\mu/T$. The case of $\mu = 1$ corresponds to commensurate frequencies, where the spin is flipped by the same amount every period. We note that the results that follow are found to be generalizable to other periodic forms, such as $\theta_j = \theta_0 + 2\pi\alpha\cos^2(\mu\pi j)$. Also, while we have considered discrete-time spin-rotations, these results should likely be generalizable to having a transverse field always on, with its strength varying in a time-periodic way (neglecting effects of the state-selective light-shifts on the microwave transitions and effects of microwave dressing on the state-selective lattice).

In what follows, we write the Hamiltonian in the form of a δ-kicked rotor, while in the simulations that follow we fully take into account the finite pulse length (assumed to be $\tau = 10$ ns). Additionally, we restrict ourselves to a discrete basis of plane wave states as in Chapter 5, here with states $|m\rangle$ having momenta $p_m = 2m\hbar k$. We then write the Hamiltonian as

$$\hat{H} = \hat{H}_0 + \hbar\hat{\phi}_L \sum_{j=1}^{N} \delta(t - jT) + \hbar \sum_{j=1}^{N} (\theta_j/2)\hat{\sigma}_y \delta(t - jT - \epsilon) \ , \tag{A.2}$$

where $\hat{H}_0 = (\hbar\kappa/2T)\sum_m m^2\hat{n}_m$ is the time-independent kinetic energy part of the Hamiltonian, the term

$$\hat{\phi}_L = \frac{K}{\kappa}\frac{(\hat{\sigma}_0 + \hat{\sigma}_z)}{2} \bigotimes \sum_m (\hat{a}^\dagger_{m+1}\hat{a}_m + \hat{a}^\dagger_{m-1}\hat{a}_m) \ , \tag{A.3}$$

accounts for state-selective lattice pulsing, and the final term accounts for the spin rotations (we have neglected spin-dependent phase accrual in the form of scalar $\hat{\sigma}_z$ terms). Here, the term $\kappa = 8E_R T/\hbar$ defines the resonances of the rotor (occurring for rational values of $\kappa/4\pi$) and $K = \kappa s E_R \tau/2\hbar$ is the stochasticity parameter, which delineates regimes of classically regular and chaotic motion. The Pauli matrices used are given by $\hat{\sigma}_0 = |a\rangle\langle a| + |b\rangle\langle b|$, $\hat{\sigma}_y = -i(|a\rangle\langle b| - |b\rangle\langle a|)$, and $\hat{\sigma}_z = |a\rangle\langle a| - |b\rangle\langle b|$. The terms $\hat{n}_m$ and $\hat{a}^\dagger_m$ ($\hat{a}_m$) are the number operator and creation (annihilation) operator for the momentum mode $|m\rangle$.

In the following section, we shall present some numerical results for the dynamical response of a spinful quantum field to spin-dependent lattice kicking and spin-rotations, as a function of the kick number N, as well as of the tunable

parameters K (relating to lattice depth) and μ (relating to the ratio of the kicking frequency to the frequency at which the microwave spin-rotation rate evolves).

A.3 Numerical simulations

We consider the case of off-resonant kicking with a lattice of wavelength $\lambda = 785.5$ nm, where the fixed pulse period $T = 29$ μs relates to $\kappa/4\pi \approx 0.43$, such that kicking the $|a\rangle$ atoms alone leads to dynamical localization (and a fixed pulse duration $\tau = 10$ ns). If no spin-rotations are applied, neither is any increase in energy achieved for mixtures of the two species (as the atoms are assumed non-interacting). Additionally, if the atoms are kicked by only a single state-independent lattice (addressing both states equally), dynamical localization is observed regardless of the form of the spin-rotation applied.

We first examine the dependence of growth on the incommensurability of the kicking frequency and the frequency at which the spin-rotation evolves, characterized by the ratio μ, where for $\mu = 0$ or 1 the same spin rotation is performed each time step. Prior to the first lattice kick, we begin with an equal superposition of the two spin states. In the definition of the j-dependent spin rotations of Eq. A.1, we set $\theta_0 = 0$, without loss of generality. To characterize the dynamical response of the system, we fit a linear dependence of the energy per atom ε (in units E_R) on the pulse number N, i.e. a rate of growth $\Delta\varepsilon/\Delta N$, fit in the range $N = 1$ to $N = 200$ pulses. We assume that a linear dependence will be a reasonable approximation to the dynamical response, for either the case of dynamical localization (where $\Delta\varepsilon/\Delta N$ will be zero) or for induced classical diffusion where we expect $\varepsilon \propto N$.

In Fig. A.2, we plot the value of this growth rate $\Delta\varepsilon/\Delta N$ as a function of the commensurability parameter μ (in a limited range), for a kicking strength of $K = 3.17$. We observe that when μ is equal to a rational number - such as for 1/2, 4/7, 3/5, 5/8, 2/3, etc. - there is very little growth (with essentially no growth for $\mu = 0, 0.5, 1$), while otherwise non-zero growth rates can be found for irrational values. This is consistent with the expectation that the addition of an incommensurate second frequency should lead to a disruption of the quantum interference that causes dynamical localization. In Fig. A.2, we also point out three values of μ in particular, which we will examine in more detail as follows. These values are $\mu = 0.6$ (rational number with small amount of continued fraction elements), 0.502 (rational number near to 1/2 and with slightly more continued fraction elements) and $2/(1+\sqrt{5}) = 0.618...$ (irrational number, the golden ratio).

We now look directly at the temporal (N) dependence for each of these

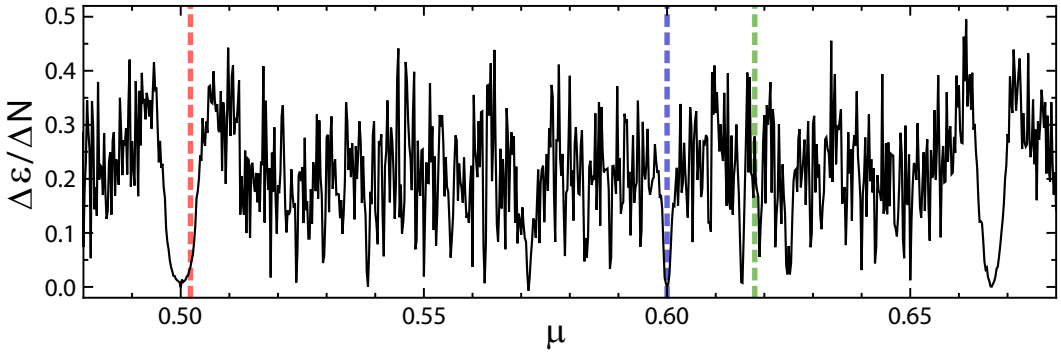

Figure A.2: Dependence of energy growth rate on the commensurability of lattice kicking and spin rotation frequencies. (a) Growth rate of the average energy per kick N, $\Delta\varepsilon/\Delta N$, as a function of the incommensurability parameter μ. The growth rate is fit between $N = 1$ and 200 kicks, for a stochasticity parameter of $K = 3.17$. The values of $\mu = 0.502$, 0.6, and 0.618034... (the golden ratio) are highlighted, as they will be examined further.

values of μ, for three different kicking strengths $K = 1.585$, 3.170, and 4.755. What we observe is that for the most rational value, $\mu = 0.6$, an oscillatory behavior is generally observed, with destructive interference causing dynamical localization. However, for very large kicking strength, some growth (possibly transient over $N = 200$ kicks) is observed. We note that by looking at the mean-energy per spin-state (as in the inset for $\mu = 0.6$ and $K = 4.755$), oscillations of a greater magnitude can often be seen than in the spin-averaged energy. The suppression of growth for rational values of μ seems to rely on a fine cancellation of this behavior. We observe for values of μ slightly away from ratios of small integers, such as for 0.502, net growth in energy with N can be achieved. For completely irrational values such as for the golden ratio, we observe that the spin-dependent kicking always leads to an essentially linear increase of ε with N, consistent with classical-like diffusion.

Lastly, we determine the dependence of the growth rate $\Delta\varepsilon/\Delta N$ on the stochasticity parameter K. We find that the rational value of $\mu = 0.6$ has a growth rate of essentially zero for most values of K (and the non-zero value at large K may be only a transient effect), and the value of $\mu = 0.502$ has a slightly irregular dependence on K, albeit with non-zero values. For the irrational ratio of the spin-rotation evolution to the kicking frequency, $\mu = 0.618...$, we find the dependence on K is in good agreement with the classical diffusion rate $D = K^2/2\kappa^2$ (with $\kappa \approx 5.42$), i.e. also suggesting that classical-like diffusion in momentum-space is occurring due to the addition of the incommensurate frequency component.

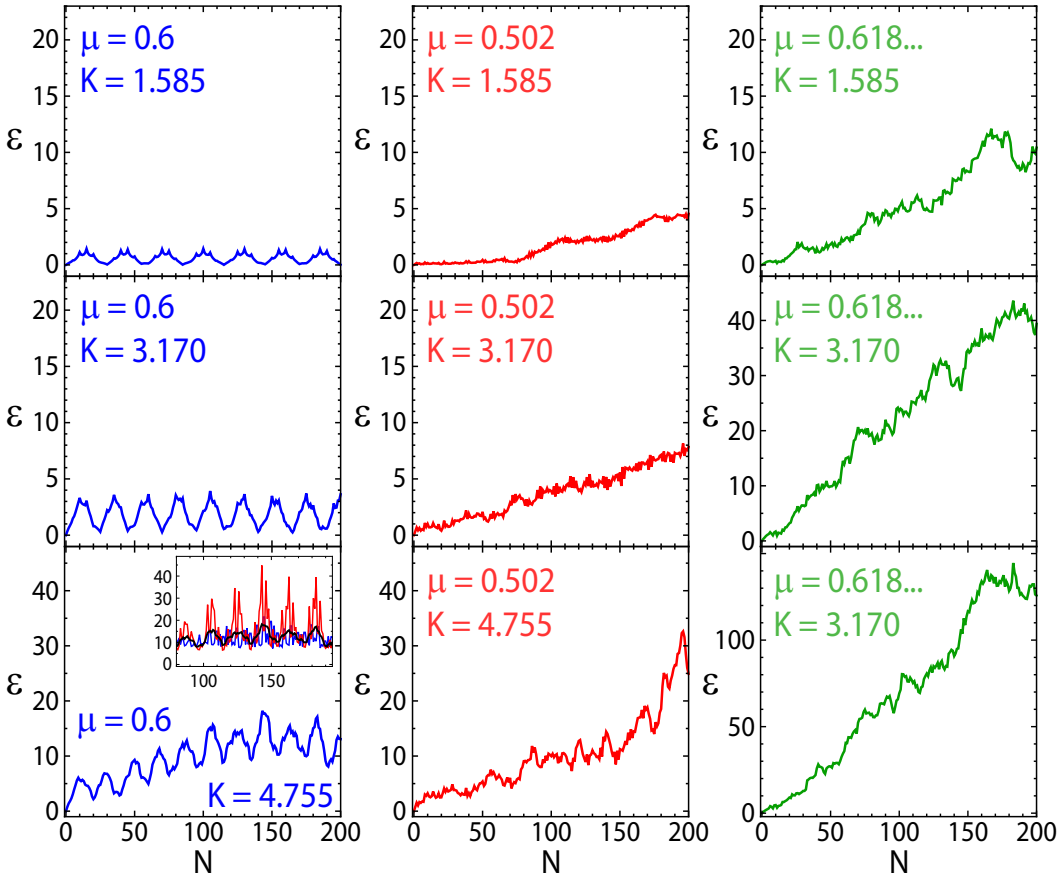

Figure A.3: Dynamics of the mean energy with increasing kick number, for different kicking strengths K and spin-rotation evolution frequencies (μ). Three stacks of plots are shown for different values of μ, with the most commensurate values on the left ($\mu = 0.6$), moving to the most incommensurate at right ($\mu = 0.502$ and $\mu = 0.618...$). For each value of μ, we show the dependence of the particle energy ε on the kick number N, for kicking strengths $K = 1.585$, 3.170, and 4.755. As an inset for the case $\mu = 0.6$ and $K = 4.755$, we show the dynamics of the total energy (black) as well as that of the $|a\rangle$ state (red) and $|b\rangle$ state (blue). Note the different scales of the energy axis for the different cases.

A.4 Concluding remarks

In conclusion, we have performed numerical simulations of a simple situation of spinful kicking of a quantum rotor, leading to classical-like diffusion when multi-frequency driving at incommensurate frequencies is present. This example highlights how added spectral noise can cause a breakdown of quantum

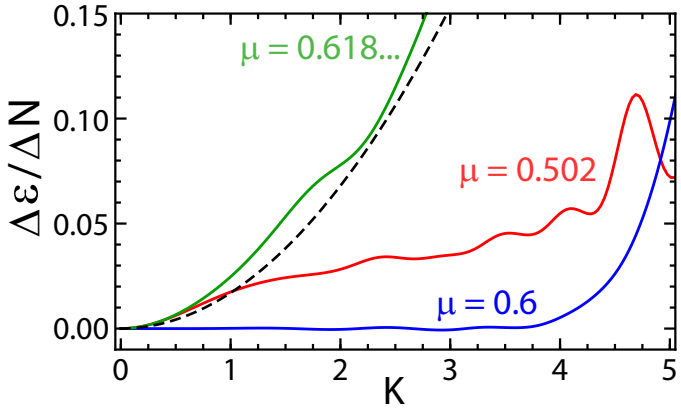

Figure A.4: Dependence of the energy growth rate $\Delta\varepsilon/\Delta N$ on the spin-selective stochasticity parameter K, as determined by a linear fit from $N = 1$ to 200 kicks. We plot the dependence on K for the cases of $\mu = 0.6$ (blue line), $\mu = 0.502$ (red line), $\mu = 2/(1+\sqrt{5}) = 0.618...$ (green line). We also show the expected classical diffusion constant $D = K^2/2\kappa^2$ (dashed black line).

interference phenomena, and also how non-separable coupling between internal and external degrees of freedom can affect the localization of spinful quantum fields.